Catalyst Pore Space Exploration using Fluorescence and X-Ray Microscopy Techniques

RAFAEL MAYORGA GONZÁLEZ

Catalyst Pore Space Exploration using Fluorescence and X-Ray Microscopy Techniques

Verkenning van de poriënruimte van katalysatoren met behulp van fluorescentie- en röntgenmicroscopietechnieken

(met een samenvatting in het Nederlands)

Proefschrift

ter verkrijging van de graad van doctor aan de
Universiteit Utrecht
op gezag van de
rector magnificus, prof. dr. H.R.B.M. Kummeling,
ingevolge het besluit van het College voor Promoties
in het openbaar te verdedigen op

maandag 1 juli 2024 des middags te 12.15 uur

door

Rafael Mayorga González

geboren op 10 september 1992

te Lima, Peru

Promotors:

Prof. dr. ir. B.M. Weckhuysen (UU)

Prof. ir. A. van den Berg (UT)

Copromotors:

Dr. F. Meirer (UU)

Dr. M. Odijk (UT)

Beoordelingscommissie:

Prof. dr. S.A. Blum

Prof. dr. K.F. Domke

Prof. dr. A. Meijerink

Prof. dr. ir. M. Roeffaers

Prof. dr. ir. V. van Speybroeck

The degree is awarded as part of a Joint Doctorate with Universiteit Twente.

Dit werk werd financieel ondersteund door het Netherlands Center for Multiscale Catalytic Energy Conversion (MCEC)

Contents

1 Introduction

1.1 Catalysis and the Role of Elementary Transport and Reaction Steps

A catalyst is a material that increases the rate of a chemical reaction without being consumed in the process. This is achieved by the creation of an alternative reaction pathway that has a lower activation energy (Figure 1.1). The lowering of the activation energy allows different things: 1) reactions can take place at lower energies and pressures than without a catalyst, which increases the energy efficiency of the process. 2) If several reactions are competing against each other, increasing the reaction rate of the desired product can increase its selectivity towards it. This results in fewer by-products and therefore a higher atomic efficiency of the process. Because of this, catalysts are crucial to make chemical processes more sustainable.[1]

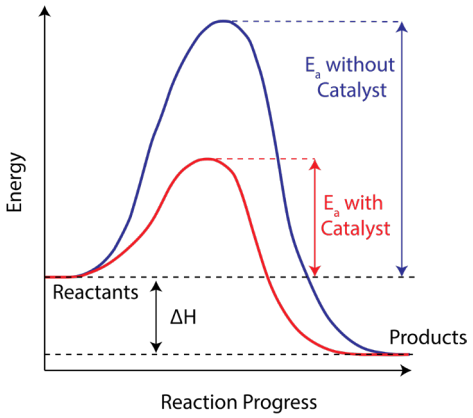

Figure 1.1 Schematic plot of the energy during a reaction process with and without a catalyst. The reaction enthalpy ΔH is the same for both cases. However, the activation energy E_a is lower in the catalyzed process. Figure adapted from Hanefeld et al.[2]

Catalysts are usually divided into two categories based on their state of matter: homogeneous catalysts are in the same phase as the reactants (mostly both are liquids). In heterogeneous catalysis, on the other hand, the catalyst is a solid, while the reactants can be liquid and/or gaseous. Since the catalyst and the reactants are not in the same phase, the separation of products is facilitated compared to homogeneous catalysts.[2] Because of this, and due to their comparably long lifetimes, heterogeneous catalysts are widely used in industrial processes.[1]

1.1.1 Porosity and Mass Transfer Properties

The reaction takes place at the active sites of a catalyst, which are usually metal nano particles or solid acid sites (e.g., Zeolites). Since the reaction rates increase with the number of available active sites, porous materials (mostly metal oxides) are used to support the active sites while keeping them accessible. Moreover, these support materials also provide chemical, thermal, and mechanical stability to the catalyst and in the case of metal active sites they can prevent deactivation due to sintering of the nanoparticles.[2]

The actual chemical reaction rate taking place at the active sites increases with the reactant concentration. However, this concentration can vary strongly in a reactor and within a catalyst particle, which also is true for the reaction products. Therefore, seven steps influence the effective reaction rate of a heterogeneous catalyst (see Figure 1.2). 1) The reactants need to diffuse from the

bulk fluid into the particle. Since the reactant is being consumed, its concentration will be lower in the particle than in the bulk of the fluid. As a consequence, a so-called stagnant layer is formed. This is a region adjacent to the particle surface that shows a gradient in reactant concentration and that does not move relative to the particle. The width of the stagnant layer depends on the fluid properties and the flow conditions in the reactor. For example, if there is no flow, the width of the stagnant layer will be larger, and the reactant concentration will be lower at the particle surface compared to the bulk of the fluid, slowing the effective reaction rate. 2) Once the reactant enters the catalyst particle, it has to diffuse through its pores before reaching the active sites. Here, the pore size, tortuosity and pore interconnectivity determine the rate at which the reactants are delivered to the active site. Moreover, the composition of these pore-walls also plays an important role, as the wall-reactant interactions can lead to adsorption on these inert surfaces and lower the effective diffusion coefficient. 3) Once the molecule reaches the active site, it adsorbs on it and the actual chemical reaction takes place (4). Later, the products desorb (5), diffuse through the pores (6) and stagnant layer (7) to reach the bulk fluid where they can be collected.[1]

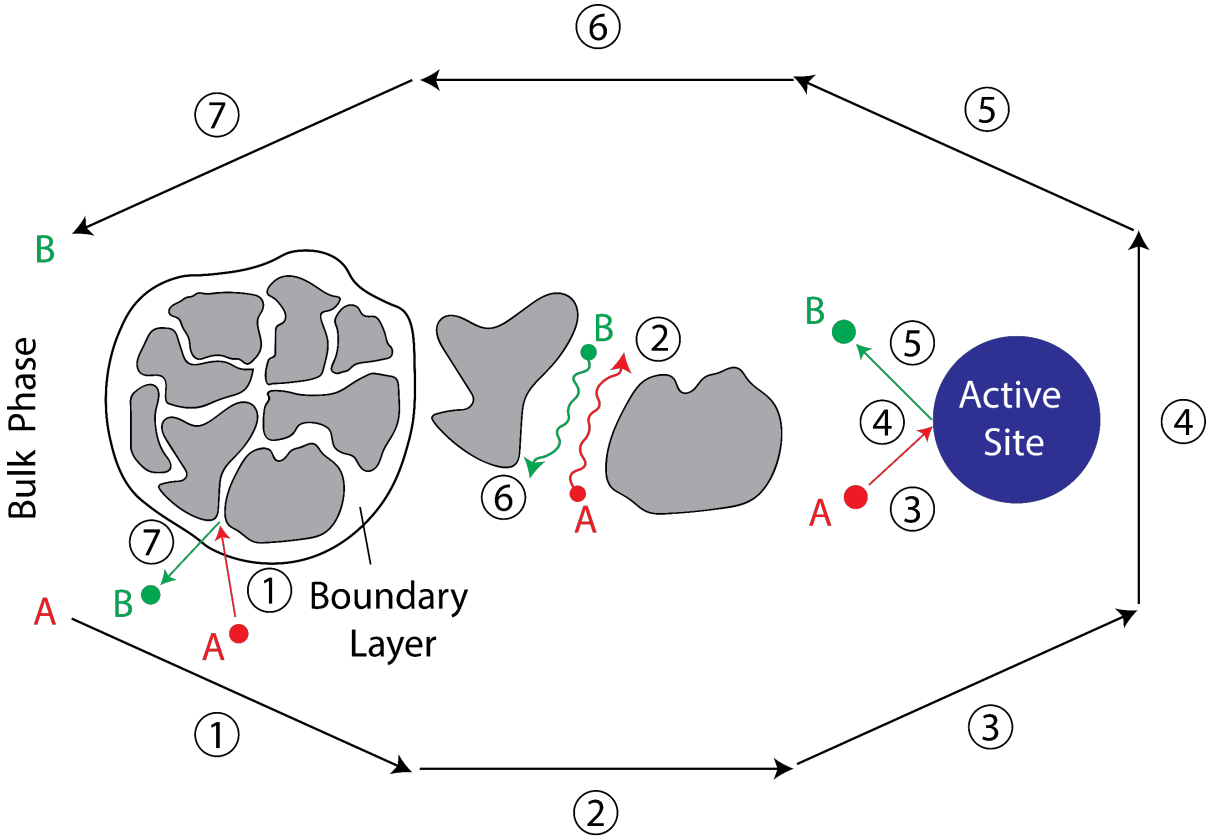

Figure 1.2 Individual steps of a heterogeneous catalytic reaction carried out on a porous catalyst in which species A reacts to species B. Adapted from Klaewkla et al.[3]

Porosity is of crucial importance for steps (2) and (6) as it determines how fast reactants reach the active site and how fast products leave the catalyst. Often, these internal diffusion processes limit the overall reaction rate of catalytic processes.[4–8] This is especially the case for reactions involving large molecules, such as biomass[9], hydrocarbons[10] and plastic[11,12]. In order to avoid internal mass transfer limitations (i.e., pore diffusion is slow compared to active-site reaction rate), the pore network of the catalyst has to be well-connected through large pores. A high pore connectivity is also important for the lifespan of a catalyst, as large products (e.g. polymers) or by-products (e.g. coke) created during the reaction can block pores and reduce the accessibility of the active sites.[5,13] However, smaller pores

can also be beneficial because they increase the available surface sites and therefore the reaction rates. Moreover, smaller pores can also improve the selectivity towards small reactants and/or products.[2] Apart from this, the support material should also provide stability (thermal, chemical and mechanical) to the catalyst particle, this is why filler materials (e.g. clay) are used to meet this criterion.[2] In order to find a good balance between the above mentioned requirements, industrial catalysts often consist of multi-component materials with complex hierarchical pore structures involving macro (> 50nm), meso (2 - 50 nm), and micropores (<2nm).[14] Rational pore space design of these pore-networks could improve catalytic performance significantly. However, this requires a much deeper understanding of the structure-performance relationship than is currently available.[15] Therefore, the development of better high-resolution and high-throughput porosity characterization techniques is necessary to understand how synthesis parameters affect the pores pace, not only on average, but also how these structures change between and within particles.

1.2 Pore Space Characterization Techniques

In this section, different porosity characterization techniques, as well as their benefits and drawbacks, will be discussed. We will further distinguish bulk and single particle techniques.

1.2.1 Bulk Techniques

Bulk pore space characterization techniques do not provide any information on the heterogeneity between and within particles. Nevertheless, they constitute well-established methods to characterize and compare catalysts samples.

a. Physisorption

Physisorption is a commonly used method to measure the total surface area of porous materials. This kind of measurement also provides information about the pore size distribution and the shape of the pores. In order to do this, a known amount of sample is first evacuated in a vessel at slightly elevated temperatures to remove water and air. Then, a known amount of adsorbate gas (usually nitrogen or argon) is admitted at very low temperatures (e.g., 77.3 K for N_2). After reaching equilibrium, the amount of adsorbed gas can be computed from the change in pressure. Usually, the adsorption behavior of the sample is evaluated through its adsorption isotherm, where pressure is normalized by the saturation pressure $P_{0.}$ [2,16]

An isotherm curve for a micro/mesoporous material is schematically depicted in Figure 1.3. At low pressures, molecules adsorb over the whole surface of the material, until a monolayer is built (see shoulder). Later the number of adsorbed species gradually grows with pressure as the pressure increases. Later, a strong increase due to capillary condensation is observed. After the saturation pressure has been reached, the pressure is gradually reduced to obtain the desorption isotherm (red curve). The hysteresis evidences the capillary condensation previously mentioned, as the pore filling and emptying mechanisms are different and occur at different pressures as a consequence. The difference between both isotherms can also vary based on the pore shape, providing information on this feature.[2,16]

The adsorption/desorption isotherms can be fitted to the Brunauer, Emmet and Teller (BET) model to obtain a total surface area for the material. Moreover, the Kelvin equation relates the pressure at which capillary condensation occurs to a pore diameter:[2,16]

$$\ln\frac{P}{P_0} = \frac{2\gamma V_m}{r_{pore} RT} \quad \text{Equation 1.1}$$

Here, P represents the pressure, P_0 the saturation pressure, γ the surface tension, V_m the molar volume, r_{pore} the pore radius, R the ideal gas constant and T the temperature. If no pores are present in the sample or they are too large (macropores) for capillary condensation to occur at the tested pressures, no capillary condensation takes place. As a result, macroporosity cannot be studied with this technique.[2,16]

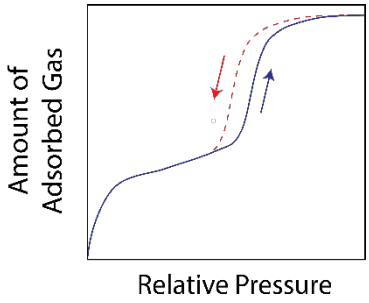

Figure 1.3 Schematic physisorption isotherm for micro-/mesoporous materials. The hysteresis suggests pore condensation. Adapted from Rahamn et al.[17]

b. Hg Intrusion Porosimetry

Mercury intrusion porosimetry is suited for the characterization of meso- and macroporous samples and offers a good complement to gas physisorption measurements. Mercury does not wet solids and its contact angle θ is usually determined on flat surfaces of the same material as the sample studied.[18] The Young Laplace equation (e) dictates that such materials have a positive capillary pressure ΔP, i.e., the liquid gets repelled by small pores. The smaller the pore radius r_{pore}, the higher the pressure needed for mercury to enter it. Hg-intrusion porosimetry makes use of this in the following way: First, the studied sample is put under vacuum to remove gas and water within the pores. Then, Hg is added to the vessel, surrounding the sample completely. The pressure of the system is then gradually increased. The resulting change in Hg-volume in the vessel provides a direct measurement of the amount of mercury entering the sample pores at different pressures. Then, the Young-Laplace equation can be used to translate the applied pressure to a pore size:[18]

$$r_{pore} = \frac{-2\,\gamma\cos(\theta)}{\Delta P} \quad \text{Equation 1.2}$$

After reaching saturation, the pressure of the system is gradually reduced, which often results in a hysteresis, similar to the one seen in gas physisorption. Comparing the intrusion and extrusion curves can provide information about the pore shape and pore interconnectivity.[18]

As previously mentioned, smaller pores require higher pressures for the mercury to fill them. In order to study meso- and micropores one would need extremely high pressures that cannot be reached with conventional porosimeters. Moreover, if the voids between the particles are comparable to the pores of the particle, the voids outside the particles can be wrongly interpreted as intra-particle porosity.[19]

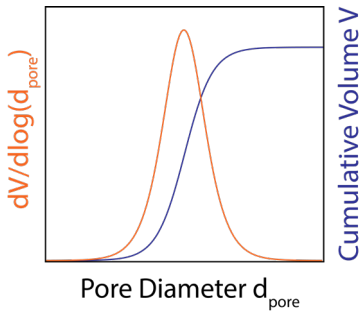

Figure 1.4 Hg Cumulative intrusion as a function of pore diameter: log derivative of the cumulative intrusion volume is strongly related to the pore size distribution.

c. Uptake Experiments

A commonly used way to characterize and compare the accessibility of catalyst particles is to perform uptake experiments.[20–23] Here, a known mass of porous particles is put in contact with a solution containing UV-active molecules in a stirred vessel. As the probe molecule gets taken up by the porous particles, its concentration in the liquid phase and therefore its UV-absorbance decreases. The uptake rate of the material per mass can be calculated from this difference in the liquid phase absorbance over time. The obtained uptake curves are then used to assess the accessibility (how easily molecules enter the porous host) and pore-interconnectivity of the material. Further, if the system reaches saturation, the effective diffusion coefficient can be extrapolated from the uptake curves.[24]

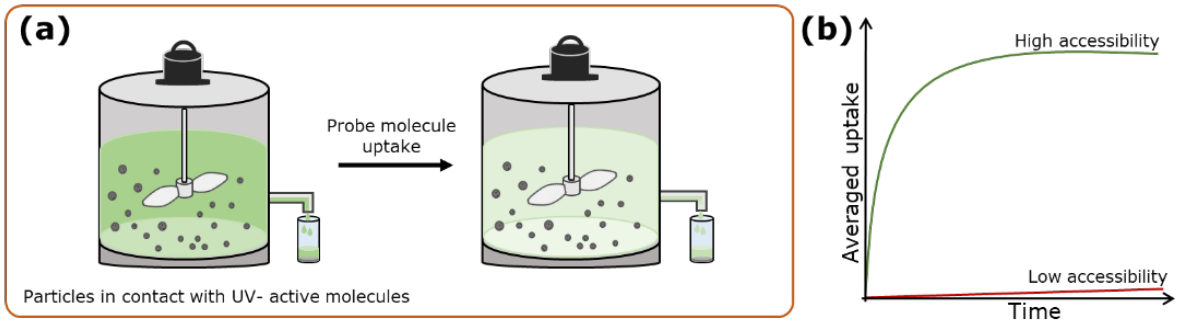

Figure 1.5 Schematic representation of experimental methods to evaluate the accessibility of particles in bulk and at the single particle level. A) Stirred tank containing UV-active molecules is put in contact with porous particles. The concentration in the solution decreases due to the uptake of the porous material. B) Based on the concentration change, the bulk uptake [mol/g(material)] is computed and used to characterize the accessibility.

The interpretation of uptake data can be divided into two categories, based on the adsorption or diffusion being the rate-limiting step. The latter represents the most common case for macroscopic adsorbent materials.[25,26] Several models have been developed to describe the experimentally obtained uptake curves.[20] However, most of these models require reaching a saturation state to extract the relevant parameters. The so-called intra-particle diffusion model[27] does not have this requirement and is therefore widely used for slow uptake experiments. Here the fractional uptake q(t) (usually expressed in mg(probe)/g(solid) is plotted as a function of $t^{0.5}$.[20,28–51] At low saturation values with an ideal mixing of the liquid phase (i.e., the dye concentration in solution is constant in space), this would initially result in a linear curve that eventually reaches a plateau, representing the saturation of the sorbent material (Figure 1.6, left). In the case of prominent external mass transfer effects (no ideal mixing), a stagnant layer, i.e., a concentration gradient in the vicinity of the particle, is formed during the uptake slowing it down and resulting in a non-linear regime for small time values

(Figure 1.6, right). [20,30] A linear regression is performed on the linear part of the uptake curve (Equation *1.3*) and its slope is used to quantify the so-called intra-particle diffusion rate constant K_p (mg/g $min^{0.5}$):[27]

$$q(t) = K_p\, t^{1/2} + C \quad \text{Equation 1.3}$$

The y-intercept C (mg/g) is typically used to evaluate the extent of the boundary layer thickness and therefore the external mass transfer effects. When the fitted line passes through the origin, the external mass transport is negligible. Otherwise, a non-zero y-intercept value indicates a relevant contribution of the boundary layer effects together with the intra-particle diffusion. Both positive [28,36–50] and negative [20,29,30,51] C values have been reported in the literature. Positive values are interpreted as fast adsorption by the material; thus, it is not possible to capture the actual starting point of the adsorption process. Negative values are related to a diffusion process retarded by the boundary layer effects. Moreover, some studies use the intercept of the fitted line with the x-axis to evaluate external mass transfer effects.[31–35] Therefore, the exact physical meaning of the C parameter proposed in the aforementioned model remains unclear. The interpretation of such results will be discussed further in Chapter 3.

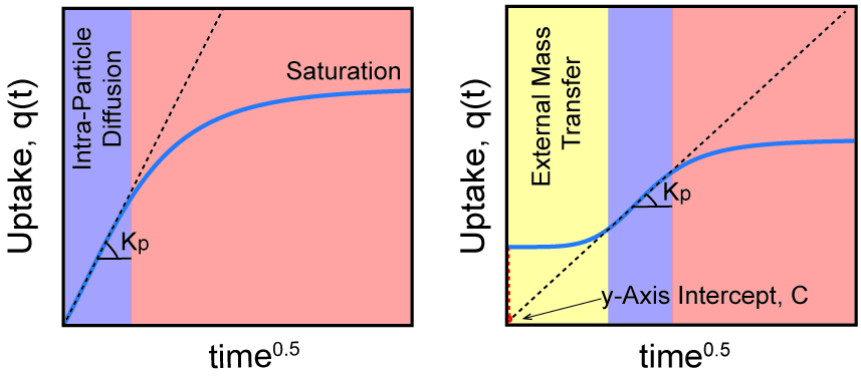

Figure 1.6 Ideal uptake curve with purely intraparticle diffusion (left) and with external mass transfer contribution (right).

d. Pulsed Field Gradient (PFG) Nuclear Magnetic Resonance (NMR)

Nuclear magnetic resonance (NMR) is based on the fact that nuclei with spin possess both a magnetic moment and a moment of inertia. Under the influence of a magnetic field, nuclei perform a rotational (‘‘precessional’’) motion with an angular frequency around the field direction. The superposition of many nuclei rotating gives rise to a rotating macroscopic magnetization. This magnetization induces a voltage in a surrounding coil, which this is recorded as the NMR signal at the resonance frequency. In pulsed field gradient (PFG) NMR, the homogeneous magnetic field is superimposed, over two short time intervals, by another field that is not homogeneous in space. The intensity of the NMR signal at a given frequency is proportional to the number of nuclei with the same resonance frequency. This frequency is a function of the magnetic field experienced by the nuclei, and this is spatially dependent due to the introduced inhomogeneous field. Therefore, the NMR signal at a certain frequency contains information on the spatial distribution of nuclear spins with the same resonance frequency along the field. Molecular movement along the magnetic field direction between two gradient pulses leads to a difference in the angular frequencies during the gradient pulses. Under equilibrium conditions the expected displacement of molecules is zero. However, nuclei displacement causes a phase shift that attenuates the NMR signal. The stronger the gradients and/or the diffusion coefficient, the higher the signal attenuation after the second gradient pulse. By varying the strength and duration of the

gradient pulses and fitting the decay to a model, it is possible to compute mean squared displacement and/or the diffusion coefficient of a molecule in a liquid.[8,52] The measured diffusion coefficients can be used to characterize the pore structure of the particle.

PFG-NMR has also been used to quantify diffusion within crystalline porous materials such a micro and meso porous zeolites[8,53], MOFs[54], FCC particles[7] and mesoporous silica catalyst supports.[55] By choosing the time in between gradient pulses favorably, mean molecular displacements between 100 nm up to tens of micrometers can be measured. This allows studying both the micro- and macroscale diffusivities in a hierarchical pore structure.[8,56] Overall, PFG NMR constitutes a non-invasive technique that can quantify different diffusion regimes within porous materials.[56] However, the time in between gradient pulses limits the size of molecular displacement that can be studied. Therefore, diffusion within microporous regions smaller than the smallest displacement cannot be studied with this technique. Quasi-elastic neutron scattering (QENS) can detect these molecular displacements and it can be used to complement PFG NMR measurements.[57,58] QENS has been successfully applied to measure self-diffusion and transport diffusion in several nanoporous materials such as zeolites and MOFs.[8] Further details on this technique can be found elsewhere.[59]

1.2.2 Single-Particle Analytical Techniques

In the above-mentioned techniques, it is assumed that the behavior of the entire system replicates the one of an individual particle. However, strong differences in terms of pore structure and composition exist within particles of the same catalyst batch.[60,61] These differences cannot be captured by ensemble-averaged measurements. This is why great efforts have been made to unravel inter-particle heterogeneities. A collection of techniques with this goal will be discussed in this section. Note that not all mentioned techniques are used in this work (see Figure 1.7).

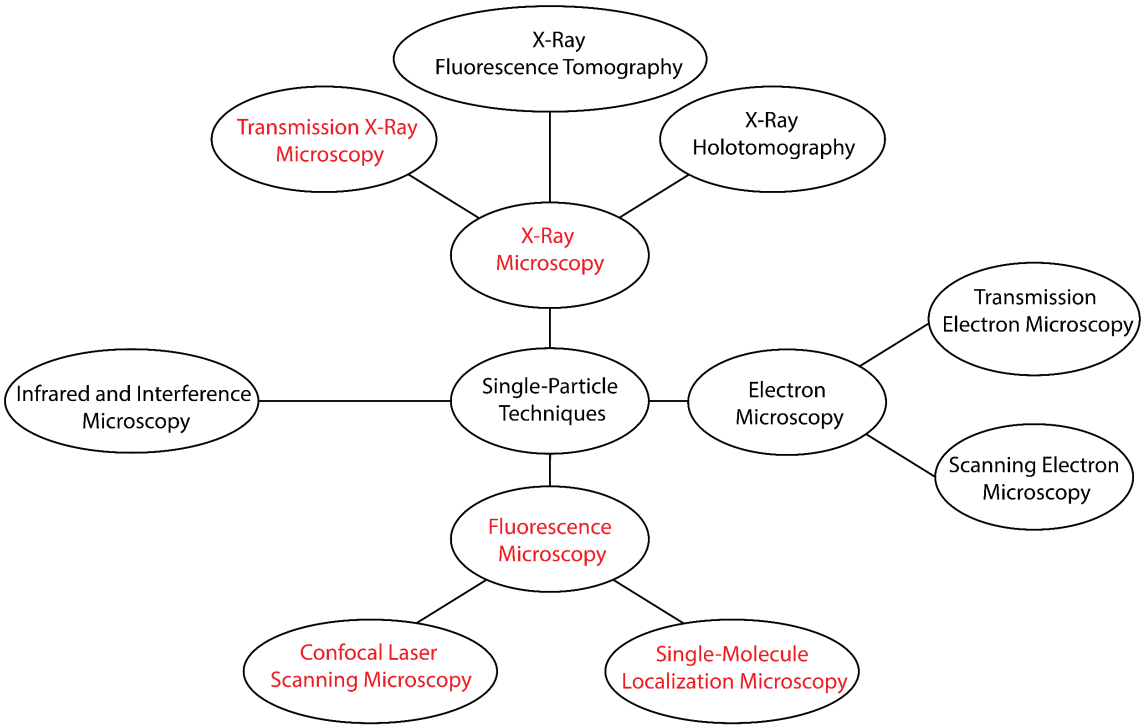

Figure 1.7 Single particle techniques discussed in this section. The Techniques marked in red represent techniques used in this work.

a. Infrared Microscopy (IRM) and Interference Microscopy (IFM)

Infrared Microscopy (IRM) and Interference Microscopy (IFM) have proved to be well suited for tracking concentration profiles during gas uptake and release in single nanoporous crystals such as MOFs and zeolites.[8,62,63] In both techniques, the nanoporous crystal under study is imaged within an optical cell connected to a vacuum system. The probe molecules are then let into the system at a certain pressure and the concentration profile within the porous particle is tracked over time. In addition, release experiments are also possible with these techniques. In infrared microscopy, the guest concentrations are determined by analyzing the characteristic absorption bands of the infrared spectra over time (see Figure 1.8a). The obtained concentration profiles can be fitted to a diffusion model (e.g., Fickian diffusion) to determine the diffusion coefficient as well as other mass transfer parameters[8]. In IFM, the interference patterns, that is, probe-induced changes in the optical density of the crystal are used to determine the local guest concentration (see Figure 1.8b). The observed profiles are actually concentration integrals $\int^L c(x,y,z)dz$ and not local concentrations. Therefore, in order to obtain concentration profiles, it is necessary to know the material thickness L as a function of x, and y. This is why well-defined crystals, ideally with a constant thickness, are used with this technique. The spatial resolution obtained with IFM is around 500 nm, whereas IRM yields values around 5-10 µm (these values might worsen with a growing particle thickness). Therefore, crystals explored with these techniques require to have sufficient size in the x-y plane for a profile to be recorded. Crystals of at least 10 µm and a few tens of µm are required for IFM and IRM respectively. Interestingly, since IRM provides a whole spectrum for each pixel imaged, different bands can be used to map the concentration of different guest-molecules. With the currently available devices, uptake and release experiments can be performed from room temperature up to about 100 °C.[8]

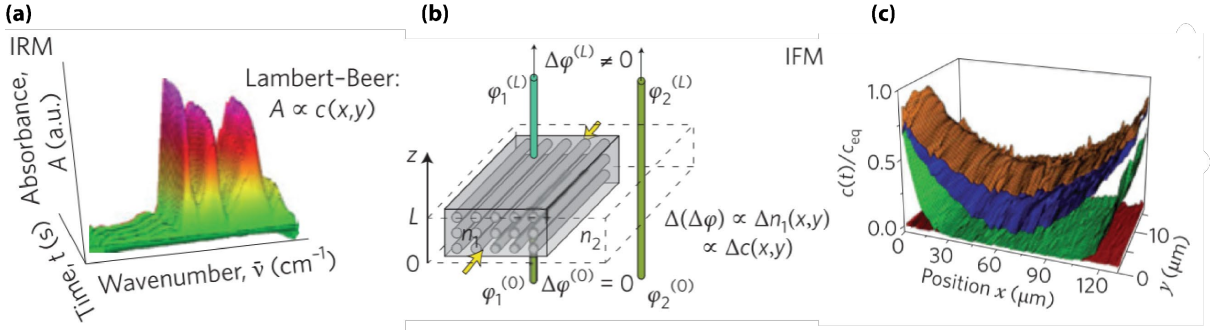

Figure 1.8 (a) Infrared microscopy (IRM): The guest concentration is determined by analyzing the characteristic absorption bands in the infrared spectra. (b) Interference microscopy (IFM): The gest concentrations are determined by the interference patterns, that is, guest-induced changes in the optical density of the crystal. (c) concentration profile at different times (different colors). φ is the phase of the light beams, *n* the optical density and c_{eq} denotes the guest concentration equilibrium with the gas phase. Figure adapted from Kärger et al.[62]

b. Electron Microscopy

Different Electron microscopy (EM) techniques are commonly used to image porous materials at different length scales in two and three dimensions. Unlike optical microscopy techniques, electrons interact with the sample instead of light. Moreover, due to the high electron energies, their de Broglie wavelengths are smaller than the ones used in optical microscopy, which results in an improved resolution.

c. Scanning Electron Microscopy

In Scanning Electron Microscopy (SEM) a beam of high-energy electrons (0.1 - 30 keV) is focused and scanned in a raster pattern across the surface of a sample.[64] The electron beam interacts with the atoms on the surface of the particle making them emit electrons which are detected and used to produce an image with resolutions up to 20 nm.[65] SEM is a relatively fast and straightforward technique to provide high-resolution imaging of the surface of a sample. However, it does not provide any importation of the internal structure. One way to overcome this issue is cutting the sample with a Focused Ion Beam (FIB) and imaging the cross section. This procedure can also be repeated several times to reconstruct a FIB-SEM tomography image of the particle.[66] Nevertheless, shadowing effects make image segmentation relatively hard to automate, which heavily complicates analysis. FIB-SEM images (and tomographies) of Zeolites [67,68], MOFs[19,69], Polymerization catalysts[70] and fluid catalytic cracking particles[66] have been successfully performed.

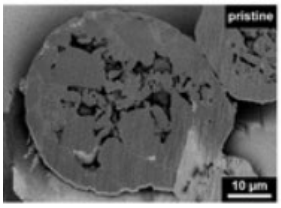

Figure 1.9 Scanning electron microscopy (SEM) images displaying a FIB-cut cross-section of a pristine Metallocene-Based Ethylene Polymerization catalyst particle.[70]

d. Transmission Electron Microscopy

Transmission Electron Microscopy (TEM), on the other hand, works by focusing a beam of high-energy electrons (80 - 300 keV) on a sample and detecting electrons the transmitted through the material.[71] As the electrons transmitted differently in different components (e.g. solids and air), TEM can image the internal pore structure. Moreover, by performing TEM measurements at a variety of angles, it is possible to reconstruct the pore structure in three dimensions. Scanning the electron beam (STEM) over the sample can provide improved resolutions in some cases down to the atomic level.[72] Further, different atoms scatter electrons at a different angle. High-angle annular dark-field (HAADF) STEM exploits this, creating an image mapping atomic number Z.[73] This can be used, for example, to differentiate metal nanoparticles from the support material. HAADF-TEM is commonly combined with Energy-dispersive X-ray spectroscopy (EDS) or electron energy-loss spectroscopy (EELS) which provide chemical information of the sample.[74]

Overall, TEM can provide high-resolution structural and chemical information. Unfortunately, this technique also presents some drawbacks. Samples need to be sufficiently thin for the electrons to transmit and reach the detector. Therefore, only sub-samples of catalyst particles can be analyzed with this technique. Moreover, cutting the sample (e.g., with a FIB) to be compatible with TEM can be challenging. Further, TEM is a destructive technique, as the high energy electrons can damage the sample. Finally, the measurements need to be performed in vacuum due to the high attenuation of the electron beam in air.[71]

e. X-Ray Microscopy and Tomography

The wavelength of X-rays are about three orders of magnitude shorter than visible light. The penetrating nature of X-rays allows X-ray microscopy (XRM) to provide sub-micron resolution 2D and

3D imaging for samples that are too thick to image with EM.[75] Moreover, contrary to TEM, X-ray microscopy (and spectroscopy) does not require vacuum and it can be performed at elevated temperatures and pressures.[76] By rotating the sample collecting several two-dimensional (2D) projections under several angles (typically 0-180°), it is possible to obtain a 3D reconstruction (tomography) of the material using dedicated algorithms.[7778] The resolution of the reconstruction will depend on a variety of factors: 1) The optics as well as the interaction of the studied material with X-rays will determine the resolution and contrast of the individual 2D projections. 2) Missing angles and large angular steps will decrease the quality of the reconstruction. 3) Motor jitter and sample movement during rotation can lead to inaccuracies in actual angle from which the sample is image and worsen the 3D resolution. Commonly, the resulting 3D spatial resolution is determined by calculating the Fourier shell correlation between two reconstructed topographies using only even and uneven angles.[79]

A collection of most commonly used X-ray microscopy techniques will be very briefly discussed in this section.

f. Transmission X-ray Microscopy (TXM)

In Transmission X-ray microscopy (TXM) the different X-ray absorption of different elements is used to create contrast. Therefore, a not necessarily coherent X-ray beam is focused on a sample getting (partially) absorbed, attenuating the intensity after transmission which is detected with a CCD camera. [80] The attenuation process can be described by Beer-Lambert's law:[81]

$$I = I_0 \exp(-\mu t) \quad \text{Equation 1.4}$$

Where I_0 is the incoming intensity, t the material thickness and μ the linear absorption coefficient of the material. The linear absorption coefficient depends on one hand, on the wavelength of the beam ($\mu \propto \lambda^3$) and on the other hand on the electron density of the material ($\mu \propto Z^4$). Thus, high beam energy (low wavelength) reduces beam adsorption and elements with a higher atomic number Z increase it. This technique therefore works best with heavy elements and often offers poor contrast for elements with a low atomic number such as carbon.

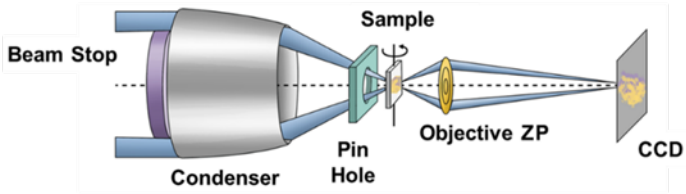

Figure 1.10 Transmission X-ray microscope (TXM) setup. ZP: zone plate, CCD: charge-coupled device detector

The X-ray absorption of elements as a function of energy displays jumps at certain wavelengths (Figure 1.11). The reason for this is that at these particular wavelengths core electrons are being excited and ejected from the atom resulting in an increased absorption probability. TXM can exploit this by scanning with energies slightly below and above the so-called absorption edge of a specific element. The difference in absorption between these two energies can be used to map the element in 2 and 3 dimensions. Here, the energy difference below and above the edge is directly proportional to the concentration of the element.[10]

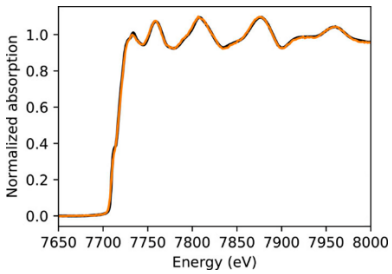

Figure 1.11 Normalized K edge absorption spectrum of a cobalt foil. Adapted from Honkanen et al.[82]

g. X-ray Holotomography

X-ray holotomography uses the phase-shift of a coherent X-ray beam to create contrast. When the beam passes through a sample, its phase and amplitude change. These changes are detected, and the phase shift is retrieved by a dedicated algorithm. The complex refractive n index of X-rays is given by:[83]

$$n = 1 - \delta + i\beta \quad \text{Equation 1.5}$$

Where δ the dispersion term (related to phase contrast) and β is the absorption term. The phase shift can be calculated as a function of δ and the wavelength of the beam.[84] Away from the absorption edge, where photoelectric effects dominate, the dispersion term is proportional to the electron density of the material.[85] At high photon energies, the phase contrast is significantly larger than absorption contrast (3 order of magnitude difference). This is why X-ray holotomography can be beneficial to study materials with low atomic numbers, such as biological samples [86] [87], Coke[13] or polymers[88]. Moreover, in this approach the phase shift contrast is collected without any further X-ray optics, which are often the limiting factor for spatial resolution in TXM. Spatial resolutions well below 100 nm have been achieved with this technique.[89]

h. X-ray Fluorescence Tomography

As mentioned above, core electrons can absorb X-rays and be ejected from the atom. When this happens, a vacancy is created at low energy orbital. As a consequence, higher energy electrons fill this vacancy, and this causes the emission of light with a wavelength corresponding to the energy difference between the two orbitals. The energy difference between orbitals, and therefore, the emitted light wavelength is unique for each element. Moreover, the number of emitted photons is proportional to the number of atoms of the specific element. X-ray fluorescence tomography makes use of this phenomenon to map the concentration of different elements within a sample by scanning an X-ray beam across the sample and collecting the emitted X-ray fluorescence at each specific point.[90] The resolution of this technique is limited by the beam spot size used for the raster scanning process. Advanced XRF focusing techniques have been applied yielding resolutions from the micron[91,92] down the nanometer level.[93–97]

i. X-ray Microscopy in Heterogeneous Catalysis

In recent years, several studies have employed synchrotron-based techniques to characterize the pore space and spatial composition of catalysts. For example, TXM tomography has been used to image FCC particles providing not only structural information, but also mapping the spatial distribution of different metals. Therefore, imaging was performed below and above the absorption edges of Nickel and Iron. The difference between the pixel values of these two tomographies was used to evaluate the concentration of the different elements across the catalyst particle.[10] Moreover, pore network

modelling was used to quantify the accessibility of FCCs with different metal loadings, showing that metal deposition mostly blocks pores close to the surface of the catalyst.[98] Later, TXM and pore network modelling were combined with XRF mapping of metals.[99] Here, the distribution of six different metals within FCC particles was mapped simultaneously. The zeolitic domains were identified by the fluorescence signal of Lanthanum, as it is commonly incorporated into them for making them thermally stable.[99] This combination of pore network analysis and metal distribution mapping was used as a basis to simulate the response to virtual aging of the catalyst particle, which suggested that the particle accessibility was rather robust against pore clogging by metal deposition.[99]

Holotomography has also been used by Vesely *et al.* to map the coke distribution of an ECAT particle.[13] Here, a particle deactivated due to coking was imaged first. Next, the same particle was calcined and re-imaged under the same conditions. The difference between the voxel values (here electron density) of the two tomographies was used to map the coke distribution along the particle. Interestingly, high amounts of coke in the core of the particle were found, which was attributed to a poor calcination during the regeneration process.[13] Holotomography also enabled the mapping of polymer within hafnocene-based catalysts. By analyzing the pore network of particles after different degrees of polymerization, Werny *et al.* observed differences in the fragmentation mechanisms at different stages of the reaction.[88]

Overall, X-ray microscopy techniques can provide high resolution 3D spatial information of the pore space and composition of whole catalyst particles in a relatively non-destructive way. However, these experiments are extremely expensive and complex.

j. Confocal Laser Scanning Microscopy

Confocal laser scanning microscopy (CLSM) enables a 3D reconstruction of fluorescent materials with an improved resolution compared to conventional fluorescence microscopy. In CLSM, a laser is first reflected on a dichroic mirror and focused on the sample. The fluorescently active material is excited and emits light with a wavelength higher than the excitation laser. This emitted light, is transmitted through the dichroic mirror. Next, the light is refocused sent through a pinhole, which filters out the light that is not in focus (Figure 1.12). The laser is scanned over the whole sample in x, y, and z resulting in a 3D reconstruction of the fluorescent signal consisting of several channels (wavelength regions).[100]

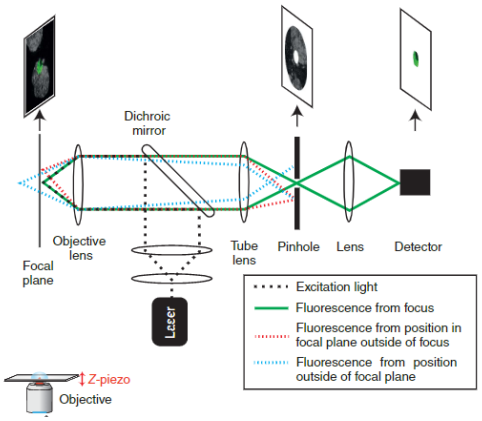

Figure 1.12 Schematic of a confocal laser scanning microscope. The excitation laser (dotted black line) is focused onto a sample. The emitted fluorescent light (solid green line) passes through the pinhole to reach the detector. Light originating from positions adjacent to the focal spot (dotted red line) or from a different focal plane will be cut out by the pinhole (dotted blue line).[100]

Staining catalysts with fluorescent probes (particles or molecules) can reveal information about the pore-space and composition of the particles. Staining with 2 different probes (thiophene and Nile red) recently proved effective to map the zeolite domains of fluid catalytic cracking (FCC) particles. The thiophene oligomerizes on the acid sites of the zeolites resulting in a fluorescent product when excited with a 488 laser. The stronger the fluorescent signal, the more reactive the zeolite domain. Nile red (ex. 633 nm), on the other hand, is a comparably large molecule, that cannot enter the small pores of the zeolites and it attached only on the support of the material. Since both fluorescent probes emit light of different colors, it was possible to distinguish between the two phases.[101,102] Further, CLSM has also been used to monitor the transient concentration profile of fluorescent probes during uptake experiments in large extrudates[5], zeolite crystals[103], MOFs[104] and silica spheres.[105,106] More recently, probe-mixtures with environment-dependent luminescence have been successfully applied to identify silica, clay, and zeolite regions within single catalyst particles.[107]

The bleaching nature of fluorophores can also be used to quantify mass transfer within porous materials. Fluorescence recovery after photobleaching (FRAP) uses a high intensity pulsed laser to photo-bleach an area of known geometry while imaging with a CLSM. Then, as other fluorophores diffuse into the bleached region it gradually recovers its fluorescence over time. The evolution of the transient concentration profile can be used to determine the effective diffusion coefficient of the fluorophore in the host, which is related to the properties of the porous host. FRAP is commonly used in biological samples[108] , but it has also been applied to study mass transfer in sol-gel silica[109,110] as well as on lithography-made model systems[111–114].

Some porous particles can also display autofluorescence. This property has been used to visualize the pore defects within single MOF crystals[115] as well as the fragmentation degree of metallocene polymerization catalysts upon reaction[116]. Further, coke formation is often involved in catalyst deactivation.[13] Since coke is fluorescent, CLSM has been successfully used to map coke formation with different degrees of conjugation within FCCs[11] and zeolites[117,118].

CLSM is a relatively simple technique, and it allows to study individual particles in a relatively high-throughput fashion. In contrast to IRM and IFM, each measured image corresponds to the intensity of a focal plane. Therefore, no well-defined structures are required here. However, it also presents some drawbacks. For example, the fluorescence light intensity coming from the center of the porous particle will be attenuated due to scattering effects.[119] This is especially the case if the particle is heterogeneous in composition because the particle's different phases cause a greater refractive index mismatch and therefore increase total internal reflection.[120] Therefore, in order to be quantitative with this technique one has to study very homogeneous materials[106], only consider sub-volumes of the particles[60] or use cut (e.g., microtomed) samples [11]. Moreover, the resolution (~250 nm)[121] of this technique is limited by diffraction making it impossible to visualize large fraction of the catalyst' pores.

k. Single-Molecule Localization Microscopy

TUnfortunately, the resolution of conventional optical and fluorescence microscopy is limited by diffraction because the objective lens effectively acts as a small aperture. Therefore, fluorescence imaging of point source emitters (e.g., molecules/nanoparticles) results in an interference pattern that consists of a bright circular center surrounded by alternating dark and bright rings of much lower intensity (Point Spread Function, PSF). The center of the PSF corresponds to the location of the emitter. Therefore, if the concentration of fluorophores is low enough, such that there is no overlap between the individual PSF circular centers, one can fit a 2D gaussian to them to determine the localization of the single emitters that are much smaller than the wavelength of light with resolutions in the order of tens of nanometers (Figure 1.13).[119]

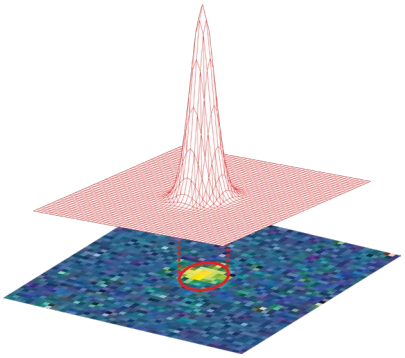

Figure 1.13 The light from individual emitters is diffracted through the microscope lens. The resulting diffraction-limited spot is fitted with a gaussian function, and its center corresponds to the localization of the fluorophore.

The reactivity of catalysts has been mapped with single-molecule localization microscopy (SMLM) by using fluorogenic molecules (i.e., molecules that become fluorescent after reaction) by a procedure called nanometer accuracy by stochastic chemical reactions (NASCA).[122–126] As the reaction takes place at the active sites of the catalyst, PSFs which appear in the field of view are localized. Photobleaching (i.e., loss of fluorescence due to photochemical degradation) of the produced species is necessary, as it prevents the PSFs from overlapping with each other and allows for a high-resolution concentration. On the other hand, solid-liquid, liquid-liquid, and gas-liquid interfaces have been reconstructed in three dimensions with sub-diffraction resolution by imaging individual reversible adsorption events of polymers over time.[127]

A typical SMLM setup (widefield fluorescence microscope) is depicted in Figure 1.14. Contrary to CLSM, light exciting the sample is collimated with a wide field lens. Moreover, there is no pinhole before the detector. Therefore, the obtained image does not correspond to a focal plane, but a focal volume. Finally, no scanning is performed with this technique, which allows for a much faster frame rate and potentially the tracking of fast-moving nanoparticles or molecules.

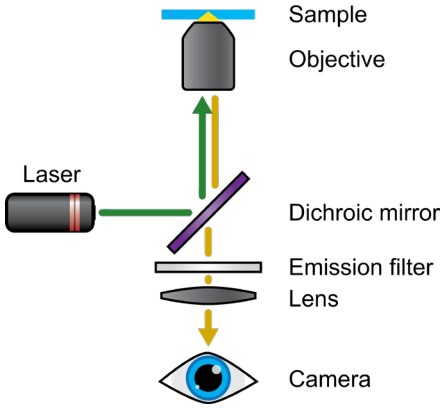

Figure 1.14 A typical wide field fluorescence microscope set-up consists of an excitation laser, a dichroic mirror, an objective lens, and a detector. The dichroic mirror reflects the short-wave excitation light, (green) but transmits the longer wavelength light (yellow) emitted by the sample. A parallel beam is used to illuminate the sample. Emission filters can be used to improve the signal-to-noise ratio.[119]

Single Particle (molecule) Tracking

SMLM can also be used to track single fluorescent probes as they diffuse (Single Particle Tracking, SPT). Therefore, single emitter PSFs are first identified and fitted with a 2D Gaussian function to

determine probe location at each frame. [128,129] Then, based on their vicinity in time and space, the localizations of different frames are grouped together to form trajectories corresponding to the path travelled by single fluorophores over time (Figure 1.15b).[128–132] Two input parameters need to be chosen for the trajectory forming process: The blinking gap and the pixel jump. The blinking gap takes into account the blinking of the fluorophore i.e., the molecule temporarily stops emitting fluorescent light [133] and it represents the maximum for which a trajectory can be interrupted. The pixel jump, on the other hand represents the maximum spatial separation between two consecutive localizations within a track. These two parameters need to be optimized for each experiment in order to obtain reliable results.[134]

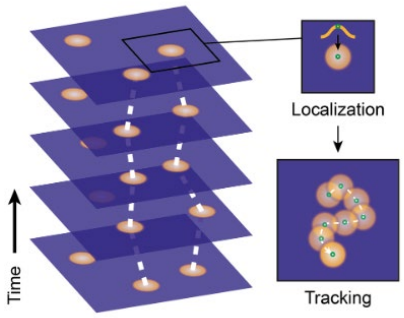

Figure 1.15 Schematic of the single particle tracking process. First, the diffraction-limited spots corresponding to single probes are identified and fitted. Then, individual localizations are grouped together to form trajectories.[119]

Mean Squared Displacement Analysis

Mean squared displacement (MSD) analysis is one of the most common ways to compute diffusion constants from single particle tracking data. For a single trajectory expressed as a timeseries with localizations $x_0, x_1, \ldots, x_N$ the MSD curve is calculated with the following formula:

$$MSD(t_n) = \frac{1}{N-n+1}\sum_{i=0}^{N-n}(x_{i+n}-x_i)^2 \qquad \text{Equation 1.6}$$

Here $t_n = n\Delta t$ represents the time delay for n = 1, 2, …, N and the frame time Δt.[135–138] For an ideal free diffusing probe, the MSD curve is a straight line crossing the origin with a slope proportional to the diffusion constant D. However, in a SPT experiment the MSD curve will be affected by photon-counting noise and well as motion blur (i.e., motion between the exposure time changing the shape of the PSF). This will result in an offset of the MSD curve that can be described as follows:[135,137]

$$\mathrm{MSD}(t_n) = 4Dt_n + 4(\sigma^2 - 2RD\Delta t) \qquad \text{Equation 1.7}$$

Here, σ represents the localization error and R the motion blur coefficient. The offset of MSD curves can therefore be used to determine the localization error of SMLM experiments.

A single-track j is not representative for the ensemble behavior. Therefore, the time-ensemble averaged (TE) MSD is commonly used to fit the diffusion coefficient and localization error:

$$TE-MSD(t_n) = \frac{1}{N_j-n+1}\sum_{i=0}^{N_j-n}(x_{j,i+n}-x_{j,i})^2 \qquad \text{Equation 1.8}$$

The shape of the MSD curve also depends on the diffusion type. If a free diffusing probe is confined, its MSD curve will reach a plateau at high time delays. The plateau-value will depend on the confinement radius R:[138,139]

$$\mathrm{MSD}(\mathrm{t_n}) = R^2\left(1 - \exp\left(\frac{\mathrm{t_n}}{\tau}\right)\right) \quad \text{Equation 1.9}$$

On the other hand, if the motion is directed, that is, there is flow in the system. The MSD curve will be parabolic and it will depend on the flow speed v:[138,139]

$$\mathrm{MSD}(\mathrm{t_n}) = 4\mathrm{Dt} + \mathrm{v}^2\mathrm{t}^2 \quad \text{Equation 1.10}$$

Anomalous diffusion mostly results in non-linear MSD curves. However, this is not always the case. Therefore, in systems where anomalous diffusion is expected, careful analysis is required to reliably compute the diffusion coefficient out of SPT data.[130,140] This will be discussed in more detail in Chapter 4.

Single-Particle Tracking in Porous Materials

Initially, several SPT studies were carried out in mesoporous silica hosts due to the high tunability of these materials in terms of pore size and surface chemistry. Strong heterogeneities in diffusion regime as well as transient trapping events were observed.[141,142 143–146]. Later, SPT started to get used to infer properties of ordered porous materials. First, Kirstein *et al.* observed different diffusion modes on pure hexagonal, pure lamellar mesoporous silica hosts. When using a third type of mesoporous silica the two diffusion modes were present, suggesting that these two pore types were present in the system.[147] More recently, Zürner *et al.*[148] directly correlated TEM images with single molecule tracks in hexagonal mesoporous silica (Figure 1.16). The motion of the molecules followed the direction of the pores. Moreover, some tracks displayed jumps between two seemingly not connected pores. This was attributed to small pore defects that connected the different mesopores and that remained obscured with TEM. Similar observations were made when Nile Red fluorophores were tracked within microporous Metal Organic Framework crystals[149]. Here, the results suggest that these materials have even more defects than the mesoporous silica systems previously studied.

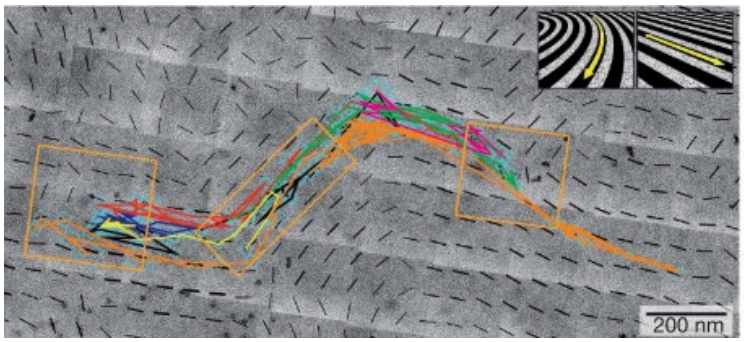

Figure 1.16 Structural elements molecular trajectories found in a real two-dimensional hexagonal mesoporous silica film. The trajectories follow the shape of the pores.[148]

Single-particle tracking shows great potential to characterize porous materials, but it also presents some challenges: 1) Similar to CLSM, light scattering due to refractive index mismatch is a common problem in SPT within porous solids. Therefore, many studies attempt to match the refractive index of the porous material to the one of the solution.[120] 2) On one hand, small probes can access and explore smaller pores. On the other hand, such fluorophores display small absorption cross sections which makes them less prone to excitation, emission, and localizing. Moreover, small probes might

move too fast, resulting in motion blur of the PSF and/or a poor signal to noise ratio. 3) Apart from size, fluorophores with a high quantum yield (i.e., photons emitted per photons absorbed) are preferred as they are more likely to be localized. This property also depends on the solvent in which the probes are dispersed. 4) Finally, bleaching, though beneficial for NASCA, is problematic for SPT as information is lost. Therefore, choosing an appropriate combination of dye, host, and solvent can be quite challenging.[119]

Single Particle Tracking in Catalysts

Recently, more complex porous materials have explored via SPT. Hendriks *et al.* tracked PDI molecules within fluid catalytic cracking (FCC) particles. As expected, a large heterogeneity between tracks was observed in terms of diffusion coefficient as well as adsorption behavior which was attributed to the large pore size distribution and heterogeneous composition of the material. Therefore, the authors introduced the idea that in such complex systems, classification of the tracks can be beneficial. They segmented the recorded tracks into so-called mobile, immobile, and hybrid tracks using a simple machine learning algorithm (classification via a hierarchical tree). The diffusion coefficient determined for the mobile tracks was similar to the one measured for vacuum gas oil molecules of similar size in uptake experiments, showing the potential of using this technique to quantify mass transfer in catalysts. However, the short duration of the tracks did not allow for reconstructing the pore space and no clear spatial information could be retrieved from the track properties.[150] In another study, film zeolites with two different pore orientations (straight and sinusoidal) were used to study diffusion anisotropy. Using the zeolite acid sites, furfuryl alcohol was used as a reactive probe and its oligomerization products were tracked as they diffused through the pores. Again, large heterogeneities were observed which required track classification.[134,139] The measured diffusion coefficient in the straight pores was one order of magnitude larger than in the sinusoidal ones, which was in line with PFG NMR measurements.[134]

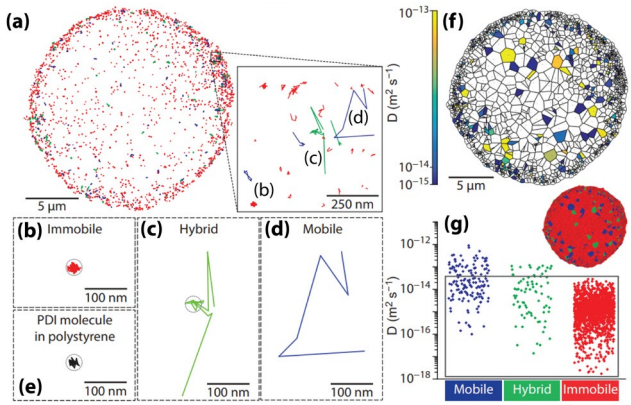

Figure 1.17 Classification and analysis of trajectories within a fluid catalytic cracking particle. (a)Trajectories recorded within the catalyst particle showing (b) immobile (red), (c) hybrid (green), and (d) mobile trajectories (blue). (e) Trajectory of the probe molecule (PDI) immobilized in a polystyrene thin film has a comparable minimum bounding circle as immobile trajectories, suggesting a correct classification. (f) Voronoi diagram showing a spatial map of single trajectory diffusion coefficients. The center of mass of the trajectories are indicated by a dot, which is surrounded by an area that is closer to that trajectory than to any other. The color of each area indicates the diffusion coefficient, with areas corresponding to immobile trajectories. (g) Diffusion coefficients of each trajectory. Adapted from Hendriks et al.[151]

Overall, SMLM has great potential to study the pore space of catalyst particles through reaction and adsorption events as well as pore space mapping through SPT. However, as we will see in chapters 3,

4, 5 and 6, complex probe-host hydrodynamic and electrostatic interactions characterize the probe dynamics and accessible porosity. The following section will discuss these interactions.

1.3 Effect of Probe-Host Interactions on Mass Transfer

The motion behavior of (individual) fluorophores within porous hosts is characterized by hydrodynamic and electrostatic interactions probe-wall interactions. In this section we will discuss their effects on motion behavior and present a collection of SPT experiments where they were found to be significant.

The hydrodynamic drag experienced by a moving particle in confinement is larger than in free solution, which results in a reduction of the diffusion coefficient. This intensified hydrodynamic drag grows with growing probe-pore-size-ratio [152] and as the probe approaches the wall.[153] Skaug et al. [120,154] tracked polystyrene beads as they diffused through two different commercial porous filtration media with similar nominal pore size and porosity. A strong heterogeneity in terms of diffusion coefficient was found within one of the hosts and these differences were attributed to hydrodynamic effects suggesting that this host material had a broader pore size distribution. In another study, the same authors observed further hydrodynamic interaction effects on accessibility by tracking particles of different sizes within porous polymer films.[155] Even though the used nanoparticles (40 - 200 nm) were significantly smaller than the mean pore size (31 µm). The pore volume explored by the fluorophores at a given time dramatically decreased as a function of particle size. Diffusion simulations considering a spatially dependent hydrodynamic drag in CLSM-reconstructed pores were compared to simulations with a space-invariant diffusion coefficient and resulted in large differences of pore-throat-escape times (Figure 1.18) explaining the observations. Potentially, the effect of probe-host hydrodynamic interactions on the local dependency of diffusion coefficients could be exploited to probe pore-sizes. This possibility will be discussed in more depth in Chapter 5.

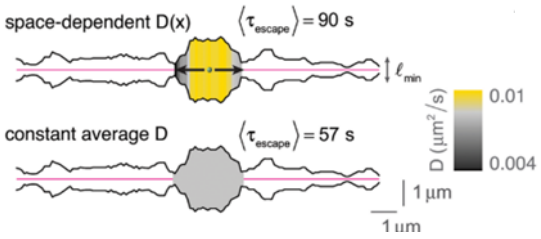

Figure 1.18 Diffusion simulation within a pore of varying diameter. A spatially dependent diffusion coefficient resulted in a larger mean escape time from the indicated void compared to the case where the diffusion coefficient was assumed to be constant. Experiments yielded similar results.[155]

The electrostatic interactions between the porous host and the fluorescent probe also play a significant role. Solids that are in contact with aqueous solutions are usually charged. For example, metal oxides are commonly terminated with OH groups that can be protonated or deprotonated depending on the pH of the system. For each metal oxide there is a pH at which the surface will be neutrally charged, this pH value is called the point of zero charge (PZC). Above the PZC, the surface charge density becomes increasingly negative and below it, it becomes increasingly positive.[2] Similar protonation/deprotonation effects take place with fluorophores changing their overall charge.[156] The electric potential of the walls in relation to the probe can result in different affinities between them and result in different motion behaviors. Wang *et al.* tracked positively charged biomacromolecules in three dimensions close to an unconfined silica-liquid (aqueous solution) interface. The surface charge density of the solid was varied by functionalizing it with different ratios of nonionic oligo (ethylene glycol) silane and a positively charged amino-silane (NH_2). As the percentage of NH_2 gradually increased, longer and more frequent trapping events took place, which resulted in a lower

apparent diffusion coefficient.[157,158] Potentially, the trapping event duration and frequency could be used to map different materials with sub-diffraction limited resolution.

When a charged surface is in contact with an aqueous solution an electric double layer (EDL) will be formed. This is a region where the liquid is not electroneutral because it contains a high concentration of counter-ions attracted by an oppositely charged surface.[159] The electric potential of the EDL first decays linearly adjacent to the surface (Helmholtz layer) and then as exp(-y/λ) in the so-called, diffuse layer, where y represents the distance from the wall and λ the Debye length. The Debye length is inversely proportional to the square root of the ionic strength.[160] This means that electrostatic interactions between the wall and the probe can be shielded by introducing ions into the system. Further, if the Debye length is comparable to the diameter of a pore, the EDL of opposite facing walls will overlap and the pore will be mainly occupied by counter-ions, impeding the entrance of charged diffusants. Wu *et. al.* tracked differently sized fluorophores in a model system consisting of a network of interconnected cavities, where each cavity had 12 holes connecting to adjacent cavities (Figure 1.19a).[161,162] The obtained MSD curves showed 3 regions (Figure 1.19b). At low time delays the curve was linear because the random walkers moved without "feeling" the confinement (slope was the same as in free solution). At moderate time delays, the curve plateaus, as movement was limited by the cavity walls. At long time delays, the grows linearly again as the probes begun to exit the cavities and reach new ones. Interestingly, the long-term diffusion coefficient turned out to be a function of the cavity radius and the cavity residence time, relating microscopic to macroscopic diffusion behavior. Further, decreasing the ionic strength in aqueous solutions resulted in an increase of the residence time and therefore the long-time diffusion coefficient. This can be explained by a reduction of the Debye length. Both probe and host were negatively charged. Therefore, reducing the Debye length resulted in weaker electrostatic repulsion between the particle and the outlet holes of the cavity and this eased nanoparticle escape.[162]

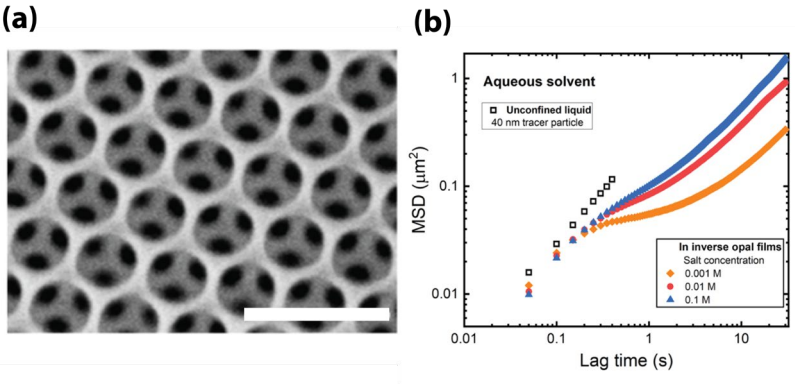

Figure 1.19 SEM images of inverse opal film model system where fluorescent probes were tracked. The scale bar in panel a represents 1 µm. Time-ensemble-averaged mean squared displacement as a function of the lag time at different salt concentrations for an aqueous solvent system. Adapted from Wu et al.[120,161]

Overall, the interactions described above need to be better understood for a reliable interpretation of SMLM/SPT and uptake experiments in porous materials. Chapters 3, 4, 5, and 6 address this challenge by studying mass transfer in porous model systems.

1.4 Scope of the PhD Thesis

The scope of this PhD thesis is to explore new methods to characterize the pore space of catalyst particles using fluorescence microscopy techniques.

In **Chapter 2,** state-of-the-art synchrotron radiation-based full-field transmission X-ray microscopy was used for the first time to investigate the macropore defects of a MIL-47(V) MOF crystal. Macropores were found heterogeneously distributed throughout the particle. However, the MOF crystal did not seem to be well-connected through a macropore network. Interestingly, the macropore defects displayed a preferential orientation.

In **Chapter 3**, a new analytical method for characterizing the accessibility of individual porous particles is presented. The method consists of monitoring the uptake of a fluorescent probe into the porous particle over time. Therefore, only a fluorescent microscope and a microfluidic device made of PDMS are required to perform experiments. Model porous silica particles were used to showcase the methodology. Conditions (pH and ionic strength) ideal for increasing the measurement sensitivity are discussed.

In **Chapter 4,** we introduce a two-dimensional silica pore made with lithography and wet etching used to characterize the motion behavior of individual fluorophores. The trapping behavior of quantum-dot-probes could be tuned and suppressed via the pH of the system. The determined non-trapping conditions were employed to map a real-life polymerization catalyst support via single particle tracking.

In **Chapter 5,** the model pore described in **Chapter 4** was modified to have different dimensions. Contrary to fluid dynamic simulations, the pore size did not have an effect in the motion behavior of the used quantum dots. Consequently, the probe-host-solvent system did not prove suitable to probe pore dimensions based on locally measured diffusion coefficients.

In **Chapter 6,** carbon dots were successfully employed as SPT probes for the first time. Their small size allowed them to enter small pores, inaccessible for the quantum dots discussed in **Chapters 4 and 5,** showing their great potential for mesopore space mapping applications. Moreover, the trapping behavior of the carbon dots was different for varying materials, suggesting that the duration of trapping events could be used to map different compositions.

In **Chapter 7,** a brief summary of the results of this thesis is given. In addition, an outlook on possible research directions is provided.

2 Visualizing Defects and Pore Connectivity within Metal-Organic Frameworks by X-ray Transmission Tomography

Metal-Organic Frameworks (MOFs) have the potential to change the landscape of molecular separations in chemical processes owing to their ability of selectively binding molecules. Their molecular sorting properties generally rely on the micro- and meso-pore structure, as well as on the presence of coordinatively unsaturated sites that interact with the different chemical species present in the feed. In this Chapter, we show a first-of-its-kind tomographic imaging of the crystal morphology of a metal organic framework by means of transmission X-ray microscopy. Corroboration with Focused Ion Beam-Scanning Electron Microscopy (FIB-SEM) images shows the potential of this strategy for further (non-destructively) assessing the inner architecture of MOF crystals. By doing this, we have unraveled the presence of large voids in the internal structure of a MIL-47(V) crystal, which are typically thought of as rather homogeneous lattices. However, the poor connectivity of these voids suggests that they do not have a large influence on the separation properties of the sample.

Based on:

Rafael Mayorga-González‡, Miguel Rivera-Torrente‡, Nikolaos Nikolopoulos, Koen W. Bossers, Roozbeh Valadian, Joaquín Yus, Beatriz Seoane, Bert M. Weckhuysen, Florian Meirer, Visualizing Defects and Pore Connectivity within Metal-Organic Frameworks by X-ray Transmission Tomography. Chem. Sci., 2021, 12, 8458-8467

†These authors contributed equally to this work.

2.1 Introduction

Metal-Organic Frameworks (MOFs) have become a very important group of multifunctional porous materials, showing the first commercial applications after years of intense fundamental and more applied research.[163–166] A broad array of uses, ranging from biomedicine and drug delivery, chemical sensing or catalysis have been extensively studied.[167–170] Perhaps two of the most studied applications are adsorption and purification of gaseous and liquid streams, such as hydrocarbon, e.g. olefin/paraffin, mixtures in refinery processes, residual traces, i.e. CO_x, NO_x, or SO_x, or the removal of contaminants from water[167,171–174] the high performance in such applications arises from their extremely high surface areas (often > 1000 $m^2 \cdot g^{-1}$), regular pore systems that allow for (in principle) homogeneous diffusion, and the presence of interacting metal sites that may undergo reversible redox processes.[175–179] This combination renders MOFs as materials of choice for advanced separations[180], being particularly interesting for mixed-matrix membranes.[181–183]

More specifically, many studies concerning diffusion and surface interactions of CO_2,[184–187] H_2[188,189], alkanes[190–193], alkenes[194], aromatics [195–200] in the pores of MIL-47(V) have been previously published. These works highlight that separation and sorption properties of MOFs heavily rely on weak and strong interactions between the adsorbates and the internal micropore surfaces, i.e., organic ligands and metal sites, of the crystal lattice. Thus, the formation of defects or hollow cavities at the macro- (i.e., pore sizes > 50 nm),[201] which may happen along with the deposition of nanosized deposits of impurities (e.g. metallic or metal oxides) disrupting the 1D channels of the structure may lead to alternative diffusion pathways, thus altering the separation properties.[201] Therefore, understanding of the macropore structure in MOFs is crucial for developing refined synthetic methods.

Examples for imaging pores in MOFs are still scarce and rely mainly on electron microscopy, which often implies beam damage.[202] Moreover, this technique remains restricted to volumes in the range of nm^3, which prevents the user from probing large structures, e.g., a whole single-crystal. Several studies have shown how X-ray 3D imaging can be used for studying the porosity at different length scales, overcoming the effects of severe beam damage, and expanding the imaged volumes. Recently, a first X-ray 3D study of HKUST-1 MOFS was published by Ferreira-Sanchez et al, addressing issues such as spatially-resolved metal speciation and by-product phase formation.[203] However, this Chapter focused on chemical heterogeneities within the crystal and not on porosity. Despite the tremendous importance of this property in the applications in which MOFs are typically used, to the best of our knowledge, no detailed studies focusing on porosity have been reported yet. Herein, we made use of full-field transmission X-ray microscopy (TXM) nanotomography to image a single MIL-47(V) crystal in 3D and map the macropore defects present within. Moreover, pore network analysis allowed us to evaluate pore connectivity as well as a preferential macro-pore orientation throughout the crystal. This allowed us to not only draw conclusions about the macro-pore architecture and its potential implications in diffusion-controlled operations, but also to formulate hypotheses on crystal growth and formation of the MIL-47(V) topology. The findings reported have been corroborated by Focused Ion Beam-Scanning Electron Microscopy (FIB-SEM) images on the same material.

2.2 Results and Discussion

2.2.1 Tomographic Reconstruction and Macro-porosity

In this chapter, the terms porosity or pores always refer to macroporosity and macropores with dimensions above the estimated spatial resolution (230 nm) respectively (see Methods). Figure 2.1a shows the 3D reconstruction of a MIL-47(V) needled-like crystal of ~65 µm length. Figure 2.1b and c, show a cross section of the reconstructed sample, and a zoom-in of the voids, respectively. The latter shows areas of lower X-ray absorption intensity (darker), exhibiting macropores in the range from a few hundreds of nanometers to 2-3 µm in size. Beyond evidencing the presence of macropores, the X-ray absorption in each voxel is directly correlated with material density as the variation in element composition in this sample is negligible. Due to the chemical homogeneity of the MOF crystal, the grayscale values can be used to qualitatively study differences in crystal defects even at resolutions smaller than the one achieved (230 nm). Figure 2.1d shows the mean voxel intensity as a function of distance from the particle surface; here one can observe that on average the density of crystal defects changes only insignificantly as a function distance from the surface (correlation coefficient: 0.0990). However, the standard deviation (shaded area) of the intensity levels increases close to the surface hinting towards a higher density of defects. This higher intensity variance on the surface is due to the presence of less intense (porous) voxels as well as high intensity outlier regions. Our hypothesis is that these high intensity regions correspond to vanadium clusters that precipitate during crystallization which would be in line with the findings of Ferreira-Sanchez et al.[203] It is worth noting that a strong variation in the concentration of elements (atomic number, Z) could also cause such variation as the X-ray absorption coefficient (note that µ∝Z^4), although the purity of the V precursor used was >99%. Hence, it seems unlikely the widespread presence of lighter or heavier elements throughout the crystal.

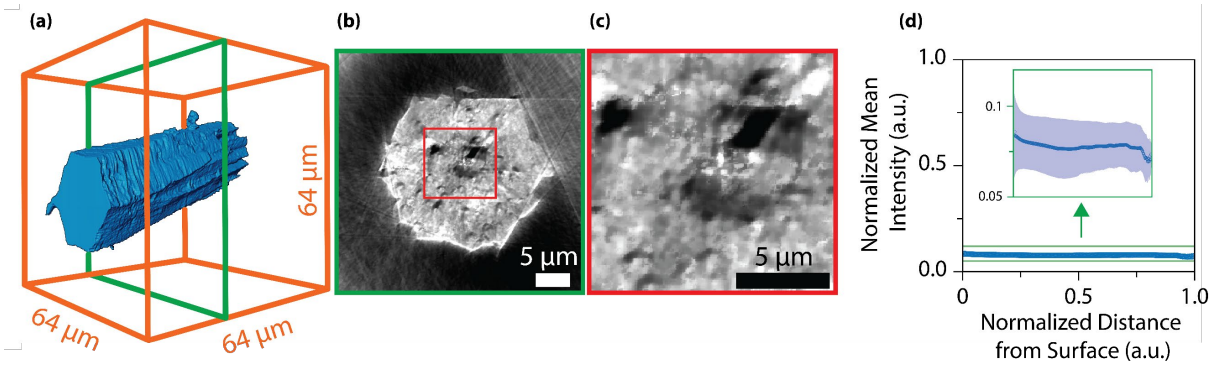

Figure 2.1 (a) 3D reconstruction of the metal-organic framework (MOF) crystal under study, namely MIL-47(V), from X-ray transmission microscopy (TXM) data; (b) A cross section vertical to the crystal axis. If the chemical composition (i.e., ratio of elements) varies only slightly over the sample, then, the per voxel variation in measured X-ray absorption (i.e., the reconstructed voxel gray scale level) directly relates to variation in material density. Therefore, the darker regions of the cross section represent areas of much lower density (such as voids), whereas the more intense pixels correspond to dense areas. Note that we used the outer space of the capillary, i.e., no matter present, as the reference absorption value for the lower end. (c) Zoom-in to a region in (b). (d) Average grayscale intensity (min-max scaled) plotted as a function of distance from the particle surface; the shaded field corresponds to standard deviation. The graph reveals no correlation between average voxel intensity and distance from surface. However, the standard deviation of the intensity decreases with the distance from the surface indicating a higher density of defects closer to the surface.

To further validate these TXM-tomography results, six crystals were sectioned by using a focused Ga+ ion beam (FIB) and imaged by scanning electron microscopy (SEM). As shown in Figure 2.2, also this method revealed macropores to be ubiquitously present. For FIB-SEM data the surface area of the observed macropores and the one of the cross-sections were segmented manually. Based on this, the porosity of the sample was estimated by calculating the fraction of pixels in the cross section identified as void space (see Methods). The estimated macroporosity of the different FIB cut cross sections varied strongly between samples. However, none of the observed cross sections displayed a porosity greater than 2 %. While confirming findings from TXM, single FIB-SEM measurements can only provide 2D information, which prevents a detailed analysis of heterogeneity and pore connectivity. The latter is, however, crucial to understand how these macro-pores affect MOF performance in separation or adsorption processes.

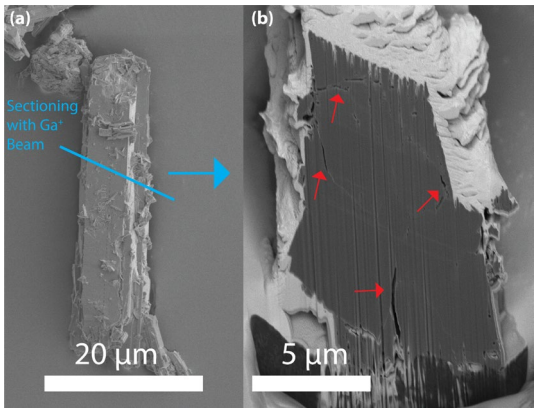

Figure 2.2 (a) Scanning electron microscopy (SEM) image of a MIL-47(V) metal-organic framework (MOF) crystal synthesized in the same way as the one studied by transmission X-ray microscopy (TXM). (b) SEM image of focused ion beam (FIB)-cut cross section of the particle displayed in (a) showing macropores. The red arrows indicate macropores observed in the cross-section of the crystal.

2.2.2 Image Segmentation

In order to analyze the macropore network of the MOF crystal, it is necessary to classify each voxel (i.e., 3D equivalent of a pixel) of the reconstructed volume into either void or solid phase to create a binarized data volume. Therefore, a grayscale threshold value must be selected. Every voxel with a grayscale intensity above this threshold will then be considered as solid while voxels below this value will be assigned as void space. As this crucial parameter can in principle be chosen arbitrarily, additional knowledge for selecting a correct value is needed. The threshold value determines the void voxel fraction of the reconstructed particle volume and is therefore directly correlated to the total porosity determined from the reconstructed data. To have an initial estimate for total porosity and in turn the threshold value, Hg-porosimetry characterization of the same material was performed resulting in a total porosity of 29% (see Methods). However, visual inspection of the grayscale cross sections (Figure 2.1b,c) and their corresponding binarized images (Figure 2.3a-h) as well as comparison with the porosities observed on other crystals with FIB-SEM (<2%), suggests that Hg-porosimetry overestimated the total porosity. As a Bulk technique, Hg-porosimetry cannot distinguish between inter- and intraparticle voids and likely misinterprets inter particle porosity as intra particle void space.

In order to achieve a segmentation that better represents the actual macroporosity of the crystal, a series of X-ray absorption thresholds (corresponding macroporosities: 2-29%) was evaluated (Figure 2.3). As a first boundary case, the highest X-ray absorption value of the of the air surrounding the crystal was used as a threshold (Figure 2.3d-j). By doing this, about 18 % of the particle volume was identified as void space. However, also this value still seemed to overestimate macroporosity when

the binarized cross sections (Figure 2.3a-h) are compared to their grayscale counterparts (Figure 2.1b,c). Besides, the FIB-SEM results suggest a much lower macroporosity than 18 %. Finally, as a third, lower boundary case, an intensity threshold was chosen based on the average intensity of the image background (Figure 2.3i,j), which results in a total porosity of 2.6 % (Figure 2.3a). The porosity estimated with FIB-SEM (< 2 %) (see Methods) is comparable to this value. In addition, the binarized cross section image resulting from this threshold, seems to be in better alignment with the particle's X-ray absorption image (Figure 2.1b,c). Therefore, we suggest that the total macro-porosity of the studied individual MOF crystal should be in the region of 2-3 %. However, we cannot exclude that this value could be higher. This is why performed we our pore-network analysis using not only one but a series of grayscale threshold values corresponding to macro-porosities of 29 %, 25 %, 20 %, 18 %, 15 %, 10 %, 5 %, and 2.6 % (Figure 2.3a-h). In the following section, we highlighted the boundary cases of 29, 18, and 2.6 % porosity (Figure 2.3a,d,h,j).

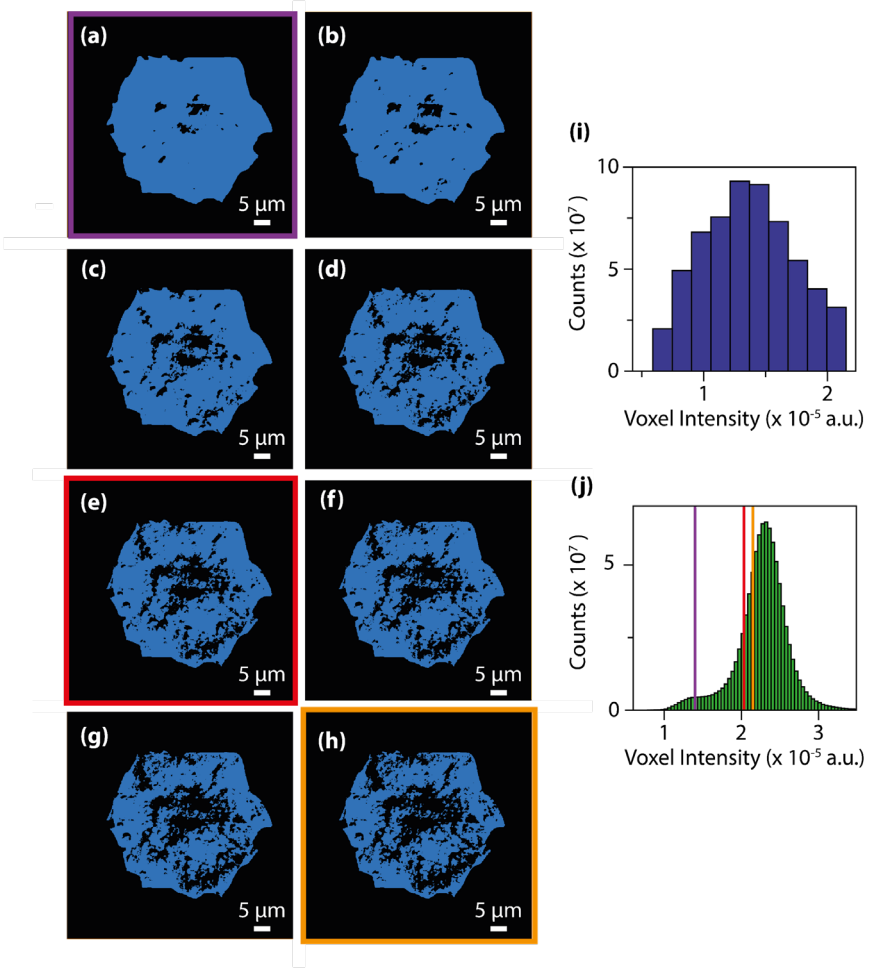

Figure 2.3 Segmented images of a cross section of the metal-organic framework (MOF) crystal assuming different total porosities. 2.6, 5, 10, 15, 18, 20, 25, 29 % (a-h). (i) Grayscale intensity histogram of the image background. (j) Grayscale intensity histogram of the particle. The boundary case thresholds are highlighted in this image. Purple: Intensity threshold based on mean of the background intensity values shown in (i) (2.6 % total porosity). Red: Intensity threshold based on highest background intensity value (18 % total porosity). Yellow: segmentation threshold based on Hg-porosimetry (29 % total porosity). The corresponding binarized images (a,e,h) are signalized with these colors as well.

2.2.3 Connected Macroporosity and Intraparticle Heterogeneity

To assess the heterogeneity in macroporosity within the MOF crystal, the porosities of 7 sub-volumes of 7.5x7.5x7.5 µm³ along the primary MOF-crystal axis were computed (Figure 2.4a). The flow permeability of a material can be used as a measure of its pore connectivity. If a porous material is not permeable, it consists only of isolated pores. By contrast, the more permeable the material the higher its pore connectivity. In order to evaluate how permeable was the reconstructed crystal, flow simulations were carried out on each of the sub-volumes using the Avizo® XLabHydro software (Figure 2.4b). A more detailed explanation can be found in the Methods section. Then, the permeabilities and total porosities of all sub-volumes were then compared. Remarkably, large intra-particle heterogeneity was revealed by this analysis: for example, when the threshold chosen for binarization was set to achieve a total porosity of 2.6 %, some sub-regions show essentially no macro-porosity (1, 4, 5). However, sub-volume 7 has a void fraction of more than 11-fold the particle average (Figure 2.4b). As the hypothetical total porosity was stepwise increased by setting higher thresholds, i.e., 5 10, 15, 18, 20, 25, and 29 %, sub-volumes 1, 4, and 5 gradually exhibited increasing porosity (Figure 2.4b). Yet, sub-volume 7 showed a porosity much higher than the total average for all the studied thresholds. Several sub-volumes exhibit porosity, but virtually no permeability (sub-regions 1-5). This is the case even when the total porosity of the MOF is assumed to be 29 % (based on Hg-porosimetry). As discussed above, this porosity value strongly exceeds the real one. This means that the macropores within these regions are isolated even if their total porosities are artificially increased. On the other hand, sub-volume 7 displayed both a high porosity as well as permeability for all segmentation thresholds indicating a high pore connectivity. From these results it can be concluded that both porosity and pore connectivity are heterogeneously distributed across the particle. Nevertheless, most of the particle does not seem to be well connected by macropores.

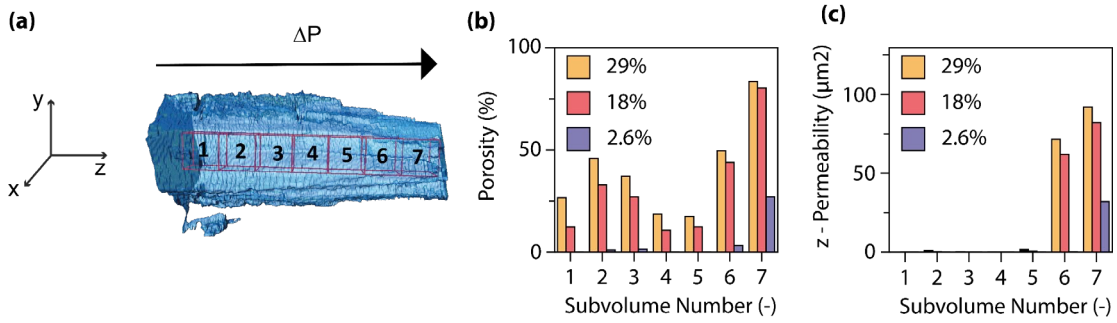

Figure 2.4 (a) Selected sub-regions (7.5x7.5x7.5 µm³) for porosity and permeability analysis of the MIL-47(V) metal-organic framework (MOF) crystal. A flow was simulated along the z-axis to determine the permeability of each sub-region (see arrow indicating pressure gradient) (b) Individual porosities of the 7 sub-volumes determined for different segmentation thresholds, i.e., total porosities of the whole crystal. (c) Permeabilities of subregions and simulated steady state flow streamlines in sub-volumes 6 and 7 assuming a total porosity of 18 %, an incompressible fluid, and a negative pressure gradient from left to right.

To assess pore connectivity in more detail, the measured pore network was expressed as a pore-network model as previously described by Meirer, Kalirai and co-workers (see Methods).[204] By doing this, the pore volume is described by a set of points, lines, and corresponding distances to pore boundaries. Figure 2.5 displays the pore network model of the MOF assuming total porosities of 2.6 % (a), 18 % (b) and 29 % (c). Here it can clearly be seen how the macropore connectivity increases with increasing porosity and goes along with the appearance of pore channels with larger diameters (red regions Figure 2.5b,c).

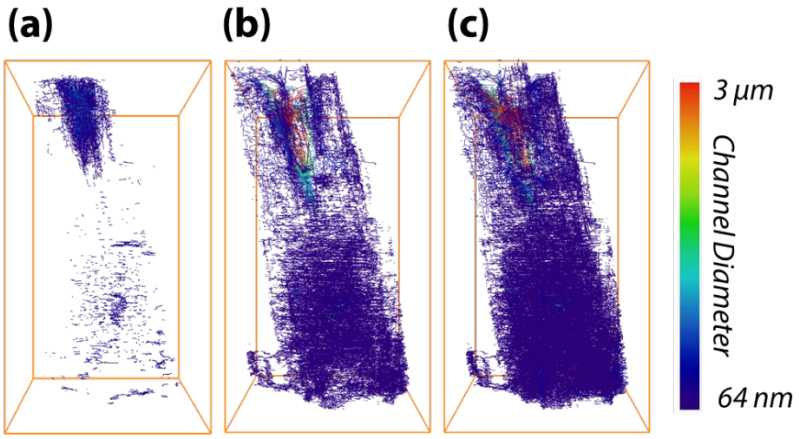

Figure 2.5 Determined pore network models of the MIL-47(V) metal-organic framework (MOF) crystal assuming total porosities of 2.6 % (a) 18 % (b) and 29 % (c). The color scale represents the diameter of the pore channels: blue corresponds to small values, whereas red represents wider channels.

To further evaluate connectivity, the different graphs, (defined as a group of connected segment points) were analyzed separately using MATLAB®. The 10 largest graphs obtained for each intensity threshold are plotted in Figure 2.6a-h. By binarizing the image based on Hg-porosimetry (29 % porosity), the whole particle volume is well connected by the biggest sub-network (blue dots in Figure 2.6h). At a total porosity of 18 %, on the other hand, the MOF pores are not entirely connected by a single network, but the first two graphs combined (orange and blue dots in Figure 2.6 e). Note that two graphs are never connected to each other. In these two cases, the macro pore network we map here would have a significant effect on mass transfer, creating diffusion "highways" and strongly reducing the separation properties of the MOF. However, for a total porosity of 2.6 %, all sub networks are very much localized (Figure 2.6a), that is, macro-pore connectivity is low, which is desired for separation processes. As mentioned above, we believe that the true macroporosity of the particle is close to this value. However, it is worth mentioning that this seemingly isolated macropore networks could be connected by smaller macropores that could not be resolved with the TXM-tomography. Since the measured X-ray absorption is correlated with material density, voxels containing pore defects smaller than the resolution (230.7 nm), led to lower voxel grayscale values compared to their defect-free counterparts. Therefore, when the hypothetical porosity is increased, more voxels containing unresolved pore defects are interpreted as void space and since these pores are not necessarily connected, this leads to an overestimation of connectivity. If the assumed total porosity is gradually increased from 2.6 % to 5 %, the extension of the resulting subnetworks increases (Figure 2.6a,b). However, they are still very localized and unconnected. This suggests that the observed macropore networks are not interconnected by macropore defects that could not be resolved with the TXM-tomography.

The porosity of 2.6 % determined above as the best estimate for this individual crystal indicates that any diffusing medium will necessarily flow through a certain fraction of micropores, which is of the upmost importance since MOFs usually rely on the functionalities present therein (e.g., coordinatively unsaturated Lewis sites, OH groups or on-purpose attached organic moieties) for molecular sorting.[171,198,199] Hence, the findings presented up to here have two implications: 1) MIL-47(V) crystals synthesized by hydrothermal methods contain defects (2-3 % of the crystal volume). 2) The connection between these macro-porous regions is not sufficient to create diffusion pathways that result in a significant loss of the MOFs sieving properties.

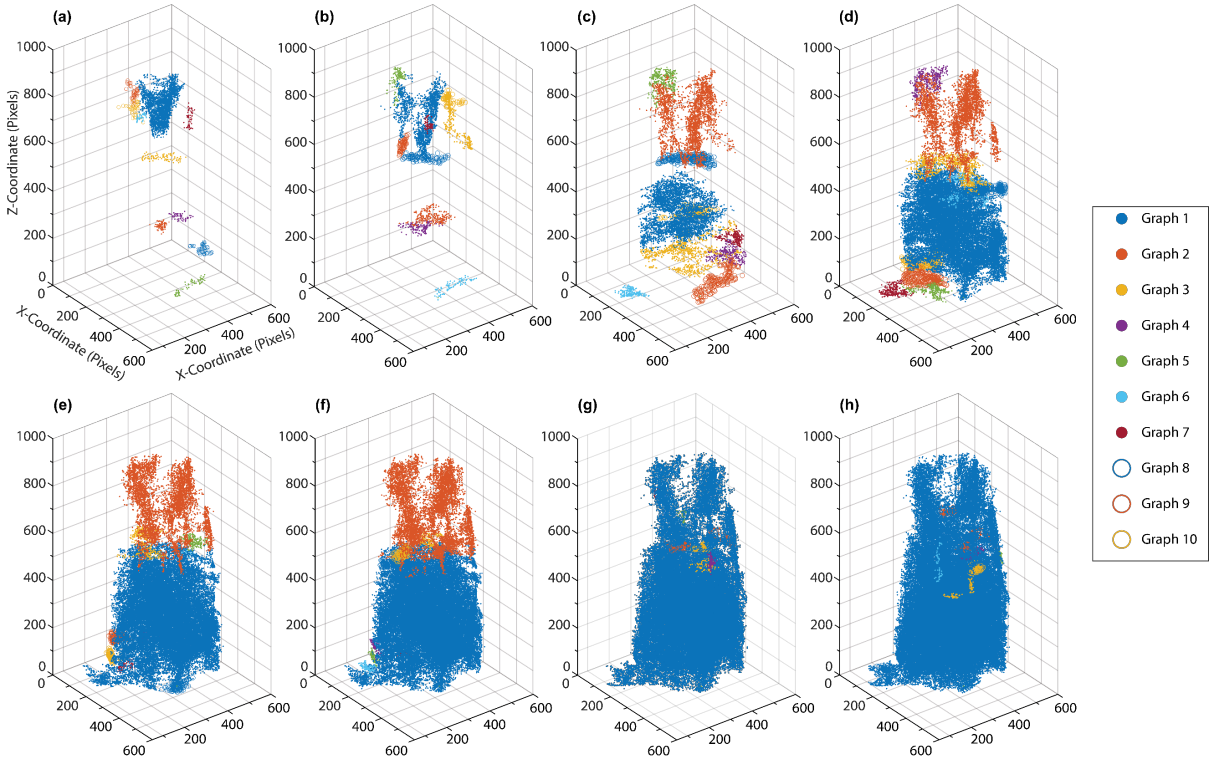

Figure 2.6 Plots with 10 graphs with the greatest volumes for different total porosities within a MIL-47(V) metal-organic framework (MOF) crystal: 2.6 %, 5 %, 10 %, 15 %, 18 % ,20 %, 25 % and 29 % (a-h). The higher the total porosity the higher the connectivity of the macropore sub-networks. At total porosities between 2.6 % and 5%, the subnetworks are very localized and poorly connected.

2.2.4 Graph Orientation

In an attempt to elucidate the origin of the detected macropores, their orientation in relation to the MOF axis was assessed by calculating the first Eigenvector (EV) of the covariance matrix of each graph (i.e., connected pore sub-network). This vector points in the direction of the greatest spread of each graph (expressed as a cloud of points in space) and can therefore be used as a measure for pore orientation. Figure 2.7 exemplifies this method by displaying the 10 sub-networks with the highest volume (a) and their corresponding first EVs (b). The position of the displayed EV corresponds to the average coordinates of the graph (point cloud) they describe.

The inset in Figure 2.7c reports the spherical coordinates of each Eigenvector, that is, the angles between each vector and the main MOF axis (as defined above, z-direction in the plot). These angles describe how parallel the graph orientation is with respect to the MOF axis (angle θ) and how the sub-network is oriented in the x-y plane (angle ϕ). Figure 2.7c and d display the orientation of the first EV of the biggest 300 sub-networks assuming a total porosity of 2.6 %. The histograms report the θ (c) and ϕ (d) angles between the first EV of the graphs and the MOF axis. Based on these results there does not seem to be a clear preferred pore network directionality when inspecting the EVs that are projected perpendicularly to the MOF axis (Figure 2.7d). On the other hand, Figure 2.7c shows that most of the graphs have an angle θ between 80° and 90°. This means that most of the macropores are oriented perpendicular to the main MOF axis. Such preferential defect directionality suggests that the main crystal growth takes place along this direction. As the crystal grows small defects can be amplified to become radially oriented macropores like the ones observed here.

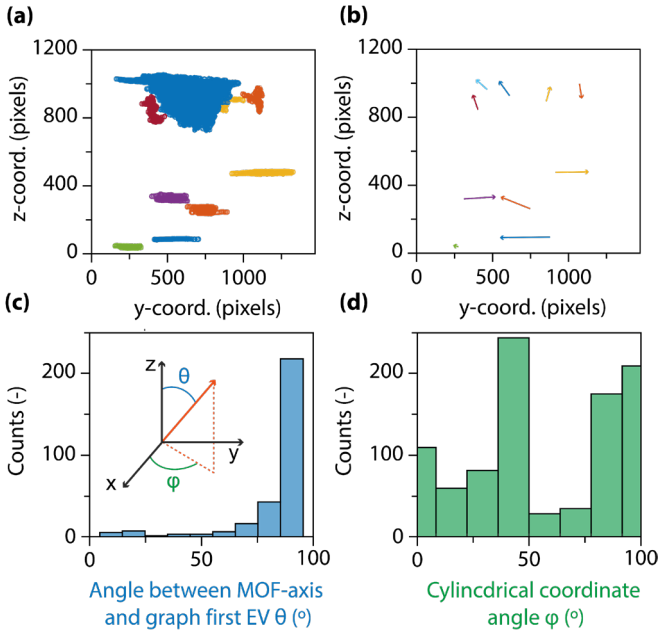

Figure 2.7 The 10 sub-networks with the largest volumes assuming 2.6 % total porosity of the individual MIL-47(V) metal-organic framework (MOF) crystal. b) Corresponding first Eigenvectors (EVs) normalized and projected to the z-y plane (the apparent length difference is caused by the projection onto the z-y plane). The position of each EV corresponds to the average coordinates of each data cloud (graph) it refers to. c) Histogram of angles between each graph's first eigenvector and the main MOF axis (θ). Spherical coordinates of the first EVs of the sub-networks. The 3D volume was rotated, so that the MOF axis is parallel to z. θ describes how parallel the EV is with respect to the main MOF-axis, Φ describes the orientation of its projection onto the x-y plane. d) First EV orientation histogram projected onto the x-y plane (angle ϕ).

Regardless of the total porosity chosen, the preferential pore direction described above could be observed (Figure 2.8a-c). However, as the total porosity grows, there is a slight shift towards smaller angles in the θ-angle histogram. This is due to an increase in connectivity along the MOF axis when the assumed porosity increases. The growth of such aligned defect domains is common in MOF [205–207] and is a potential explanation for the presence and orientation of the voids observed. Further *in-situ* imaging studies of a growing crystal would be necessary to confirm this hypothesis.

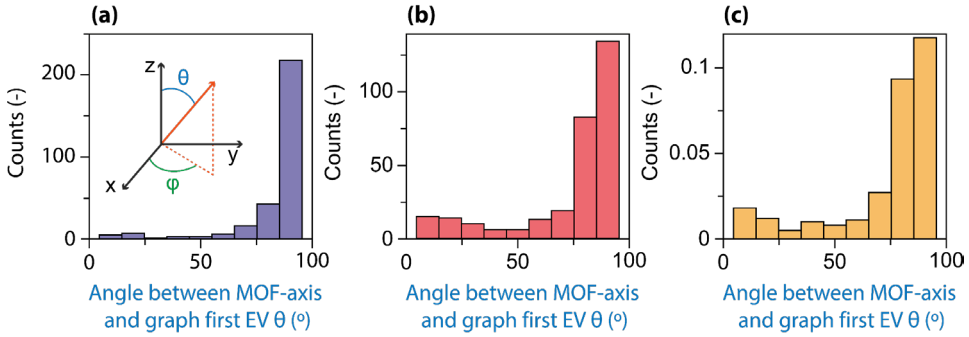

Figure 2.8 Histogram of angles between Graph first eigenvector and the MIL-47(V) metal-organic framework (MOF) axis (θ) assuming a total porosity of (a) 2.6, (b) 18 and (c) 29 %. As the porosity increases, there is a slight shift towards the left in the θ-angle histogram due to an increase in connectivity along the MOF axis.

2.3 Conclusions

This Chapter shows that it is possible to map the macropore defects of a single MIL-47(V) MOF crystal with X-ray nanotomography in a non-destructive way. In contrast to Hg intrusion porosimetry, the TXM methodology allowed to estimate the total microporosity of the sample (2-3 %). Furthermore, permeability simulations and pore-network modelling revealed that the observed macropores are not distributed homogeneously across the particle and their connectivity seems to be very poor. Therefore, the macropore defects presumably only have a limited effect on the separation properties of the MOF crystal. By analyzing the tilting angle of the pore regions, a preferred network orientation was observed. The pore sub-networks are mostly spread perpendicularly to the main MOF-axis, which could lead to anisotropies in diffusion and permeability.

2.4 Materials and Methods

2.4.1 Materials

vanadium metal powder (Sigma-Aldrich, 99.9%), terephthalic acid (Sigma-Aldrich, +98%), hydrofluoric acid (Sigma-Aldrich, 48-51 % wt. aq. solution), Deionized (DI) water, Dimethylformamide (DMF) (Sigma-Aldrich, 99.8%). All chemicals were used as received with no further purification.

Hydrothermal preparation of the crystals was carried out as described by Barthelet et al.[208] In short, vanadium metal powder, terephthalic acid, hydrofluoric acid, and DI water (molar ratio 1:0.25:2:250) were introduced in a Teflon-lined Parr steel autoclave for four days in an isothermal oven at 473 K (autogenous pressure, filling rate: 50%). The green-yellow solid was collected by centrifugation and washed 3 times with DMF and ethanol (50 mL), then dried at 423 K under vacuum for 24 h.

2.4.2 Characterization

a. Hg Intrusion Porosimetry

MIL-47(V) crystals (m = 0.634 g) were outgassed for 24 h in air flow at 150°C prior to loading them in the tube. Intrusion experiments were performed using an Hg porosimeter Micromeritics Autopore IV 9510 in the pressure range p = 0.05 to 420 MPa. We used Washburn's equation $p = -4\gamma\cos(\theta)/d$, with γ, mercury surface tension, and θ, contact angle, with values of 0.485 N·m-1 and 130°, respectively, to calculate the pore diameter, d.

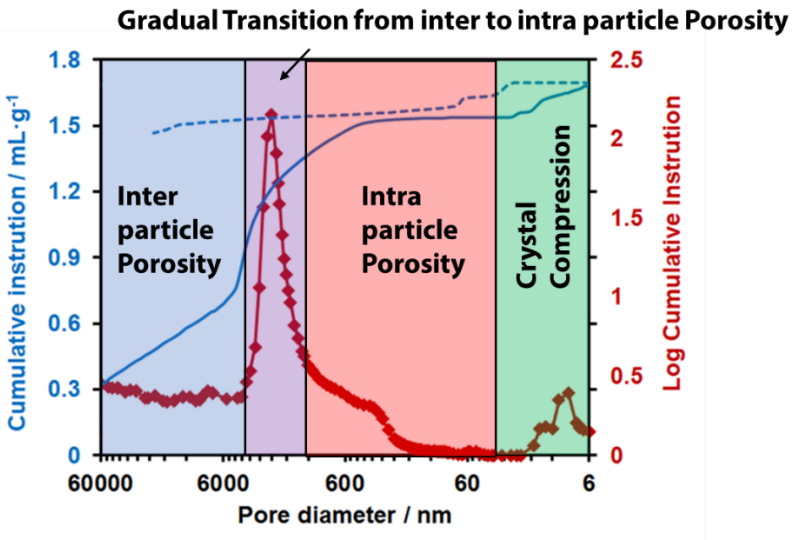

Figure 2.9 Cumulative and incremental volumes of intruded Hg as a function of the effective pore diameter. The steep increase in Hg cumulative intrusion corresponding to pores in the 6×10^3 to 6×10^4 nm range is associated to interparticle porosity (region I). Here, voids within and in between particles are filled with mercury. The greater the intrusion pores of this regime, the more inter particle porosity is being probed (region II). Conversely, when smaller pores are filled, they are more likely to be a consequence of intra particle porosity. The rather small mesopores measured in region IV are a result of a compression of the crystal due to high pressures.[209] The described regimes cannot be quantified during this experiment, this figure displays their ranges only qualitatively.

In Figure 2.9 cumulative and incremental volumes of intruded mercury as a function of the effective, mercury cumulative intrusion and pore size distribution obtained thereof, shows the presence of two peaks at around 0.1 (~2-3·103 nm, region II in Figure 2.9) and 100 MPa (~8-6 nm, region IV Figure 2.9). The latter has been previously assigned to the reversible compression of the lattice, due to the poor wetting of the MOF surface, preventing Hg from penetrating the micropores and the former, has been ascribed to space between crystals. [209] The minimum pore diameter which may be probed at 420 MPa is 2.96 nm, as per Washburn's equation (γ = 0.485 mN·m-1, θ = 130º).

However, as seen in Figure 2.1b,c, cross-sections of different parts of the crystal show areas of lower X-ray absorption intensity, exhibiting macropores that are up to 2-3 µm in size. This is of great importance, because both bulk and intraparticle pores with such dimensions could be present in region II of Figure 2.9. Porosity was determined as the percentage of volume that can be intruded with Hg between 0.2 and 20 MPa, which represents the adsorption plateau at which the larger pores and interparticle space have been filled with Hg but before mechanical compression:

$$\left(\frac{V_{Hg}(0.2\ MPa)}{V_{Hg}(20\ MPa)}\right)\times 100 = \frac{0.43}{1.51}\times 100 = 28.47\ \% \qquad \text{Equation 2.1}$$

b. Focused Ion Beam-Scanning Electron Microscopy

Prior to measurements, the sample was coated with a Pt/Pd layer (~10 nm) with a Cressington HQ280 sputter coater. Measurements were performed with a FEI Helios Nanolab 600 FIB-SEM instrument. The sample was placed on an aluminum stub using a carbon sticker. A protective layer of Pt (~3 µm) was deposited on top of the region of interest before performing the measurements. For the FIB experiments, a trench was made by milling perpendicularly to the surface, next to the Pt-deposited area. After milling the trench, a cleaning step with Ga+ ions were performed before imaging. SEM

images of the cross section were recorded in backscatter electron (BSE) mode (2 kV, 50 pA) and in secondary electron mode (2kV, 0.1 nA). These images were manually segmented to determine the porosity of the cross sections (Figure 2.10).

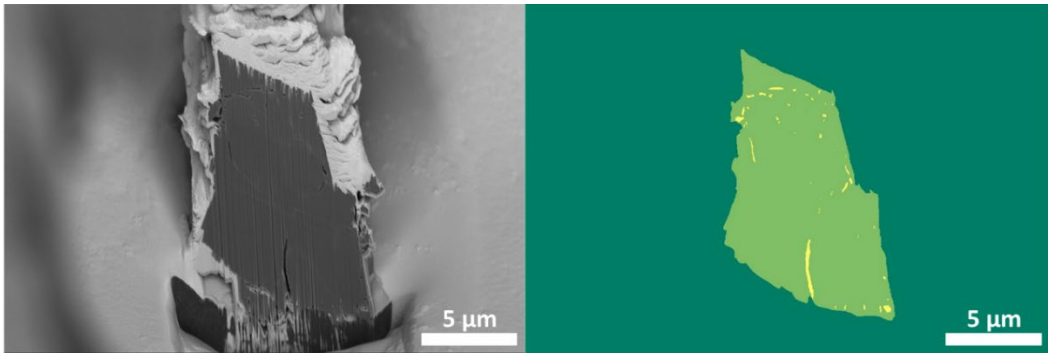

Figure 2.10 Manual segmentation of the cross section and pores. The fraction of yellow pixels (pores) within the light green area (particle cross section) corresponds to the porosity estimated from these data.

c. Powder X-ray Diffraction

Powder X-ray diffraction (PXRD) was performed using a Bruker-AXS D2 Phaser powder X-ray diffractometer in Bragg-Brentano geometry, using Co Kα1,2 = 1.79026 Å, operated at 30 kV (Figure 2.11). Measurements were carried out between 5 and 70° using a step size of 0.05° and a scan speed of 1 s.

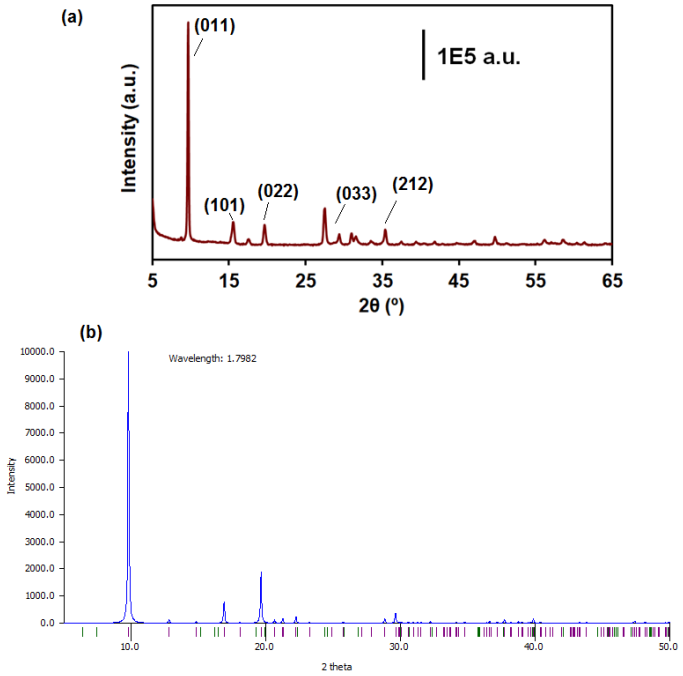

Figure 2.11 (a) Experimental X-ray diffraction (XRD) pattern of the MIL-47(V) metal-organic framework (MOF) material as synthesized powder; and (b) simulated XRD pattern from Mercury 3.7 (FWMH = 0.1, Kα = 1.7892) with the .cif file reported in reference.[210]

2.4.3 Transmission X-ray Microscopy Tomography

a. Sample Preparation

The crystals were suspended in ethanol and loaded into 1 mm diameter Kapton® tubes by capillarity. After loading the samples, the solvent was evaporated and dried in air, after which both ends of the tubes were sealed with epoxy resin. The capillaries were then loaded into glass jars and evacuated in a diaphragm pump connected to a glovebox, where the samples were stored prior to measurement. The tube was loaded onto the rotatory stage at beamline 6-2c, and a He bag with constant 10 mL/min flow at the outlet tube was placed over the sample and X-ray emitting pinholes to prevent air absorbance.

b. Tomography Data Collection

Full-field transmission hard X-ray microscopy (TXM) was performed at beamline 6-2C of the Stanford Synchrotron Radiation Lightsource (SSRL) at the Synchrotron Linear Acceleration Center (SLAC) National Accelerator Laboratory. Details of the experimental setup can be found elsewhere.[80,211] The X-ray energy was calibrated by measuring at the V K-edge of a reference metal foil. X-ray nano tomography was conducted below and above the V K-edge energies (5460.0 and 5482.0 eV) five times per angle with an angular step size of 1 degree over a range of 180 degrees, enabling a high-quality reconstruction of the 3D structure of the MOF single-crystal with the TXM-Wizard software package.[212] The total duration of the scan was 260 minutes.

Each stack of 2-D projection images was aligned manually to correct for motor jitter and sample movement. Later, the 3-D tomographic slices were reconstructed with an iterative algebraic reconstruction technique (iART). TXM tomography data was binned from a 32 nm isotropic voxel size to a voxel size of 64x64x64 nm^3. Each slice of the obtained 3D image was segmented manually, to determine the total particle volume (including pores) using Avizo Fire© software.

2.4.4 Data Analysis

a. Pore Network Modelling

The void space was represented by its topological skeleton, i.e., a thinned version of the pore shape. After skeletonization, the pore volume is described by a set of points, lines, and corresponding distances to pore boundaries. The skeletonization of the segmented pore volumes was performed using the Avizo© XSkeleton Pack software. The distance of every pore voxel to its closest boundary was calculated and then voxels were removed one by one from the segmented object until only a string of connected voxels remained. These resulting lines were then translated into points, segments (connecting points), and nodes (points where more than two lines meet) forming a topological model of the pore-network (Figure 2.12). Each pore channel can be represented by a cylinder, in which the height is the distance between two segment points and the radius is their average distance to the solid walls. By summing the volumes of these cylinders, the total volume of the pore network can be computed.

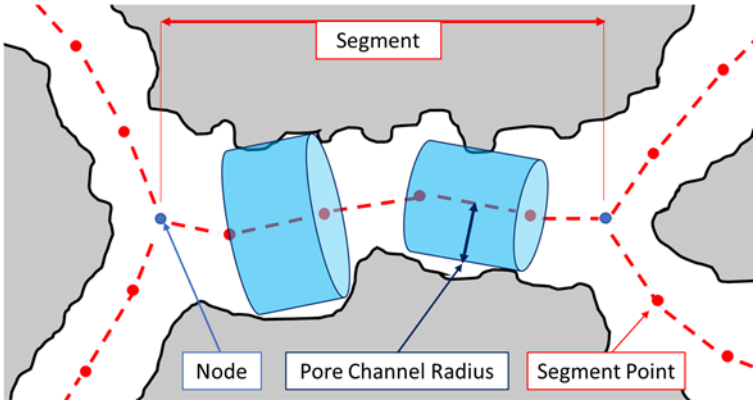

Figure 2.12 Schematics of the topological representation of the pore network. The measured pore space is modelled by a set of segment points, segments, nodes, and pore channel radii. Adapted from Meirer et al.[98]

b. Permeability Simulations

Permeability simulations in (Figure 2.4) were carried out on each sub-volume using Avizo® XLabHydro. This software estimates the steady state velocity field of an incompressible fluid (water) by numerically solving the continuity and Navier-Stokes equations:

$$\nabla \cdot \vec{u} = 0 \qquad \text{Equation 2.2}$$

$$\mu \nabla^2 \vec{u} - \Delta p = 0 \qquad \text{Equation 2.3}$$

where μ is the medium viscosity, u its velocity and Δp is the pressure gradient of the causing the flow. The permeability is determined using Darcy's Law:

$$Q = \frac{kA\Delta p}{\mu L} \qquad \text{Equation 2.4}$$

where Q is the global volume flow rate of the fluid, k is permeability and A and L are the cross-sectional area and the length of the sample volume respectively.

c. Fourier Shell Correlation Analysis

A Fourier Shell correlation (FRC) was performed to estimate the 3D resolution. Therefore, the projection images of the tomography data were separated into two different datasets. One of the datasets contains all images recorded at even angles and the other corresponds to odd recording angles. The analysis was performed for 400 slices of the reconstructed odd and even datasets as described by van Heel et al.[79] Figure 2.13 displays the average FSC of all 400 slice pairs. The resolution was determined using the intersection point of the FRC curve with the ½ bit curve. Using this criterion, the resolution calculated was 230.7 nm (0.277 reciprocal pixels of 32 nm size).

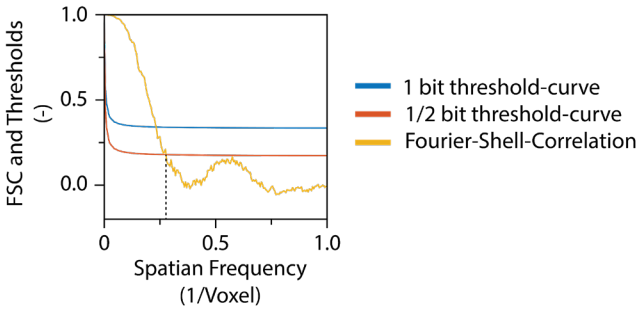

Figure 2.13 Fourier Shell Correlation (FSC) analysis of the tomography 400 arbitrarily selected slices of the reconstructed data.4 The intersection at 0.277 (discontinuous line) reciprocal pixels corresponds to an estimated 3D spatial resolution was 230.7 nm (1/2 bit).

3 Accessibility Study of Porous Materials at the Single Particle Level as Evaluated within a Multiplexed Microfluidic Chip with Fluorescence Microscopy

Uptake experiments of UV-Vis-active or fluorescent probes represent a direct way for elucidating mass transfer phenomena. However, interparticle heterogeneity cannot be discerned with it as it is a bulk technique. In this Chapter, we propose a new analytical method to evaluate the accessibility of porous particles at the single-particle level in a relatively high throughput fashion. It involves using a Polydimethylsiloxane microfluidic device and a fluorescence microscope to assess the uptake of fluorescent molecules in porous particles over time. The device allows for studying the differences between and within three samples contemporaneously under the same conditions. We further showcase the method by studying the diffusion and adsorption properties of a dye in different reference porous particles. Our approach allowed for probing accessibility as well as probe-host interactions, thus revealing the limiting factors in the uptake process.

Based on:

Alessia Broccoli†, Luca Carnevale†, Rafael Mayorga González†, Joren Dorresteijn, Bert M. Weckhuysen, Wouter Olthuis, Mathieu Odijk, and Florian Meirer, Accessibility Study of Porous Materials at the Single-particle Level as Evaluated within a Microfluidic Chip with Fluorescence Microscopy, Chem Catal. 2023, 3, 100791.

†These authors contributed equally to this work.

3.1 Introduction

Molecular transport is a key aspect in most functional porous material applications, as it strongly influences their performance as adsorbents or catalysts.[8] The efficiency of these materials depends on diffusion and adsorption processes taking place inside their pores, which are in turn influenced by the interactions between the pore walls and the guest molecules. [6–8,21] Therefore, understanding these phenomena is essential for designing superior functional materials, with improved performances.

A direct way for investigating mass transfer in porous materials is based on uptake and release experiments of UV-active or fluorescent probes, directly providing a pore accessibility measure (i.e., how easily molecules enter the porous host). One common approach used in industry is the so-called Akzo Nobel Accessibility Index (AAI) test introduced for Fluid Catalytic Cracking (FCC) particles[21–23]. Here, the uptake of UV-Vis-active molecules into catalyst particles is measured by measuring the relative concentration of the molecules in solution over time (Figure 3.1a,b), providing a measure of the penetration rate. In this approach, it is assumed that the behavior of the entire system replicates the one of an individual particle. However, within a catalyst batch[60,61], structural and compositional differences exist that cannot be captured by these ensemble-averaged measurements.

Characterizing the pore space and mass transfer properties of individual particles would be beneficial to supplement the data obtained from bulk methods, and also to capture heterogeneities among particles. Single particle techniques such as confocal laser scanning fluorescence microscopy (CLSM) [5,101,106,213,214] infrared microscopy (IR)[7,215,216], electron microscopy [65,217–222] and X-ray microscopy[12,13,19,98,223,224] have shown great potential to achieve this. However, these techniques require expensive equipment and/or sample preparation, and some of them are destructive. Furthermore, the number of particles that can be studied with these methods is limited, leading to poor statistics.

In this Chapter, we propose a fast, cheap, and reproducible analytical method to compare mass transfer in porous samples at the single-particle level in a high-throughput fashion. By using a Polydimethylsiloxane (PDMS) microfluidic device and a conventional fluorescence microscopy setup, we imaged and compared the uptake of fluorescent molecules by individual mesoporous silica particles. Moreover, we varied the solution conditions and found that the guest-host electrostatic interactions have a significant effect on the overall uptake process.

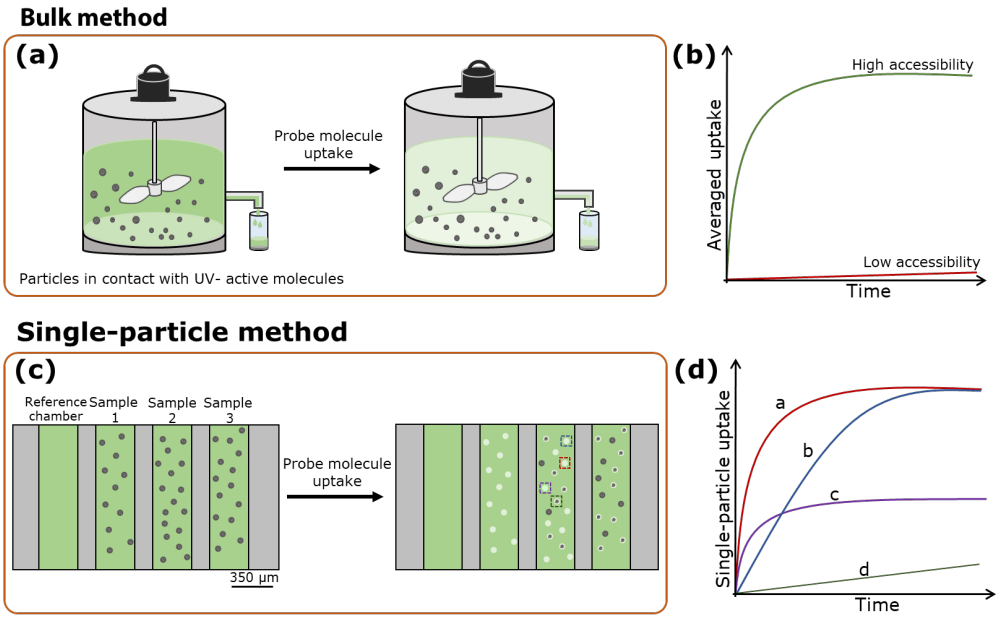

Figure 3.1 Schematic representation of experimental methods to evaluate the accessibility of particles in bulk and at the single particle level. (a) A stirred tank containing UV-active molecules is put in contact with porous particles. The concentration in the solution decreases due to the uptake on the porous material. (b) Based on the concentration change, the bulk uptake [mol/g(material)] is computed and used to characterize the accessibility. (c) A multiplexed microfluidic device containing 4 chambers is filled with different porous particles and a liquid containing a fluorescent dye. One reference chamber (left) is left empty to control for photobleaching. As fluorescent molecules enter the porous particles, their fluorescence increases. (d) The fluorescence of individual particles (in the highlighted squares) is tracked over time to assess their accessibility. Curves A and B correspond to particles with the same accessible adsorption capacity (both plateau at the same value), but different accessibilities (A>B). Curve C represents the uptake of a particle that is rather accessible (saturation is reached quickly) but total uptake of fluorophores is less than in particles corresponding to curves A and B. Curve D corresponds to a particle with very low accessibility (saturation is not reached during the time of the experiment).

3.2 Results and Discussion

The experiments were performed using microfluidic devices consisting of two PDMS layers, attached to a glass slide, further details on the device can be found in the Methods section and elsewhere.[225,226] The chip contains four chambers, which allow for the performance of three experiments in parallel under the same conditions while keeping a reference chamber to control for photobleaching (Figure 3.1c). In each experiment, each chamber is loaded with different porous particles. Then, all chambers are filled with water, such that the pores of the hydrophilic material are quickly (less than a second) filled by capillary forces.[227] Finally, the chambers are filled with a fluorescent dye solution. The mean fluorescence intensity, as a measure of dye concentration, of each particle is tracked individually as a function of time resulting in individual uptake curves (Figure 3.1d, Methods). The features of each uptake curve can provide the following information: 1) the final slope of the curve contains information about the saturation state of the particle. If it is flat, equilibrium has been reached. Otherwise, the uptake is still taking place. 2) The intensity value reached after saturation contains information about the adsorption properties of the system. The higher this value, the more adsorption took place, which can be related to the surface area of the material. 3) The shape of the curve, i.e.,

how the curve slope changes over time, contains information about the accessibility of the particle. The faster saturation is reached, the more accessible the particle.

To showcase the method, we used SiO_2 particles with monodisperse pore size distributions (50 nm, 35 nm, and 23 nm) (Figure 3.4a) often used as catalyst support.[228,229] Rhodamine 110 (Rh110) (Figure 3.4b) was used as a fluorescent probe due to its photostability[25,26], high quantum yield, and fluorescent intensity proportional to its concentration (see Methods). Therefore, particle fluorescent intensity values were directly used to obtain the uptake curves i.e., the intensity was used to measure concentration. The particles were placed in the chambers leaving one empty that was used as a reference to check the photostability of the dye. Uptake experiments were conducted for 5h and images were acquired every minute. Figure 3.2a,b displays a cropped version of the fluorescence images recorded at the beginning (a) and end (b) of the experiments using 50 nm pore size particles showing an overall, but heterogeneous increase in intensity. Some particles display an intensity (concentration) gradient within them, whereas others show a more homogeneous dye distribution, hinting towards different pore connectivities. Figure 3.2c shows the mean intensities of particles of the same sample as a function of time (the initial intensity of each particle was subtracted). Even particles that belong to the same batch, differ strongly on their uptake curves and therefore accessibilities. Traditional bulk experiments could not have measured this, which highlights the importance of the proposed method for elucidating inter-particle heterogeneity.

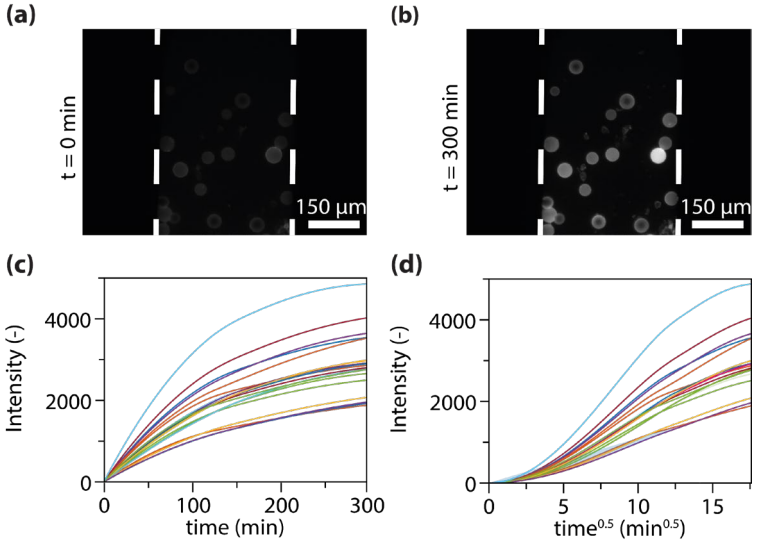

Figure 3.2 (a) Cropped fluorescence image of a microfluidic chamber containing silica particles with 50 nm pores at the beginning and (b) end of the experiment. (c) Uptake curves of particles shown in (a,b). (d) Uptake curves are linearized when plotted over $t^{0.5}$.

3.2.1 Uptake Curve Interpretation

Various models have been developed to interpret the shape of the uptake curves obtained from bulk uptake experiments[20]. However, most of these models require reaching a saturation state to extract the relevant parameters, which represents a problem for our slow, non-saturating uptake experiments. Conversely, The so-called intra-particle diffusion model[230] does not have this requirement and is often used in these cases. Here, the fractional uptake q(t) (usually in mg(probe)/g(solid), but expressed with an intensity in our case) is plotted as a function of $time^{0.5}$. If external mass transfer effects are negligible (i.e., constant concentration in the bulk solution as a function of space), the curve will be linear at low $time^{0.5}$ values until saturation starts to take place,

flattening the curve after an inflection point. On the other hand, in the case of prominent external mass transfer effects (no ideal mixing), a stagnant layer, i.e., a concentration gradient in the vicinity of the particle, is formed during the uptake process, slowing it down and resulting in a non-linear regime for small time$^{0.5}$ values (Chapter 1).[20,30] The latter was the case in our experiments (Figure 3.2d) because no flow (or mixing) was present in the chambers of the chip. For such systems, a linear regression is usually performed on the linear part of the uptake curve and its slope is used to quantify the so-called intra-particle diffusion rate constant[27] K_p (usually in mass(probe)/(mass(particle)time$^{0.5}$), but expressed in intensity/time$^{0.5}$ in our experiments) which we refer to as accessibility index (Equation 3.1).[21]

$$q(t)=K_p\ t^{0.5} + C_y \quad \text{Equation 3.1}$$

The presence of a non-zero y-intercept C_y (sigmoid-like uptake curve shape), has been attributed to external mass effects as well as adsorption events. Furthermore, different interpretations of its value have been proposed, leaving its physical origin unclear (see Chapter 1). To investigate the significance of the accessibility index K_p and the y-intercept C_y for the uptake curves, mass transfer simulations were performed assuming that the uptake is governed by three parameters: 1) the internal particle diffusion coefficient D (m^2/s), which increases with the pore size and pore interconnectivity; 2) the external mass transfer coefficient k (m/s), which depends on diffusion and convection outside the particle as well as the intra-particle diffusion (Equation 3.6, see Methods) and 3) the adsorption coefficient R (-) (unitless if adsorbed concentration is expressed as g/m^3, see Methods). The latter depends on the wall-molecule interactions as well as the number of accessible adsorption sites. We performed a sensitivity analysis to assess how these three parameters affect the uptake curve shape and its parameters K_p and C (Methods). Our simulations showed that the unlike the y-intercept C_y, the accessibility index K_p correlates positively with all three parameters and represents a good measure of particle accessibility (Methods). Interestingly, our experimental results showed a strong correlation between the accessibility index and the y-axis intercept (Figure 3.3), proving the redundancy of using both parameters to characterize porous materials. Therefore, we will discuss only the accessibility index K_p values obtained in the experiments to characterize and compare the processes.

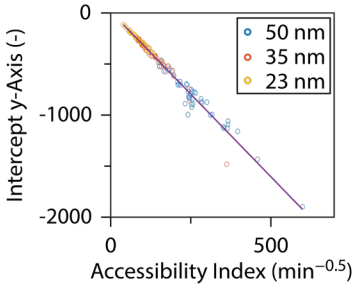

Figure 3.3 Experimental data- scatter plot to show the correlation of accessibility index and y-axis intercept (pH = 7). The different colors in the scatter plot represent particles with different nominal pore sizes.

3.2.2 Effect of Probe-Host Electrostatic Interactions on Uptake

In addition to varying the pore size of the particles to compare their effect on the uptake rates, we investigated how the guest-host electrostatic interactions affected the overall uptake process. We explored this by changing the pH as well as the ionic strength of the solution. On one hand, the pH affected the charge of the dye[156] and the pore-wall surface charge density[231] without changing the fluorescent properties of the probe (Methods). On the other hand, the ionic strength of the solution influenced the extent of the electrical double layer (EDL), a region where the liquid is not electroneutral because it contains a high concentration of counter-ions attracted by an oppositely

charged surface[159]. If the characteristic length of the EDL (Debye length) is greater than the pore radius, there is an overlap between EDLs extending from opposite surfaces in the pores (schematically shown Figure 3.4c). This slows down or even prevents the entrance of (probe) molecules with the same charge as the counter-ions due to electrostatic repulsion.

We performed experiments using 3 different solutions: 1) pH = 4.3, 2) pH = 4.3, and 0.01M NaCl as supporting electrolyte, and 3) pH = 7 (Figure 3.4c-e). Solution 1 and 2 had the same pH but different ionic strengths ($1.3 \cdot 10^{-4}$ and $9.4 \cdot 10^{-3}$ mol/l, respectively) which translate into different Debye lengths (26 nm in solution 1 and 3 nm in solutions 2 and 3). On the other hand, solutions 2) and 3) have the same ionic strength (Debye length), but different pH which affects the charge of the probes and pore walls. The solutions used in the experiments had a pH above the point of zero charge (PZC) of silica (pH~2).[232] Therefore, the oxide surface hydroxyls are deprotonated and the silica surface is negatively charged [233]. For all solutions used, the uptake speed increased as a function of pore size and all experiments seem to be affected by external mass transfer as they show a non-linear regime at low $t^{0.5}$ values (Figure 3.4f-h). However, mass transfer varied dramatically for the different conditions. Solution 1 (pH = 4.3) displayed the slowest uptake, with its linearized curve not reaching an inflection point and showing small differences between samples with different pore sizes (Figure 3.4f). Solution 2 (pH = 4.3, and 0.01M NaCl) reached the inflection point showing moderate differences based on pore size (Figure 3.4g). Solution 3 (pH = 7) proved to be fastest showing clear signs of saturation (i.e., the linearized uptake curve surpassed its inflection point) and the largest differences between the different porous silica samples (Figure 3.4h).

This behavior can be explained by the electrostatic interactions of the different systems: solution 1 (pH = 4.3) causes Rh110 and silica to be positively [156] and negatively charged [232] respectively. Moreover, due to the low ionic strength of the system, an overlapping EDL (Debye length: 26 nm > r_{pore}) predominantly containing cations is formed in the vicinity of the pore walls. These cations interact repulsively with the incoming Rh110+, slowing the diffusion process down (Figure 3.4c,f). Solution 2 (pH = 4.3, and 0.01M NaCl), with higher ionic strength, results in a smaller Debye length (3 nm) leading to moderate repulsive electrostatic interactions between the EDL and the guest molecules as well as faster mass transport (Figure 3.4d,g). Similar Debye length effects of pore diffusion have been reported previously. [161,234] Solution 3 (pH = 7) has the same ionic strength as solution 2 (pH = 4.3, and 0.01M NaCl) and therefore a comparable Debye length. Moreover, at pH = 7, while silica has a higher negative surface density [231], Rh110 forms zwitterions due to the deprotonation of the carboxyl group and the amino group carries a positive charge.[156] Therefore, the guest-host electrostatic interactions are the lowest in this case, which results in a faster uptake and saturation (Figure 3.4e,h). As the strength of electrostatic interactions decreases (Figure 3.4c-e), the pore size and structure become more dominant for the uptake process. This explains why we observe small moderate and large uptake differences between pore sizes in solutions 1, 2, and 3 respectively in our experiments (Figure 3.4f,g,h).

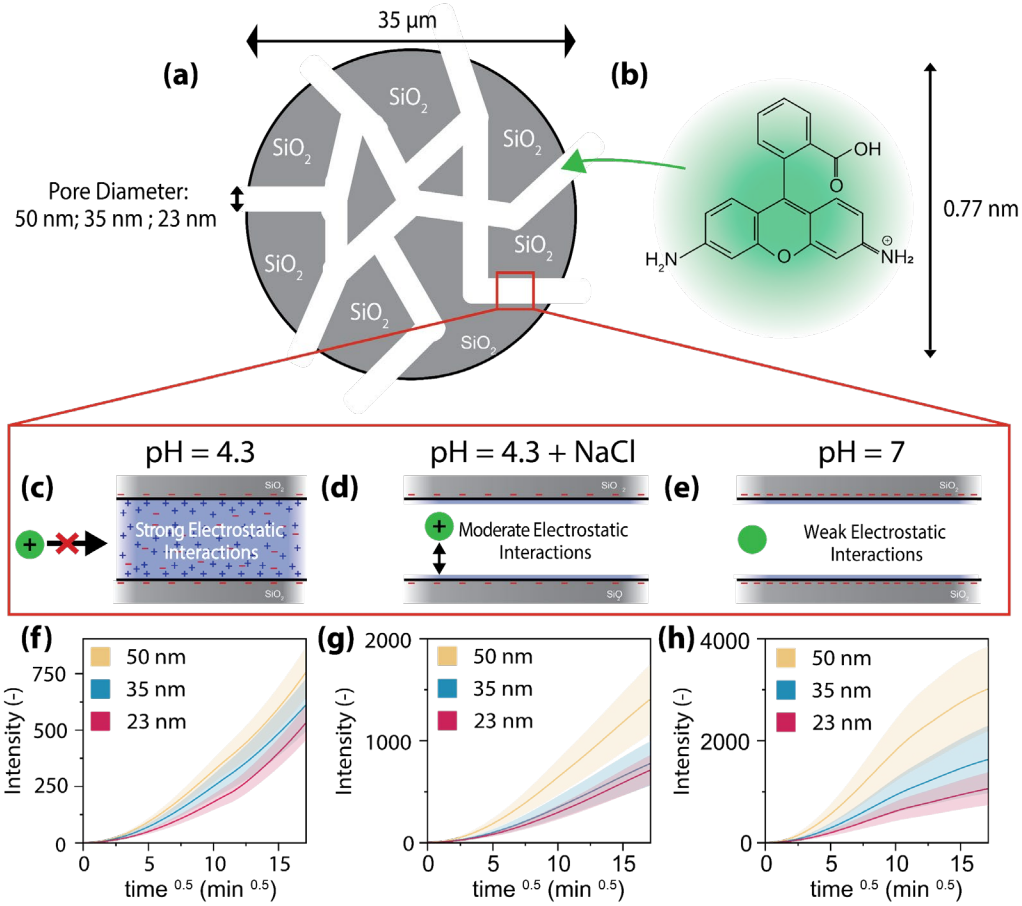

Figure 3.4 (a) Schematic of model silica particles (diameter: 35 µm) with uniform pore size distributions. Three pore sizes were used: 50, 35, and 23 nm. (b) Rhodamine 110 (Rh110) chemical structure. Rh110 has a hydrodynamic diameter of 0.77 nm and is positively charged when solved in water.[235] (c-e) Schematic of electrostatic interactions between Rh110 and the negatively charged pore-walls under different conditions. (c) pH = 4.3 (strong interactions): A cationic electric double layer overlap (blue-shaded area) is present inside the pore which repulses the Rh110(+). (d) pH = 4.3 and 0.01M NaCl (moderate interactions): Increasing the ionic strength reduces the Debye length and creates a neutrally charged region within the pore that allows Rh110(+) to enter the pore more easily. E) pH = 7 (weak interactions): The surface charge density of the pore-walls is more negative. However, Rh110(±) is neutrally charged, therefore probe-wall electrostatic interactions are the weakest in this case. F, G, H) Uptake curves corresponding to the conditions described in C D, and E, respectively. Decreasing the electrostatic interactions has 2 effects on the uptake curves: it speeds up the uptake process and it also increases the difference between samples as the pore size gradually becomes more relevant (note the difference in the y-axis scale). The shaded areas in (f-h) represent the standard deviation of ~50 particles.

Figure 3.5a shows the obtained accessibility index distribution varying pore size and wall-probe electrostatic interactions. The accessibility was evaluated from the slope of the uptake curve inflection point tangent (see Methods). It is worth mentioning that this analysis approach cannot be used if the first derivative of the uptake curve does not reach a maximum during the experiment (i.e., the curve has no inflection point). The experiments performed with strong electrostatic interactions (pH = 4.3, Figure 3.4c) do not meet this criterion and cannot be analyzed in this fashion (Figure 3.4f). As qualitatively described by the uptake curves, the accessibility index decreases with pore size, and the differences are more pronounced for weak electrostatic interactions (Figure 3.5a). The difference

between 35 nm and 23 nm for moderate electrostatic interactions (pH = 4 + 0.01M NaCl) falls within the error bar of the measurement. At pH = 7 (weak electrostatic interactions), the measurement remains sensitive to these differences. Therefore, by suppressing the probe-wall electrostatic interactions, it is possible to more sensitively probe the accessibility purely based on the pore structure. This becomes clear if one compares the accessibility index distribution at pH = 7 (Figure 3.5b) with the pore size distribution obtained with N_2 physisorption (Figure 3.5c). Note that both distributions show a significant overlap of the 35 nm sample with both the 23 nm and the 50 nm samples. Further, the relative peak positions are similarly distributed with respect to each other. Overall, as probe-host electrostatic interactions are suppressed, the accessibility index increasingly becomes a good parameter to probe pore size.

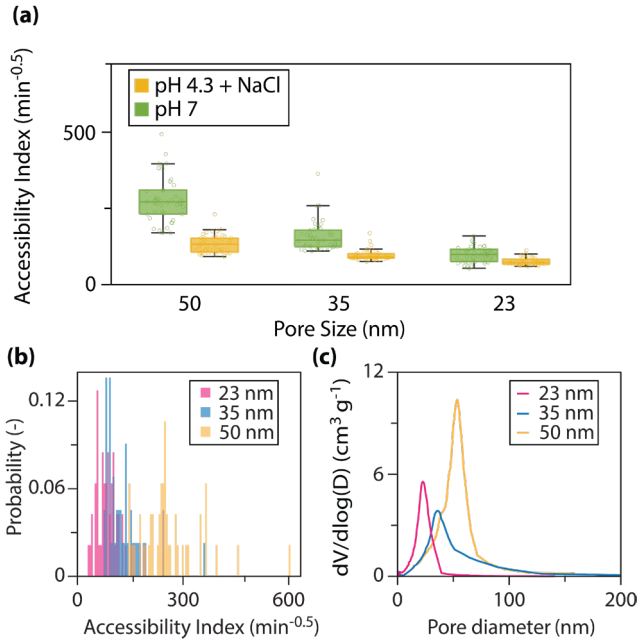

Figure 3.5 (a) Comparison of accessibility index distribution of silica particles with different pore sizes (50, 35, and 23 nm) obtained by performing the experiments with fluorescent solutions at different pH but with the same ionic strength (N=50). For both pH conditions, the accessibility increases as a function of pore size. At pH 7 the accessibility varies more strongly with pore size because the electrostatic interactions are the weakest and pore structure effects become more dominant. (b) and the pore size distribution measured with N_2-physisorption (c) show similarities in terms of peak position and overlap. The BET surface areas were ~ 523 m²/g (23 nm sample), ~ 439 m²/g (35 nm sample) and ~ 344 m²/g (50 nm sample).

3.2.3 Effect of Probe-Host Electrostatic Interactions on Adsorption

In order to study the adsorption behavior of the system, we performed an uptake experiment for two weeks and measured the fluorescence of individual particles after equilibrium was reached (Figure 3.6). For all evaluated conditions, the same trend could be observed for the pore size: the equilibrium intensity, and therefore the equilibrium concentration, increases as the pore size decreases. All model particles have roughly the same total porosity (~30%). If the total porosity is constant, the surface area available for adsorption decreases as a function of pore size. This explains why the amount of adsorbed Rh110 increases when particles with smaller pores are probed – intensity therefore directly correlates with surface area (see BET results in the Methods section). Nevertheless, the amount of adsorbed Rh110 also seems to depend strongly on the conditions used for the experiment. Interestingly, when Rh110 is neutrally charged (pH = 7), the saturation intensity values are the lowest

even though these conditions showed the fastest diffusion (Figure 3.4h and Figure 3.5a). This is probably due to the weak electrostatic interactions between the probe and the walls. On the other hand, in the case of strong electrostatic interactions (pH = 4.3), Rh110(+) and the silica(-) walls have opposite charges, which results in a higher amount of probe electrostatically adsorbed on the walls after reaching equilibrium. Despite the repulsive electrostatic interactions between the EDL and Rh110 that slow diffusion down (Figure 3.4c,f), after long time periods, the Rh110 molecules eventually cross the predominantly positively charged EDL and adsorb on the negatively charged pore walls. If the Debye length is reduced by adding salt (Solution 2, pH = 4.3 + NaCl), the interactions with the EDL are substantially reduced and the uptake is accelerated (Figure 3.4g). Curiously, the final amount of adsorbed species in this case is also the largest of all. Possibly, regions of the pore space of the particles remain inaccessible when a large EDL is present. This could be the case for regions connected through narrow bottle-necks where the EDL overlap is the highest, impeding Rh110 to access the whole (or a larger fraction) particle void volume. While N2-physisorption provides a single BET-surface for an ensemble of particles. Our method, on the other hand, provides an intensity for each individual particle. Furthermore, N_2-physisorption provides the accessible surface area under specific (inert) conditions, while our method proved to be sensitive to electrostatic interactions. This could be potentially exploited to determine the accessible surface area for a specific guest-molecule (e.g., different molecules within a catalyst particle). Moreover, the porous silica particles used in this study are, as mentioned above, commonly impregnated with metallocenes as active centers and used as olefin polymerization catalysts.[229] The chemosensitivity of our effective surface area measurements could be used to characterize silica support particles regarding their impregnation potential.

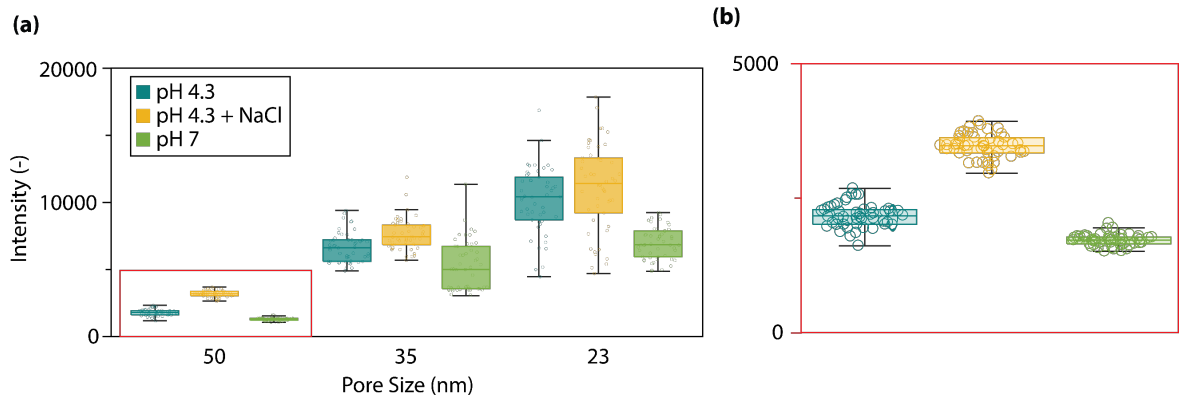

Figure 3.6 (a) Distribution of saturation mean fluorescent intensities of the silica model particles under different conditions. Smaller pores result in higher saturation intensities, as they imply larger surface areas (samples have the same total porosity). At pH =7, the equilibrium concentrations are the lowest since Rh110(±) is neutrally charged and less attracted to the silica(-) walls. At pH 4.3 silica(-) and Rh110(+) have opposite charges increasing the affinity between them and resulting in higher saturation concentrations. Adding salt to the pH = 4.3 solution decreases the Debye length to the point where there is no EDL overlap. Pores connected through narrow bottle-necks with high EDL overlap become accessible as the pore entrance is no longer fully occupied by positively charged ions. Therefore, the total accessible porosity increases compared to the case of pH 4.3. As a result, the available surface area and the saturation concentrations increases as well. b) Zoom-in of red rectangle in (a). The box plots display the median, the lower and upper quartiles as well as non-outlier minima and maxima.

3.3 Conclusions

A simple and reproducible analytical method to study the accessibility of individual porous particles in a high-throughput fashion was proposed and showcased using reference porous silica spheres.

Particles from the same batch showed great heterogeneity in terms of accessibility and number of accessible adsorption sites, which could not have been resolved with traditional bulk methods. Furthermore, the probe-wall electrostatic interactions proved to be of paramount importance for mass transfer within mesoporous materials. Therefore, conditions where these interactions are suppressed were employed to probe particles accessibility as dominated by porosity. The pore-size probing sensitivity of our approach was similar to the one obtained with N_2-physisorption. Evaluating the saturation intensities proved to be suitable for studying surface area at the single particle level. Contrary to gas-physisorption methods, the changes in accessible surface area based on probe-host interactions can be investigated with this method, which is relevant for catalyst support impregnation studies. Two linearized uptake curve parameters were found to be relevant for these types of experiments: the accessibility index and the saturation intensity. The y-axis intercept, proved to be redundant, as it strongly correlated with the accessibility index. The validated method we developed can be used to conduct experiments using different probes and complex porous materials. Moreover, modifications to the microfluidic device can be made in order to make it compatible with organic solvents, expanding the application to the use of hydrophobic dyes and particles.

3.4 Materials and Methods

3.4.1 Materials

PDMS (RTV615, Permacol), The SiO_2 particles (SUNSPERA, AGC Si- Tech Co., Ltd), deionized water (PURELAB flex), Rhodamine 110 Chloride (≥ 99%, Sigma-Aldrich), NaCl (≥ 99%, Sigma-Aldrich), NaOH (≥ 99%, Sigma-Aldrich). All chemicals were used as received with no further purification.

The microfluidic devices were obtained by standard photolithography as previously reported by Vollertsen et al.[226] SU8 (MicroChem) was used for the control layer wafers, with 20 µm high channels, while for the flow layers wafers SU8 was used to first obtain channels with rectangular sections (~48 µm high) in the areas without valves, and AZ40XT (MicroChemicals) was used to create channels ~35 µm high with a rounded profile. In the area with valves, the rounded profile of the flow channels is needed to ensure their correct closing without leakage.
The chips were obtained by multilayer soft lithography. PDMS (RTV615, Permacol) base and curing agent were mixed to obtain the flow (7:1 w/w base to curing agent) and control layers (20:1 w/w base to curing agent). The PDMS was degassed for about 2 hours.
A ~30 µm thick layer of PDMS was obtained on the control layer by spin coating, while the flow layer was obtained by pouring the PDMS on the mold. Both wafers were cured at 60°C for 45 min. Once cooled, the PDMS flow layer was cut from the wafer and the inlets and outlets were punched with a 1 mm hole puncher. The SiO_2 particles (SUNSPERA, AGC Si- Tech Co., Ltd) were manually deposited in the chip chamber of the flow layer by using a needle (SEIRIN J-type needle No.3). Due to the sticky nature of PDMS, once placed on the layer the particles don't move. After the deposition of the particles on the flow layer, it was aligned on the control wafer using a stereomicroscope (Olympus), and the layers were cured overnight at 60°C.
The chip was cut from the wafer and the control inlet was punched out with a 0.75 mm biopsy puncher. Finally, the chip was bonded to a microscope glass slide using a plasma cleaner (model CUTE, Femto Science).
The valves of the microfluidic chip were driven by pneumatic actuation. The channels of the control layer were filled with water and pressurized with air (1.5 bar) by solenoid valves (Festo), controlled via a custom LabView program.

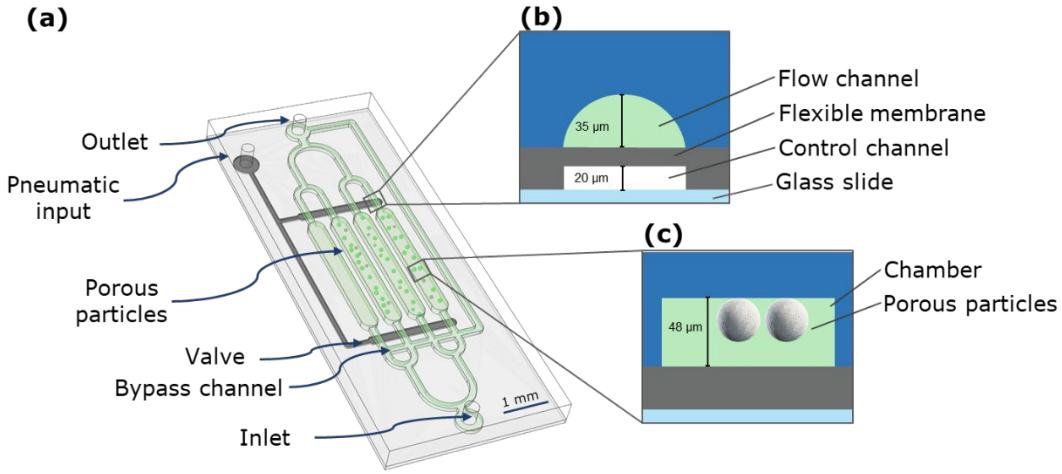

Figure 3.7 Schematic and cross-section of the microfluidic device used for the uptake experiments. (a) shows the chip 4 chambers: one is empty and used as a reference chamber while the other 3 are filled with porous particle samples. The bypass channel is used to purge the channels without contaminating the chambers when switching liquids. (b) Valve cross-section in open configuration. The channels in the flow layer are shown in green, while the control layer channel is shown in white. The rounded profile of the flow channel is needed to ensure the closing of the valve without leaking. (c) Chamber cross section showing the position of the particles. Due to the loading procedure and the sticky nature of PDMS, the particles tend to stay attached to the top layer.

3.4.2 Dye Characterization

a. Concentration Intensity Calibration

We varied the concentration of Rh110 in a chamber that did not contain silica particles. The measured intensity grew linearly as a function of the concentration (Figure 3.8a). Then, we repeated the experiments, in chambers containing particles and measured the intensity within them Figure 3.8b. Also here, there was a linear relationship between intensity and concentration. These results suggest that the fluorescence intensity both within and without the particles can be used as a measure of concentration in the used concentration range.

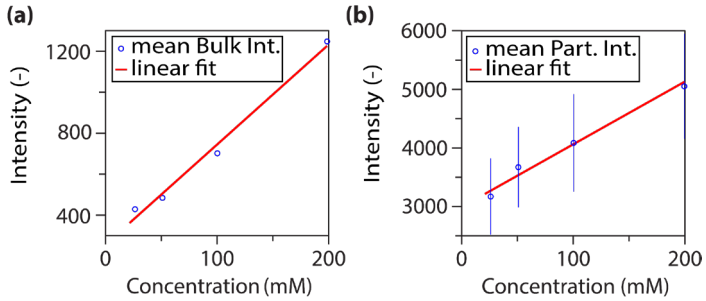

Figure 3.8 Calibration curves of Rhodamine 110 (a) in the bulk solutions (pH = 7) and (b) in the particles (d_{pore}=35 nm). In (b) the particles were in contact with the solutions at different concentrations until they reached the equilibrium. The standard deviation of the particles is represented by the error bar.

b. Photostability

The measured intensities within the reference chambers did not change significantly as a function of time, suggesting that photobleaching did not take place to a large extent (Figure 3.9).

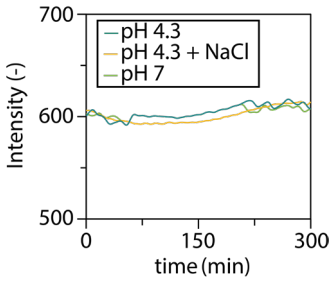

Figure 3.9 Mean intensities over time of the solutions of Rhodamine 110 used for the uptake experiments as evaluated from the reference chamber. Under all tested conditions, the solutions show photostability within the 5 hours of the experiment.

3.4.3 Porous Silica Particle Characterization

Focused Ion Beam Scanning Electron Microscopy (FIB-SEM) and N_2 physisorption were performed on the SiO_2 particle samples to visualize and check their mesoporosity. Focused Ion Beam Milling Scanning Electron Microscopy (FIB-SEM) was performed on an FEI Helios NanoLab G3 UC microscope. Samples were loaded on Al stubs with carbon tape and sputter-coated with 10 nm of Pt, before the measurement. Beam currents of 0.1 nA and 2 kV were used to image particles with dwell times varying between 1 and 5 µs, depending on the imaging mode. External morphologies were imaged by collecting secondary electrons (SE) with an Everhart–Thornley detector (ETD), while cross-sections were imaged by collecting back scattered electrons (BSE) with a through-the-lens detector (TLD) with a dual scanning electron microscope focused-ion beam. Cross-sections were obtained with a Gallium FIB operating at 2.5 nA for milling, removing half of the particle material. Then, Pt deposition was performed with 0.77 nA for a protective layer on top of the surface of the particle and subsequent cleaning with precision milling operating at 2.5 nA the exposed cross-section. N_2 physisorption measurements of the SiO_2 particles were performed using a Micromeritics TriStar 3000 instrument operating at −196 °C. Before performing the measurements, the particles were dried for 15h at 200 °C under N_2. The resulting surface area values were 344 m²/g; 439 m²/g; 523 m²/g for the 50, 35, and 23 nm pore size particles, respectively.

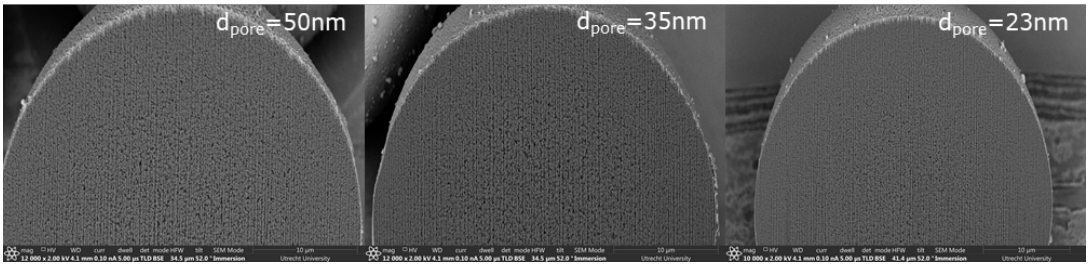

Figure 3.10 Scanning electron microscopy (SEM) images of focused ion beam (FIB)-cut particles showing their mesopores.

3.4.4 Uptake Experiments

For the uptake experiments, the chip chambers were first filled with deionized water (PURELAB flex) so that the particles were soaked in the solvent. Rhodamine 110 Chloride (Sigma Aldrich) 100 µM in deionized water was used as fluorescent solution at pH 4.3 (solution 1) and ionic strength $1.3 \cdot 10^{-4}$ mol/L. Higher ionic strength ($9.4 \cdot 10^{-3}$ mol/L) of solution 2 and 3 was obtained by adding respectively

NaCl (Sigma Aldrich) 0.01M as supporting electrolyte and NaOH (Sigma Aldrich) 0.01M to adjust the pH to 7. The solutions were injected from the inlet by using a pressure pump (Fluigent, Germany) regulating the flow from a fluid reservoir to the flow layer. After that, the chambers were closed by pressurizing the valve and the chip channels were filled with a fluorescent solution of Rhodamine 110 Chloride (Sigma Aldrich) 100 µM by using a bypass channel. The solutions at pH 7 were prepared by adjusting the pH with 0.01M NaOH. Once the solution is uniformly present in the channels, the chambers were opened and filled with it. For the image acquisition, a fluorescence microscope (Leica DMi 5000M) and a Hamamatsu ORCA-Flash4.0 camera were used with a pE300ultra LED illumination system (CoolLED, U.K.). The images were acquired every minute using the MicroManager software.

a. Image Processing

The fluorescence images (Figure 3.11a,b) were processed using a home-built MATLAB code. The pixels that correspond to particles are segmented using the Segmentation Editor from ImageJ (Figure 3.11c). The mean pixel intensity of each of these regions is calculated for each picture. Figure 3.11d shows the intensity changes over time$^{1/2}$ for individual particles of the same batch.

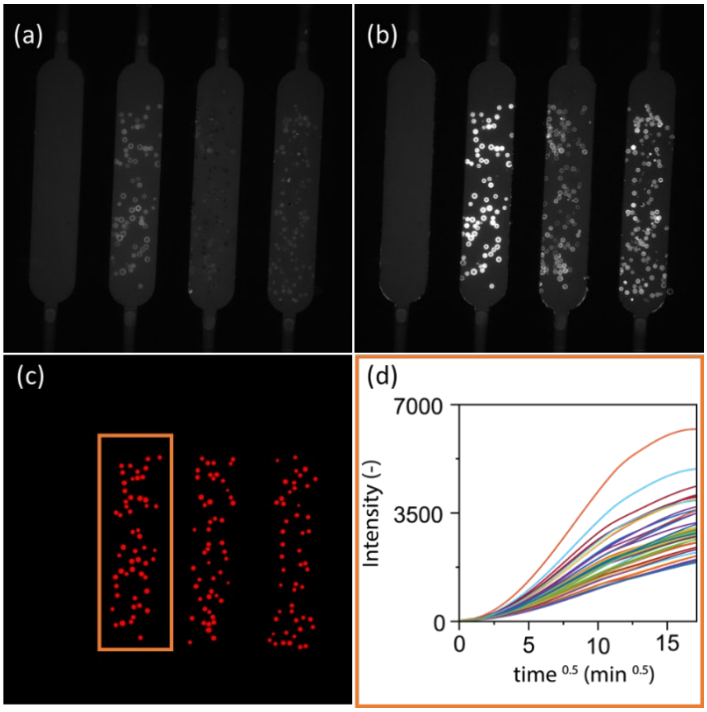

Figure 3.11 (a) Fluorescence image recorded at the beginning of the uptake process. (b) Fluorescence image recorded after 5 hours of uptake displays higher intensities for each particle. (c) The pixels that belong to particles were segmented. The mean intensity of each of these regions was calculated for each time. (d) Mean intensity changes within the chamber on the left as a function of the time1/2. The initial intensity values were subtracted so that the curves begin at an intensity equal to 0. Each uptake curve corresponds to a particle.

b. Accessibility Index Determination

In order to quantify the speed of the uptake process, many published studies fit a line to a fraction of the uptake-$t^{1/2}$ curve. However, to the best of our knowledge, no publication clarifies how the “linear part” of the curve was chosen. Performing a linear regression on different, arbitrarily chosen, parts of the curve can lead to different results on the same dataset. To quantify our data in a systematic way, we determined the inflection point of each uptake- $t^{0.5}$ curve as well as its first derivative. The inflection

point tangent was used to replace the linear fit usually used in literature. Figure 3.12 displays an uptake curve together with its inflection point tangent used to approximate the “linear part of the curve”.

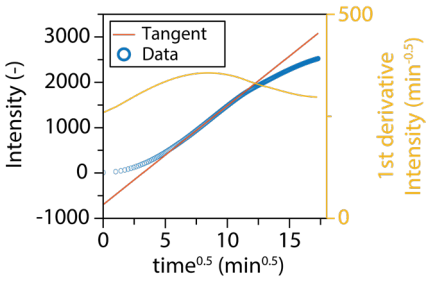

Figure 3.12 Experimental data of uptake of the solution at pH 7 from one silica particle with 50 nm pores. The linear region is identified by plotting the inflection point tangent.

3.4.5 Uptake Simulations

The variables used for the uptake simulations as well as the assumptions made are schematically depicted in Figure 3.13.

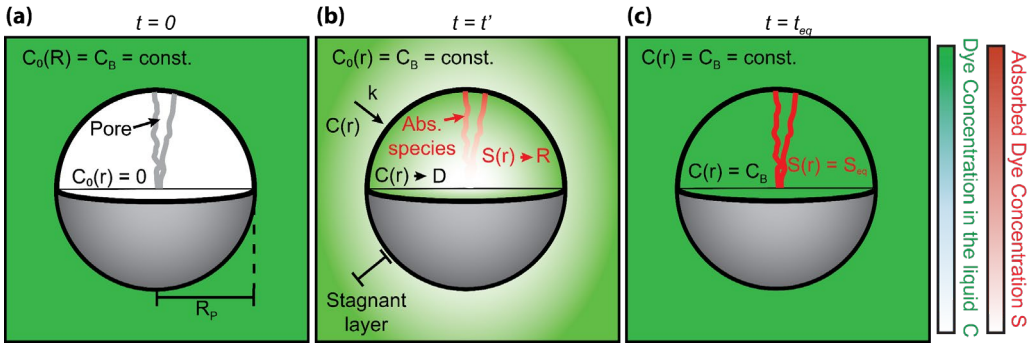

Figure 3.13 Schematic of the uptake process showing the variables used and assumptions made. (a) Initial conditions: at the beginning of the process, we assume that the dye concentration outside of the particle is constant, C_B. Within the particle, the adsorbed concentration C_B, as well as the concentration in the liquid phase C_0, are assumed to be 0. (b) Uptake process: the concentration far away from the particle is assumed to be constant C_B. In the vicinity of the particle, a stagnant layer, i.e., a concentration gradient characterized by the external mass transfer coefficient k, is formed. Within the particle, the adsorbed and liquid concentrations are spatially dependent, these concentration profiles are characterized by the internal diffusion coefficient D and the adsorption constant R. (c) Saturation: there are no concentration gradients on either the liquid or adsorbed phase. Since there are no concentration gradients, there is no driving force for diffusion or adsorption. The particle is in equilibrium and cannot take up more dye.

The concentration profile changes within a porous particle during the uptake process were simulated by solving Fick's second law (Equation 3.2).

$$\frac{\partial C}{\partial t} = \frac{D}{r^2}\frac{\partial}{\partial r}\left(r^2\frac{\partial C}{\partial r}\right) - \frac{\partial S}{\partial t} \qquad \text{Equation 3.2}$$

Therefore, the porous particle was modeled as pseudo homogenous sphere with an internal liquid phase diffusion coefficient *D*, an adsorption coefficient *R*, and an external mass transfer coefficient *k*. By Varying these parameters, we explored their influence on the accessibility index Kp and the y-

intercept C of the uptake curves. We assumed diffusion to be the limiting step in the sorption process. Therefore, we modelled the adsorbed concentration S to depend linearly on the concentration in the solution *C:*

$$\mathrm{S} = \mathrm{RC} \qquad \text{Equation 3.3}$$

By combining Equation 3.2 and Equation 3.3 Fick's law can be rewritten to

$$\frac{\partial \mathrm{C}}{\partial \mathrm{t}} = \frac{\mathrm{D}'}{\mathrm{r}^2}\frac{\partial}{\partial \mathrm{r}}\left(\mathrm{r}^2\frac{\partial \mathrm{C}}{\partial \mathrm{r}}\right) \qquad \text{Equation 3.4}$$

where D' represents an effective diffusion (including adsorption):

$$D' = \frac{\mathrm{D}}{1+\mathrm{R}} \qquad \text{Equation 3.5}$$

The initial dye concentration inside the particle's pores $C0$ as well as the adsorbed concentration S0 were assumed to be 0.

$$\mathrm{C} = \mathrm{C}_0 = 0 \qquad \mathrm{t} = 0 \;\forall\; \mathrm{r} \qquad \text{Equation 3.6}$$
$$\mathrm{S} = S_0 = 0 \qquad \mathrm{t} = 0 \;\forall\; \mathrm{r} \qquad \text{Equation 3.7}$$

Further, the following boundary conditions (BCs) were implemented:
BC 1) The molecular flow at both sides of the liquid-solid interface has to be the same (Equation 3.8). This boundary condition relates internal and external mass transfer. This is why the effective diffusion coefficient D' and the external mass transfer coefficient k are positively correlated.

$$D'\left(\frac{\partial C}{\partial r}\right)_{r=R} = k\ (C_B - C) \qquad t > 0 \qquad \text{Equation 3.8}$$

where C_B is the concentration in the bulk solution, which was assumed to be constant over time.

BC 2) Due to the symmetry of the system the first derivative of the concentration profile should be zero at the center of the spherical particle:

$$D'\left(\frac{\partial C}{\partial r}\right)_{r=0} = 0 \qquad t > 0 \qquad \text{Equation 3.9}$$

The total probe molecule concentration profile consists of the sum of the concentration in the pore space of the particle (*C*), and the concentration adsorbed on the pore-walls (*S*):

$$C_{tot}(\mathrm{r}) = \mathrm{S}(\mathrm{r}) + \mathrm{C}(\mathrm{r}) \qquad \text{Equation 3.10}$$

This value was integrated over the whole radius of the particle for each time step n and used to calculate the uptake as:

$$q = \frac{(C - C_0)}{m_C}V_s \qquad \text{Equation 3.11}$$

with m_c (g) the sorbent amount and V_s (mL) the volume of the solution. The calculated uptake was plotted as function of $t^{1/2}$ results in the uptake curve of the particle (Figure 3.14). Increasing the

internal diffusion coefficient *D* of the particle resulted in a higher slope of the linear part of the uptake, i.e., higher accessibility index K_p, and a more negative y-axis intercept *C* (Figure 3.14a,d). A similar effect on K_p is observed by increasing *k* (reducing the external mass transfer limitations). However, it also shifts the linear regime of the uptake curve to shorter times, which results in less negative y-intercept (Figure 3.14 b,e). Finally, increasing the adsorption coefficient *R* increases the accessibility index K_p and decreases the y-intercept *C* (Figure 3.14c,f). It is worth noting that the external mass transfer coefficient *k* and the effective diffusion coefficient $D' = \frac{D}{1+R}$ which includes adsorption, are positively correlated due to the boundary conditions equating flow at the two sides of the solid-liquid interphase (Equation 3.8). Hence, increasing the internal particle diffusion coefficient *D* will result in higher external mass transport (higher *k*) and vice-versa. However, both parameters contribute differently to the y-axis intercept *C*. Since the y-axis intercept is determined by several parameters, it should not be used to evaluate external mass transfer only.

In an uptake experiment, while using particles of the same material and pore volume, but different pore sizes, one varies the internal diffusion coefficient *D* and therefore the external mass transfer coefficient *k* as well as the adsorption coefficient *R* (as different surface areas are obtained). All of these values correlate positively with the amount of adsorbed material (uptake, *q(t)*) and the accessibility index K_p.

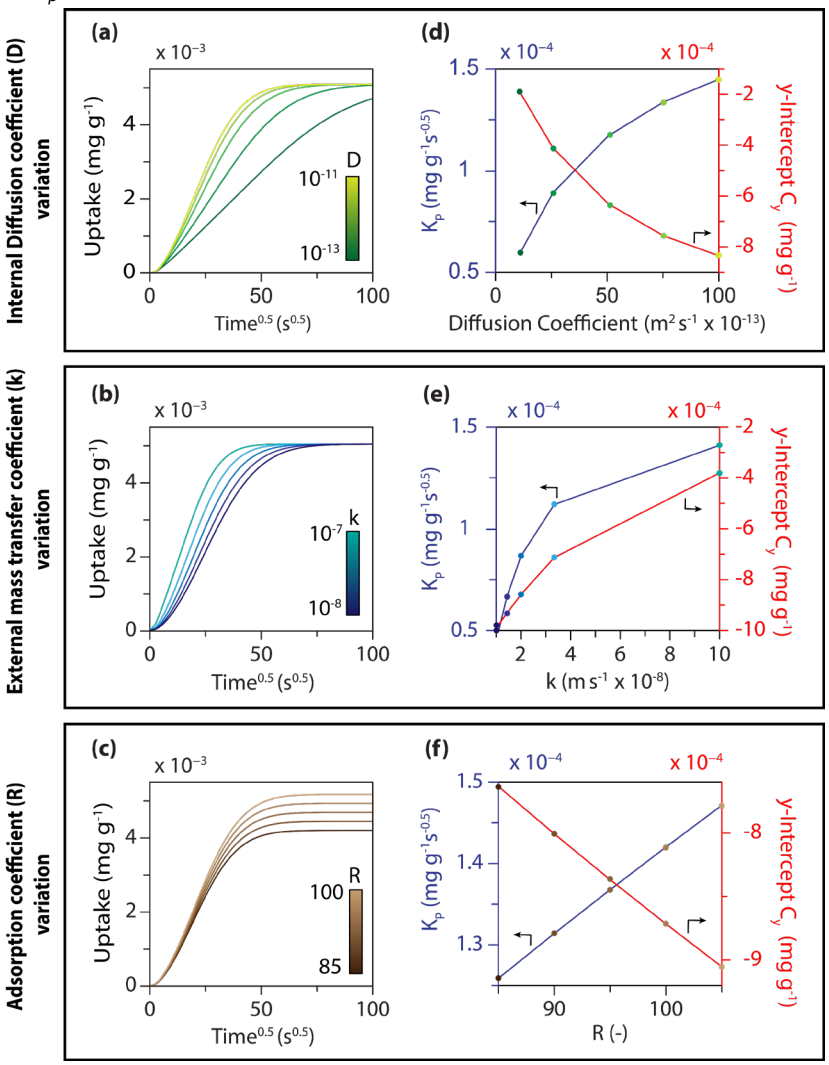

Figure 3.14 Uptake simulations obtained considering a 35 µm spherical particle. A) Uptake curves obtained changing the internal diffusion coefficient D (k = 10-8 m/s and R = 100) B) the external mass

transfer coefficient k (D = 10-12 m^2/s and R = 100) and C) the adsorption coefficient R (D = 10-12 m^2/s and k = 10-8 m/s). D), E) and F) show the slopes (accessibility indices) and y-intercepts of the inflection point tangents of the uptake curves shown in A), B) and C) respectively.

4 Fluorescent-Probe Characterization for Pore-Space Mapping with Single-Particle Tracking

Porous solids are often characterized by a complex network of interconnecting pores of various dimensions. Tracking individual fluorescent probes as they diffuse through the porous material can be used to characterize a pore network at tens of nanometers resolution. However, understanding how the motion behavior of fluorophores changes in confinement is essential to reliably derive properties of the pore network. In this Chapter, we introduce well-defined lithography-made model pores developed to study probe behavior in confinement. We investigate the influence of probe–host interactions on diffusion and trapping of confined single-emitter quantum-dot probes. Using the pH-responsiveness of the probes, we were able to largely suppress their trapping at the pore wall and in turn define experimental conditions that allowed mapping of the accessible pore space of a one-dimensional pore array as well as a real-life polymerization-catalyst support particle. Finally, we propose a protocol to ensure the pore space is fully mapped with single particle tracking experiments.

Based on:

Rafael Mayorga González†, J.J. Erik Maris†, Marita Wagner, Yadolah Ganjkhanlou, Johan G. Bomer, Maximilian J. Werny, Freddy T. Rabouw, Bert M. Weckhuysen, Mathieu Odijk, Florian Meirer, Fluorescent-Probe Characterization for Pore-Space Mapping with Single-Particle Tracking, Angew. Chem. Int. Ed. 2023, 62, e202314528

†These authors contributed equally to this work.

4.1 Introduction

Efficient molecular transport through functional porous solids improves their performance and lifetime in applications such as heterogeneous catalysis.[99] Therefore, the accessibility and interconnectivity of the pore structure is of paramount importance for catalytic efficiency. The pore structure of solid catalysts is often a complex network of macropores (> 50 nm diameter), mesopores (2−50 nm diameter), and micropores (< 2 nm diameter) with a heterogeneous composition.[4,5,236,237] A more rational pore space design holds great promise for the improvement of catalysts. High-resolution characterization of the pore volume is needed to investigate the relation between synthesis parameters and resulting pore networks. However, this requires complex and expensive analytical techniques such as electron tomography or X-ray imaging using synchrotron radiation.[19,66,99,217,224,238]

A promising addition is single-molecule (particle) localization microscopy (SMLM) for the characterization of porous solids.[143,148,150,239–241] These experiments are relatively inexpensive and fast to perform. Fluorescent probes are tracked with a resolution on the order of 10 nm as they diffuse through the accessible pore network. The travelled paths of the probes, or trajectories, contain information about the accessibility and interconnectivity.[143,148] Furthermore, the size and surface properties of the pores might be derived from the duration and frequency of trapping events as well as diffusivity of the probes, but this has not yet been experimentally demonstrated.[242–244] Imaging of the uptake of fluorescent tracers using confocal laser scanning microscopy has proven effective to reconstruct the probe accessibility in catalysts.[4] However, the resolution of this method is restricted by the diffraction limit (~250 nm), and is — in this respect —clearly outperformed by SMLM.[100]

To reconstruct the pore space of a porous solid, understanding of the relation between the probe's trajectory and the local pore environment is required. This is complicated by the observation that diffusion of single-molecule probes in porous materials is heterogeneous and temporary immobilization ('trapping') characterizes the motion behaviour.[150,245,246] The physical origin of the heterogeneous motion is hard to fully resolve because of the complexity of the catalyst material in which the probe moves. Therefore, a thorough characterization of the trapping and diffusion behavior of the fluorescent probes in well-defined pore structures is essential for a proper interpretation of SMLM experiments in more complex porous solids.

In this Chapter, we introduce well-defined lithography-made model pores with known geometry and composition to address the challenges outlined above. We first studied the motion and behavior of commercially available quantum dots (QDs) using SMLM in a two-dimensional (2D) pore, that is, where confinement is present in only one direction. The used nanoparticles are promising probes due to their bright fluorescence and small diameter of ~ 15 nm. In these experiments we investigated the influence of probe–host interactions on diffusion and trapping of confined, single QDs. Based on this probe characterization, we defined a set of experimental conditions that allowed for the (partial) mapping of two pore systems with increasing level of complexity: 1) A lithography-made one-dimensional (1D) pore (i.e., confinement in two directions) and 2) a real-life polymerization-catalyst support particle.

4.2 Results and Discussion

The developed model pore system is a microfluidic device constructed via nanolithography and wet etching from silica wafers (Figure 4.1a). The 2D model pores are slit-shaped patches with a depth of 50 nm, imposing confinement only in the depth direction while allowing for free diffusion in the plane perpendicular to the confinement. In these two dimensions, we tracked motion of the fluorescent probes keeping the whole depth of the slit within the focal depth of 800 nm).

We recorded the trajectories of Polyethylene Glycol (PEG)-coated QDs (Figure 4.1b) suspended in a water/glycerol mixture, while diffusing inside the 2D pore (Figure 4.1c). The tracks were long

compared to previous studies with some of exceeding 1000 localizations tracked over 30s.[150] Trajectories displaying permanent, transient, or no trapping were observed (Figure 4.1d). We will demonstrate the detailed analysis of the QD trajectories recorded in different pH conditions to characterize the effect of the pH on the trapping behavior and diffusion dynamics. Once we understand the QD's behavior in confinement, we can design an experiment with the right conditions to explore the pore volume of more complex pore systems.

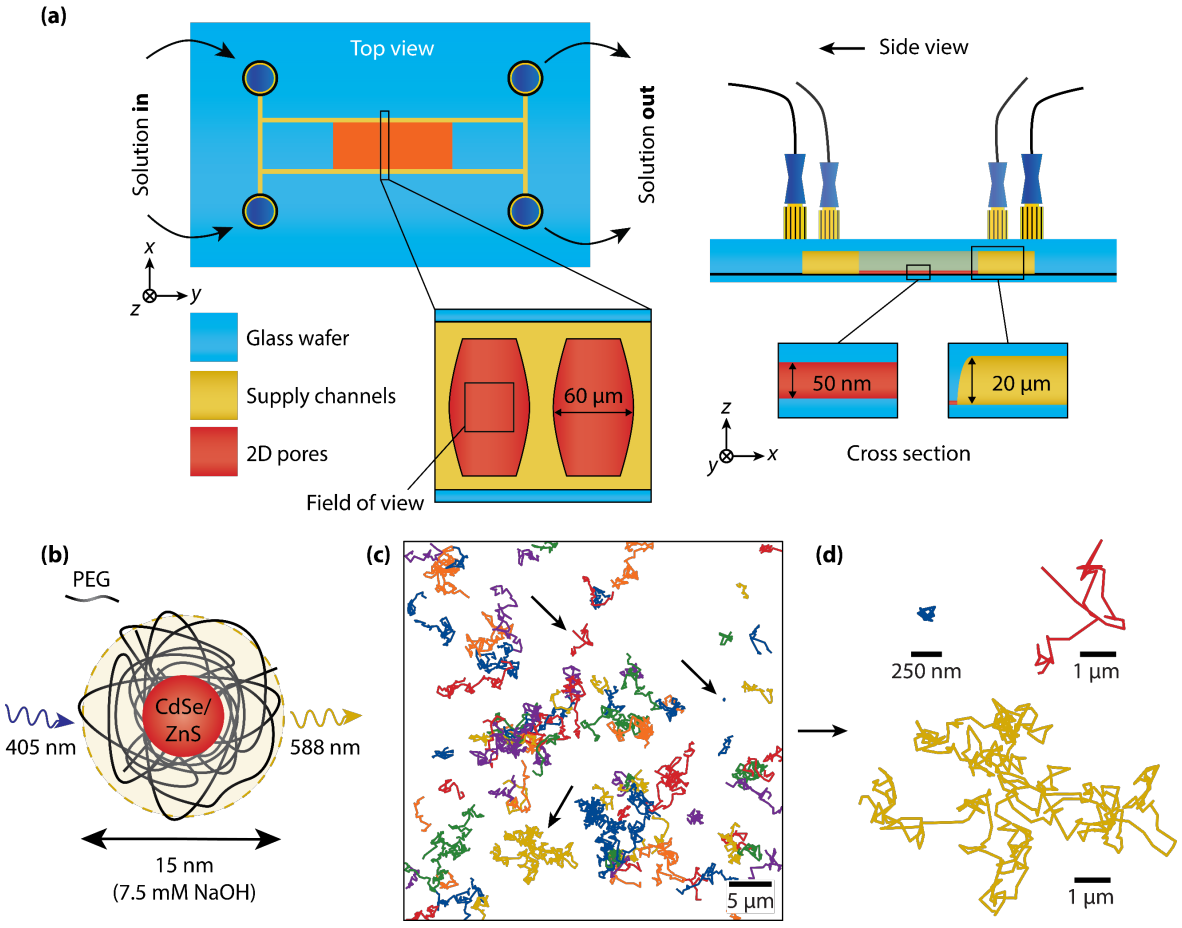

Figure 4.1 (a) Schematic representation of the microfluidic device. (b) Polyethylene Glycol (PEG)-coated CdSe/ZnS Quantum Dots (QDs). (c) Selection of observed trajectories. (d) Three enlarged trajectories, as indicated by the arrows in (c).

4.2.1 Characterisation of Probe Trapping within a 2D Pore

In this section, we will focus on the characterization of QD trapping as a function of different pH conditions. Both probe–pore wall adsorption and increased hydrodynamic drag near the wall can cause QD trapping in the model pore. Here, adsorption is the trapping of the QD in a potential energy minimum at the silica surface. Furthermore, the hydrodynamic drag force increases dramatically when a nanoparticle approaches the pore wall, which can cause the particle to slow down and appear trapped.[152,153] We cannot discriminate between adsorption and hydrodynamic drag effects in our experiment. Therefore, we will refer to both as trapping.

To assess the trapping behavior in confinement, solutions with different pH were loaded in the 2D model pore. Two timeframes were investigated: *short* trapping events with durations of 5–100 frames (35 ms/frame) and *long* trapping events lasting more than 100 up to thousands of frames. We

identified long trapping events via a 2D histogram of the localization coordinates, which displays the spatial distribution of all recorded localization during a single movie of 4000 frames (Figure 4.2). Bins with significantly more counts than their direct neighbors indicate the presence of trapped particles. Visual inspection of the histogram revealed long trapping events at 7.5 mM NaOH concentration (Figure 4.2a), while only one was observed at 20 mM NaOH (Figure 4.2b).

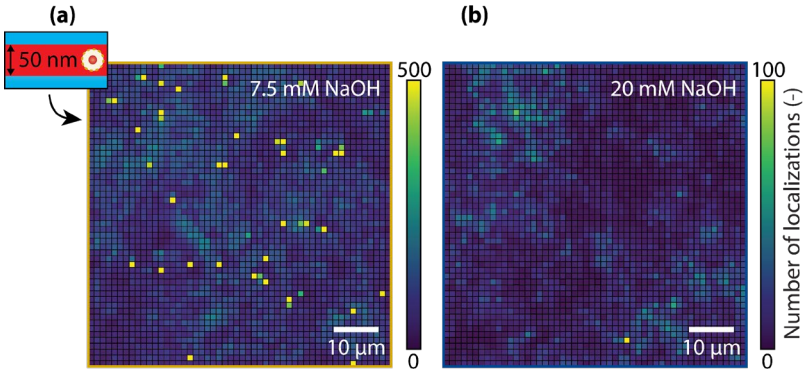

Figure 4.2 Two-dimensional histogram of the single-particle coordinates in the two-dimensional pore during 4000 frames in (a) 7.5 mM and (b) 20 mM NaOH (right); bin-size: 0.87 × 0.87 µm^2. The color coding is given in the bottom left corner as localizations per 4000 frames. The 7.5 mM NaOH sample had an additional 2.5 mM NaCl to keep the Debye length < 2.5 nm.

Unexpectedly, the long trapping events resulted in artefacts in the trajectory generation process because trajectories belonging to moving particles were often wrongly linked to trapped ones. If the trapped particle is not detected, e.g., due to blinking, a localization belonging to a mobile QD can be included in its trajectory. This happens when the localization belonging to the trapped QD is closer than a localization belonging to a mobile one (detailed visual explanation in Figure 4.3a). In the datasets presented in this chapter, the QDs travel many pixels per frame (i.e., pixel jump is 16 pixels), which increases the probability that such an artefact occurs. These artefacts add large displacements to trajectories of trapped QDs and can even swap trajectory segments of a mobile and trapped particle. The artefacts can be recognized in a plot of all trajectories as *star-shaped* trajectories in the vicinity of trapped particles (arrows in Figure 4.3b,c). The centers of the stars are the localizations of the trapped probes, and the spikes are caused by sporadic erroneous linking with nearby passing particles. We removed trajectories close to the positions of long trapping events based unless otherwise stated (Figure 4.3d,e). Note that this filtering step leads to undesired blind spots with no reliable trajectory data, which can be seen in Figure 4.3e. Therefore, non-trapping probes are necessary to fully map pore spaces.

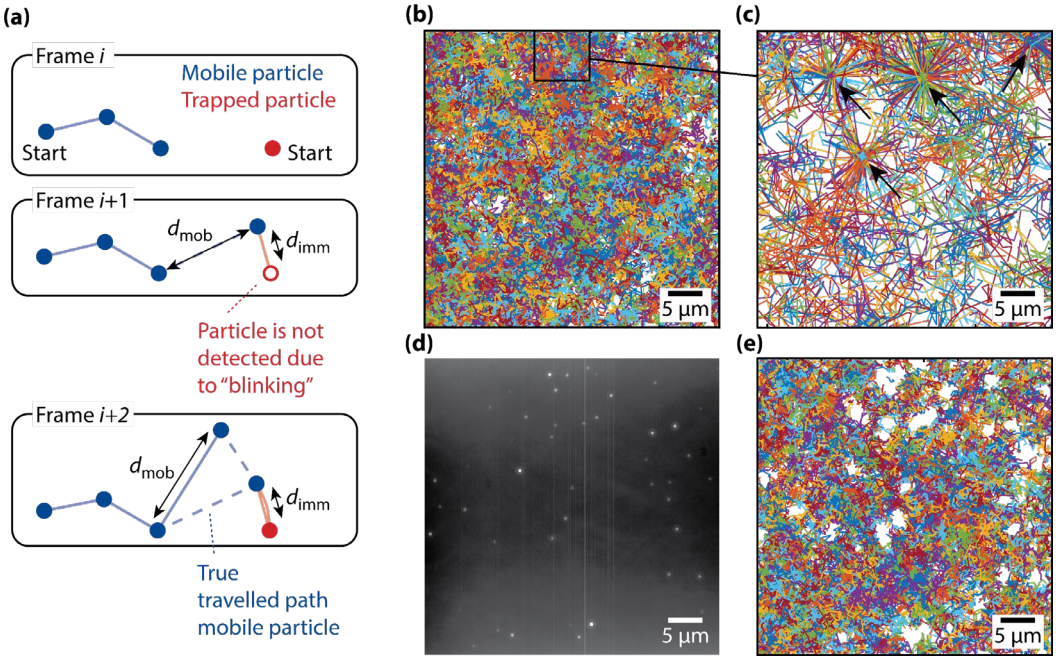

Figure 4.3 (a) Example of an artefact created by the presence of a mobile particle that closely passes by a trapped, non-detected particle. Two nearby trajectories of a mobile (blue) and trapped particle (red) are shown in frame i. In the next frame i+1, the trapped particle is not detected. The sum d_{mob}^2 + d_{imm}^2 (i.e., cost) is minimized when the localization of the mobile trajectory is added to the trajectory of the trapped particle. No localization is added to the mobile trajectory. In the frame i+2, the trapped particle is detected and the sum d_{mob}^2 + d_{imm}^2 is minimized when the mobile localization is added to the mobile trajectory and the trapped one to the trajectory of the trapped particle. This process can occur several times resulting in a trajectory with star shape (arrows in panel c). (b,c) Overlay of trajectories obtained during 4000 frames in the two-dimensional model pore at 7.5 mM NaOH. A zoom of panel b is shown in panel c. The black arrows point to artefacts, which were caused by particles that were trapped for hundreds of frames. (d) Average intensity of the fluorescence microscopy video used to track the trajectories in panels a,b. Particles that correspond to long trapping events can be easily recognized. (e) Overlay of trajectories after removal of trajectories close to the trapped particles. Note that the empty regions correspond to the trapped particles visible in panel d.

Since long-lasting trapping events were present in the data, we anticipated the occurrence of shorter events that could not be detected visually. Hence, we conducted trapping analysis to identify short, transient, events within single trajectories (see Methods). This analysis captures both transient adsorption and the QDs' slowing down due to increased hydrodynamic drag forces near the pore wall. As a result, the frequency at which the probe could approach the pore wall was measured by the occurrence of short trapping events. Figure 4.4 shows the outcome of the trapping analysis, revealing trapping in both pH conditions. Fewer and shorter trapping events were observed at 20 mM compared to 7.5 mM NaOH, consistent with the trend shown for long-lasting trapping events.

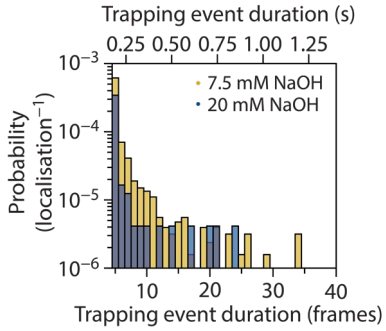

Figure 4.4 Frequency of short trapping events in the two-dimensional pore in the same conditions as reported in Figure 4.2. The histogram is normalized by the total number of localizations in the dataset and corrected for the number of expected false positives (see Methods). Here, only trajectories displaying mobility in their initial and final localizations were considered to ensure that solely complete trapping events were included in the analysis. Trajectories with long trapping events spanning of hundreds of frames were not considered.

To cross-check these observations the pH dependent experiments were repeated using an unconfined liquid–silica interface. Here, a similar trapping trend was observed with the only difference that no trapping events at all were detected on the unconfined interface at 20 mM NaOH (Figure 4.5). This highlights the necessity to characterize trapping in confinement. This difference in trapping can be explained by an increase in the electrostatic repulsion between the QDs and silica pore-wall at increasing pH. The relationship between the QD size and its charge will be discussed in the following section.

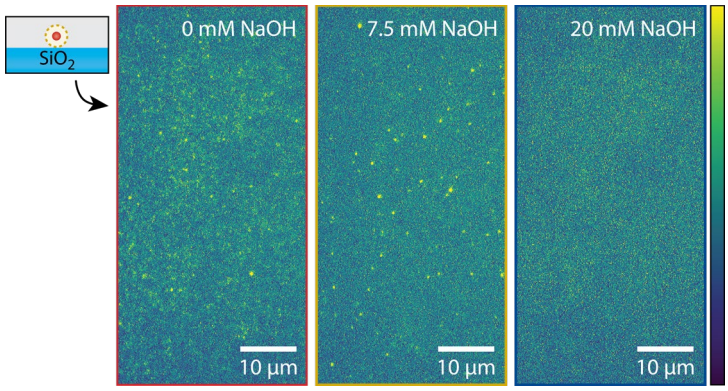

Figure 4.5 Quantum Dots (QDs) as probes trapped on the surface of a silica coverslip as a function of NaOH base concentration. NaCl was added to the 7.5 mM NaOH sample to keep the Debye length < 2.5 nm.

4.2.2 Hydrodynamic Radius and QD Charge

The hydrodynamic size of the quantum dot particles was investigated as function of pH (Figure 4.6). To determine the size of the particles at the experimental conditions, the quantum dots were tracked in a water glycerol (15/85; m/m) solution with different NaOH concentrations. The high glycerol content was necessary to slow the particles down within the regime they could be tracked in free solution. The first four points of the time–ensemble averaged mean squared displacement (TE-MSD) curves were fitted to obtain the diffusion coefficients under each condition (Figure 4.6a). The particle's effective hydrodynamic radius r_h was computed from the Stokes–Einstein equation:

$$r_h = \frac{k_B T}{6\pi\eta D} \quad \text{Equation 4.1}$$

with k_B Boltzmann's constant, T the temperature, η the viscosity, and D the diffusion constant. We used η = 0.11084 Pa·s for the calculation of the hydrodynamic radius.[247] Adding base to decrease trapping of quantum dots led to a reduction in size from circa 14 nm to 7–8 nm (Figure 4.6b,c). We ascribe this to shrinking of the PEG shell, as it has been previously reported in literature that suspended polyethylene glycol shrinks when the ionic strength of the solution increases.[248] Furthermore, zeta potential measurements on the QDs in water revealed that the nanoparticles were negatively charged with a zeta potential of −23.9 ± 0.6 mV. For increasing pH, we concluded that the hydrodynamic radius of the negatively charged QDs decreased due to contraction of the PEG shell,[248,249] likely increasing electrostatic repulsion between the QD and negatively charged silica 2D pore wall.[250] This repulsion prevents the QD from getting close to the silica, keeping it outside the regime where probe–wall attraction dominates and/or the hydrodynamic drag increases dramatically.

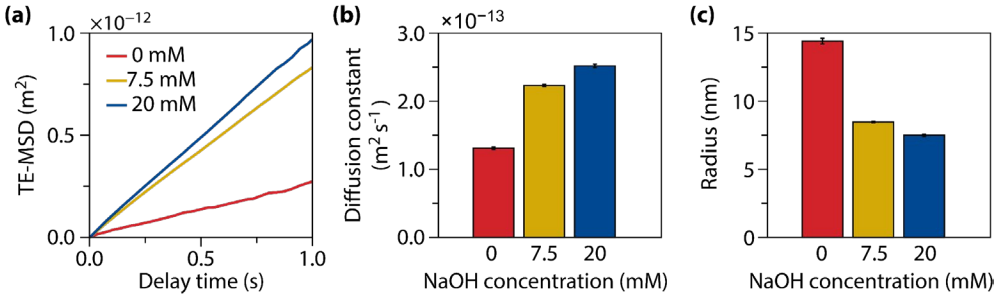

Figure 4.6 (a) Time–ensemble averaged mean squared displacement (TE-MSD) of CdSe/ZnS-PEG quantum dots in a water/glycerol (15/85; m/m) solution with different NaOH concentrations. The higher the base concentration, the greater the displacement exhibited by the particles. (b) Fitted diffusion coefficients using the first four points of the TE-MSD curves in (a). (c) Computed hydrodynamic radii as function of NaOH concentration computed from the diffusion constants reported in (b) and the Stokes–Einstein equation (Equation 4.1).

4.2.3 Mean Squared Displacement Analysis in 2D Pores

We investigated the diffusion dynamics of QDs in the 2D model pore, and whether it is affected by the short, transient trapping characterized in the previous section. The time–ensemble averaged mean squared displacement (TE-MSD) curve in conditions where transient trapping does (7.5 mM NaOH) and rarely does (20 mM NaOH) occur is shown in Figure 4.7a. The TE-MSD of the sample with transient trapping is non-linear and this shape suggests anomalous diffusion. Anomalous diffusion has been reported to occur in cellular environments, for instance as a result of crowding or due to specific interactions in the cell.[130] In simulated data sets with transient trapping, although in three dimensions, it has been shown that the TE-MSD can level off when there is a correlation between the number of localizations in a trajectory and the diffusion constant.[139] This could lead to the incorrect interpretation that the fluorophores exhibit anomalous diffusion.

We therefore investigated whether the single-particle motion is in fact anomalous. The TE-MSD curves are shown for groups of trajectories with the same span (Figure 4.7b,c). We defined the span of a trajectory as the number of frames between the first and last localization of the trajectory, which can be larger than the number of localizations in a trajectory if the particle intermittently goes to a non-fluorescent state, i.e., it "blinks". In conditions where the fluorophores undergo trapping (7.5 mM NaOH), the shorter trajectories had a steeper slope indicating a higher diffusion constant than the longer trajectories (arrows in Figure 4.7b). Such a correlation is not obvious in the conditions where trapping rarely occurs (Figure 4.7c). Remarkably, the individual TE-MSD curves in Figure 4.7b appear linear, in contrast to their average in Figure 4.7a. This strongly indicates that trajectories with a longer

span have a lower diffusion constant, but do not exhibit inherent anomalous diffusion behavior. To investigate this further, we obtained the diffusion constant from a linear fit of the TE-MSD curves in Figure 4.7b,c. From Figure 4.7d, it is clear that there is a correlation between the span and diffusion constant of a trajectory. This correlation is much stronger for the sample with the most transient trapping events (7.5 mM NaOH). We found that longer trajectories have a larger fraction of immobile steps (i.e., steps < 139 nm), and this correlation also is stronger for the sample with more transient trapping events (Figure 4.7e). When trajectories are generated, the linking step will fail if the distance the emitter travelled between two frames exceeds the pixel jump. This means that trajectories with transient trapping events have a lower probability for having a failed linking step, because they have fewer mobile segments. We therefore conjecture that the flattening of the TE-MSD is a consequence of the property that longer trajectories have a higher fraction of immobile steps, and thus contribute stronger at longer delay times with a lower diffusion constant, i.e., slope. Inspection of individual TE-MSD's, such as shown in Figure 4.7f, revealed linear MSD curves for trajectories with a similar span, which points to normal diffusion of the quantum dots in the 2D pores.

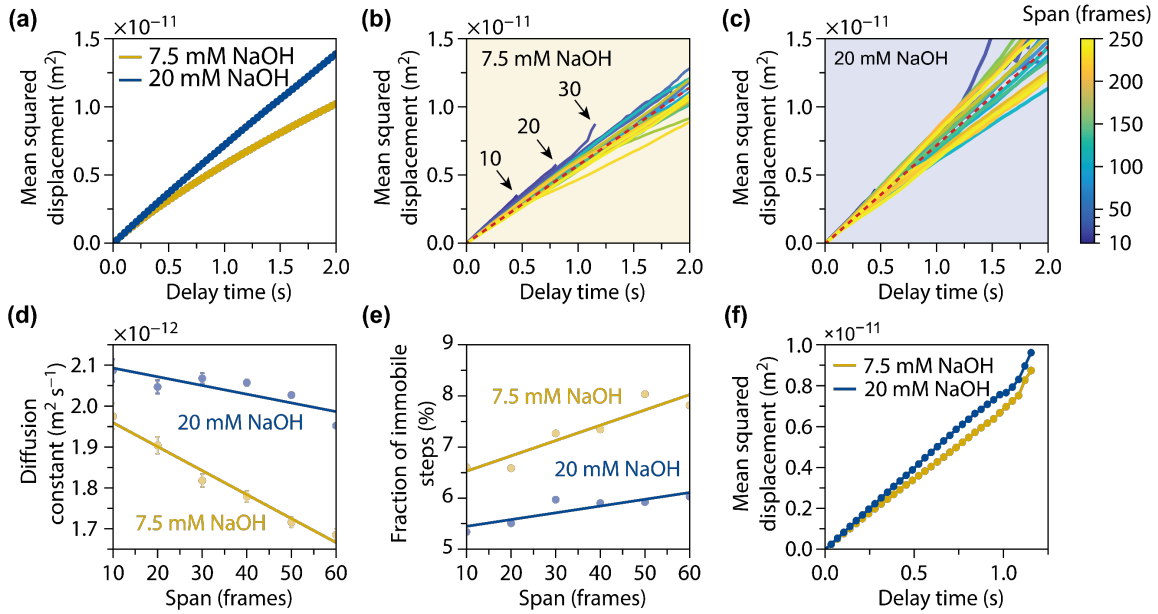

Figure 4.7 (a) Time–ensemble averaged mean squared displacement (TE-MSD) curve of all trajectories with a varying NaOH base concentration. The TE-MSD curve with a base concentration of 7.5 mM NaOH is non-linear. (b–c) TE-MSD computed for a group of trajectories with the same span, i.e., the number of frames between the first and last localization of the trajectory, for a 7.5 mM (b) and 20 mM (c) NaOH concentration. The bandwidth is 10 frames, which means that a span of 10 frames constitutes trajectories with a span of 5–14 frames. The red dashed line is a guide to the eye to assess linearity of the TE-MSD. The arrows in (b) indicate the span of the shortest three TE-MSD curves. (d) The diffusion constant obtained from a fit of the TE-MSD curves in (b) and (c) as function of the span of the trajectories. The error bars indicate the standard error in the TE-MSD fit, and the solid lines are a linear regression to the data points. (e) The average fraction of immobile steps (< 139 nm) per trajectory as function of the span of the trajectories. The solids lines represent linear regression lines to the data points. (f) The TE-MSD for trajectories with a span of 30 frames, that is, in the range of 25–34 frames. Both TE-MSD curves are linear.

The TE-MSD can be linear even though the underlying motion is anomalous. This is known to occur in situations where there is "weak ergodicity breaking" as a result of time-dependent and space-dependent diffusion [130,140]. We investigated whether there is time-dependent diffusion by plotting the MSD with a fixed delay time as a function of the starting time in the experiment (Figure 4.8 a-d).We

coin this the ensemble-averaged MSD (E-MSD). If the system 'ages', e.g., due to pore narrowing by adsorption of organic material or heating by the laser, the E-MSD is expected to change during the experiment. A linear fit was performed on the E-MSDs as a function of the experiment time for different delay times. For single videos recorded in the same conditions, we found both positive and negative slopes of the linear fits, and two examples are shown in (Figure 4.8a,b). To demonstrate that the fitted slopes converge towards zero on average, we show the same analysis for all (10) videos in the data sets (Figure 4.8c,d). In both conditions, the slopes are close to zero excluding anomalous diffusion as a result of time-dependent diffusion. Further, we investigated whether there is space-dependent diffusion via the spatial distribution of the E-MSD (Figure 4.8e). The spatially homogeneous distribution of the TE-MSD does not indicate the occurrence of weak ergodicity breaking on the tens-of-micrometer length scale. We conclude from this distribution and the absence of temporal aging effects that the fluorescent probes do not exhibit anomalous diffusion.

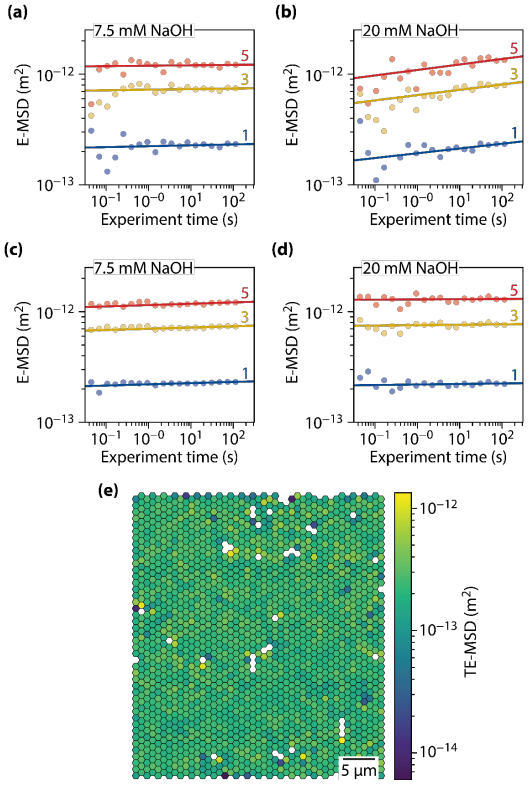

Figure 4.8 (a–d) Time–ensemble-averaged mean squared displacement (TE-MSD) as a function of the experiment time for delay times of one (blue), three (yellow), and five frames (red dots). Both a 7.5 mM NaOH concentration (panels a,c) and 20 mM NaOH concentration (panels b,d) are shown for one video (panels a,b) and averaged over all (ten) videos (panels c,d). The slope of the individual TE-MSD with the same delay time as a function of experiment time was obtained with a weighted linear fit in the log–log plot (solid lines). All slopes were close to zero, which indicates no ergodicity breaking. Only trajectories after artefact removal were considered (Figure 4.3). (e) Spatial distribution of the average TE-MSD in panel a for a delay time of one frame. Each hexagonal bin is 1 µm in size. The center of mass of each pair of consecutive localizations within a trajectory (i.e., localization of displacement) was used for the binning. Only bins with ten and more displacements are displayed. Note that the TE-MSD is displayed with a logarithmic color scaling.

4.2.4 pH Dependency of Diffusion Coefficient

We computed the average diffusion coefficient per span and weighted it by the number of displacements of the trajectories contributing to that span obtaining average diffusion coefficients of

$1.816 \pm 0.009 \times 10^{-12}$ m^2 s^{-1} and $1.963 \pm 0.004 \times 10^{-12}$ m^2 s^{-1} in 7.5 mM and 20 mM NaOH, respectively. The difference of 7.5 ± 0.6% in the average diffusion coefficient at the different pH could be due to the different QD size or trapping behavior. We estimated the drag force of the QDs using the 2D pore depth and the hydrodynamic radii of the QDs measured in bulk by performing a 5th degree polynomial interpolation on drag force data published by Keh et al.[242] This resulted in a slowing down of 5.4% (8.5%) for a QD positioned at 25 nm (12.5 nm) from the wall. The agreement in the computed and measured diffusivity ratio suggests that the diffusion behavior could be mainly explained by the size of the QDs. A large effect of trapping on the measured diffusivity would have been evident from a larger slowing down in 7.5 mM NaOH conditions than purely based on the computed hydrodynamic drag. To better understand the difference diffusivity in the measured conditions, three-dimensional particle coordinates or a simulated distribution of the distance between the QD and pore wall should be available. Because the QD size in free solution was determined in 85/15 (m/m) glycerol/water, whereas the experiments in the 2D pore were done in 50/50 glycerol/water, we assumed that the QD radius was the same in both solutions. Altogether, our analysis suggests that the diffusivity of the particles is governed by their size. However, as we will see in Chapter 5, the current probe-host-solvent-system shows some anomalies in terms of hydrodynamic drag. The continuum model cannot describe the drag force experienced by the QDs and their resulting diffusion coefficients.

4.2.5 Exploring More Complex Pore Spaces

We found that trapping was suppressed in 20 mM NaOH, which prevents blind-spots in the pore-space map due to linking artefacts and allows for a more rapid porosity exploration. Therefore, these conditions were used to map more (complex) pore spaces. First, we explored a 1D pore demonstration system fabricated in a similar way as the 2D pore. The main differences were: (1) the model-pores were thinner, that is, 2.1 µm; (2) the model-pores were only accessible from the two ends; (3) the depth of the model-pores was two times larger, that is, 100 nm, than in the 2D pores; and (4) the supply channels were only connected through the 1D pores and a pressure difference on both ends, induced a flow along them (Figure 4.9a). QD trapping was prevented by operating in 20 mM NaOH, which allowed for (partially) mapping of the pore system (Figure 4.9b). The individual 1D pores can be readily discerned. The width of the 1D pores in the overlay matches their width on the lithography mask. Some localizations appear outside the 1D pores, and these are random unphysical localizations sometimes found in the camera noise by the localization algorithm. Indeed, the even distribution of localizations within the 1D pore and the abrupt decrease in localizations beyond the pore wall in *y* indicates that the quantum dots are closely confined in the pores (Figure 4.9c). The quantum dots appear to be localized more frequently close to the pore wall in the y-direction, possibly due to increased drag close to the pore wall resulting in a longer residence time at these locations.

Next, we used the TE-MSD in the *x* and *y* directions to characterize the confinement (Figure 4.9d). From the *y*-TE-MSD curve, we estimated a nanoslit width of 1.8 µm by fitting the curve with a confinement model.[138,139] The *x*-TE-MSD curve was parabolic and could be described by a directed diffusion model accounting for flow along the direction of the pores. [138,139] To double check this, the total displacement in *x*-direction of all tracks, i.e., the distance between the first and last localization along the 1D pores, was plotted in a histogram (Figure 4.9e). For a system without flow, a zero-centered Gaussian distribution would be expected. Nevertheless, the distribution is asymmetric as demonstrated by the longer tail on the left and non-zero mean. This confirms that there is flow along the *x*-direction of the demonstration system's 1D pores.

In the 1D pore, a fraction of the trajectories contained frequent transient trapping events and moved considerably slower than the rest of the trajectories. The number of these kind of trajectories increased with a pore depth from 100 to 150 nm. We believe that these trajectories represent QD

clusters. These trajectories were filtered out in mean squared displacement analysis by removing all trajectories with a diffusion coefficient < 1.29×10^{-12} m^2 s^{-1}. This will be discussed further in Chapter 5.

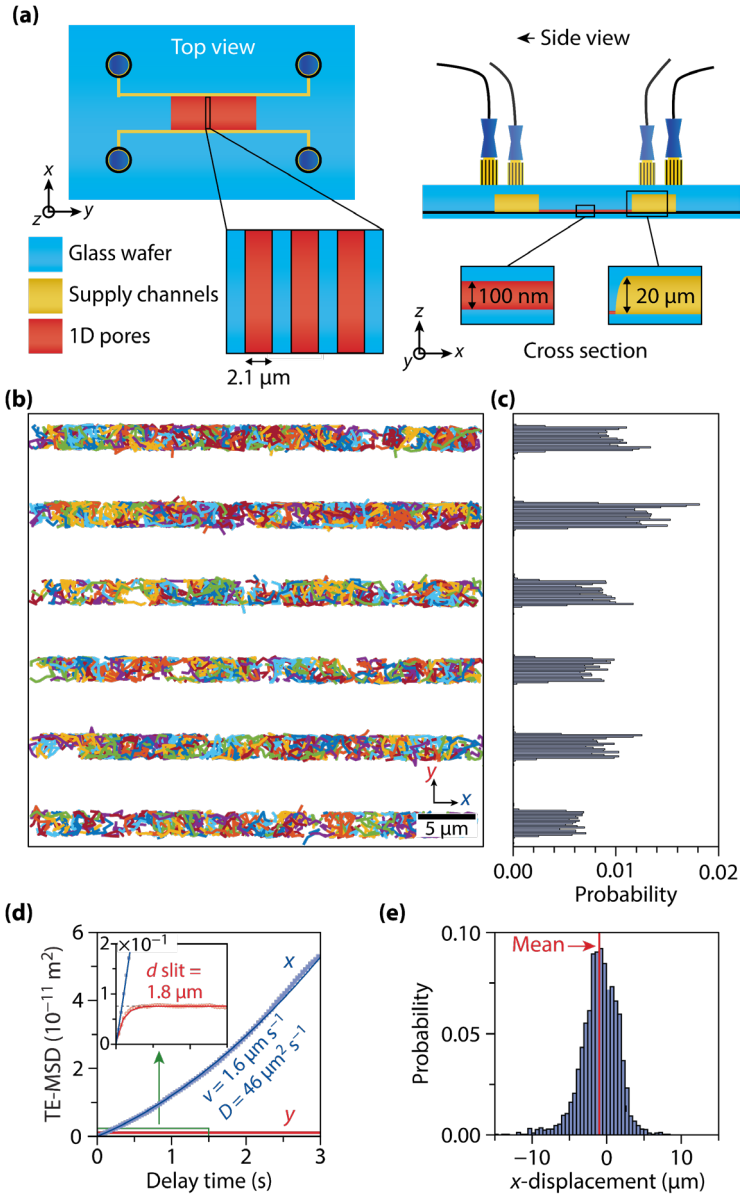

Figure 4.9 Schematic representation of the microfluidic device consisting of lithography-patterned 1D pores. (b) Overlay of trajectories obtained over 140 s. (c) Histogram of y-coordinate localizations aligned with panel (b). (d) TE-MSD in x and y as a function of time of the trajectories in (b). The solid lines show the fit of a normal diffusion model accounting for flow in x and a confinement diffusion model in y.[138,139] (e) Histogram of the total displacement in the x-direction for all trajectories. The distribution has a tail on the negative side and a mean value below zero. In a system without flow, a symmetric distribution mean-centered at zero displacement would be expected.

Finally, we tested the approach by exploring the accessible porosity of a real-life silica-supported polymerization catalyst (Figure 4.10a). Due to the pH of the system, adsorption could be prevented here as well. All trajectories are in the center of the particle, suggesting that most of the accessible porosity is in this region. We imaged the cross section of a catalyst support particle of the same batch prepared via focused ion beam milling using scanning electron microscopy (FIB–SEM) (Figure 4.10b). The morphology of the pores matches qualitatively: there are large pores in the inner particle as well

as a denser crust in the outer part. The QD motion in the particle changed considerably as result of confinement. Even at a delay time of one frame, we found that the displacements are shorter inside the catalyst support particle than outside (Figure 4.10c). The limited distance over which a QD can travel before it hits a pore wall as well as the increased hydrodynamic drag in the pore contribute to these shorter displacements. At longer delay times, the mean travelled distance is even further reduced by confinement and a flattening of the TE-MSD is observed (inset Figure 4.10c).

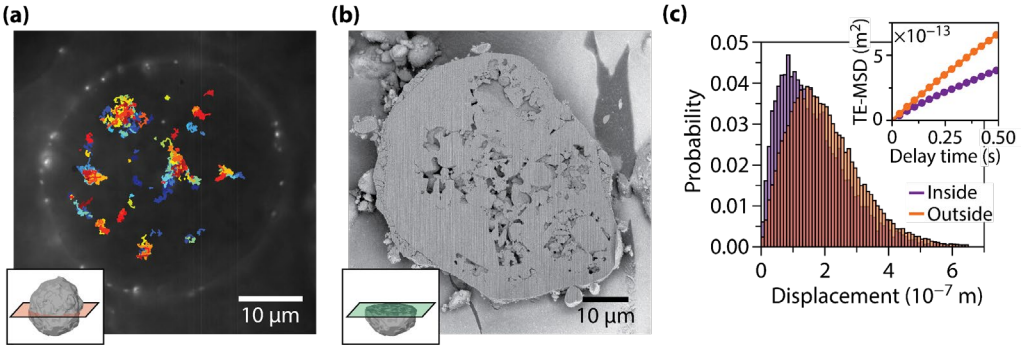

Figure 4.10 (a) Trajectories overlaid with the summed fluorescence intensity obtained within an olefin polymerization catalyst support over 70 s. (b) Focused ion beam-Scanning electron microscopy (FIB–SEM) image of another particle of the same batch showing a similar pore morphology. (c) Histogram of displacements of trajectories inside and outside the catalyst support particle (35 ms delay time). The time–ensemble-averaged mean squared displacement (TE-MSD) is shown in the inset.

4.2.6 Pore Space Mapping with Single-Particle Tracking

After showing feasibility of the approach the question that arises is: how much tracking time is required to ensure complete pore space mapping? The answer to this question cannot be known prior to running the experiment, as the time needed depends on 1) the accessibility and size of the pores; 2) the local diffusion coefficients and concentrations of the probes; and 3) the desired resolution for pore space mapping. In this section we explain our mapping approach. Further, we propose a protocol to ensure a complete mapping of the pore space with single particle tracking. Finally, we discuss whether our experiment times were sufficient for a complete porosity mapping.

In order to translate the obtained tracks to a mapped pore space we converted the localizations into a binary image where each pixel is classified as either “pore space” or “solid”. Our procedure will be discussed using a simulated track within a squared pore of 15 µm^2 as an example (Figure 4.11 a). We created a 2D image in which each pixel corresponds to different localization bins, the number of pixels depends on the min and max coordinates of the track in *x* and *y* direction. Every time a particle was localized within a pixel-bin, that pixel was segmented as a pore (yellow areas in Figure 4.11 b,c). The number of all pixels segmented as pores multiplied by the pixel area was used to calculate the mapped pore area. Moreover, the size of the 2D bins used determines the resolution of the mapped porosity. However, the chosen mapping resolution cannot be smaller (better) than the localization error (e.g., 37 nm in the 2D pores). In Figure 4.11b,c the pixel-bin sizes used were 37 nm and 50 nm, respectively. Larger pixels are more likely to contain localizations and therefore to be segmented as pores. As a result, the mapped porosity with 50 nm pixel-bins is larger than with 37 nm ones, even though the 2D images were created based on the same track (Figure 4.11 b, c). Moreover, the chosen resolution also influences the time required to entirely map the pore space, as larger pixels get “filled” with localizations faster. This means that the total mapping time can be reduced at the cost of reduced spatial resolution. Figure 4.11d shows the total mapped pore area of a simulated track as a function of time as well as pixel-bin size. As time progresses, larger fractions of the pore space are explored. Therefore, the increment of the mapped porosity is reduced over time, until the curve plateaus at a

maximum value close to the true pore area. Here, one can clearly see that the time at which the porosity-vs-time curves reach their plateau is reduced with growing pixel-bin sizes. One should also consider that the space discretization we use will result in a slight porosity overestimation, especially with larger pixel sizes (Figure 4.11,d).

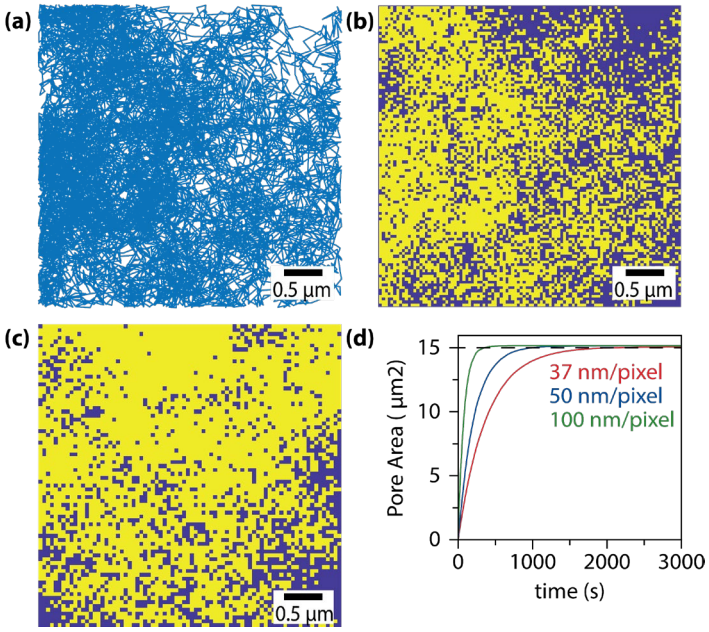

Figure 4.11 (a) Simulated track within a 15 µm2 pore with 10000 localizations. Simulation assumptions: (b,c) Binary Images of mapped pore space (yellow pixels) by the track shown in (a) using pixel-bin sizes of 37 nm and 50 nm respectively. The total mapped porosity is larger when larger pixel-bin sizes are used. (d) Porosity mapped by simulated tracks with varying number of localizations and pixel-bin sizes. The better the spatial resolution chosen, the longer time is required for the curve to plateau (i.e., fully map the pore space). The dashed black line represents the true pore area of 15 μm^2. All curves slightly overestimate the pore area. This overestimation grows with an increasing chosen pixel size. The following assumptions were made for the simulations: 1) only one random walker is present in the pore; 2) the diffusion coefficient of the random walker is not affected by confinement and has the same value as measured in free solution at 20 mM NaOH (Figure 4.6b); 3) the random walker bounces back elastically when colliding with the wall; 4) the time in between localizations corresponds to the frame time of our experiments (35 ms).

Ideally, when performing a tracking-based porosity mapping experiment, the results should be analyzed in parallel: The probes should be tracked within a chosen region of interest (i.e., a porous particle). Then, the localizations should be binned to map the pore space as described above. Finally, the mapped porosity should be plotted as a function of time as the experiment progresses. Once the porosity increment is smaller than a chosen threshold, the measurement can be stopped, and one can assume that the total accessible porosity has been mapped.

In order to test whether the tracking time used was sufficient to fully map the 1D pores and the pore space of the polymerization catalyst support with sub-diffraction limit resolution, we determined the mapped the pore space using different pixel-bin sizes (Figure 4.12a-c Figure 4.13a-c) and plotted the total mapped pore areas as a function of the tracking time Figure 4.12d and Figure 4.13d. In both experiments the binary images (Figure 4.12a-c Figure 4.13a-c) of the pores contain “holes” suggesting that the pore space was not fully explored, especially when low pixel-bin sizes were used. Accordingly, the mapped porosities as a function of time were still growing at the end of the experiment (Figure 4.12d and Figure 4.13d). This means that the measurement time was not sufficient to fully map the

pore space, even at resolutions above the diffraction limit. However, based on these experiments, it can be stated that, at any of these resolutions, the true pore area was always larger than the pore areas determined via this approach, that is, the data provide a lower limit for the porosity of the material studied.

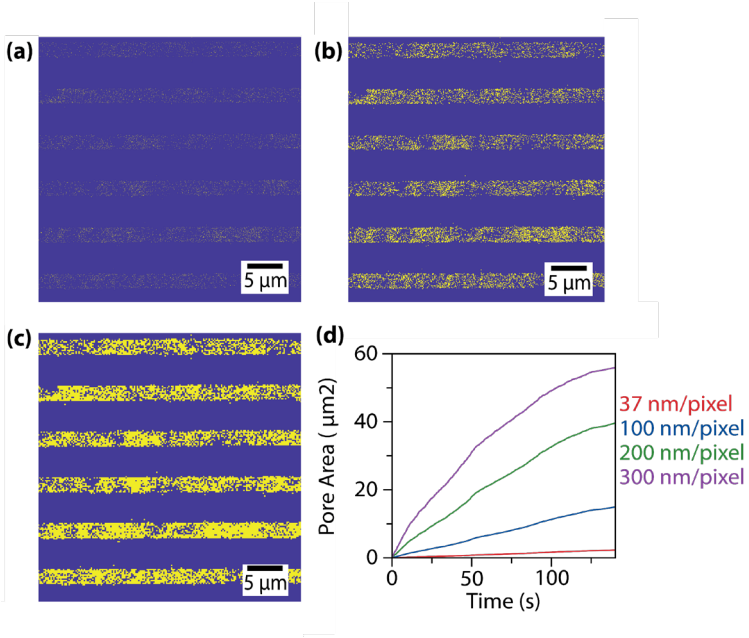

Figure 4.12 (a-c) Binary Images of mapped pore space (yellow pixels) by the tracks shown in Figure 4.9b using pixel-bin sizes of 37 nm, 100 nm, and 200 nm respectively. (d) Total mapped pore spaces area as a function of experiment time and pixel-bin size. The smaller the pixel size chosen, the lower the mapped porosity and the steeper the curves at the end of the experiment. Even with a pixel size of 300 nm (above the diffraction limit), the mapped total porosity as a function of time did not plateau at the end of the experiment. Here, longer tracking times would be required to fully map the pore area (true value 106 μm^2).

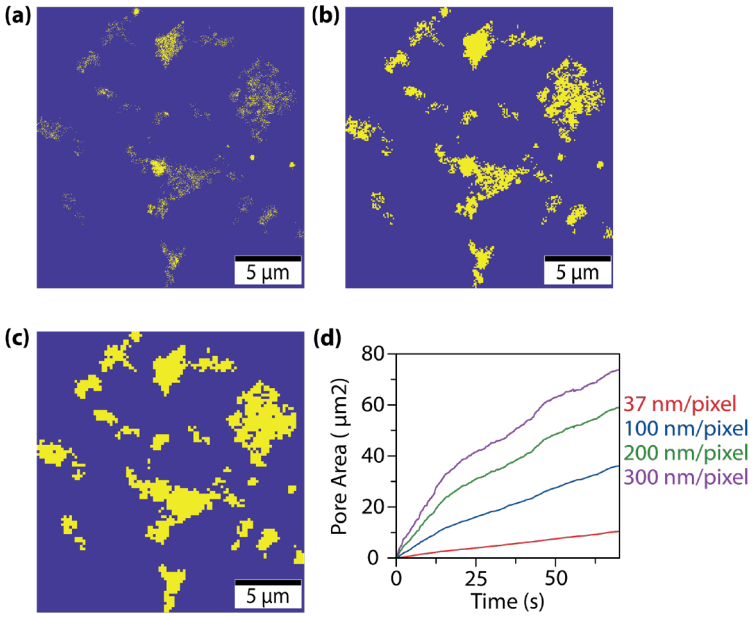

Figure 4.13 (a-c) Binary images of mapped pore space (yellow pixels) by the tracks shown in Figure 4.10a using pixel-bin sizes of 37 nm, 100 nm and 200 nm respectively. Their mapped pore areas are 10 µm^2, 36 µm^2 and 59 µm^2 which corresponds to 2%, 7.2% and 11.8 % porosity respectively. Based on these results, we know that at each given resolution, the true porosity cannot be lower than these values. The total area of the particle was segmented manually from the mean fluorescence image displayed in Figure 4.10 using ImageJ. This value was divided by the mapped pore areas to determine the mapped porosities in %. (d) Mapped pore spaces as a function of experiment time and pixel-bin size. The better the resolution chosen, the lower the total mapped porosity and the steeper the curves at the end of the experiment. Even with a pixel size of 300 nm (above the diffraction limit), the mapped porosity as a function of time did not plateau at the end of the experiment. This shows that, longer tracking times are required to fully map the pore space.

4.3 Conclusions

Well-defined 2D and 1D model pores have been developed to characterize both diffusion and trapping behavior of individual fluorophores in confinement. The model pore design was pivotal for obtaining of long single-QD trajectories, which allowed for detailed probe characterization. In this Chapter we have shown that QD trapping could be reduced via solution pH, likely because of a larger electrostatic repulsion between QDs and pore walls. Using the 2D model pore, we quantified transient trapping events and found that these were almost completely suppressed in 20 mM NaOH. We successfully demonstrated the use of QDs under nearly non-trapping conditions for pore-space mapping of 1D silica pores and a real-life polymerization catalyst support particle, potentially with resolutions in the order of tens of nanometers. A protocol to ensure a complete porosity exploration in future SPT-mapping experiments was introduced. Further research should be focused on the systematic characterization of the relation between the measured diffusion coefficient in the model pore and the pore size, -shape, and probe–wall interactions. The compatibility of the microfluidic device with organic solvents (e.g., toluene) should be exploited to study the behavior of hydrophobic dyes. This will provide further insights in the factors that promote mass transport through porous solids and/or can be used to validate diffusion models for these materials. The application of our model-pore platform is not limited to pure silica systems since the device can be modified for the characterization of fluorescent probes in metal oxide and carbon-based pore environments.

4.4 Materials and Methods

4.4.1 Materials

CdSe/ZnS core–shell quantum dots (QDs) with polyethylene-glycol functionalization (900246-250UL, Sigma-Aldrich), ES70X silica (PQ Corporation), glycerol (≥ 99.5%, Sigma-Aldrich), 170 µm and 500 µm thick MEMpax wafers (Schott), sodium chloride (≥ 99%, Sigma-Aldrich), sodium hydroxide (analysis grade, Merck KGaA). All chemicals were used as received with no further purification except water, which in all cases was purified through a Milli-Q system to a resistivity of 18.2 MΩ·cm. The ES70X silica material used is a microspheroidal silica gel that is typically employed as a support for industrial-grade polymerization catalysts. The particles are characterized by relatively large networks of macropores with a D_{50} = 50.0 µm, S_{BET} = 295 m^2/g, and V_{pore} = 1.6 mL/g.

4.4.2 Characterization

a. Quantum-Dot Fluorescence

Fluorescence spectroscopy was performed using a home-built setup equipped with a 405 nm laser and 520 nm long pass filter for excitation. The fluorescence emission was collected under a 90° angle with an Ocean Optics HR4000 spectrophotometer. The zeta potential was measured with a Malvern Zetasizer Nano ZS using a folded capillary zeta cell (DTS1070, Malvern). The average value over a series of five measurements was reported. Transmission electron microscopy was performed with a FEI Tecnai-F20 (200 keV) transmission electron microscope equipped with a field emission gun.

b. Polymerization Catalyst Support Porosity

Focused ion beam–scanning electron microscopy (FIB–SEM) was done with a FEI Helios NanoLab G3 UC scanning electron microscope, following procedures from the literature.[66,70] For each experiment, the catalyst sample was dispersed onto double-sided adhesive, conductive carbon tape, which was attached to an aluminum SEM stub. Using a Cressington 208HR sputter coater, a Pt coating of ~6 nm was applied. During the process of FIB cutting, slices were milled horizontally to the SEM stub surface using a 45° angled SEM stub at a suitable stage tilt angle. Cross-sectional SEM images were recorded in backscattered electron (BSE) mode at 2 kV and 0.1 nA using a “through the lens detector” and an immersion lens.

4.4.3 Microfluidic Device

The workflow of the nanofluidic chip fabrication is shown in Figure 4.14. The one-dimensional (Figure 4.9a) and two-dimensional (Figure 4.1a) pores were patterned in 500 µm thick MEMpax wafers (Wafer A). To avoid under etching, a 15 nm Cr layer was first sputtered on the wafer with a home-built T’COathy system (MESA+, NanoLab). A positive photo resist (Olin OlR908-17) layer was spin-coated on top and locally exposed with UV light using a lithography maskaligner (EVG®620). After removing the exposed photoresist, the wafer was submerged in a Cr etchant. Then, the glass in the UV-exposed area was etched by submerging the wafer with 12.5 % buffered HF, creating the model pores. The supply channels were patterned in a similar way, but 25% HF was used for their etching and a Cr/Au layer as a mask. The inlet holes were also lithography patterned and powder blasted using a Harke i-HE100 foil. A second, 170 µm thick MEMpax wafer (Wafer B) was thermally bonded to Wafer A at 625 °C. The thickness of Wafer B is within the range where the microscope objective corrects most optimally for optical aberrations.

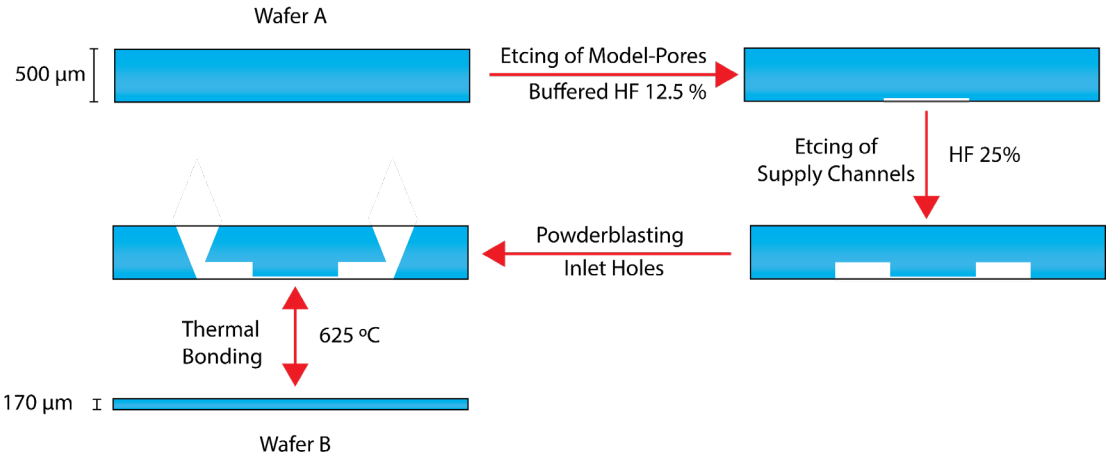

Figure 4.14 Microfluidic device simplified workflow. First, the 1D and 2D model-pores were patterned with lithography and etched with a buffered HF solution (1%). Then, the supply channels were patterned and etched with HF (25%). After this, the backside of the wafer was covered by a light-sensitive foil that was lithography- patterned in order to powder-blast the inlet holes. Finally, wafer A and B were thermally bonded in a furnace at 650 °C.

The depth of the 2D pores was measured with a stylus profilometer (DektakXT, Bruker) before the two silica wafers were bonded together (Figure 4.14). The profile is displayed in Figure 4.15b,c and shows that the slit depth is 48 nm. The surface roughness was measured with atomic force microscopy over a 500×500 nm^2 region (Figure 4.15d). The resulting root-mean-square (rms) roughness was found to be 5.4 nm.

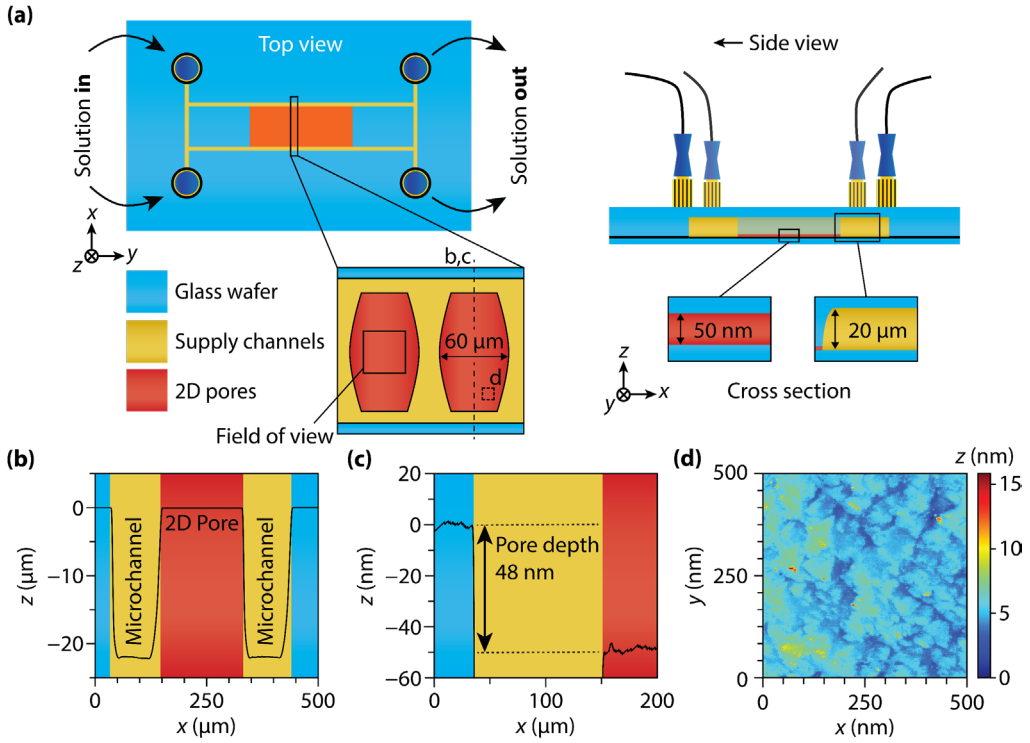

Figure 4.15 (a) Schematic representation of the microfluidic device containing model pores. The top view, side view, and a cross section through a two-dimensional (2D) pore and a supply channel is shown. (b) Measured profile with a stylus profilometer displaying the supply channels. The profile is depicted with the dashed line in panel a. (c) Zoom of panel b displaying the height difference in z between the lithography-patterned 2D pores and the unexposed part of the wafer, prior to bonding.

(d) Surface roughness as measured with atomic force microscopy. The mapped area is depicted with the dashed box in panel a (not to scale).

a. Stability of Silica

We measured a pH oh 10.8 for our 20 mM NaOH Water/Glycerol 50/50 wt.% solution. Importantly, it is known that the solubility of silica increases strongly at pH values higher than 9.[251] In order to test whether the silica microfluidic device was dissolving at a significant rate under the applied conditions, we performed lithography on a MEMpax wafer and put the exposed area in contact with 100 µl of the solution we used at room temperature (100 µl >> $V_{2D\ pore}$). After 35 minutes, i.e., the time it took to load the chips and perform the measurements, the wafer was rinsed with water and the photoresist was removed ($HNO_3$and plasma cleaning). The profile of the border between the exposed area and the rest of the wafer was measured with a white light interferometer (Bruker) and no signs of etching were found, meaning that the 2D pore-walls did not dissolve significantly during the experiment.

b. Chip Holder and Loading

Prior to fluorescence microscopy, the microfluidic device was placed in dedicated chip holder (Figure 4.16) and loaded with a fluorescent probe solution with a syringe pump (kdS scientific) at a flow rate of 10 mL/min. Microfluidic connectors and fittings (IDEX Health & Science) as well as plastic tubing (Avantor Fluid Handling) and fused silica capillaries (Molex) were used to transport the liquid from the syringe into the powder-blasted inlet holes of the microfluidic chip (Figure 4.16a-d). After loading, the system was sealed with caps (IDEX Health & Science) to avoid evaporation during imaging (Figure 4.16c).

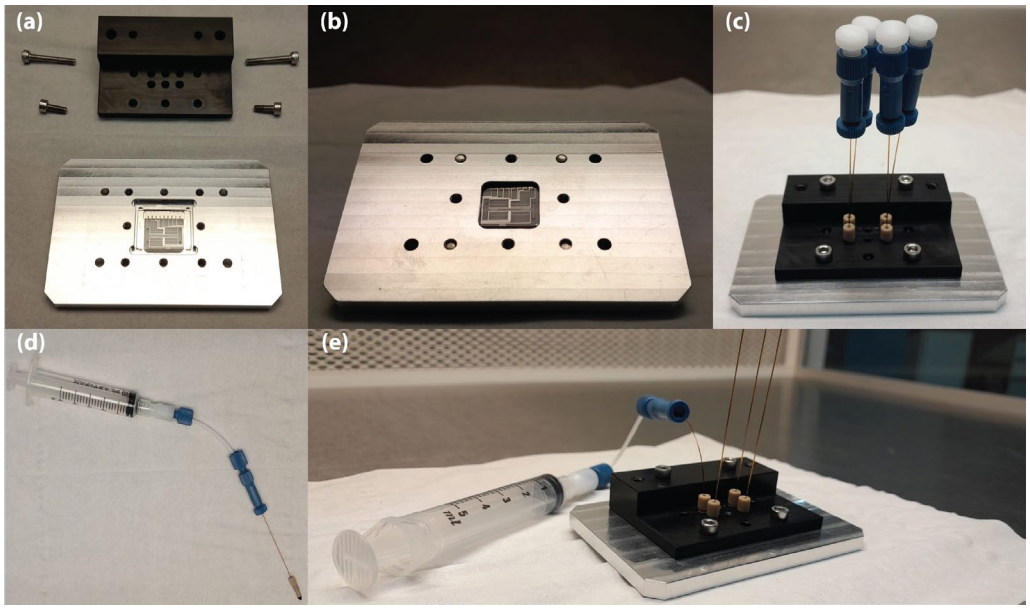

Figure 4.16 Microfluidic device placed in the chip holder before mounting viewed from the top (a) and the bottom (b). The oil immersion objective approaches the chip through the shown hole from below. (c) Sealed system after fluorescent probe solution loading. (d) Microfluidic connections, fitting and tubing used to transport the liquid from the syringe to the chip. (e) Syringe connected to chip through microfluidic device.

4.4.4 Fluorescence Microscopy

Single-particle tracking experiments were performed on a home-built fluorescence microscope. This setup consisted of a Nikon Ti–U inverted microscope equipped with an oil-immersion objective (Nikon CFI Plan Apochromat Lambda 100×, NA 1.45). The excitation light source was a 405 nm (PicoQuant D-C-405) operated in continuous wave and focused on the back focal plane of the objective with a 150 mm achromat lens. The laser was used in conjunction with appropriate dichroic and long-pass mirrors as well as a 585/40 nm band-pass filter to remove background from the fluorescence emission signal. The filtered emission signal was collected with an electron-multiplying charge-coupled device detector (EMCCD; Andor iXon Ultra 888) operated at a gain of 300, exposure time of 30 ms, and frame time of 35 ms.

The quantum dots were 1000x diluted from the stock (4 µM in H_2O) to reach a 50/50 (m/m) water/glycerol mixture. NaOH was added to the quantum dot suspension to obtain slightly basic conditions of 7.5 mM and 20 mM NaOH. The 7.5 mM NaOH sample had an additional 2.5 mM NaCl to keep the Debye length < 2.5 nm.

4.4.5 Data Analysis

a. Localization and Tracking

The recorded fluorescence microscopy movies were analyzed with the DoM plugin (Detection of Molecules for ImageJ.[128] The localization of fluorescent events was done by independent classification of each frame into emissive spots and background. A list of initial emitter positions was determined with a sub-diffraction limited spatial resolution by fitting a two-dimensional Gaussian using the Levenberg−Marquardt least-squares algorithm. For trajectory analysis, molecules were allowed to blink (i.e., the molecule is fluorescing intermittently) for a maximum of 35 ms. Moreover, only trajectories with more than four localizations were considered to ensure sufficient displacements per trajectory for MSD analysis and to remove unphysical trajectories originated from incorrect localizations. All trajectory data shown has been filtered to >4 localizations. Trajectory classification, analysis and plotting were done in MATLAB® (MathWorks®) using DiffusionLab, a software developed in our group for the classification and motion analysis of single-molecule trajectories.[139]

Motion analysis was performed with mean squared displacement (MSD) analysis of individual trajectories or a set of trajectories, i.e., a population. A definition and explanation of the time-averaged MSD (T-MSD) used for the analysis of individual trajectories and time–ensemble averaged MSD (TE-MSD) used for population analysis can be found in Maris et al.[139] The diffusion coefficient and localization error were obtained from a linear fit of the MSD curve. MSD analysis on individual trajectories was done including the first 25% of the delay times and at least three points. For the measurements in free solution, only the first four points were used in the fit of the TE-MSD, because the number of trajectories contributing to the MSD was constant within this fit range.

b. Transient Trapping Analysis

We identified transient trapping by the evaluation of the probability that an unconstrained diffuser with a known diffusion coefficient would spontaneously stay within a certain spatial domain.[252–254] When this probability is smaller than a certain threshold value, it is unlikely that spontaneous fluctuations make the diffuser appear bound. Then, the trajectory — or segment thereof — is considered *trapped*. The probability ψ that a unconstrained diffuser remains in a region $r < R$ for all times ≤ t given its diffusion coefficient D was presented by Saxton et al., which for $Dt/R^2 > 0.1$ is the relation.[253]

$$\log \psi = 0.2048 - 2.5117 \left(\frac{Dt}{R^2}\right) \quad \text{Equation 4.2}$$

for a fixed D and circle radius R. The probability ψ decreases for an increased t because the diffuser has more time to explore the space, which reduces the probability that it spontaneously appears trapped. The diffuser is considered trapped if the probability ψ is smaller than a threshold ψ_c. We implemented this approach using a sliding window of n frames with a $t = (n-1)\ t_{frame}$ and t_{frame} the frame time. The algorithm is depicted in Figure 4.17. The selection of the threshold ψ_c is discussed below. We reported the trapping event duration as the number of frames in the segment (i.e., $t + t_{frame}$). The minimum length of a segment with trapping is equal to n frames.

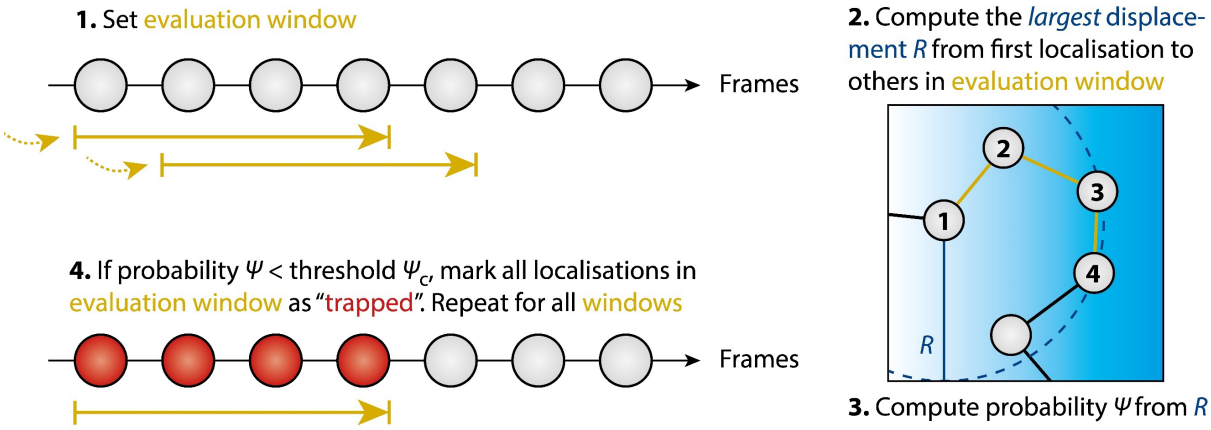

Figure 4.17 Schematic representation of the trapping analysis in four steps. (1) The evaluation window (yellow arrow) is a sliding window starting at the first localization (grey circles). Only windows spanning exactly the window length n are considered; n = 4 in this example. Steps 2–4 are performed for each evaluation window in the trajectory. (2) All displacements from the first localization to all other localizations in the evaluation window are computed and the largest displacement R is found. (3) The largest displacement R is used to compute the probability ψ (Equation 4.2). (4) All localizations in the sliding window are marked as trapped if ψ is smaller than the threshold ψ_c. Repeat the procedure for all evaluation windows.

We optimized the threshold ψ_c for our experiment using simulations of unconstrained diffusers. The threshold ψ_c is dependent on the diffusion coefficient and the sliding window time, and it must be optimized for every combination thereof. To find a value of ψ_c that did not include a larger amount of false positives, i.e., localizations incorrectly marked as trapped, we lowered ψ_c until a negligible number of false positive were present in simulated trajectories of unconstrained diffusers (following the protocol of Vrljic et al.[254]). For this, we used the quantum-dot (QD) diffusion in the two-dimensional pore as reference experiment to set ψ_c. We simulated two-dimensional Brownian motion with a displacement probability in x and y given by a normal distribution with a standard deviation of $\sqrt{2Dt}$, with D the diffusion coefficient and t the delay time.[255] We assumed that the error in the localizations is normally distributed with a standard deviation of σ. We used simulation parameters that matched the experiment, that is D = 2 × 10^{-12} m^2 s^{-1} and σ = 36 nm, and simulated 1000 trajectories, each with 1000 localizations. The localization error used in the simulation was estimated from fully trapped trajectories in the experimental data (Figure 4.18a). The mean of the distribution of the localization error was taken for the simulation. We found that a sliding window of n < 5 frames required extremely low ψ_c, which resulted in poor performance; therefore, we used n = 5 throughout the analysis. To use a short sliding window, we accepted a small number of false positives and found

$\psi_c = 2 \times 10^{-9}$ (i.e., $Dt/R^2 = 8.05$ and $R = 187$ nm) being a good trade-off between a low number of false positives and sufficiently high sensitivity to trapping.

This short sliding window provided the highest time resolution possible, which maximizes the probability to find trapping events in conditions with little QD trapping (as expected in 20 mM NaOH conditions). A histogram of the trapping event duration in the simulation is shown in Figure 4.18b. The sliding window of 5 frames restricted the detection of trapping event shorter than five frames (175 ms). The measured trapping event duration correspond to false positives as no QD trapping was included in these simulations. We demonstrate the trapping analysis for an experimentally obtained trajectory with transient trapping in Figure 4.18c,d. Overall, the number of false positives in simulations is at least an order of magnitude lower than the total number of measured trapping events in the experiment. This indicates that in both 7.5 mM and 20 mM NaOH conditions, a significant number of trapping events is recorded.

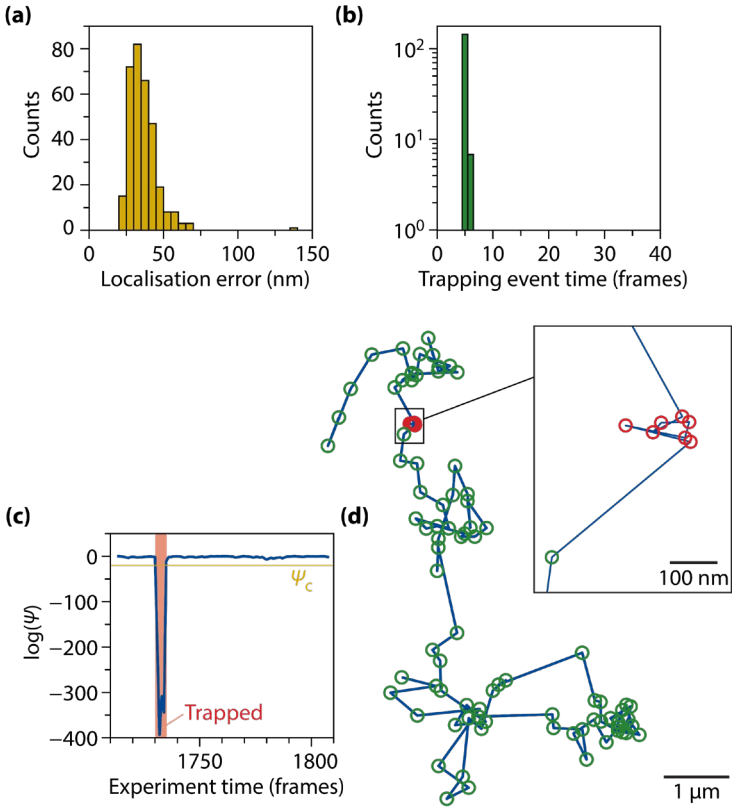

Figure 4.18 (a) Histogram of the experimental localization error as determined from the standard deviation of the localizations in x and y of individual trajectories representing immobile quantum dots (QDs). All trajectories with 100 or more localizations and a minimum bounding circle radius of maximum 400 nm were considered. The QD trajectories were recorded in basic conditions (7.5 mM NaOH). (b) Histogram of the trapping event duration of trajectories simulated with two-dimensional normal diffusion with a diffusion coefficient of 2×10^{-12} m^2 s^{-1} and a localization error of 36 nm. The sliding window time n = 5 frames restricted the detection of trapping events with a duration n < 5 frames. (c, d) Demonstration of the trapping analysis on an individual trajectory recorded from QD diffusion in the two-dimensional pore (7.5 mM NaOH). The trajectory is shown with the individual localizations marked either as non-trapped (green) or trapped (red) in panel (d). The logarithm of the probability ψ is given as a function of the experiment time for the trajectory in panel (c). A drop in ψ below the trapping threshold ψc marks the trapped time domain, which matches the red localizations in panel (d).

5 Using the Diffusion Coefficient of Individual Probes to Measure Local Pore Sizes

Hydrodynamic interactions between diffusants and pore walls play a significant role in liquid-phase mass transfer processes. Therefore, the local diffusion coefficients measured with single particle tracking could be used to determine the effective pore size. However, this has not been experimentally demonstrated yet. In this Chapter, we continue the work of Chapter 4 by performing single particle tracking experiments under non-trapping conditions in well-defined two-dimensional model pores with varying depths. Further, we performed fluid dynamic simulations to estimate the drag experienced by the fluorescent nanoparticles and we compared the resulting effective diffusion coefficients to the values obtained experimentally. Even though simulations predicted large differences, the motion behaviour did not vary as a function of pore size during the experiments, showing that this probe-solvent-host system cannot be used to estimate pore size via the local diffusion coefficient.

5.1 Introduction

As mentioned in Chapters 1 and 4, hydrodynamic interactions between the pore-walls and the diffusing probes can play a significant role in mass transfer. The hydrodynamic drag force F_{drag} experienced by a body moving in a fluid depends on the shape and volume of the object, its velocity v relative to the medium and moving direction, as well as the density ρ and the viscosity η of the fluid. These parameters determine the velocity and pressure fields of the liquid around the moving object which in turn give rise to the two forces that compose the hydrodynamic drag: the pressure gradient force and the viscous force.[256] The pressure gradient force is generated by the difference in pressure acting on the surface of an object. As the object moves, the static pressure on the "front" side will be the highest and it gradually decreases towards the "back side". This pressure results in a force acting in the opposite direction of the movement, slowing the object down. If the pressure field is known, it can be used to compute the pressure gradient force (Equation 5.1).[256] Here p is the pressure, n is the vector indicating the direction perpendicular to the surface and dA is the differential surface area. It should be noted, however, that for very low Reynolds numbers and high viscosity media (liquids), the contribution of this force to the drag force is negligibly small.[257]

$$\vec{F}_p = \iint p\vec{n}dA \qquad \text{Equation 5.1}$$

In contrast, the viscous force arises from friction between the object and the fluid. This friction is characterized by the viscous shear stress $\tau_{viscous}$ of the medium at the surface of the object. In a Newtonian fluid, the shear stress at a wall is proportional the velocity gradient (red line in Figure 5.1, Equation *5.2*).[258] The steeper the velocity gradient dv(y)/dy, the larger the shear stress and the viscous drag experienced by the object. Here, the proportionality constant η is the dynamic viscosity. Therefore, the viscosity of the medium also influences the experienced drag.

$$\tau_{viscous} = \eta \frac{dv(y)}{dy} \qquad \text{Equation 5.2}$$

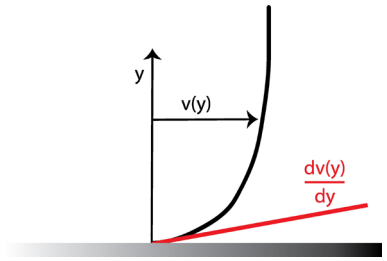

Figure 5.1 Schematic velocity profile of a flow over a surface. Assuming no-slip conditions means that the velocity at the surface is 0 and gradually increases with the distance perpendicular to the surface. The steeper the velocity gradient at the wall (red line), the larger the shear stress experienced by the surface.

If the velocity profile around the object is known, one can compute the total drag force by integrating the shear stress over the whole surface of the object.[257]

$$\vec{F}_{viscous} = \iint \tau dA \qquad \text{Equation 5.3}$$

By adding the pressure gradient force and the viscous force the total Hydrodynamic drag force can be computed:[256]

$$\vec{F}_{drag} = \vec{F}_{viscous} + \vec{F}_p \qquad \text{Equation 5.4}$$

Importantly, the drag force experienced by an object moving in a liquid and by a resting object in a flow approaching the object with the same relative velocity is the same. Therefore, aero- and hydrodynamic drag are usually studied by letting a medium flow around an object experimentally or computationally.[257]

The drag force of a sphere moving slowly (laminar flow, low Reynolds number) relative to a fluid can be approximated with the following formula:[259]

$$F_{drag,s} = -6\pi r\eta v \qquad \text{Equation 5.5}$$

However, when the sphere is confined, the flow profile around it changes (Figure 5.2). Let us consider a sphere between two parallel walls (Figure 5.2b). Here the velocity gradients below and above the particle are significantly larger, which increases the hydrodynamic drag. The resulting drag force parallel to the walls $F_{drag\,||}$ can be described by multiplying the unconfined drag force $\mathrm{F_{drag}}$, by a confinement factor $\lambda_{||}$ that takes these profile changes into account:[152]

$$F_{drag\,||} = F_{drag,s}\lambda_{||}(z,r,h) \qquad \text{Equation 5.6}$$

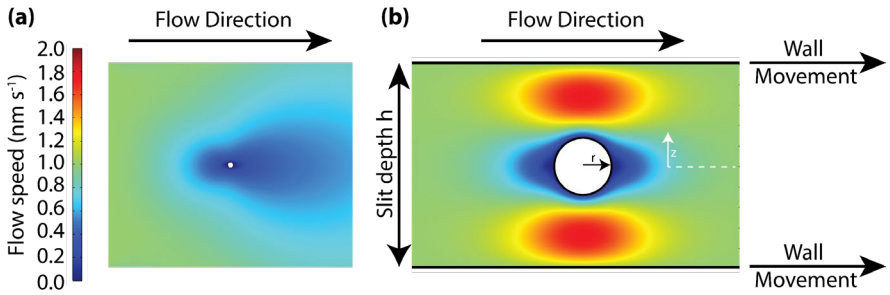

Figure 5.2 (a) Simulated flow profile around a hard sphere with a radius of 7 nm. (b) Simulated flow profile of the same sphere confined within two walls placed at 50 nm from each other. Note that the velocity gradients on top and below the particle are much larger than in (a). This is the reason for the increased drag force in confinement. Simulations were performed using the laminar flow package of COMSOL Multiphysics®. To replicate the relative movement of a diffusing particle with respect to the wall, the walls were set to move at the same speed as the liquid (wall speed = approaching liquid speed = 1 nm s^{-1}).

The confinement factor $\lambda_{||}$ depends on the distance between the walls h, the radius of the sphere r and the position of the sphere in z direction as these factors influence the flow speed profile around the particle (Figure 5.2b). The larger the ratio between the sphere radius and the distance between the walls, the higher $\lambda_{||}$ and the resulting drag force. Moreover, as the sphere approaches the walls, $\lambda_{||}$ and the resulting drag force grow significantly.[153,260]

Similarly, if the particle moves perpendicular to the wall, the flow profile around it will change with respect to free solution. As a result, the particle will experience an increased drag force in this

direction $\mathrm{F_{drag\perp}}$, slowing it down when approaching the wall. The effects of this flow profile change can also be simplified by a perpendicular confinement factor $\lambda_{\perp}$ in this case: [152,260]

$$F_{drag\perp} = F_{drag,s}\lambda_{\perp}(z,r,h) \qquad \text{Equation 5.7}$$

Colloids are affected by hydrodynamic drag as well. Therefore, the diffusion coefficient of a nanoparticle confined in a pore will decrease as a function of pore size. The components of the diffusion coefficient parallel and perpendicular to the pore walls $\mathrm{D_{||}}$ and $\mathrm{D_{\perp}}$ can be described by the following relations:[152]

$$D_{||} = \frac{D_{Free\ Solution}}{\lambda_{||}(z,r,h)} \qquad \text{Equation 5.8}$$

$$D_{\perp} = \frac{D_{Free\ Solution}}{\lambda_{\perp}(z,r,h)} \qquad \text{Equation 5.9}$$

This means that one could use the measured diffusion coefficients in a two-dimensional (2D) single particle tracking experiment to probe the local three-dimensional (3D) pore size. In order to test the feasibility of such an experiment we implemented a slight modification to the 2D model pore system presented in Chapter 4.

In this Chapter, we have varied the etching time of the 2D pores to obtain different pore depths of 50 nm, 100 nm, and 150 nm (Figure 5.3). Further, we have loaded the microfluidic devices with a solution containing PEG-coated CdSe quantum dots (QDs) using the pH conditions at which trapping was found to be suppressed in Chapter 4 (20mM NaOH). By tracking the QDs in two dimensions as they moved in the model pore, we unravelled the presence of clusters in the 100 and 150 nm pores. Surprisingly, after removing the effect of the clusters from the analysis, the measured diffusion coefficients $\mathrm{D_{||}}$ (and trapping behaviour) were virtually the same for all three pore sizes. This strongly contradicted fluid dynamic simulations, where diffusion parallel to the walls was predicted to vary significantly as a function of pore depth.

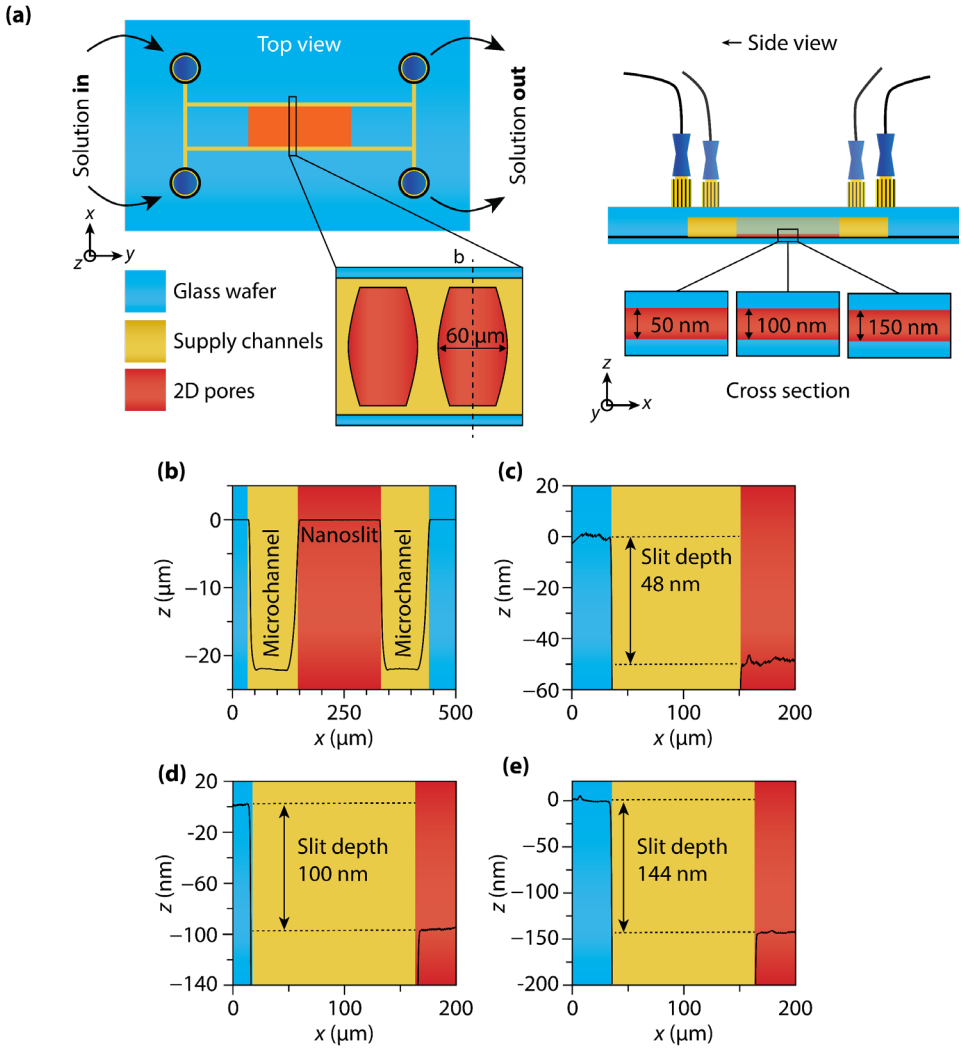

Figure 5.3 (a) Schematic representation of the microfluidic device containing model pores. The top view, side view, and a cross section through a two-dimensional (2D) pore and a supply channel is shown. 2D pores with three different depths were made (50 nm, 100 nm, 150 nm). (b) Profile of the 50 nm-pore microfluidic device measured with a stylus profilometer displaying the supply channels (yellow). The profile is depicted with the dashed line in panel a. (c-e) Zoom of the measured profiles displaying the height difference in z between the lithography-patterned 2D pores and the unexposed part of the wafer, prior to bonding. Panels (c), (d), and (e) correspond to 2D pores with depths of 50 nm, 100 nm, and 150 nm respectively.

5.2 Results and Discussion

Similar to the research work reported in Chapter 4, a large number (>1000 localizations) and also long tracks (> 30 s) were obtained here because the depths of the 2D pores were smaller than the depth of view of the microscope (800 nm). This allowed for the tracked QDs to remain in focus throughout the experiments. Moreover, the out-of-focus signal was very low, as no fluorescent material was present above or below the 2D pores, which resulted in a high signal to noise ratio and facilitated tracking.

The number of QDs in the field of view increased as a function of pore depth (Figure 5.2). If the probe concentration within a pore is constant, larger pores will be able to host more fluorescent probes. Consequently, larger pores will display more localizations over the same time. As described in the previous chapter, the 2D pores were made by wet etching a glass wafer and thermally bonding it to

another one (See Chapter 4). However, the depth of the 2D pores could only be measured before the bonding process (Figure 5.2 b-e). The measured difference in QD localizations, suggests that the pores indeed had different dimensions even after bonding. Surprisingly, the number of localizations does not grow linearly with pore size, which means that the concentration of QDs was not the same in all pore depths. A possible explanation for this could be the formation of QD clusters in the solution. If the clustering process is fast enough, slight differences in the times between solution sonication, loading, and measurement could lead to different concentrations of single QDs.

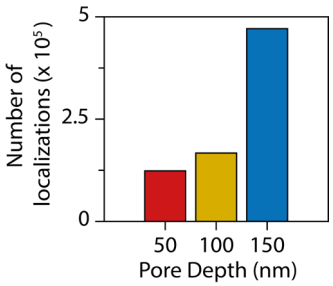

Figure 5.4 Total number of localizations as a function of 2D pore depth. For each pore depth, ten videos of 4000 frames (140 s) were recorded.

We first investigated the presence of clusters via the distribution of diffusion coefficients measured in all three pores (Figure 5.5a). The measured diffusion coefficients in all cases were quite similar. However, as the pore size increased, the number of tracks with diffusion coefficients significantly lower than the median grew (see distribution whiskers Figure 5.5a). Visual inspection of the recorded videos revealed the presence of a few above-average slow and bright particles in both the 100 nm and the 150 nm pores. These were probably large QD clusters that were not be able access the 50 nm pore because of their large size. To confirm this, we plotted the number of localizations of each track against their track length in a scatter plot (see Figure 5.5 b). If all particles were the same, these two track properties should be strongly correlated, i.e., the points should be scattered around a straight line. However, some tracks behaved in a different way (discontinuous line in Figure 5.5b). As the pore size increased, a growing number of outliers was observed, indicating that clusters were indeed present in the solution and that they accessed larger pores more easily. In order to extract a pore size from measured diffusion coefficients, the exploring probe needs to have a homogeneous size distribution. Therefore, we removed tracks that corresponded to clusters from the analysis and filtered out all tracks with a number-of-localizations/track-length-ratio smaller than 3. Ideally, however, in order to perform these experiments in a more straightforward fashion, conditions at which both trapping on the pore walls and nanoparticle clustering do not occur would be found.

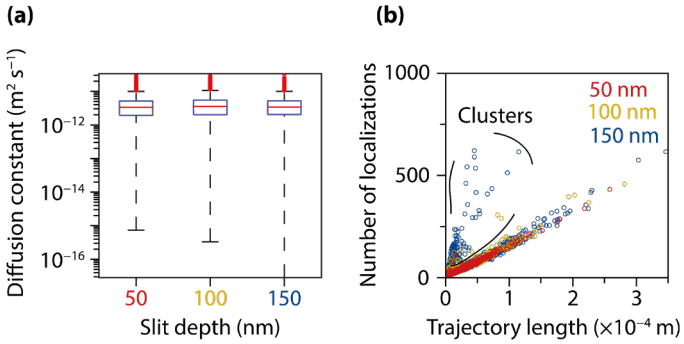

Figure 5.5 (a) Distribution of diffusion coefficients as a function of 2D pore size. The median diffusion coefficients as well as the upper and lower quartile values are almost the same for all three pore depths. The lower end of the distributions is shifted to lower values as the pore depth increases. The

first 25% points of the MSD curve of each track were fitted to determine the individual diffusion coefficients. (b) Comparison of the number of localizations with the trajectory length for all measured tracks. At a constant diffusion coefficient, these two properties should be correlated. That is, the points should be scattered around a straight line, which applies to most tracks. Nevertheless, there are some outliers (QD-clusters) with a high number of localizations, but a low trajectory length, i.e., a much lower diffusion coefficient. Trajectories close to the positions of permanently trapped QDs were removed to avoid linking artefacts as described in Chapter 4.

After filtering out the tracks that belonged to clusters, we observed virtually no differences in terms of diffusion when the 2D pore depth was varied. This is particularly obvious when the histogram of displacements for all tracks after a time delay of one frame is observed (Figure 5.6). At this point we have to conclude from these results that the host-probe-solution system used is not suitable to map local sizes based on locally measured diffusion coefficients, because unexpectedly, the hydrodynamic drag experienced by these QDs does not seem to vary with pore size under these conditions.

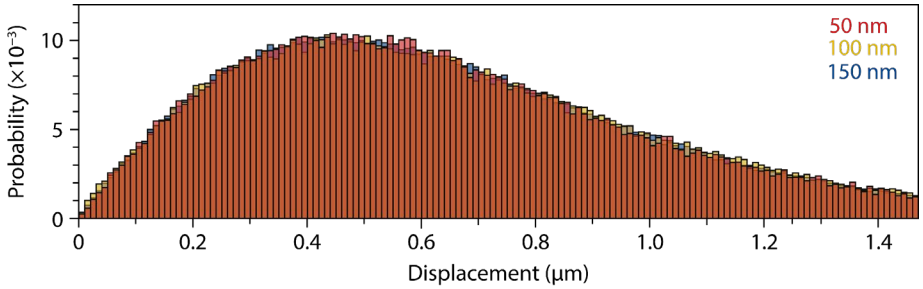

Figure 5.6 The histogram of displacements after a time delay of one frame (35 ms) shows virtually no difference between different 2D pore depths. Trajectories belonging to clusters were removed from this analysis. Trajectories close to the positions of long trap events were removed to avoid linking artefacts as described in Chapter 4.

To double check our experimental results, we performed fluid dynamic simulations with COMSOL Multiphysics® to study the effect of hydrodynamic drag on the diffusion behaviour of the QDs in confinement (Figure 5.2). Therefore, we simulated the QDs as hard spheres with a radius of 7 nm (see also Chapter 4) and we assumed fluid properties (i.e., viscosity and density) based on the experimentally used water glycerol mixture (35wt% glycerol).[247,261] We solved the Navier Stokes equations to determine the velocity profile around the particle in confinement and in free solution. These profiles were then used to determine the total drag force in each case. Since we track our particles only in the direction parallel to the pore walls, the simulations only include flow in this direction (Figure 5.2b).

The resulting confinement drag force was compared to the one obtained by the particle in free solution using Equation 5.7 to determine the confinement coefficient $\lambda_{||}$. This procedure was repeated for different QD positions relative to the pore walls and for different pore depths (Figure 5.7a). Here one can see that for all particle positions, the confinement coefficient $\lambda_{||}$ increases non-linearly as the pore depth decreases. Further, as the particle approaches the wall, a dramatic increase in friction can be observed for all pore depths. In order to determine the reduction of the diffusion coefficient in 2 dimensions (perpendicular to pore depth) we assumed a homogeneous distribution of QDs along the pore depth. Then, we calculated the mean confinement coefficient $\lambda_{||}$ as a function of particle position in z. Here, we excluded $\lambda_{||}(z)$ values where the surface of the particle had a distance to the pore wall smaller than the Debye length of the system (ca. 2 nm).[262] Using Equation 5.8 we computed the expected diffusion coefficient parallel to the pore walls and compared it to the measured values (Figure 5.7b). We estimated a diffusion coefficient in free solution of 1.09×10^{-11} m^2/s based on the

probe radius measured in Chapter 4 (7 nm) and the Stokes-Einstein equation.[263] The lower measured diffusion coefficients in the 2D pores indicate that the QDs were indeed slowed down due to confinement. Further, the measured and simulated diffusion coefficients have the same order of magnitude. However, the continuum model predicts significant differences in terms of diffusion coefficient that could not be observed experimentally. Overall, particles were slowed down when confined in the 2D pores, but notably, in the experiment the hydrodynamic drag does not seem to vary as a function of pore depth in the studied range of 50 nm -150 nm.

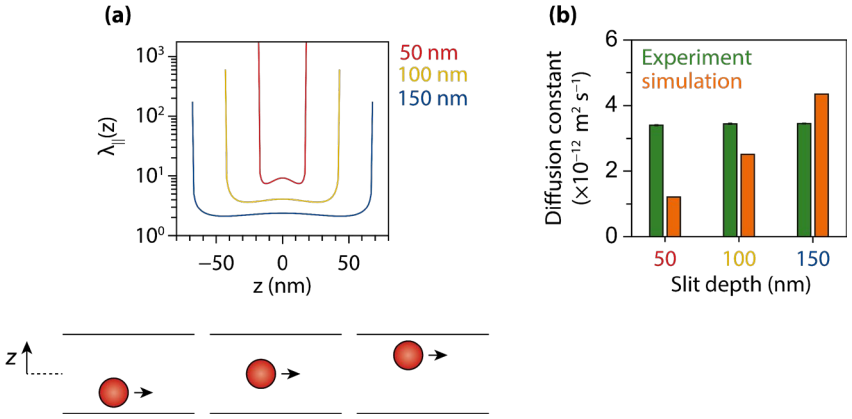

Figure 5.7 (a) Confinement parameter $\lambda_{||}$ for a hard sphere (r = 7 nm) as a function of its z-position within 2 parallel walls placed at different distances. The stronger the confinement, the higher the hydrodynamic drag (confinement parameter $\lambda_{||}$). As the shpere approaches the walls, the hydrodynamic drag increases dramatically. The flow speed used for this simulation was 1 nm/s. (b) Measured and simulated diffusion coefficients assume a homogeneous distribution of particles along the depth of the pore. According to the hydrodynamic drag force simulations, the diffusion coefficients should vary with pore depth. However, the measured diffusion coefficients were not affected by the depth of the pores. The experimental diffusion coefficients were obtained by linear fits to the first 25% of the time-ensemble-average mean squared displacement curve of each dataset.

In order to explore the effect of confinement on particle trapping, we performed a transient trap analysis as described in Chapter 4. Also here, transient trap events were found in all datasets. The duration of the trap events was very similar in all three cases (Figure 5.8). The small differences in terms of trap event frequency and duration could be explained by differences in the roughness of the 2D pores (see section Methods). Overall, trapping events took place in the different 2D pores, however, their frequency and duration does not seem to be affected by the pore depth.

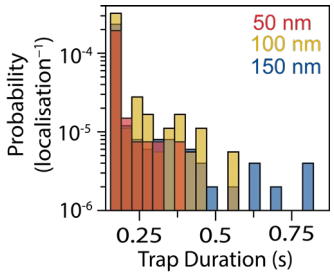

Figure 5.8 Transient trap event duration distribution as a function of pore depth. The histogram is normalised by the total number of localisations in the dataset (Chapter 4). Here, only trajectories displaying mobility in their initial and final localisations were considered to ensure that solely complete trap events were included in the analysis. Trajectories displaying permanent trapping were removed from the analysis (see Chapter 4).

Our results raise the following question: Why is the hydrodynamic drag (and motion behaviour) unaffected by the 2D pore depth? It is possible that one of the two wafers bent while they were thermally bonded together (Chapter 4). This could result in deeper pores and reduced hydrodynamic drag. However, the QDs were never out of focus throughout experiments, which means that the depth of 2D pores cannot be larger than depth of view of the objective (800 nm). Even at this probe-pore-size ratio COMSOL simulations already show increased drag force effects compared to free solution (10 % difference). Furthermore, the differences in the number of localizations (Figure 5.4) as well as the accessibility of QD clusters (Figure 5.5) indicates that the 2D pore sizes display significant differences. On the other hand, a study by Tas et al. suggests that the viscosity of aqueous solutions can change in confinement. However, one would expect viscosity to decrease as a function of pore size and not the other way around. Moreover, these visco-electric effects are minimized when the ionic strength of the system is increased.[264] Due to the ionic strength used in this experiment (20 mM), it is unlikely that this phenomenon can explain our results. Other studies have shown that confinement could lead to a microphase separation in aqueous liquid mixtures (e.g., waster and ethanol).[265] Arguably this could lead to a reduced viscosity/drag force with respect to the one predicted by the continuum model. However, this has been observed at the lower end of the mesopore scale (2.4 nm).[265] It is therefore unlikely that this phenomenon is taking place at the length scales discussed here.

In Chapter 4, we measured a 7.5% diffusion coefficient difference when the pH of the system was changed. This could be due to a change in trap behaviour and/or to a small difference in probe size under different pH conditions. The probe-pore-size ratios measured ($\frac{\text{diameter}_{\text{QD}}}{\text{depth}_{\text{pore}}} = 0.15$; 0.17) could explain the difference in diffusion coefficient when drag forces are taken into account (Chapter 4).[242] However, in this Chapter, the difference in probe-pore-size ratio was significantly higher ($\frac{\text{diamter}_{\text{QD}}}{\text{depth}_{\text{pore}}} =$ 0.05; 0.15) and it did not alter diffusion. Notably, in this probe-host-solvent system, the diffusion coefficient seems to be more strongly correlated with the trapping event duration (i.e., the QDs affinity to the surface) than with the probe-pore-size ratio. This suggests that diffusion within the 2D pore is dominated by the probe-host-electrostatic interactions (trapping events) rather than the hydrodynamic drag. In order explore this further, it is necessary to perform experiments under different conditions: 1) Varying the probe-pore-size ratio. 2) Varying pH to change the charge of the walls and probes. 3) Varying the ionic strength of the system to see the effects of the electric double layer. 4) Functionalizing both probes and pore walls to tune the interactions. Finally, more complex simulations should be performed to better understand experimental results. Therein, detailed electrostatic interactions as well as colloid elasticity (CdSe-PEG QDs have a soft shell) and rotational movement should be included.

5.3 Conclusions

In this Chapter, we successfully performed single particle tracking experiments within a 2D model pore with different depths. The number of localizations found within each pore as well as the 2D pore characterization confirmed that the 2D pore depths were different. We unravelled the presence of clusters in the larger pores and removed them from the analysis. The cluster-free trajectories displayed virtually the same diffusion coefficients and transient trap event durations for all studied pore depths. This contradicts hydrodynamic drag simulations, where the diffusion coefficient was predicted to grow with the 2D pore depth. The reason for this lack of friction effects remains unclear and should be investigated further. Nevertheless, based on our results, we can conclude that this probe-host-solvent system is not suitable to determine pore sizes between 50 nm and 150 nm based on the measured diffusion coefficient.

5.4 Materials and Methods

This Chapter builds on the previous one, further details on the experiments as well as the analysis can be found there. Furthermore, CdSe/ZnS core–shell quantum dots (QDs) with polyethylene-glycol functionalization (900246-250UL, Sigma-Aldrich), glycerol (≥ 99.5%, Sigma-Aldrich), 170 µm and 500 µm thick MEMpax wafers (Schott), sodium chloride (≥ 99%, Sigma-Aldrich), sodium hydroxide (analysis grade, Merck KGaA) were used. All chemicals were used as received with no further purification except water, which in all cases was purified through a Milli-Q system to a resistivity of 18.2 MΩ·cm.

5.4.1 Atomic Force Microscopy

The surface roughness was mapped with atomic force microscopy (Dimension FastScan, Bruker) on 500x500 nm^2 squares within the etched 2D pores prior to bonding Figure 5.9. The root-mean-square surface roughnesses measured were 5.4 nm 4.7 nm and 3.4 nm for the 50 nm, 100 nm and the 150 nm pores respectively.

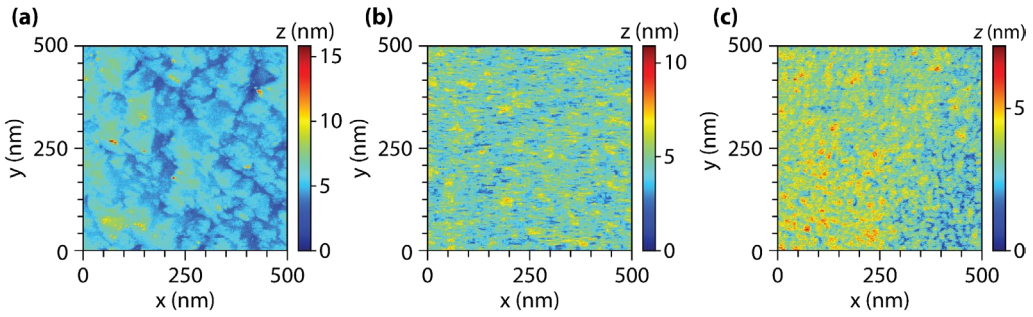

Figure 5.9 Surface roughness of the etched 2D pores as measured with atomic force microscopy (AFM). Pore Depth: (a) 50 nm, (b) 100 nm (c) 150 nm.

5.4.2 Hydrodynamic Drag Simulations

We solved the Navier-Stokes equations (Chapter 2) using the laminar flow module of the COMSOL Multiphysics software to determine the flow profile around an unconfined particle and a particle confined between two walls (Figure 5.2). To replicate the relative movement of a diffusing particle with respect to the wall, the walls were set to move at the same speed as the liquid. The particles were simulated as hard spheres with a diameter of 14 nm and the system was simplified to be two-dimensional. We integrated the total shear stress in the direction of the flow (parallel to the walls) over the surface of the particle to obtain the hydrodynamic drag force acting in this direction. By dividing the confined hydrodynamic force in confinement by its unconfined counterpart, we obtained the confinement parameter $\lambda_{||}$. This procedure was repeated placing the particle at different positions relative to the walls to obtain $\lambda_{||}(z)$ Figure 5.7a. Assuming a homogeneous distribution of QDs along the depth of the 2D pore, we used the mean confinement coefficient as a function of z to estimate the resulting diffusion coefficient in confinement (Equation 5.8). The simulations were repeated using different approaching velocities (1, 10 and 100 nm/s). The results remained unaffected by this variation.

5.4.3 Fluorescence Microscopy

Single-particle tracking experiments were performed on a home-built fluorescence microscope. This setup consisted of a Nikon Ti–U inverted microscope equipped with an oil-immersion objective (Nikon CFI Plan Apochromat Lambda 100×, NA 1.45). The excitation light source was a 405 nm (PicoQuant D-C-405) operated in continuous wave and focused on the back focal plane of the objective with a 150 mm achromat lens. The laser was used in conjunction with appropriate dichroic and long-pass mirrors as well as a 585/40 nm band-pass filter to remove background from the fluorescence emission signal.

The filtered emission signal was collected with an electron-multiplying charge-coupled device detector (EMCCD; Andor iXon Ultra 888) operated at a gain of 300, exposure time of 30 ms, and frame time of 35 ms.

6 Carbon Dots as Super Resolution Microscopy Probes for Pore Space Characterization

As demonstrated in Chapter 4, tracking individual probes as they move within porous materials can be used to map their pore space with resolutions in the order of tens of nanometers. However, to map pores at the mesoscale level, smaller probes are required. In this Chapter, we investigate the use of carbon dots for pore space characterization via single-particle tracking. Tracing individual carbon dots in a high viscosity medium allowed for determining their size distribution. Additionally, loading the carbon dots into our 2D pores led to the observation of individual trapping events, but carbon dot movement was too fast to be tracked. Nevertheless, carbon dots were successfully tracked within mesoporous silica particles, which were not accessible for the larger quantum-dot probes previously employed in this PhD Thesis. Furthermore, different trap event durations were observed on unconfined surfaces with varying compositions, indicating the potential use of this trajectory property to probe composition with sub-diffraction-limit resolution. Finally, staining experiments followed by confocal laser scanning fluorescence microscopy imaging suggested that the silica surface affinity of carbon dots could be adjusted via the pH, reducing trapping, and potentially improving pore space mapping.

6.1 Introduction

Carbon dots (CDs) were accidentally discovered by Xu et al. in 2004 as a byproduct of carbon nanotube purification and were shown to be bright fluorophores, photostable, economical, non-toxic, and easy to synthesize [266,267]. The origin of the photo-luminescent (PL) properties of CDs remains a topic of ongoing debate in the literature[268–270]. Recent studies have shown that fluorophores such as citrazinic acid can be formed during the synthesis of CDs, suggesting that their fluorescence emission mainly originates from embedded fluorophores in the CD-carbon matrix[271,272]. Due to their environment-dependent photoluminescence properties, CDs have been utilized as chemo-sensors to detect metal ions in various solvents and to get information about the local pH within biological systems.[273–275] Their use to characterize porous solids, on the other hand, has not been explored thoroughly.[107] The combination of their bright fluorescence and small size makes carbon dots promising probes for single-particle-tracking-based pore space characterization. Individual carbon dots have been successfully localized with single molecule(particle) localization microscopy (SMLM) on dried coverslips.[273,276–279] However, to the best of our knowledge, their application in exploring porous solids with single particle tracking (SPT) has not yet been investigated.

In this Chapter, we investigated the potential of carbon dots as SMLM probes to study porous materials. We synthesized CDs containing embedded resorufin with improved brightness and trackability. As a result, we successfully tracked individual CD in a high viscosity medium for the first time. Contrary to dynamic light scattering and electron microscopy, SPT allowed us to determine the probe size distribution. When loaded in the 2D model pore system (see Chapters 4 and 5), we were not able to track the CD, but individual trapping events could be observed. Further, the CDs displayed different trapping event durations on surfaces with different compositions, indicating that this property can be used to probe different types of surfaces. Finally, confocal laser scanning fluorescence microscopy staining experiments, suggested that the CDs' affinity to silica can be tuned via the pH.

6.2 Results and Discussion

Figure 6.1a shows the UV-Vis absorbance spectra of CDs with and without embedded resorufin. Notably, both spectra exhibit a peak around 531 and are similar in appearance. However, an extra absorbance peak was observed for the sample with embedded resorufin at 571 nm. This corresponds to the wavelength at which resorufin shows the highest absorption.[280] This is a strong indication that resorufin was indeed embedded in the sample, as non-embedded molecular resorufin would have been filtered out by the dialysis process due to its small size of 0.7 nm (see Methods).[281]

We measured the fluorescence intensity at varying wavelengths (Figure 6.1b) and observed peaks in the blue-green region that shifted in position at different wavelengths. Carbon dots commonly show such an excitation dependent emission because they are embedded with different fluorophores that emit and are excited at different wavelengths.[271,272,282] On one hand, the group of peaks around 460 nm have been previously assigned to fluorophores with single aromatic rings such as citrazinic acid or similar molecules. [271,272,283] On the other hand, the group of peaks around 550 nm have been attributed to fluorophores with two or more aromatic rings.[283] Additionally, we observed a dominant luminescence peak at 583 nm that did not vary with the excitation wavelength, indicating its origin to be a single fluorophore. This wavelength corresponds to the emission wavelength of resorufin, which shows again that we successfully embedded it in the carbon dots. In order to avoid saturating the detector, its gain had to be reduced when exciting with wavelengths greater than 500 nm. The difference between the CD peaks (400-550 nm) and the resorufin peak is much higher than depicted in Figure 6.1b. Overall, embedding resorufin strongly increased the fluorescence intensity of the CDs.

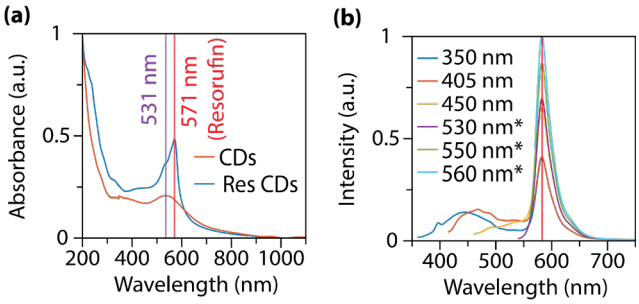

Figure 6.1 (a) UV-Vis spectrum of carbon dots with and without embedded resorufin. Both spectra are similar and display a peak at 531 nm. However, the carbon dots containing resorufin show a further peak at 571 nm. This value corresponds to the excitation wavelength of resorufin. (b) Photoluminescence spectrum of the carbon dots with embedded resorufin. The sample shows an excitation dependent emission in the blue-green part of the spectrum, that is characteristic of carbon dots. [282,284] Additionally, the spectrum displays a dominant luminescence peak at 583 nm that does not shift with the wavelength. This value corresponds to the emission of resorufin. (*) The gain of the detector needed to be lowered to avoid saturation. Therefore, the difference between the carbon dot peaks and the resorufin one is higher than depicted here.

HRTEM images of the CD samples were collected with the aim of measuring the CD size. Nevertheless, this proved impossible as QDs clustered together during the drying process (see section Methods). Next, we attempted to measure the size of the CD with dynamic light scattering (DLS), which also proved extremely challenging. There are two possible reasons for this: 1) The SNR was too low because the fluorescent light emitted by the CDs interfered with the signal of the scattered light. 2) We observed that the CDs show aggregation at the concentrations required for DLS and this technique works best with a uniform particle size distribution.[285]

Since HRTEM and DLS were did not yield reliable results, we attempted to use single particle tracking to determine the CD size. By tuning the viscosity, refractive index, and CD concentration, we were able to track individual carbon dots as they moved in free solution (see Methods and Figure 6.2a). We then calculated the mean squared displacement (MSD) as a function of time for each track and determined their diffusion coefficient. Finally, we used the distribution of diffusion coefficients to compute the particle size distribution with the Stokes-Einstein equation (see Chapter 4). The mode of the diameter distribution was around 2 nm. This small probe size represents a huge advantage compared to the 14 nm CdSe-PEG QDs used in Chapters 4 and 5, as these CDs would be able to explore much smaller pores. However, some larger particles (15-45 nm), possibly CD-clusters, were also detected in the experiment, which could lead to misinterpretations of pore space exploration experiments. Therefore, the presence of these particles should be avoided either by either filtering them out, preventing clustering, or by tuning the synthesis method. Due to their aggregation behavior and luminescence properties, determining the size distribution of CD samples can be challenging. Interestingly, single particle tracking proved to be a suitable method to study this.

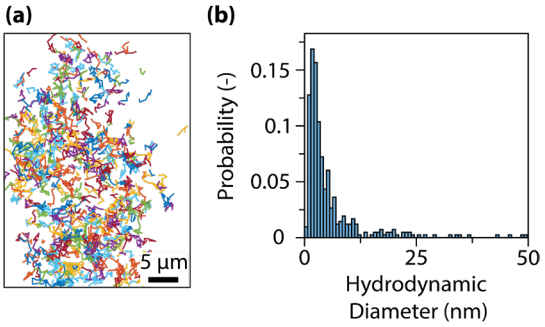

Figure 6.2 (a) Overlay of carbon dot (CD)-tracks obtained over 17.5 s in a (15/85 m/m) water/glycerol mixture. (b) Particle size distribution calculated based on the individual diffusion coefficients using the Stokes-Einstein equation. The individual diffusion coefficients were obtained by performing a linear fit on the first 4 points of the MSD(t) curve of each track.

After demonstrating the potential of CD as SPT-probes, we loaded them into our 2D model pore (see Chapters 4 and 5). The pressure needed to load the microfluidic devices increases strongly with the viscosity of the liquid. Therefore, in order to be able to load the chips, the glycerol content of the solution needed to be reduced to 50 wt.%. Due to the resulting decrease in viscosity, the diffusion of the CDs was too fast, and we could not track them as they moved. Interestingly, individual point spread functions (PSF) appearing and disappearing over time could be observed. We believe that these belong to transient trapping events (adsorption and immobilization due to hydrodynamic drag cannot be discriminated with this experiment, we refer to both as 'trapping event'). The CDs move fast compared to the acquisition time of the camera, which results in motion blur and renders tracking impossible. However, when the CDs are trapped at the pore walls, motion blur does not take place and the particles can be easily identified and localized. We performed experiments using two different pore depths, 50 nm, and 100 nm (Chapters 4 and 6). Since all the localizations belonged to trapped particles, we used the number of localizations over time to study how the pore size affected amount of trapping events over time (Figure 6.3a). The values were relatively stable over time indicating either no probe photobleaching or an equilibrium between photobleaching and probe replenishment through diffusion into the field of view. The 100 nm channels showed a slightly higher number of localizations over time than the 50 nm ones. At a constant probe concentration, more probes will be present in larger (i.e., deeper) pores. Consequently, if more probes are present in the pore and they frequently collide with the walls, more of them will get trapped over time. This result is in line with the number of localized CdSe-PEG quantum dots as a function of pore size shown in Chapter 5 and it further demonstrates that the different 2D pores have indeed varying pore depths. We further evaluated the duration of the individual trapping events (Figure 6.3b). Similar to the results of Chapter 4, the distribution of trap event duration was almost the same for both pore depths, proving that this property cannot be used to probe pore size.

Overall, the CDs could enter the 50 nm 2D pores, but the viscosity was too low to slow them down enough to be individually traced. Therefore, we attempted to track them within porous silica particles with a uniform pore size of 50 nm (see Chapter 3) using a higher viscosity liquid (see section Methods). Unlike the larger probes used in Chapters 4 and 5, individual CDs could be observed within these porous particles, showing the potential of these small CD to map pores at the mesoscale (Figure 6.3c). However, the concentration of CDs was too low to map the pore space and most of the fluorophores were fully trapped on the pore walls. Finding conditions at which the trapping behavior of this probe-host-solvent is reduced are required to reliably map the pore space without the presence of "blind spots" (see approach as presented in Chapter 4).

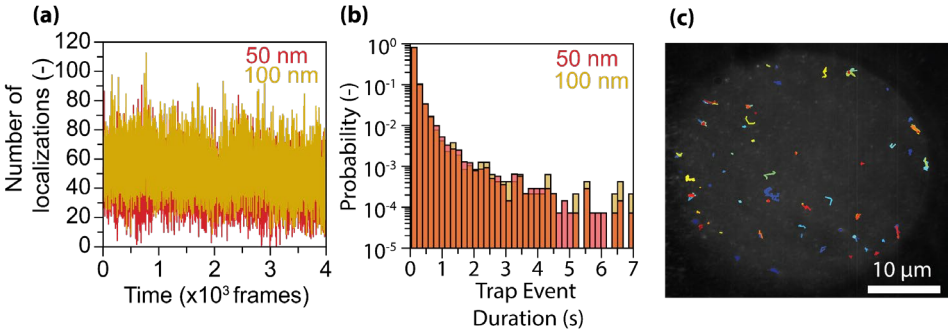

Figure 6.3 (a) Number of carbon dot (CD) localizations within 2D pores as a function of time. Each localization corresponds to a trapped CD on the pore walls. (b) The histogram of the trapping event duration shows virtually no difference as a function of pore depth. Tracks obtained within a porous silica particle with a uniform pore size distribution (d_{pore} = 50 nm). The CDs were slowed down using a water/glycerol solution (15/85 m/m).

Figure 6.3a and Chapter 5 report an increasing number of localizations as pore size increases. This indicates that pore size could be probed using this parameter. However, these results were obtained on model systems with the same composition and accessibility as well as similar roughnesses (Chapter 5). In Chapter 4, we showed that the frequency of adsorption events also depends on the probe-wall electrostatic interactions. That is, probes that have a higher affinity to a surface, will not only show longer trap event durations, but also a higher frequency of trap events. If one desires to examine pore sizes on a catalyst by looking at trap event frequency, it becomes problematic because catalysts are complex and heterogeneous in terms of connectivity, pore size, and pore accessibility and all these parameters would affect the frequency of trapping events.

On the other hand, the duration of transient trapping events did not vary with pore size (Figure 6.3b), but it did change as a function of the probe-host electrostatic interactions (Chapter 5). Potentially, if the composition of the host is changed, it will interact differently with the fluorophores, and this will result in differences in trapping event duration. In order to test this hypothesis, we put a CD solution in contact with a silica and a silica/alumina (50-50) surface and imaged the fluorescence at the liquid-solid interface (see Methods). Again, we were able to observe transient trapping events on both surfaces. However, their frequency and duration were higher on the alumina-containing surface (Figure 6.4a), suggesting that the CDs have a higher affinity towards it. Based on these results one can conclude that the duration of trapping events could be used to probe the composition of porous materials with sub-diffraction limit resolution. Nevertheless, it should be noted that the surface roughness of the two different surfaces used here could vary and affect our results. Ideally, metal oxide thin films should be sputtered on coverslips with the same roughness to ensure that the results we observe are indeed a result of the composition. Further, silica surfaces of different roughnesses (e.g., made by etching coverslips with different methods) should be compared to test whether trapping event duration is affected by this property as well. Finally, we envision experiments in which lithography patterned surfaces with different properties (composition, roughness, functional groups) are put in contact with fluorophores and where the trapping event duration accurately creates a 2D composition map. The obtained knowledge could then be used to map the composition of heterogeneous porous materials with sub-diffraction-limit resolution.

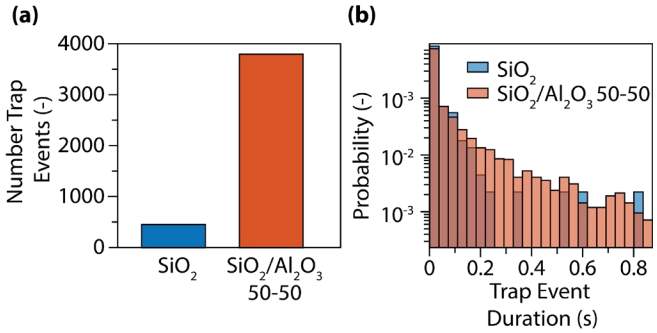

Figure 6.4 (a) Number of carbon dot (CD) transient trap events recorded over 400 frames (frame time: 35 ms) on surfaces with different compositions (Silica and Silica/Alumina 50-50). (b) Histogram of trapping event durations on the two surface types. On average, the trapping events are longer on the Silica/Alumina 50-50 surface. The liquid phase consisted of pure water.

6.2.1 Tuning Probe-Host Electrostatic Interactions via pH

In order to test the pH dependency of the trapping behavior CDs on silica pores, we stained porous silica particles with a uniform pore size of 35 nm (Chapter 3) at different conditions (acidic, basic, neutral) and imaged them with confocal laser scanning fluorescence microscopy (CLSM) (Figure 6.5a). In all cases, we observed an increase in intensity inside the particle with respect to a blank measurement, suggesting that the resorufin-CDs were able to access the mesopores of the particles. The different conditions changed the luminescence properties of the CDs (Figure 6.5b). The fluorescence of resorufin has been shown to display a similar pH dependency[286], suggesting that the embedded resorufin is responsible for this effect. In order to quantify the amount of CD trapped on the particles' surfaces taking into account the pH dependency of the fluorescence, we determined the fluorescence intensity between 500 nm and 550 nm within each particle and subtracted the background intensity from it. If this intensity difference is positive, it suggests that the CD concentration inside the particle is considerably higher than outside. The concentration in the liquid phase of the pores is unlikely to be higher than in the bulk solution. This is why high positive values suggest trapping on the pore walls. On the other hand, intensity difference values close to 0 mean that the concentrations within and without the particle are similar, indicating decreased trapping. If trapping is entirely prevented, the fluorescence of the particle would originate only from fluorophores in the liquid phase within its pores. As a result, the intensity of the particle would be lower than the background (negative intensity difference). One should note that scattering effects could result in increased intensities within the particle and lead to misinterpretations of the results. In order to prevent this, we used homogeneous porous silica spheres with a uniform pore size distribution (see Chapter 3). However, these experiments should be ideally repeated using a solution that is better refractive index matched with silica.

At pH=4, we expect the silica walls to be negatively charged.[232] The CDs, on the other hand, could be close to or below their point of zero charge under these conditions. Due to relatively low repulsive (or even attractive) probe-wall electrostatic interactions at this pH, the CDs show a significant affinity to the pore walls. At neutral conditions, both silica and CDs are negatively charged (a negative zeta potential was measured at this pH for the CDs) and the difference in charge density is reduced, causing less probe-wall repulsion. Consequently, the measured intensity difference is lower than at pH=4. Finally, at pH=10, both silica and CDs are even more negatively charged, and repulsion is increased. As a consequence, CD trapping on the pore walls is further reduced, which is signified by a slightly negative intensity difference. These results suggest that the affinity to silica of the CDs can be tuned via the pH of the system as shown with Rhodamine 110 and CdSe-PEG quantum dots in Chapters 3 and 4 respectively. One should note, however, that the solubility of silica is strongly increased at pH

values above 9, which potentially influences our results.[251] Therefore, this experiment should be repeated under milder basic conditions. If successful, these mild basic pH conditions should be investigated with SMLM within the 2D model pores in order to check if the measured trap event durations decrease indeed. Conveniently, CDs proved to have the highest fluorescent signal in basic conditions which would facilitate tracking (Figure 6.5b).

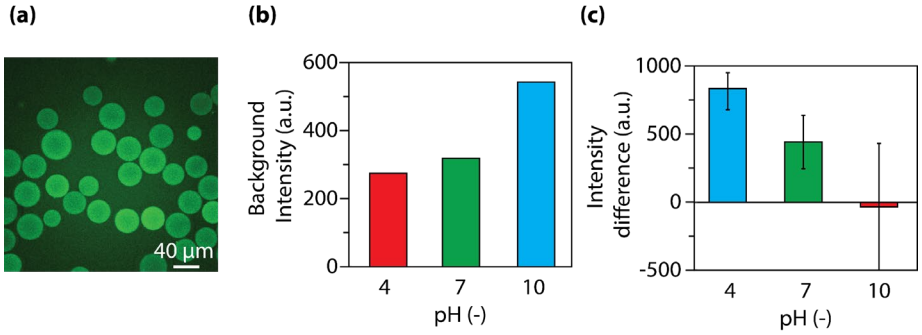

Figure 6.5 Confocal laser scanning fluorescence microscopy image of porous silica particles (pore diameter: 35 nm) stained with carbon dots (pH = 4). Mean background intensity values at different pH conditions. As pH increases the carbon dots display an increased fluorescence. Mean intensity of all particles subtracted by the background intensity. As the pH increases, the concentration of fluorophores within the particle decreases, most likely indicating a reduction in trapping events. The error bars represent the standard deviation of the mean intensity measured in all particles. The intensity values of (b) and (c) correspond to the signal collected between 500 nm and 550 nm.

6.3 Conclusions

Carbon dots embedded with resorufin were synthesized and characterized. Their improved fluorescence due to the embedded resorufin allowed us to track them individually in a high viscosity medium and calculate their size distribution. The relatively small median probe diameter of 2 nm made it impossible for us to track them within our 2D model pore. However, transient trap events could be observed, and their duration did not vary as a function of pore size. Unlike the SPT probes used in Chapters 4 and 5, carbon dots were able to access and explore mesoporous silica particles. Further, we demonstrated that CDs could be used to probe different materials, as they displayed different trapping event durations on surfaces with different compositions. Finally, confocal laser scanning microscopy staining experiments suggest that the CD affinity to silica is reduced as the pH increases, potentially preventing trapping, and allowing for pore space mapping in the mesoscale.

6.4 Materials and Methods

6.4.1 Materials

Citric acid (≥ 99.5%, Sigma-Aldrich), DMM silica (PQ Corporation), glycerol (≥ 99.5%, Sigma-Aldrich), 170 µm and 500 µm thick MEMpax wafers (Schott), resazurin sodium salt (~80%, Sigma-Aldrich), sodium chloride (≥ 99%, Sigma-Aldrich), sodium hydroxide (analysis grade, Merck KGaA), and urea (≥ 99%, Sigma-Aldrich) Buffers. All chemicals were used as received with no further purification except water, which in all cases was purified through a Milli-Q system to a resistivity of 18.2 MΩ·cm.

6.4.2 Synthesis

The synthesis of the CDs was conducted via an adaptation of the protocol by Strauss et al.[287] Carboxylic acid (CA) monohydrate and urea was added to a vial in a 1:2 ratio (w/w). Resazurin dye was added in the same ratio as CA, this molecule is reduced to the fluorescent resorufin due to the presence of urea. The vial was placed in an aluminum reaction block on top of a hot plate and a magnetic stirrer

was used for mixing. The hot plate was programmed to heat up to 250° C, at which the temperature was kept for 15 minutes. Once the sample was cooled down to room temperature, it was dissolved in water. The sample was subsequently filtered through a 0.2 µm PFTE filter and poured into a dialysis membrane (high retention seamless cellulose tubing (MWCO 12.4kDa, Sigma-Aldrich). Dialysis was performed for one week. The dialysate was disposed of and replaced with fresh deionized water on a daily basis. Before disposal, the luminescence of the dialysate was checked with a 405 nm laser pointer (5 mW). After a week, no luminescence could be detected in the dialysate, ensuring that small molecules, such as individual fluorophores or reactants were filtered out.

6.4.3 Carbon Dot Characterization

a. Fluorescence Spectroscopy

Photoluminescence emission spectra were recorded with a Jasco spectrofluorometer (FP 8300) at 200 nm/min. Emission spectra were gathered using varying excitation wavelengths between 350 and 600 nm, while emission intensity values were collected at wavelengths 10 nm above the excitation wavelength up until 750 nm.

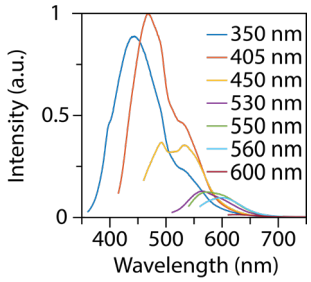

Figure 6.6 b) Photoluminescence spectrum of the carbon dots with embedded resorufin. The sample shows an excitation dependent, that is characteristic of carbon dots. [282,284] Unlike the resorufin-embedded carbon dots, this sample did not show an excitation independent peak. The Carbon dot emission peaks are significantly lower than the one of embedded resorufin shown in Figure 6.1b.

b. Quantum Yield

The absorbance and the fluorescence were measured at varying concentrations to estimate the quantum yield (QD) using the following formula:[288]

$$\Phi_s = \Phi_{ref}\left(\frac{slope_s}{slope_{ref}}\right)\left(\frac{\eta_s}{\eta_{ref}}\right)^2 \quad \text{Equation 6.1}$$

Here, Φ_s and Φ_{ref} denote the relative QY of the sample and reference fluorophore respectively. $slope_s$ and $slope_{ref}$ represent the slope of the fluorescence as a function of the absorbance. Lastly, η is the refractive index. Rhodamine B was chosen as a reference sample as it has been well studied and has a similar excitation and emission region, ensuring a good relative QY calculation. The regression line for the rhodamine B was obtained by averaging the absorbance for 550-555 nm and plotting the result against the fluorescence averaged over 570-575 nm for 4 samples with varying concentrations.

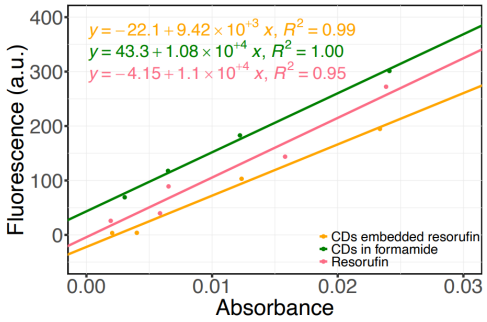

Figure 6.7 Absorbance *versus* fluorescence at different concentrations of resorufin, rhodamine B and carbon dots.

Sample	Maximum Excitation Wavelength (nm)	Quantum Yield (-)
Rhodamine B	554*	0.31
Carbon Dots	560	0.175
Resorufin	560	0.204

Interestingly, the determined quantum yield of the CDs is (0.175) is lower than the one of pure resorufin. Probably, the light emitted from the embedded resorufin interacts with the surrounding CD carbon structures getting partially absorbed.[289]

c. UV-Vis absorption spectroscopy

The UV-Vis absorption spectrum of the CD solution was recorded at room temperature using a UV-Vis CARY 200 spectrophotometer.

d. High-Resolution Transmission Electron Microscopy

High-Resolution Transmission Electron Microscopy (HRTEM) images of CD samples were collected with a TALOS F200x Transmission Electron Microscope (Figure 6.8). Samples were prepared by pipetting 5 µl sample on a TEM grid (formvar on 3mm, 300 mesh Cu grid) and leaving the sample to dry under a clean glass beaker. Thereafter, the grid containing the sample was placed in the sample holder and imaged at 390kx magnification.

The drying process resulted in the formation of large CD clusters (Figure 6.8a), which prevented us from determining the probe size distribution. Interestingly, small crystalline domains could be observed within the clusters (Figure 6.8b,c). We investigated the grayscale profile of a crystalline domain (green line in Figure 6.8c) and obtained a d-spacing of 3.18 ± 0.16 A˚. A similar lattice spacing for CDs was observed by Liu et al. (2014).[290] This value is comparable to the (002) lattice plane of graphite 3.36 A˚.[291]

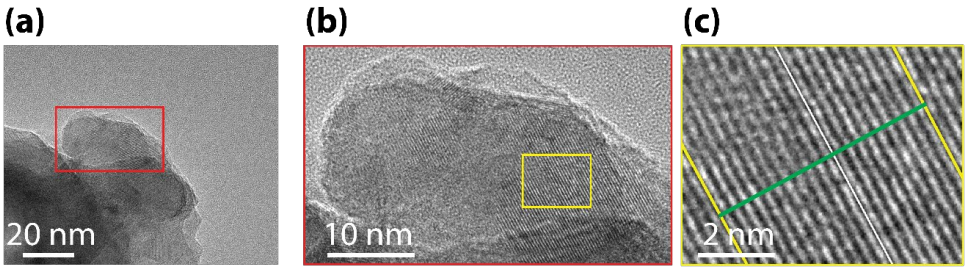

Figure 6.8 (a) High-resolution transmission electron microscopy (HRTEM) image (390 kx zoom) of CDs with embedded resorufin, clustering observable. (b) Zoomed-in image of (a) showing different crystalline domains. (c) Zoomed-in image of b) showing clear lattice fringes and the profile line (green) used to determine the d-spacing.

6.4.4 Single Molecule Localization Microscopy

Single particle tracking experiments were performed on a home-built fluorescence microscope. This setup consisted of a Nikon Ti–U inverted microscope equipped with an oil-immersion objective (Nikon CFI Plan Apochromat Lambda 100×, NA 1.45). The excitation light source was a 561 nm diode laser (PicoQuant LDH-D-TA-560B) operated in continuous wave and focused on the back focal plane of the objective with a 150 mm achromat lens. The 561 nm laser side bands were removed with a clean-up band-pass filter, and the light was led through a linear polarizer followed by a lambda ¼ plate to obtain circularly polarized light through the objective. The laser was used in conjunction with appropriate dichroic and long-pass mirrors as well as a 585/40 nm band-pass filter to remove background from the fluorescence emission signal. The filtered emission signal was collected with an electron-multiplying charge-coupled device detector (EMCCD; Andor iXon Ultra 888) operated at a gain of 300, exposure time of 30 ms, and frame time of 35 ms.

a. Carbon Dot Tracking in Free Solution

We place a Thermo Scientific™ 25 µl Gene Frame (AB0576) on top of a plasma cleaned coverslip. Meanwhile, the CDs were sonicated for 25 minutes to avoid aggregates. Then, the CDs were diluted 100x using glycerol/water 85/15 m/m solution and pipetted into the Gene Frame. We closed the Gene Frame using a provided coverslip and placed the sample inside of the sample holder of the microscope. The use of the glycerol/water 85/15 m/m was crucial to slow the CD down to the point in which they could be localized. Further, it provided a better refractive index matching between the coverslip and the liquid and therefore increased the signal to noise ratio. The data was analyzed using DoM plugin of ImageJ (see Chapter 4).[128] The MSD analysis on individual trajectories was done including the first four points of the delay times. All trajectories containing 4 points or less were removed from the analysis.

b. Transient Trap Event Duration Analysis

Unlike the fluorophores of Chapters 4 and 5, in this work the CDs could not be tracked using a 1/1 m/m water/glycerol solution (or lower glycerol contents). Therefore, we only observed transient trap events on both the 2D pore and the unconfined silica and silica/alumina surfaces. Therefore, the transient trap event analysis was done in a different way that is not limited by the size of the sliding window used (Chapter 4). We used the DoM ImageJ plugin to localize the particles at each frame.[128] Then, we tracked them using a pixel jump of 1 pixel and a blinking gap of 2 frames. Since all recorded

tracks were immobile, the difference between the first and last localization frame of each track was used to measure the trap event duration. Further, each localization corresponds to a trapped particle. Therefore, the number of localizations in each frame represents the number of trapped particles at a given time and the total number of tracks corresponds to the number of trap events registered.

6.4.5 Silica and Aluminosilicate Surface Synthesis

To prepare the silica thin film, a solution of TEOS (tetraethyl orthosilicate) in ethanol (1:9 vol%) was dropcasted on glass coverslip and dried with air at room temperature. Next, the coverslip was calcined at 400 ^{o}C for 4 h.

To prepare the aluminosilicate thin film a solution of aluminum nitrate and TEOS in ethanol with desired ratio is prepared. After dropcasting, the film was dried with air at room temperature and then calcined at 400 ^{o}C for 4 h.

The dropcasted volume was 0.1 mL in both cases.

6.4.6 Confocal Laser Scanning Fluorescence Microscopy

Microscope slides were prepared by first applying a Thermo Scientific^{TM} 25 µl Gene Frame (AB0576) on a thin objective glass. Then, a small amount of porous silica spheres (∼20 µm diameter, pore size ∼35 nm) were added inside the Gene Frame. Before adding the carbon dots, 18 µl of a buffered solution was added to the Gene Frame. The reason for this was to wet the particles and prevent the carbon dots from being forced into the particles by capillary forces. Finally, 4 µl of a carbon dot containing solution were added and the Gene Frame was sealed. The samples were left to equilibrate for 2 weeks before the concentration of the CDs was studied. The intensity values within the particles were compared to blanks (i.e., same solution with no CDs). In all cases the measured intensities were higher when CDs were present in the system, suggesting that the CDs were able to enter the pores of the silica particles.

7 Summary and Outlook

7.1 Summary

Mass transport is a crucial aspect in heterogeneous catalysis as it can influence activity, selectivity, and the overall lifespan of a catalyst material. Therefore, rational pore space design, synthesis and control have immense potential for further improving catalytic performance in existing solid catalysts and also for making new porous catalyst materials. In order to investigate how the synthesis parameters affect the catalyst materials pore networks, high-resolution and high-throughput porosity characterization techniques are required. However, the currently available characterization techniques face some challenges. On one hand, several techniques rely on bulk analytical measurements, ignoring the heterogeneity within and between catalyst particles. On the other hand, high resolution techniques are extremely complex, expensive, and often offer very poor statistics (in terms of measuring a large number of particles). The scope of this PhD thesis is to explore new analytical methods to study the pore space of heterogeneous catalysts using fluorescent probes.

In **Chapter 2**, we employed synchrotron radiation-based transmission X-ray microscopy (TXM), a state-of-the-art high-resolution technique, to study the macroporosity of a MIL-47(V) metal organic framework (MOF) crystal for the first time. Macropore defects up to the micron scale were present throughout the catalyst particle, which was confirmed by focus ion beam (FIB) cutting and scanning electron microscopy (SEM) imaging. However, it was found that the macropore networks within MIL-47(V) were very localized and poorly connected. Therefore, these defects probably have only a limited effect on mass transfer within the MOF crystal. Interestingly, the macropore networks display a preferential orientation that could be related to the MOF crystal growth.

In **Chapter 3**, a cheap and simple analytical method to characterize the accessibility of individual porous particles is presented. Here, the uptake of a fluorophore into the solid catalyst particles over time is used to characterize them. The equipment needed to perform these experiments consists of a conventional fluorescence microscopy setup and a PDMS-made microfluidic device and can study tens of solid catalyst particles simultaneously. In order to showcase the method, we used model porous silica particles with uniform pore size distributions and similar porosities. Interestingly, even though the particles within a sample are relatively homogeneous, significant uptake heterogeneities between these particles were observed, highlighting the importance of studying materials at the single-particle-level. Furthermore, the accessibility of the particles correlated positively with pore size. Importantly, varying the probe-host electrostatic interactions via the pH and the ionic strength of the system resulted in significant mass transfer differences. If these electrostatic interactions are suppressed (e.g., via pH conditions), the pore structure becomes dominant for the uptake process, resulting in a higher sensitivity towards the features of the pore network.

Chapters 4, 5 and 6 explore the possibility of using single molecule(particle) localization microscopy (SMLM) and single particle tracking (SPT) to explore and map porous catalyst materials with sub-diffraction limit resolution.

Due to the probe-host interactions, the motion behavior observed in SPT experiments in confinement is extremely complex and heterogeneous. Therefore, in order to retrieve properties from the pore space, it is necessary to first understand the probe motion behavior in well-defined pores with known dimensions and composition. To tackle this problem, we introduce a two-dimensional (2D) silica model pore system made with lithography and wet etching in **Chapter 4**. Here, we investigated how the diffusion and adsorption behavior of quantum-dots (QDs) as sensitive and local probes is affected

by pH within 2D pore systems. In our experiments, adsorption cannot be distinguished from probe immobilization due to a significant increase of hydrodynamic drag close to the pore walls. We, therefore, refer to both phenomena as *trapping*. The duration and frequency of trap events could be tuned via the pH. Under basic conditions, trapping could be almost entirely suppressed, possibly due to an increased probe-host electrostatic repulsion. Further, we successfully demonstrated the use of QDs under nearly non-trapping conditions for pore-space mapping of one-dimensional silica pores and a real-life polymerization catalyst support particle, potentially with resolutions in the order of tens of nanometers. Finally, we propose a protocol to ensure a complete porosity exploration in future SPT-mapping experiments.

It has been previously shown that the hydrodynamic drag experienced by colloids increases significantly in confinement which leads to a diffusion coefficient reduction. In **Chapter 5**, we investigate whether we can exploit this to probe pore sizes in three dimensions based on local diffusion coefficients measured with SPT. Therefore, we modified the 2D model pore presented in **Chapter 4** to have varying pore depths and studied the motion behavior of individual quantum dots under non-trapping conditions. The concentration of probes within the 2D pores correlated positively with pore-depth confirming that the pores indeed had different dimensions. Furthermore, we unraveled the presence of clusters within the larger pores, and managed to remove them from the analysis. Surprisingly, the cluster-free trajectories displayed virtually the same diffusion coefficients and transient trap event durations for all studied pore depths. This contradicted hydrodynamic drag simulations we performed, where the diffusion coefficient was predicted to vary notably with the 2D pore depth. Although more work is needed to understand these highly intriguing results, we can at this stage conclude that this probe-host-solvent system is not suitable for probing pore sizes between 50 nm and 150 nm just based on the measured diffusion coefficient.

The quantum-dot probes used in **Chapters 4 and 5** are larger (diameter: ~14 nm) than a significant fraction of the pores that are typically present in hierarchically complex porous catalysts. We therefore investigated the use of smaller carbon dot probes for pore space exploration in **Chapter 6**. We successfully embedded the carbon dots with resorufin improving their fluorescent properties and trackability. This allowed us to track carbon dot free diffusion in a high viscosity liquid for the first time and determine their size distribution. Their small size (mode diameter: 2 nm) made it impossible for us to track them within our 2D model pore. However, transient trapping events could be observed and quantified, showing that their duration does not depend on pore size. Furthermore, we could track carbon dots within porous silica particles that were inaccessible to the probes used in **Chapters 4 and 5,** showing their potential to explore materials with smaller pores. Furthermore, different transient trapping event durations were observed on unconfined surfaces with different compositions. Potentially, this parameter could be used to map materials with different compositions. Finally, confocal laser scanning microscopy imaging of stained mesoporous silica particles suggested that the trapping behavior could also be tuned via the pH of the system.

7.2 Outlook

The spatial resolution achieved in the TXM study presented in **Chapter 2** was 230 nm. However smaller macro- and mesopore defects are present in the sample. This is often the case when studying catalyst materials with synchrotron-based techniques. Potentially, regions containing unresolved pores could be visualized by intruding the particle with an element with a higher density (e.g., pressurized Xe gas) and comparing the X-ray absorption values before and after the intrusion. Then, a negative image of the pore space can be obtained, where areas containing unresolved pores become visible. This procedure is schematically depicted in Figure 7.1.

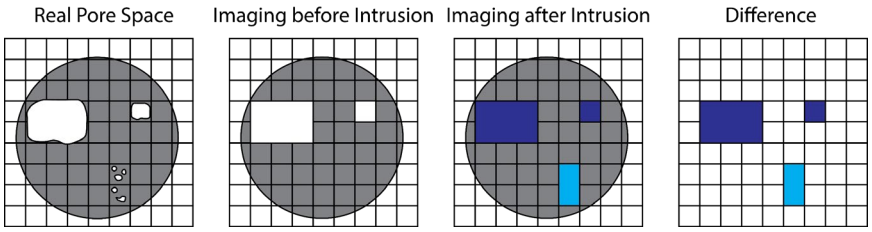

Figure 7.1 Schematic of the differential contrast imaging procedure. First a tomography of the studied material is recorded. Pores smaller than the resolution of the method will remain obscured due to high X-ray absorption of the solid surrounding them. Then, a material with larger X-ray absorption than air (e.g., pressurized Xe gas) intrudes the particle followed by another tomography. Then the X-ray absorption in the now filled pore regions is larger than in the first tomography. In the next step, the tomographies are aligned and the difference between the grayscale values after and before intrusion is calculated obtaining a negative of the pore space, where regions containing unresolved pores "light up" and become visible.

We attempted to perform a TXM experiment using Xe gas at up to 20 bar as intrusion gas to map regions with unresolved porosity within a fluid catalytic cracking (FCC) particle (Figure 7.2). The contrast of the image could be varied due to the presence and pressure of Xenon. Unfortunately, motor jitter, fluctuations in the beam, and missing projection angles did not allow for a good 3D reconstruction quality. These measurements should therefore be repeated.

Potentially, if even higher pressures could be reached during imaging, even reaching pressures that could lead to gas capillary condensation in pores with difference sizes. This would result in a significantly higher contrast (of a liquid phase), and it would allow us to study the underlying processes in gas physisorption. A similar approach could be used to study Hg-porosimetry more fundamentally. A dedicated setup for this kind of experiments is not currently available and needs to be developed.

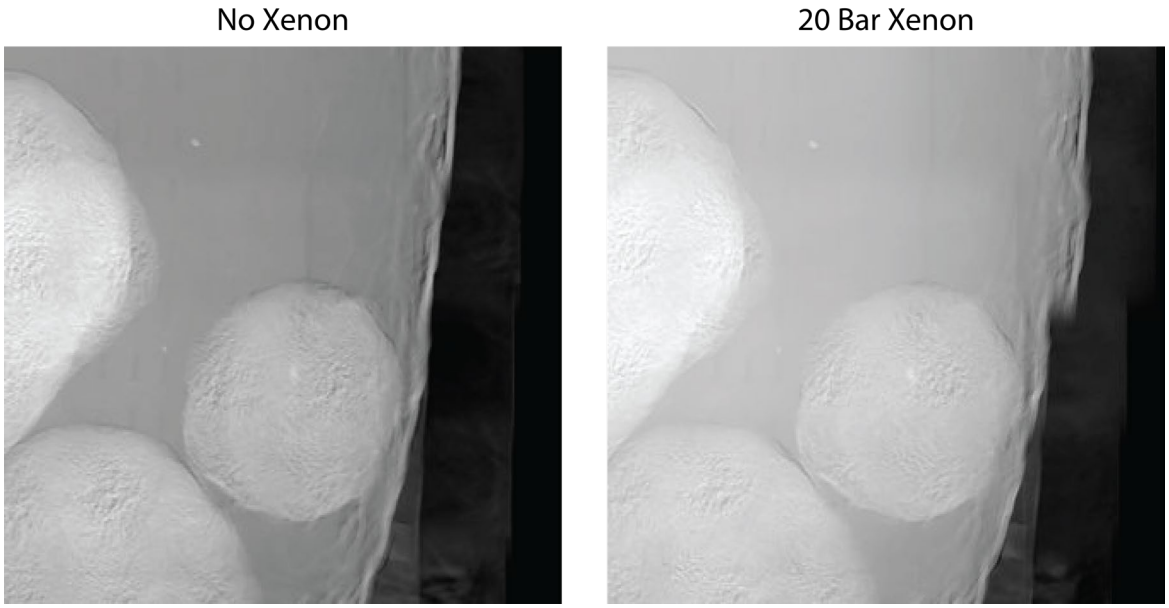

Figure 7.2 Transmission X-ray microscopy (TXM) projection of a fluid catalytic cracking (FCC) particle within a silicon nitride capillary with and without pressurized xenon at beamline 6-2c the Stanford Synchrotron Radiation Lightsource (SSRL). The beam energy was 6.9 keV.

Differential contrast imaging could also be used to map polymer intrusion into catalyst particles. We performed holotomography on a dedicated microreactor containing an FCC particle and

polypropylene beads. We increased the temperature such that the polymer melted and intruded the particle. After stopping the heating ramp, we performed another tomography. The polypropylene showed significant contrast under the conditions used and could easily be identified (Figure 7.3). However, missing projection angles resulted in noise which heavily complicated the alignment of both tomographies.

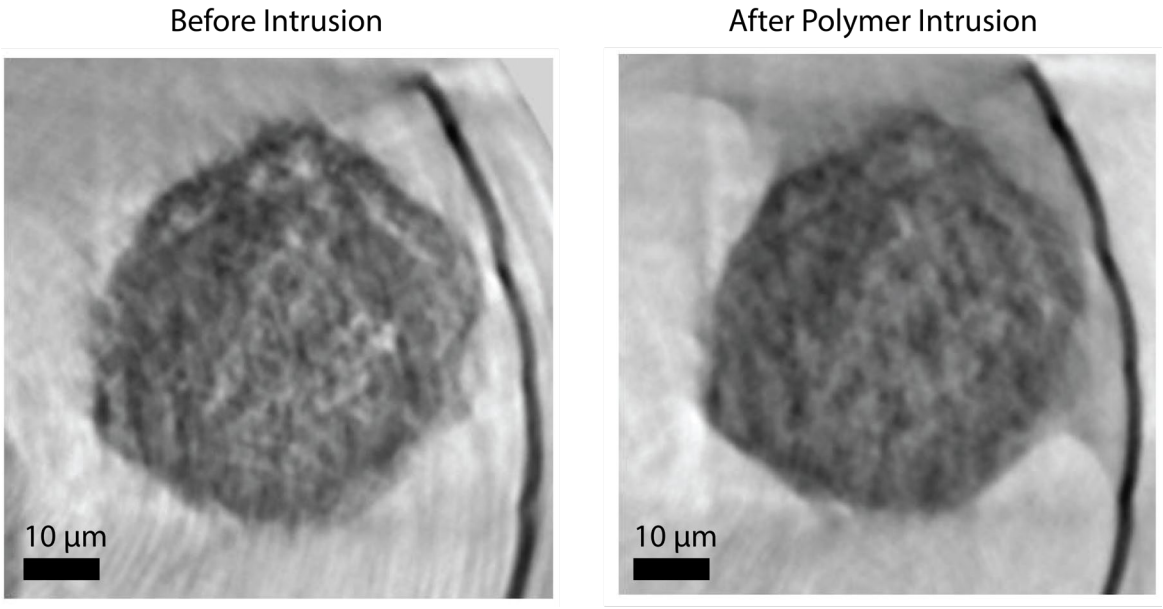

Figure 7.3 left: Reconstructed holotomography slice of a fluid catalytic cracking (FCC) particle within the microreactor. Right: The same catalyst particle is intruded by melted polypropylene (PP). Note that the particle becomes darker (density increases), because of the polymer intrusion. The polypropylene meniscus is also visible on the upper right of the image. The images were recorded at beamline P05 at the Deutsches Elektronen-Synchrotron (DESY) using a beam energy of 17 keV. Further details on the microreactor can be found in the PhD thesis of Dr. Luca Carnevale.[292]

The results of **Chapters 3-6** showed that the probe-host interactions heavily influence diffusion and trapping within porous materials. Therefore, different fluorophores, porous materials and solvents should be tested under a variety of conditions.

The microfluidic device, as presented in **Chapter 3**, could be modified to be compatible with organic solvents, allowing the application hydrophobic dyes. Further, the observed concentrations fronts within the porous particle could be quantified and fitted with a mass transfer model to provide spatially resolved information. Finally, more complex materials, such as real-life solid catalyst materials, should be studied with this method.

The 2D model pore presented in **Chapters 4 and 5** should be employed to characterize a variety of fluorescent probes of varying sizes, surface charge densities, and surface functional groups. Moreover, the 2D pore walls could be functionalized to have different affinities to the solvents and fluorophores. Furthermore, the probe-wall electrostatic interactions should be systematically changed by varying the pH and ionic strength of the system or by using different solvents. In addition, the pore dimensions should be varied to study the effects of probe-wall hydrodynamic interactions. Since the interpretation of these experiments is far from trivial, more complex mass transfer simulations should be carried out in parallel in order to provide a better understanding of the experimental results. Once we understand the motion behavior of the fluorophores in confinement, we can use them to study more complex pore structures (Figure 7.4). The larger the fluorescent probe “toolbox” that we have, the better we can study the porous material, as different probes can be used to study different

properties. Finally, the X-ray microscopy and SPT pore space exploration could be correlated in order to validate mass transfer simulations within real-life solid catalyst materials.

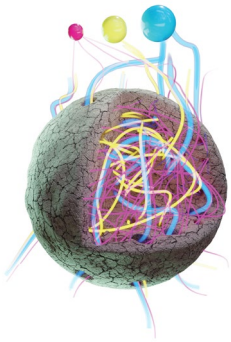

Figure 7.4 Artist's impression of fluorophores exploring the pore space of a catalyst. Different probes with (e.g., different sizes) can be used to map pore space regions with different accessibilities (only small probes can access smaller pores).

As seen in **Chapters 4 and 6**, the probe-wall affinity determines the duration of transient trapping events. Potentially, this could be exploited to map different compositions within a heterogeneous catalyst. In order to prove the feasibility of this, surfaces with different properties (i.e., composition, roughness, and functional groups) should be put in contact with fluorophores. After understanding how the trapping event duration distribution of a fluorophore relates to wall composition, we envision an experiment in which a lithographically patterned surface containing different materials is mapped recording trapping event duration. If successful, the approach should be applied to real-life solid catalyst materials.

References

(1) Ertl, G.; Knözinger, H.; Schüth, F.; Weitkamp, J. (Eds.), *Handbook of Heterogeneous Catalysis*, Wiley-VCH, Weinheim, 2nd Ed., **2008**.

(2) Hanefeld, U.; Lefferts, L. (Eds.), *Catalysis: An Integrated Textbook*, Wiley-VCH, Weinheim, **2018**.

(3) Klaewkla, R.; Arend, M.; F., W. A Review of Mass Transfer Controlling the Reaction Rate in Heterogeneous Catalytic Systems. In *Mass Transfer - Advanced Aspects*; InTech, **2011**. https://doi.org/10.5772/22962.

(4) Vogt, E. T. C.; Weckhuysen, B. M. Fluid Catalytic Cracking: Recent Developments on the Grand Old Lady of Zeolite Catalysis. *Chem. Soc. Rev.* **2015**, *44* (20), 7342–7370. https://doi.org/10.1039/c5cs00376h.

(5) Whiting, G. T.; Nikolopoulos, N.; Nikolopoulos, I.; Chowdhury, A. D.; Weckhuysen, B. M. Visualizing Pore Architecture and Molecular Transport Boundaries in Catalyst Bodies with Fluorescent Nanoprobes. *Nat. Chem.* **2019**, *11* (1), 23–31. https://doi.org/10.1038/s41557-018-0163-z.

(6) Chmelik, C.; Heinke, L.; Valiullin, R.; Kärger, J. A New View of Diffusion in Nanoporous Materials. *Chemie-Ingenieur-Technik* **2010**, *82* (6), 779–804. https://doi.org/10.1002/cite.201000038.

(7) Chmelik, C.; Kärger, J. In Situ Study on Molecular Diffusion Phenomena in Nanoporous Catalytic Solids. *Chem. Soc. Rev.* **2010**, *39* (12), 4864–4884. https://doi.org/10.1039/c0cs00100g.

(8) Kärger, J.; Ruthven, D. M. Diffusion in Nanoporous Materials: Fundamental Principles, Insights and Challenges. *New J. Chem.* **2016**, *40* (5), 4027–4048. https://doi.org/10.1039/c5nj02836a.

(9) Luna-Murillo, B.; Pala, M.; Paioni, A. L.; Baldus, M.; Ronsse, F.; Prins, W.; Bruijnincx, P. C. A.; Weckhuysen, B. M. Catalytic Fast Pyrolysis of Biomass: Catalyst Characterization Reveals the Feed-Dependent Deactivation of a Technical ZSM-5-Based Catalyst. *ACS Sustain. Chem. Eng.* **2021**, *9* (1), 291–304. https://doi.org/10.1021/acssuschemeng.0c07153.

(10) Meirer, F.; Morris, D. T.; Kalirai, S.; Liu, Y.; Andrews, J. C.; Weckhuysen, B. M. Mapping Metals Incorporation of a Whole Single Catalyst Particle Using Element Specific X-Ray Nanotomography. *J. Am. Chem. Soc.* **2015**, *137* (1), 102–105. https://doi.org/10.1021/ja511503d.

(11) Vollmer, I.; Jenks, M. J. F.; Mayorga González, R.; Meirer, F.; Weckhuysen, B. M. Plastic Waste Conversion over a Refinery Waste Catalyst. *Angew. Chem. Int. Ed.* **2021**, *60* (29), 16101–16108. https://doi.org/10.1002/anie.202104110.

(12) Bossers, K. W.; Valadian, R.; Zanoni, S.; Smeets, R.; Friederichs, N.; Garrevoet, J.; Meirer, F.; Weckhuysen, B. M. Correlated X-Ray Ptychography and Fluorescence Nano-Tomography on the Fragmentation Behavior of an Individual Catalyst Particle during the Early Stages of Olefin Polymerization. *J. Am. Chem. Soc.* **2020**, *142* (8), 3691–3695. https://doi.org/10.1021/jacs.9b13485.

(13) Veselý, M.; Valadian, R.; Merten Lohse, L.; Toepperwien, M.; Spiers, K.; Garrevoet, J.; Vogt, E. T. C.; Salditt, T.; Weckhuysen, B. M.; Meirer, F. 3-D X-Ray Nanotomography Reveals Different Carbon Deposition Mechanisms in a Single Catalyst Particle. *ChemCatChem* **2021**, *13* (10), 2494–2507. https://doi.org/10.1002/cctc.202100276.

(14) Rouquerol, J.; Avnir, D.; Fairbridge, C. W.; Everett, D. H.; Haynes, J. M.; Pernicone, N.; Ramsay, J. D. F.; Sing, K. S. W.; Unger, K. K. Recommendations for the Characterization of Porous Solids (Technical Report). *Pure Appl. Chem.* **1994**, *66* (8), 1739–1758. https://doi.org/10.1351/pac199466081739.

(15) Weckhuysen, B. M. Solid Catalysts under the Spotlight. *Nat. Catal.* **2018**, *1* (2), 101–102. https://doi.org/10.1038/s41929-018-0024-6.

(16) Thommes, M.; Kaneko, K.; Neimark, A. V.; Olivier, J. P.; Rodriguez-Reinoso, F.; Rouquerol, J.; Sing, K. S. W. Physisorption of Gases, with Special Reference to the Evaluation of Surface Area and Pore Size Distribution (IUPAC Technical Report). *Pure Appl. Chem.* **2015**, *87* (9–10), 1051–1069. https://doi.org/10.1515/pac-2014-1117.

(17) Rahman, M. M.; Shafiullah, A. Z.; Pal, A.; Islam, M. A.; Jahan, I.; Saha, B. B. Study on Optimum IUPAC Adsorption Isotherm Models Employing Sensitivity of Parameters for Rigorous Adsorption System Performance Evaluation. *Energies* **2021**, *14*, 7478. https://doi.org/10.3390/en14227478.

(18) Rouquerol, J.; Baron, G.; Denoyel, R.; Giesche, H.; Groen, J.; Klobes, P.; Levitz, P.; Neimark, A. V.; Rigby, S.; Skudas, R.; Sing, K.; Thommes, M.; Unger, K. Liquid Intrusion and Alternative Methods for the Characterization of Macroporous Materials (IUPAC Technical Report). *Pure Appl. Chem.* **2012**, *84* (1), 107–136. https://doi.org/10.1351/PAC-REP-10-11-19.

(19) Mayorga-González, R.; Rivera-Torrente, M.; Nikolopoulos, N.; Bossers, K. W.; Valadian, R.; Yus, J.; Seoane, B.; Weckhuysen, B. M.; Meirer, F. Visualizing Defects and Pore Connectivity within Metal-Organic Frameworks by X-Ray Transmission Tomography. *Chem. Sci.* **2021**, *12* (24), 8458–8467. https://doi.org/10.1039/d1sc00607j.

(20) Brandani, S. Kinetics of Liquid Phase Batch Adsorption Experiments. *Adsorption* **2021**, *27* (3), 353–368. https://doi.org/10.1007/s10450-020-00258-9.

(21) Connor, P. O.; Nl, H. (12) United States Patent. **2004**, *2* (12), Patent No.: US 6,828,153 B2.

(22) Rainer, D. R.; Rautiainen, E.; Imhof, P. Novel Lab-Scale Deactivation Method for FCC Catalyst: Inducing Realistic Accessibility Responses to Iron Poisoning. *Appl. Catal. A Gen.* **2003**, *249* (1), 69–80. https://doi.org/10.1016/S0926-860X(03)00203-5.

(23) Psarras, A. C.; Iliopoulou, E. F.; Nalbandian, L.; Lappas, A. A.; Pouwels, C. Study of the Accessibility Effect on the Irreversible Deactivation of FCC Catalysts from Contaminant Feed Metals. *Catal. Today* **2007**, *127* (1–4), 44–53. https://doi.org/10.1016/j.cattod.2007.05.021.

(24) Crank, J. *The Mathematics of Diffusion*, Clarendon Press, London, 1975.

(25) Klein, G.; Ruthven, D. *Principles of Adsorption and Adsorption Processes*, 62nd ed.; John Wiley and Sons Inc: New York, **1985**. https://doi.org/10.1061/JSEDAI.0000430

(26) Do, D. D. *Adsorption Analysis: Equilibria And Kinetics (With Cd Containing Computer Matlab Programs) Volumen 2 de Series On Chemical Engineering*; World Scientific, Singapore, **1998**.

(27) Weber, W. J.; Asce, A. M.; Carrell, J. *KINETICS OF ADSORPTION ON CARBON FROM SOLUTIONa*; Proceedings of the American Society of Civil Engineers. **1963**, 89, 31–59.

(28) Wu, F. C.; Tseng, R. L.; Juang, R. S. Initial Behavior of Intraparticle Diffusion Model Used in the

Description of Adsorption Kinetics. *Chem. Eng. J.* **2009**, *153* (1–3), 1–8. https://doi.org/10.1016/j.cej.2009.04.042.

(29) Yang, Y.; Lin, X.; Wei, B.; Zhao, Y.; Wang, J. Evaluation of Adsorption Potential of Bamboo Biochar for Metal-Complex Dye: Equilibrium, Kinetics and Artificial Neural Network Modeling. *Int. J. Environ. Sci. Technol.* **2014**, *11* (4), 1093–1100. https://doi.org/10.1007/s13762-013-0306-0.

(30) Medley, J. A.; Andrews, M. W. *The Effect of a Surface Barrier on Uptake Rates of Dye into Wool Fibers*. Text. Res. J. **1959**, 29, 398–403.

(31) Cheung, W. H.; Szeto, Y. S.; McKay, G. Intraparticle Diffusion Processes during Acid Dye Adsorption onto Chitosan. *Bioresour. Technol.* **2007**, *98* (15), 2897–2904. https://doi.org/10.1016/j.biortech.2006.09.045.

(32) Sze, M. F. F.; McKay, G. An Adsorption Diffusion Model for Removal of Para-Chlorophenol by Activated Carbon Derived from Bituminous Coal. *Environ. Pollut.* **2010**, *158* (5), 1669–1674. https://doi.org/10.1016/j.envpol.2009.12.003.

(33) Alexander, F.; Poofs, V. J. P.; McKay, G. Adsorption Kinetics and Diffusional Mass Transfer Processes during Color Removal from Effluent Using Silica. *Ind. Eng. Chem. Process Des. Dev.* **1978**, *17* (4), 406–410. https://doi.org/10.1021/i260068a005.

(34) Sun, Q.; Yang, L. The Adsorption of Basic Dyes from Aqueous Solution on Modified Peat-Resin Particle. *Water Res.* **2003**, *37* (7), 1535–1544. https://doi.org/10.1016/S0043-1354(02)00520-1.

(35) Özer, D.; Dursun, G.; Özer, A. Methylene Blue Adsorption from Aqueous Solution by Dehydrated Peanut Hull. *J. Hazard. Mater.* **2007**, *144* (1–2), 171–179. https://doi.org/10.1016/j.jhazmat.2006.09.092.

(36) Pholosi, A.; Naidoo, E. B.; Ofomaja, A. E. Intraparticle Diffusion of Cr(VI) through Biomass and Magnetite Coated Biomass: A Comparative Kinetic and Diffusion Study. *South African J. Chem. Eng.* **2020**, *32*, 39–55. https://doi.org/10.1016/j.sajce.2020.01.005.

(37) Ali, H. E.; Nasef, S. M.; Gad, Y. H. Remediation of Astrazon Blue and Lerui Acid Brilliant Blue Dyes from Waste Solutions Using Amphoteric Superparamagnetic Nanocomposite Hydrogels Based on Chitosan Prepared by Gamma Rays. *Carbohydr. Polym.* **2022**, *283*, 119149. https://doi.org/10.1016/j.carbpol.2022.119149.

(38) Hashem, A.; El-Khiraigy, K. Bioadsorption of Pb(II) onto <I>Anethum</I> <I>Graveolens</I> from Contaminated Wastewater: Equilibrium and Kinetic Studies. *J. Environ. Prot.*. **2013**, *04* (01), 108–119. https://doi.org/10.4236/jep.2013.41012.

(39) Teixeira, R. N. P.; Sousa Neto, V. O.; Oliveira, J. T.; Oliveira, T. C.; Melo, D. Q.; Silva, M. A. A.; Nascimento, R. F. Study on the Use of Roasted Barley Powder for Adsorption of Cu2+ Ions in Batch Experiments and in Fixed-Bed Columns. *BioResources* **2013**, *8* (3), 3556–3573. https://doi.org/10.15376/biores.8.3.3556-3573.

(40) Largitte, L.; Pasquier, R. A Review of the Kinetics Adsorption Models and Their Application to the Adsorption of Lead by an Activated Carbon. *Chem. Eng. Res. Des.* **2016**, *109*, 495–504. https://doi.org/10.1016/j.cherd.2016.02.006.

(41) Özcan, A. S.; Özcan, A. Adsorption of Acid Dyes from Aqueous Solutions onto Acid-Activated Bentonite. *J. Colloid Interface Sci.* **2004**, *276* (1), 39–46. https://doi.org/10.1016/j.jcis.2004.03.043.

(42) Özcan, A.; Özcan, A. S. Adsorption of Acid Red 57 from Aqueous Solutions onto Surfactant-Modified Sepiolite. *J. Hazard. Mater.* **2005**, *125* (1–3), 252–259. https://doi.org/10.1016/j.jhazmat.2005.05.039.

(43) Kannan, N.; Sundaram, M. M. Kinetics and Mechanism of Removal of Methylene Blue by Adsorption on Various Carbons - A Comparative Study. *Dye. Pigment.* **2001**, *51* (1), 25–40. https://doi.org/10.1016/S0143-7208(01)00056-0.

(44) El Mouzdahir, Y.; Elmchaouri, A.; Mahboub, R.; ElAnssari, A.; Gil, A.; Korili, S. A.; Vicente, M. A. Interaction of Stevensite with Cd^{2+} and Pb^{2+} in Aqueous Dispersions. *Appl. Clay Sci.* **2007**, *35* (1–2), 47–58. https://doi.org/10.1016/j.clay.2006.08.002.

(45) Önal, Y. Kinetics of Adsorption of Dyes from Aqueous Solution Using Activated Carbon Prepared from Waste Apricot. *J. Hazard. Mater.* **2006**, *137* (3), 1719–1728. https://doi.org/10.1016/j.jhazmat.2006.05.036.

(46) El-Khaiary, M. I. Kinetics and Mechanism of Adsorption of Methylene Blue from Aqueous Solution by Nitric-Acid Treated Water-Hyacinth. *J. Hazard. Mater.* **2007**, *147* (1–2), 28–36. https://doi.org/10.1016/j.jhazmat.2006.12.058.

(47) Akmil-Başar, C.; Önal, Y.; Kiliçer, T.; Eren, D. Adsorptions of High Concentration Malachite Green by Two Activated Carbons Having Different Porous Structures. *J. Hazard. Mater.* **2005**, *127* (1–3), 73–80. https://doi.org/10.1016/j.jhazmat.2005.06.025.

(48) Lorenc-Grabowska, E.; Gryglewicz, G. Adsorption of Lignite-Derived Humic Acids on Coal-Based Mesoporous Activated Carbons. *J. Colloid Interface Sci.* **2005**, *284* (2), 416–423. https://doi.org/10.1016/j.jcis.2004.10.031.

(49) Çiçek, F.; Özer, D.; Özer, A.; Özer, A. Low Cost Removal of Reactive Dyes Using Wheat Bran. *J. Hazard. Mater.* **2007**, *146* (1–2), 408–416. https://doi.org/10.1016/j.jhazmat.2006.12.037.

(50) Singh, K. K.; Rastogi, R.; Hasan, S. H. Removal of Cadmium from Wastewater Using Agricultural Waste "Rice Polish." *J. Hazard. Mater.* **2005**, *121* (1–3), 51–58. https://doi.org/10.1016/j.jhazmat.2004.11.002.

(51) Huo, M. X.; Jin, Y. L.; Sun, Z. F.; Ren, F.; Pei, L.; Ren, P. G. Facile Synthesis of Chitosan-Based Acid-Resistant Composite Films for Efficient Selective Adsorption Properties towards Anionic Dyes. *Carbohydr. Polym.* **2021**, *254*, 117473. https://doi.org/10.1016/j.carbpol.2020.117473.

(52) Pagès, G.; Gilard, V.; Martino, R.; Malet-Martino, M. Pulsed-Field Gradient Nuclear Magnetic Resonance Measurements (PFG NMR) for Diffusion Ordered Spectroscopy (DOSY) Mapping. *Analyst* **2017**, *142* (20), 3771–3796. https://doi.org/10.1039/c7an01031a.

(53) Mehlhorn, D.; Valiullin, R.; Kärger, J.; Cho, K.; Ryoo, R. Exploring Mass Transfer in Mesoporous Zeolites by NMR Diffusometry. *Materials* **2012**, *5* (12), 699–720. https://doi.org/10.3390/ma5040699.

(54) Hertel, S.; Wehring, M.; Amirjalayer, S.; Gratz, M.; Lincke, J.; Krautscheid, H.; Schmid, R.; Stallmach, F. NMR Studies of Benzene Mobility in Metal-Organic Framework MOF-5. *Eur. Phys. J. Appl. Phys.* **2011**, *55* (2), 20702. https://doi.org/10.1051/epjap/2011100370.

(55) Rottreau, T. J.; Parlett, C. M. A.; Lee, A. F.; Evans, R. Diffusion NMR Characterization of Catalytic Silica Supports: A Tortuous Path. *J. Phys. Chem. C* **2017**, *121* (30), 16250–16256. https://doi.org/10.1021/acs.jpcc.7b02929.

(56) Hwang, S.; Kärger, J. Diffusion in Nanopores: Correlating Experimental Findings with "First-Principles" Predictions. *Adsorption* **2020**, *26* (7), 1001–1013. https://doi.org/10.1007/s10450-

020-00237-0.

(57) Jobic, H. *Catalyst Characterization*, in Imelik, B., Vedrine, J. C. (Eds.), *Fundamental and Applied Catalysis*; Springer, Boston, **1994**. https://doi.org/10.1007/978-1-4757-9589-9.

(58) Jobic, H. *Adsorption and Diffusion*, in Karge, H. G., Weitkamp, J. (Eds.), *Molecular Sieves*, Springer, Berlin, **2008**. https://doi.org/10.1007/978-3-540-73966-1.

(59) Kruteva, M. Dynamics Studied by Quasielastic Neutron Scattering (QENS). *Adsorption* **2021**, *27* (5), 875–889. https://doi.org/10.1007/s10450-020-00295-4.

(60) Buurmans, I. L. C.; Weckhuysen, B. M. Heterogeneities of Individual Catalyst Particles in Space and Time as Monitored by Spectroscopy. *Nat. Chem.* **2012**, *4* (11), 873–886. https://doi.org/10.1038/nchem.1478.

(61) Velthoen, M. E. Z.; Meeldijk, J. D.; Meirer, F.; Weckhuysen, B. M. Intra- and Interparticle Heterogeneities in Solid Activators for Single-Site Olefin Polymerization Catalysis as Revealed by Micro-Spectroscopy. *Chem. Eur. J.* **2018**, *24* (46), 11944–11953. https://doi.org/10.1002/chem.201801714.

(62) Kärger, J.; Binder, T.; Chmelik, C.; Hibbe, F.; Krautscheid, H.; Krishna, R.; Weitkamp, J. Microimaging of Transient Guest Profiles to Monitor Mass Transfer in Nanoporous Materials. *Nat. Mater.* **2014**, *13* (4), 333–343. https://doi.org/10.1038/nmat3917.

(63) Kärger, J.; Heinke, L.; Kortunov, P.; Vasenkov, S. *Looking into the Crystallites: Diffusion Studies by Interference Microscopy*, Elsevier, Amsterdam, **2007**. https://doi.org/10.1016/S0167-2991(07)80915-3.

(64) Omidi, M.; Fatehinya, A.; Farahani, M.; Akbari, Z.; Shahmoradi, S.; Yazdian, F.; Tahriri, M.; Moharamzadeh, K.; Tayebi, L.; Vashaee, D. *Characterization of Biomaterials*, in *Biomaterials for Oral and Dental Tissue Engineering*, Elsevier, Amsterdam, **2017**; pp. 97–115. https://doi.org/10.1016/B978-0-08-100961-1.00007-4.

(65) Midgley, P. A.; Dunin-Borkowski, R. E. Electron Tomography and Holography in Materials Science. *Nat. Mater.* **2009**, *8* (4), 271–280. https://doi.org/10.1038/nmat2406.

(66) De Winter, D. A. M.; Meirer, F.; Weckhuysen, B. M. FIB-SEM Tomography Probes the Mesoscale Pore Space of an Individual Catalytic Cracking Particle. *ACS Catal.* **2016**, *6* (5), 3158–3167. https://doi.org/10.1021/acscatal.6b00302.

(67) Karwacki, L.; de Winter, D. A. M.; Aramburo, L. R.; Lebbink, M. N.; Post, J. A.; Drury, M. R.; Weckhuysen, B. M. Architecture-Dependent Distribution of Mesopores in Steamed Zeolite Crystals as Visualized by FIB-SEM Tomography. *Angew. Chem. Int. Ed.* **2011**, *50* (6), 1294–1298. https://doi.org/10.1002/anie.201006031.

(68) Bae, K.; Kim, J. W.; Son, J. won; Lee, T.; Kang, S.; Prinz, F. B.; Shim, J. H. 3D Evaluation of Porous Zeolite Absorbents Using FIB-SEM Tomography. *Int. J. Precis. Eng. Manuf. - Green Technol.* **2018**, *5* (2), 195–199. https://doi.org/10.1007/s40684-018-0019-4.

(69) Lin, R.; Hou, J.; Li, M.; Wang, Z.; Ge, L.; Li, S.; Smart, S.; Zhu, Z.; Bennett, T. D.; Chen, V. Interfacial Engineering of a Polymer-MOF Composite by: In Situ Vitrification. *Chem. Commun.* **2020**, *56* (25), 3609–3612. https://doi.org/10.1039/d0cc00664e.

(70) Werny, M. J.; Zarupski, J.; ten Have, I. C.; Piovano, A.; Hendriksen, C.; Friederichs, N. H.; Meirer, F.; Groppo, E.; Weckhuysen, B. M. Correlating the Morphological Evolution of Individual Catalyst Particles to the Kinetic Behavior of Metallocene-Based Ethylene Polymerization Catalysts. *JACS Au* **2021**, *1* (11), 1996–2008.

https://doi.org/10.1021/jacsau.1c00324.

(71) Zuo, J. M.; Spence, J. C. H. *Advanced Transmission Electron Microscopy*, Springer, New York, **2017**. https://doi.org/10.1007/978-1-4939-6607-3.

(72) Mitchell, S.; Michels, N.-L.; Kunze, K.; Pérez-Ramírez, J. Visualization of Hierarchically Structured Zeolite Bodies from Macro to Nano Length Scales. *Nat. Chem.* **2012**, *4* (10), 825–831. https://doi.org/10.1038/nchem.1403.

(73) Nellist, P. D.; Pennycook, S. J. *The Principles and Interpretation of Annular Dark-Field Z-Contrast Imaging*, in *Advances in Imaging and Electron Physics*, Elsevier, Amsterdam, **2000**, pp. 147–203. https://doi.org/10.1016/S1076-5670(00)80013-0.

(74) Collins, S. M.; Midgley, P. A. Progress and Opportunities in EELS and EDS Tomography. *Ultramicroscopy* **2017**, *180*, 133–141. https://doi.org/10.1016/j.ultramic.2017.01.003.

(75) Kirz, J.; Jacobsen, C. The History and Future of X-Ray Microscopy. *J. Phys. Conf. Ser.* **2009**, *186*, 012001. https://doi.org/10.1088/1742-6596/186/1/012001.

(76) Mao, W. L.; Lin, Y.; Liu, Y.; Liu, J. Applications for Nanoscale X-Ray Imaging at High Pressure. *Engineering* **2019**, *5* (3), 479–489. https://doi.org/10.1016/j.eng.2019.01.006.

(77) Fiddy, M. A. The Radon Transform and Some of Its Applications. *Opt. Acta Int. J. Opt.* **1985**, *32* (1), 3–4. https://doi.org/10.1080/713821644.

(78) Shepp, L. A.; Vardi, Y. Maximum Likelihood Reconstruction for Emission Tomography. *IEEE Trans. Med. Imaging* **1982**, *1* (2), 113–122. https://doi.org/10.1109/TMI.1982.4307558.

(79) Van Heel, M.; Schatz, M. Fourier Shell Correlation Threshold Criteria. *J. Struct. Biol.* **2005**, *151* (3), 250–262. https://doi.org/10.1016/j.jsb.2005.05.009.

(80) Andrews, J. C.; Meirer, F.; Liu, Y.; Mester, Z.; Pianetta, P. Transmission X-Ray Microscopy for Full-Field Nano Imaging of Biomaterials. *Microscopy Research and Technique*. **2011**, pp 671–681. https://doi.org/10.1002/jemt.20907.

(81) Lambert, J. H. Hotometria Sive de Mensura et Gradibus Luminis, Colorum et Umbrae. *Augustae Vindelicorum sumptibus viduae Eberhardi Klett typis Chist. Petri Detleffsen* **1760**.

(82) Honkanen, A.-P.; Ollikkala, S.; Ahopelto, T.; Kallio, A.-J.; Blomberg, M.; Huotari, S. Johann-Type Laboratory-Scale x-Ray Absorption Spectrometer with Versatile Detection Modes. *Rev. Sci. Instrum.* **2019**, *90* (3), 033107. https://doi.org/10.1063/1.5084049.

(83) Turner, L. D.; Dhal, B. B.; Hayes, J. P.; Mancuso, A. P.; Nugent, K. A.; Paterson, D.; Scholten, R. E.; Tran, C. Q.; Peele, A. G.; Schmahl, G.; Rudolph, D.; Guttmann, P.; Sayre, D.; Howells, M.; Kirz, J.; Rarback, H.; Gureyev, T. E.; Cookson, D. F.; Paganin, D.; Barnea, Z. *X-Ray Phase Imaging: Demonstration of Extended Conditions with Homogeneous Objects References and Links "Phase Contrast x-Ray Microscopy-Experiments at the BESSY Storage Ring," in X-Ray Microscopy II*, Springer-Verlag, Berlin, **1988**; (56), 2960-2965. http://www.opticsexpress.org/abstract.cfm?URI=OPEX-11-19-2278.

(84) Diaz, A.; Trtik, P.; Guizar-Sicairos, M.; Menzel, A.; Thibault, P.; Bunk, O. Quantitative X-Ray Phase Nanotomography. *Phys. Rev. B - Condens. Matter Mater. Phys.* **2012**, *85*, 020104(R) https://doi.org/10.1103/PhysRevB.85.020104.

(85) Endrizzi, M. X-Ray Phase-Contrast Imaging. *Nuclear Instruments and Methods in Physics Research, Section A: Accelerators, Spectrometers, Detectors and Associated Equipment*, Elsevier, Amsterdam, **2018**, pp 88–98. https://doi.org/10.1016/j.nima.2017.07.036.

(86) Robisch, A.-L.; Eckermann, M.; Töpperwien, M.; van der Meer, F.; Stadelmann-Nessler, C.; Salditt, T. Nanoscale X-Ray Holotomography of Human Brain Tissue with Phase Retrieval Based on Multienergy Recordings. *J. Med. Imaging* **2020**, *7*, 013501 . https://doi.org/10.1117/1.JMI.7.1.013501.

(87) Khimchenko, A.; Bikis, C.; Pacureanu, A.; Hieber, S. E.; Thalmann, P.; Deyhle, H.; Schweighauser, G.; Hench, J.; Frank, S.; Müller-Gerbl, M.; Schulz, G.; Cloetens, P.; Müller, B. Hard X-Ray Nanoholotomography: Large-Scale, Label-Free, 3D Neuroimaging beyond Optical Limit. *Adv. Sci.* **2018**, *5* (6), 1700694. https://doi.org/10.1002/advs.201700694.

(88) Werny, M. J.; Valadian, R.; Lohse, L. M.; Robisch, A.-L.; Zanoni, S.; Hendriksen, C.; Weckhuysen, B. M.; Meirer, F. X-Ray Nanotomography Uncovers Morphological Heterogeneity in a Polymerization Catalyst at Multiple Reaction Stages. *Chem Catal.* **2021**, *1* (7), 1413–1426. https://doi.org/10.1016/j.checat.2021.10.008.

(89) Flenner, S.; Kubec, A.; David, C.; Storm, M.; Schaber, C. F.; Vollrath, F.; Müller, M.; Greving, I.; Hagemann, J. Hard X-Ray Nano-Holotomography with a Fresnel Zone Plate. *Opt. Express* **2020**, *28* (25), 37514. https://doi.org/10.1364/OE.406074.

(90) Jacobsen, C. *X-Ray Microscopy*, Cambridge University Press, Cambridge, **2019**. https://doi.org/10.1017/9781139924542.

(91) Ruiz-Martínez, J.; Beale, A. M.; Deka, U.; O'Brien, M. G.; Quinn, P. D.; Mosselmans, J. F. W.; Weckhuysen, B. M. Correlating Metal Poisoning with Zeolite Deactivation in an Individual Catalyst Particle by Chemical and Phase-Sensitive X-Ray Microscopy. *Angew. Chem. Int. Ed.* **2013**, *52* (23), 5983–5987. https://doi.org/10.1002/anie.201210030.

(92) Beale, A. M.; Jacques, S. D. M.; Gibson, E. K.; Di Michiel, M. Progress towards Five Dimensional Diffraction Imaging of Functional Materials under Process Conditions. *Coord. Chem. Rev.*, **2014**, *277-278*, 208–223. https://doi.org/10.1016/j.ccr.2014.05.008.

(93) Bare, S. R.; Charochak, M. E.; Kelly, S. D.; Lai, B.; Wang, J.; Chen-Wiegart, Y. K. Characterization of a Fluidized Catalytic Cracking Catalyst on Ensemble and Individual Particle Level by X-Ray Micro- and Nanotomography, Micro-X-Ray Fluorescence, and Micro-X-Ray Diffraction. *ChemCatChem* **2014,** 6 (5), 1427-1437 . https://doi.org/10.1002/cctc.201300974.

(94) Winarski, R. P.; Holt, M. V.; Rose, V.; Fuesz, P.; Carbaugh, D.; Benson, C.; Shu, D.; Kline, D.; Stephenson, G. B.; McNulty, I.; Maser, J. A Hard X-Ray Nanoprobe Beamline for Nanoscale Microscopy. *J. Synchrotron Radiat.* **2012**, *19* (6), 1056–1060. https://doi.org/10.1107/S0909049512036783.

(95) Chen, S.; Deng, J.; Yuan, Y.; Flachenecker, C.; Mak, R.; Hornberger, B.; Jin, Q.; Shu, D.; Lai, B.; Maser, J.; Roehrig, C.; Paunesku, T.; Gleber, S. C.; Vine, D. J.; Finney, L.; VonOsinski, J.; Bolbat, M.; Spink, I.; Chen, Z.; Steele, J.; Trapp, D.; Irwin, J.; Feser, M.; Snyder, E.; Brister, K.; Jacobsen, C.; Woloschak, G.; Vogt, S. The Bionanoprobe: Hard X-Ray Fluorescence Nanoprobe with Cryogenic Capabilities. *J. Synchrotron Radiat.* **2014**, *21* (1), 66–75. https://doi.org/10.1107/S1600577513029676.

(96) Nazaretski, E.; Lauer, K.; Yan, H.; Bouet, N.; Zhou, J.; Conley, R.; Huang, X.; Xu, W.; Lu, M.; Gofron, K.; Kalbfleisch, S.; Wagner, U.; Rau, C.; Chu, Y. S. Pushing the Limits: An Instrument for Hard X-Ray Imaging below 20 Nm. *J. Synchrotron Radiat.* **2015**, *22* (2), 336–341. https://doi.org/10.1107/S1600577514025715.

(97) Kalirai, S.; Boesenberg, U.; Falkenberg, G.; Meirer, F.; Weckhuysen, B. M. X-Ray Fluorescence Tomography of Aged Fluid-Catalytic-Cracking Catalyst Particles Reveals Insight into Metal Deposition Processes. *ChemCatChem* **2015**, *7* (22), 3674–3682.

https://doi.org/10.1002/cctc.201500710.

(98) Meirer, F.; Kalirai, S.; Morris, D.; Soparawalla, S.; Liu, Y.; Mesu, G.; Andrews, J. C.; Weckhuysen, B. M. Life and Death of a Single Catalytic Cracking Particle. *Sci. Adv.* **2015**, *1* (3), e1400199. https://doi.org/10.1126/sciadv.1400199.

(99) Liu, Y.; Meirer; Krest, C. M.; Webb, S.; Weckhuysen, B. M. Relating Structure and Composition with Accessibility of a Single Catalyst Particle Using Correlative 3-Dimensional Micro-Spectroscopy. *Nat. Commun.* **2016**, *7*, 12634. https://doi.org/10.1038/ncomms12634.

(100) Naredi-Rainer, N.; Prescher, J.; Hartschuh, A.; Lamb, D. C. *Confocal Microscopy*, in *Fluorescence Microscopy*; Wiley-VCH, Weinheim, **2017**, pp. 165–202. https://doi.org/10.1002/9783527687732.ch5.

(101) Buurmans, I. L. C.; Ruiz-Martínez, J.; Knowles, W. V.; Van Der Beek, D.; Bergwerff, J. A.; Vogt, E. T. C.; Weckhuysen, B. M. Catalytic Activity in Individual Cracking Catalyst Particles Imaged throughout Different Life Stages by Selective Staining. *Nat. Chem.* **2011**, *3* (11), 862–867. https://doi.org/10.1038/nchem.1148.

(102) Buurmans, I. L. C.; Ruiz-martínez, J.; Leeuwen, S. L. Van; Beek, D. Van Der; Bergwerff, J. A.; Knowles, W. V; Vogt, E. T. C.; Weckhuysen, B. M. Staining of Fluid-Catalytic-Cracking Catalysts : Localising Brønsted Acidity within a Single Catalyst Particle. *Chem. Eur. J.* **2012**, *18* (4), 1094–1101. https://doi.org/10.1002/chem.201102949.

(103) Maris, J. J. E. Mapping Porous Solid Catalysts with Fluorescent Molecules and Nanoparticles, Utrecht University, **2023**. https://doi.org/10.33540/1774.

(104) Han, S.; Hermans, T. M.; Fuller, P. E.; Wei, Y.; Grzybowski, B. A. Transport into Metal-Organic Frameworks from Solution Is Not Purely Diffusive. *Angew. Chem. Int. Ed.* **2012**, *51* (11), 2662–2666. https://doi.org/10.1002/anie.201108492.

(105) Fu, Q.; Rao, G. V. R.; Ista, L. K.; Wu, Y.; Andrzejewski, B. P.; Sklar, L. A.; Ward, T. L.; López, G. P. Control of Molecular Transport through Stimuli-Responsive Ordered Mesoporous Materials. *Adv. Mater.* **2003**, *15* (15), 1262–1266. https://doi.org/10.1002/adma.200305165.

(106) Sato, T.; Nakatani, K. Analysis of Distribution and Intraparticle Diffusion of a Fluorescent Dye in Mesoporous Silica Gel by Confocal Fluorescence Microspectroscopy. *Anal. Sci.* **2017**, *33* (2), 179–183. https://doi.org/10.2116/analsci.33.179.

(107) Maris, J. J. E.; Ganjkhanlou, Y.; Versluis, C.; Mayorga González, R.; Nikolopoulos, N.; Rabouw, F. T.; Vogt, E. T. C.; Weckhuysen, B. M.; Meirer, F. Carbon Dots and Their Conjugated Fluorophores for Mapping Heterogeneous Catalyst Composition and Properties. **2023**, In Preparation.

(108) Schütz, G. J.; Schindler, H.; Schmidt, T. Single-Molecule Microscopy on Model Membranes Reveals Anomalous Diffusion. *Biophys. J.* **1997**, *73* (2), 1073–1080. https://doi.org/10.1016/S0006-3495(97)78139-6.

(109) Amico, M. D.; Schiro, G.; Cupane, A.; Alfonso, L. D.; Leone, M.; Militello, V.; Vetri, V.; Archira, V.; Palermo, I.-. High fluorescence of thioflavinT confined in Mesoporous Silica Xerogels. Langmuir **2013**, 29, 32, 10238–10246. https://doi.org/10.1021/la402406g.

(110) Weiss, A. M.; Saraidarov, T.; Reisfeld, R. Confocal Microscopy for Characterization of Porous Sol ± Gel Glasses Incorporating Luminescent Dyes. *Optical Materials* **2001**, *16*, 15–20. https://doi.org/10.1016/S0925-3467(00)00054-9

(111) Cuenca, A.; Bodiguel, H. Fluorescence Photobleaching to Evaluate Flow Velocity and

Hydrodynamic Dispersion in Nanoslits. *Lab Chip* **2012**, *12* (9), 1672–1679. https://doi.org/10.1039/c2lc21232c.

(112) Persson, F.; Fritzsche, J.; Mir, K. U.; Modesti, M.; Westerlund, F. Lipid-Based Passivation in Nano fluidics. *Nano Lett*. **2012**. 12, 5, 2260–2265. https://doi.org/10.1021/nl204535h.

(113) Carroll, N. J.; Jensen, K. H.; Parsa, S.; Holbrook, N. M.; Weitz, D. A. Measurement of Flow Velocity and Inference of Liquid Viscosity in a Microfluidic Channel by Fluorescence Photobleaching. *Langmuir* **2014**, *30* (16), 4868–4874. https://doi.org/10.1021/la404891g.

(114) Zhang, L.; Cao, X.; Cai, W. Observations of the Effect of Confined Space on Fluorescence and Diffusion Properties of Molecules in Single Conical Nanopore Channels*. J. Fluoresc.* **2011**, 21 1865–1870. https://doi.org/10.1007/s10895-011-0881-8.

(115) Teng, X.; Li, F.; Lu, C. Visualization of Materials Using the Confocal Laser Scanning Microscopy Technique. *Chem. Soc. Rev.* **2020**, *49* (8), 2408–2425. https://doi.org/10.1039/C8CS00061A.

(116) Werny, M. J.; Siebers, K. B.; Friederichs, N. H.; Hendriksen, C.; Meirer, F.; Weckhuysen, B. M. Advancing the Compositional Analysis of Olefin Polymerization Catalysts with High-Throughput Fluorescence Microscopy. *J. Am. Chem. Soc.* **2022**, *144* (46), 21287–21294. https://doi.org/10.1021/jacs.2c09159.

(117) Bienz, S.; van Vreeswijk, S. H.; Pandey, Y.; Bartolomeo, G. L.; Weckhuysen, B. M.; Zenobi, R.; Kumar, N. Probing Coke Formation during the Methanol-to-Hydrocarbon Reaction on Zeolite ZSM-5 Catalyst at the Nanoscale Using Tip-Enhanced Fluorescence Microscopy. *Catal. Sci. Technol.* **2022**, *12* (19), 5795–5801. https://doi.org/10.1039/D2CY01348G.

(118) Mores, D.; Stavitski, E.; Verkleij, S. P.; Lombard, A.; Cabiac, A.; Rouleau, L.; Patarin, J.; Simon-Masseron, A.; Weckhuysen, B. M. Core–Shell H-ZSM-5/Silicalite-1 Composites: Brønsted Acidity and Catalyst Deactivation at the Individual Particle Level. *Phys. Chem. Chem. Phys.* **2011**, *13* (35), 15985. https://doi.org/10.1039/c1cp21324e.

(119) Maris, J. J. E.; Fu, D.; Meirer, F.; Weckhuysen, B. M. Single - Molecule Observation of Diffusion and Catalysis in Nanoporous Solids. *Adsorption* **2021**, (27),423–452. https://doi.org/10.1007/s10450-020-00292-7.

(120) Wu, H.; Schwartz, D. K. Nanoparticle Tracking to Probe Transport in Porous Media. *Acc. Chem. Res.* **2020**, *53* (10), 2130–2139. https://doi.org/10.1021/acs.accounts.0c00408.

(121) Vangindertael, J.; Camacho, R.; Sempels, W.; Mizuno, H.; Dedecker, P.; Janssen, K. P. F. An Introduction to Optical Super-Resolution Microscopy for the Adventurous Biologist. *Methods Appl. Fluoresc.* **2018**, *6,* 022003. https://doi.org/10.1088/2050-6120/aaae0c.

(122) Chen, P.; Zhou, X.; Shen, H.; Andoy, N. M.; Choudhary, E.; Han, K.-S.; Liu, G.; Meng, W. Single-Molecule Fluorescence Imaging of Nanocatalytic Processes. *Chem. Soc. Rev.* **2010**, *39*, 4560-4570. https://doi.org/10.1039/b909052p.

(123) De Cremer, G.; Roeffaers, M. B. J.; Bartholomeeusen, E.; Lin, K.; Dedecker, P.; Pescarmona, P. P.; Jacobs, P. A.; De Vos, D. E.; Hofkens, J.; Sels, B. F. High-Resolution Single-Turnover Mapping Reveals Intraparticle Diffusion Limitation in Ti-MCM-41-Catalyzed Epoxidation. *Angew. Chem. Int. Ed.* **2010**, *49* (5), 908–911. https://doi.org/10.1002/anie.200905039.

(124) Janssen, K. P. F.; De Cremer, G.; Neely, R. K.; Kubarev, A. V.; Van Loon, J.; Martens, J. A.; De Vos, D. E.; Roeffaers, M. B. J.; Hofkens, J. Single Molecule Methods for the Study of Catalysis: From Enzymes to Heterogeneous Catalysts. *Chem. Soc. Rev.* **2014**, *43* (4), 990–1006. https://doi.org/10.1039/C3CS60245A.

(125) Roeffaers, M. B. â. J.; DeCremer, G.; Libeert, J.; Ameloot, R.; Dedecker, P.; Bons, A.-J.; Buckins, M.; Martens, J. A.; Sels, B. F.; De Vos, D. E.; Hofkens, J. Super-Resolution Reactivity Mapping of Nanostructured Catalyst Particles. *Angew. Chem. Int. Ed.* **2009**, *48* (49), 9285–9289. https://doi.org/10.1002/anie.200904944.

(126) Weckhuysen, B. M. Chemical Imaging of Spatial Heterogeneities in Catalytic Solids at Different Length and Time Scales. *Angew. Chem. Int. Ed.* **2009**, *48* (27), 4910–4943. https://doi.org/10.1002/anie.200900339.

(127) Aloi, A.; Vilanova, N.; Albertazzi, L.; Voets, I. K. IPAINT: A General Approach Tailored to Image the Topology of Interfaces with Nanometer Resolution. *Nanoscale* **2016**, *8* (16), 8712–8716. https://doi.org/10.1039/C6NR00445H.

(128) Katrukha, E. A., Cloin, B., Teeuw, J. & Kapitein, L. C. Detection of Molecules Plugin for ImageJ. Utrecht University. **2017**. https://github.com/UU-cellbiology/DoM_Utrecht.

(129) Dedecker, P.; Duwé, S.; Neely, R. K.; Zhang, J. Localizer: Fast, Accurate, Open-Source, and Modular Software Package for Superresolution Microscopy. *J. Biomed. Opt.* **2012**, *17* (12), 126008. https://doi.org/10.1117/1.JBO.17.12.126008.

(130) Manzo, C.; Garcia-Parajo, M. F. A Review of Progress in Single Particle Tracking: From Methods to Biophysical Insights. *Reports Prog. Phys.* **2015**, *78* (12), 124601. https://doi.org/10.1088/0034-4885/78/12/124601.

(131) Crocker, J. C.; Grier, D. G. Methods of Digital Video Microscopy for Colloidal Studies. *J. Colloid Interface Sci.* **1996**, *179* (1), 298–310. https://doi.org/10.1006/jcis.1996.0217.

(132) Wöll, D.; Kölbl, C.; Stempfle, B.; Karrenbauer, A. A Novel Method for Automatic Single Molecule Tracking of Blinking Molecules at Low Intensities. *Phys. Chem. Chem. Phys.* **2013**, *15* (17), 6196. https://doi.org/10.1039/c3cp44693j.

(133) Vogelsang, J.; Kasper, R.; Steinhauer, C.; Person, B.; Heilemann, M.; Sauer, M.; Tinnefeld, P. A Reducing and Oxidizing System Minimizes Photobleaching and Blinking of Fluorescent Dyes. *Angew. Chem. Int. Ed.* **2008**, *47* (29), 5465–5469. https://doi.org/10.1002/anie.200801518.

(134) Fu, D.; Maris, J. J. E.; Stanciakova, K.; Nikolopoulos, N.; Heijden, O.; Mandemaker, L. D. B.; Siemons, M. E.; Salas Pastene, D.; Kapitein, L. C.; Rabouw, F. T.; Meirer, F.; Weckhuysen, B. M. Unravelling Channel Structure–Diffusivity Relationships in Zeolite ZSM-5 at the Single-Molecule Level. *Angew. Chem. Int. Ed.* **2022**, *61* (5). https://doi.org/10.1002/anie.202114388.

(135) Berglund, A. J. Statistics of Camera-Based Single-Particle Tracking. *Phys. Rev. E* **2010**, *82* (1), 011917. https://doi.org/10.1103/PhysRevE.82.011917.

(136) Michalet, X.; Berglund, A. J. Optimal Diffusion Coefficient Estimation in Single-Particle Tracking. *Phys. Rev. E - Stat. Nonlinear, Soft Matter Phys.* **2012**, *85* (6), 1–14. https://doi.org/10.1103/PhysRevE.85.061916.

(137) Vestergaard, C. L.; Blainey, P. C.; Flyvbjerg, H. Optimal Estimation of Diffusion Coefficients from Single-Particle Trajectories. *Phys. Rev. E* **2014**, *89* (2), 022726. https://doi.org/10.1103/PhysRevE.89.022726.

(138) Qian, H.; Sheetz, M. P.; Elson, E. L. Single Particle Tracking. Analysis of Diffusion and Flow in Two-Dimensional Systems. *Biophys. J.* **1991**, *60* (4), 910–921. https://doi.org/10.1016/S0006-3495(91)82125-7.

(139) Maris, J. J. E.; Rabouw, F. T.; Weckhuysen, B. M.; Meirer, F. Classification-Based Motion Analysis of Single-Molecule Trajectories Using DiffusionLab. *Sci. Rep.* **2022**, *12* (1), 9595.

https://doi.org/10.1038/s41598-022-13446-0.

(140) Metzler, R.; Jeon, J. H.; Cherstvy, A. G.; Barkai, E. Anomalous Diffusion Models and Their Properties: Non-Stationarity, Non-Ergodicity, and Ageing at the Centenary of Single Particle Tracking. *Phys. Chem. Chem. Phys.* **2014**, *16* (44), 24128–24164. https://doi.org/10.1039/c4cp03465a.

(141) Jung, C.; Hellriegel, C.; Michaelis, J.; Bräuchle, C. Single-Molecule Traffic in Mesoporous Materials: Translational, Orientational, and Spectral Dynamics. *Adv. Mater.* **2007**, *19* (7), 956–960. https://doi.org/10.1002/adma.200602173.

(142) Jung, C.; Hellriegel, C.; Platschek, B.; Wöhrle, D.; Bein, T.; Michaelis, J.; Bräuchle, C. Simultaneous Measurement of Orientational and Spectral Dynamics of Single Molecules in Nanostructured Host−Guest Materials. *J. Am. Chem. Soc.* **2007**, *129* (17), 5570–5579. https://doi.org/10.1021/ja0684850.

(143) Hellriegel, C.; Kirstein, J.; Bräuchle, C. Tracking of Single Molecules as a Powerful Method to Characterize Diffusivity of Organic Species in Mesoporous Materials. *New J. Phys.* **2005**, *7* (23), 23–23. https://doi.org/10.1088/1367-2630/7/1/023.

(144) Hellriegel, C.; Kirstein, J.; Bräuchle, C.; Latour, V.; Pigot, T.; Olivier, R.; Lacombe, S.; Brown, R.; Guieu, V.; Payrastre, C.; Izquierdo, A.; Mocho, P. Diffusion of Single Streptocyanine Molecules in the Nanoporous Network of Sol−Gel Glasses. *J. Phys. Chem. B* **2004**, *108* (38), 14699–14709. https://doi.org/10.1021/jp049412a.

(145) McCain, K. S.; Hanley, D. C.; Harris, J. M. Single-Molecule Fluorescence Trajectories for Investigating Molecular Transport in Thin Silica Sol−Gel Films. *Anal. Chem.* **2003**, *75* (17), 4351–4359. https://doi.org/10.1021/ac0345289.

(146) Seebacher, C.; Hellriegel, C.; Deeg, F.-W.; Bräuchle, C.; Altmaier, S.; Behrens, P.; Müllen, K. Observation of Translational Diffusion of Single Terrylenediimide Molecules in a Mesostructured Molecular Sieve. *J. Phys. Chem. B,* **2002**, *106* (22), 5591–5595. https://doi.org/10.1021/jp013198y.

(147) Kirstein, J.; Platschek, B.; Jung, C.; Brown, R.; Bein, T.; Bräuchle, C. Exploration of Nanostructured Channel Systems with Single-Molecule Probes. *Nat. Mater.* **2007**, *6* (4), 303–310. https://doi.org/10.1038/nmat1861.

(148) Zürner, A.; Kirstein, J.; Döblinger, M.; Bräuchle, C.; Bein, T. Visualizing Single-Molecule Diffusion in Mesoporous Materials. *Nature* **2007**, *450* (7170), 705–708. https://doi.org/10.1038/nature06398.

(149) Liao, Y.; Yang, S. K.; Koh, K.; Matzger, A. J.; Biteen, J. S. Heterogeneous Single-Molecule Diffusion in One-, Two-, and Three-Dimensional Microporous Coordination Polymers: Directional, Trapped, and Immobile Guests. *Nano Lett.* **2012**, *12* (6), 3080–3085. https://doi.org/10.1021/nl300971t.

(150) Hendriks, F. C.; Meirer, F.; Kubarev, A. V.; Ristanović, Z.; Roeffaers, M. B. J.; Vogt, E. T. C.; Bruijnincx, P. C. A.; Weckhuysen, B. M. Single-Molecule Fluorescence Microscopy Reveals Local Diffusion Coefficients in the Pore Network of an Individual Catalyst Particle. *J. Am. Chem. Soc.* **2017**, *139* (39), 13632–13635. https://doi.org/10.1021/jacs.7b07139.

(152) Eichmann, S. L.; Anekal, S. G.; Bevan, M. A. Electrostatically Confined Nanoparticle Interactions and Dynamics. *Langmuir* **2008**, *24* (3), 714–721. https://doi.org/10.1021/la702571z.

(153) Lin, B.; Yu, J.; Rice, S. A. Direct Measurements of Constrained Brownian Motion of an Isolated

Sphere between Two Walls. *Phys. Rev. E* **2000**, *62* (3), 3909–3919. https://doi.org/10.1103/PhysRevE.62.3909.

(154) Skaug, M. J.; Schwartz, D. K. Tracking Nanoparticle Diffusion in Porous Filtration Media. *Ind. Eng. Chem. Res.* **2015**, *54* (16), 4414–4419. https://doi.org/10.1021/ie503895b.

(155) Skaug, M. J.; Wang, L.; Ding, Y.; Schwartz, D. K.; Engineering, B.; Engineering, M.; Science, M.; Program, E.; Boulder, C.; States, U. Hindered Nanoparticle Diffusion and Void Accessibility in a Three- Dimensional Porous Medium. *ACS Nano* **2015**, *9 (2)*, 2148–2156 . https://doi.org/10.1021/acsnano.5b00019.

(156) Blom, H.; Hassler, K.; Chmyrov, A.; Widengren, J. Electrostatic Interactions of Fluorescent Molecules with Dielectric Interfaces Studied by Total Internal Reflection Fluorescence Correlation Spectroscopy. *Int. J. Mol. Sci.* **2010**, *11* (2), 386–406. https://doi.org/10.3390/ijms11020386.

(157) Wang, D.; Wu, H.; Schwartz, D. K. Three-Dimensional Tracking of Interfacial Hopping Diffusion. *Phys. Rev. Lett.* **2017**, *119* (26), 268001 https://doi.org/10.1103/PhysRevLett.119.268001.

(158) Wang, D.; Schwartz, D. K. Non-Brownian Interfacial Diffusion: Flying, Hopping, and Crawling. *J. Phys. Chem. C* **2020**, *124* (37), 19880–19891. https://doi.org/10.1021/acs.jpcc.0c05834.

(159) Sen, T.; Barisik, M. Internal Surface Electric Charge Characterization of Mesoporous Silica. *Sci. Rep.* **2019**, *9* (1), 137. https://doi.org/10.1038/s41598-018-36487-w.

(160) Sparreboom, W.; Van Den Berg, A.; Eijkel, J. C. T. Principles and Applications of Nanofluidic Transport. *Nat. Nanotechnol.* **2009**, *4* (11), 713–720. https://doi.org/10.1038/nnano.2009.332.

(161) Wu, H.; Wang, D.; Schwartz, D. K. Connecting Hindered Transport in Porous Media across Length Scales: From Single-Pore to Macroscopic. *J. Phys. Chem. Lett.* **2020**, *11* (20), 8825–8831. https://doi.org/10.1021/acs.jpclett.0c02738.

(162) Wu, H.; Sarfati, R.; Wang, D.; Schwartz, D. K. Electrostatic Barriers to Nanoparticle Accessibility of a Porous Matrix. *J. Am. Chem. Soc.* **2020**, *142* (10), 4696–4704. https://doi.org/10.1021/jacs.9b12096.

(163) Chen, Z.; Li, P.; Anderson, R.; Wang, X.; Zhang, X.; Robison, L.; Redfern, L. R.; Moribe, S.; Islamoglu, T.; Gómez-Gualdrón, D. A.; Yildirim, T.; Stoddart, J. F.; Farha, O. K. Balancing Volumetric and Gravimetric Uptake in Highly Porous Materials for Clean Energy. *Science* **2020**, *368* (6488), 297–303. https://doi.org/10.1126/science.aaz8881.

(164) Sung Kim, H.; Weston, M.; Fuller, P.; Siu, P. US Patent Application US20150352519A1, **2015**.

(165) G. M. Tom, P. W.-M. Siu, J. Arno, O. K. F. and R. V. US Patent Application US20190091620A1, **2018**.

(166) Weston, S. P. W.-M. and M. H. US Patent, 10260148B2, **2019**.

(167) Furukawa, H.; Cordova, K. E.; O'Keeffe, M.; Yaghi, O. M. The Chemistry and Applications of Metal-Organic Frameworks. *Science* **2013**, 341 (6149), 1230444 . https://doi.org/10.1126/science.1230444.

(168) Morven Duncan , St Andrews , Fife ; Stewart Warrender , St Andrews , Fife ; Russell Edward Morris , St Andrews , Fife ; Damiano Cattaneo , St Andrews, F. US Patent Application US20180264033A1, **2018**.

(169) Horcajada, P.; Gref, R.; Baati, T.; Allan, P. K.; Maurin, G.; Couvreur, P.; Férey, G.; Morris, R. E.; Serre, C. Metal-Organic Frameworks in Biomedicine. *Chem. Rev*., **2012**, 112, 2, 1232–1268. https://doi.org/10.1021/cr200256v.

(170) Sun, L.; Campbell, M. G.; Dincă, M. Elektrisch Leitfähige Poröse Metall-Organische Gerüstverbindungen. *Angew. Chem. Int. Ed.* **2016**, *55* (11), 3566–3579. https://doi.org/10.1002/ange.201506219.

(171) Li, J. R.; Sculley, J.; Zhou, H. C. Metal-Organic Frameworks for Separations. *Chem. Rev.* **2012**, 112(2), 869–932. https://doi.org/10.1021/cr200190s.

(172) Li, J. R.; Kuppler, R. J.; Zhou, H. C. Selective Gas Adsorption and Separation in Metal-Organic Frameworks. *Chem. Soc. Rev.* **2009**, *38* (5), 1477–1504. https://doi.org/10.1039/b802426j.

(173) Savage, M.; Cheng, Y.; Easun, T. L.; Eyley, J. E.; Argent, S. P.; Warren, M. R.; Lewis, W.; Murray, C.; Tang, C. C.; Frogley, M. D.; Cinque, G.; Sun, J.; Rudić, S.; Murden, R. T.; Benham, M. J.; Fitch, A. N.; Blake, A. J.; Ramirez-Cuesta, A. J.; Yang, S.; Schröder, M. Selective Adsorption of Sulfur Dioxide in a Robust Metal–Organic Framework Material. *Adv. Mater.* **2016**, *28* (39), 8705–8711. https://doi.org/10.1002/adma.201602338.

(174) Han, X.; Godfrey, H. G. W.; Briggs, L.; Davies, A. J.; Cheng, Y.; Daemen, L. L.; Sheveleva, A. M.; Tuna, F.; McInnes, E. J. L.; Sun, J.; Drathen, C.; George, M. W.; Ramirez-Cuesta, A. J.; Thomas, K. M.; Yang, S.; Schröder, M. Reversible Adsorption of Nitrogen Dioxide within a Robust Porous Metal–Organic Framework. *Nat. Mat*., **2018**, (17), 691–696. https://doi.org/10.1038/s41563-018-0104-7.

(175) Leclerc, H.; Vimont, A.; Lavalley, J. C.; Daturi, M.; Wiersum, A. D.; Llwellyn, P. L.; Horcajada, P.; Férey, G.; Serre, C. Infrared Study of the Influence of Reducible Iron(Iii) Metal Sites on the Adsorption of CO, CO_2, Propane, Propene and Propyne in the Mesoporous Metal-Organic Framework MIL-100. *Phys. Chem. Chem. Phys.* **2011**, *13* (24), 11748–11756. https://doi.org/10.1039/c1cp20502a.

(176) Yoon, J. W.; Seo, Y. K.; Hwang, Y. K.; Chang, J. S.; Leclerc, H.; Wuttke, S.; Bazin, P.; Vimont, A.; Daturi, M.; Bloch, E.; Llewellyn, P. L.; Serre, C.; Horcajada, P.; Grenèche, J. M.; Rodrigues, A. E.; Férey, G. Controlled Reducibility of a Metal-Organic Framework with Coordinatively Unsaturated Sites for Preferential Gas Sorption. *Angew. Chem. Int. Ed.* **2010**, *49* (34), 5949–5952. https://doi.org/10.1002/anie.201001230.

(177) Murray, L. J.; Dinca, M.; Yano, J.; Chavan, S.; Bordiga, S.; Brown, C. M.; Long, J. R. Highly-Selective and Reversible O_2 Binding in Cr_3(1,3,5-Benzenetricarboxylate)$_2$. *J. Am. Chem. Soc.* **2010**, *132* (23), 7856–7857. https://doi.org/10.1021/ja1027925.

(178) Reed, D. A.; Keitz, B. K.; Oktawiec, J.; Mason, J. A.; Runcevski, T.; Xiao, D. J.; Darago, L. E.; Crocellà, V.; Bordiga, S.; Long, J. R. A Spin Transition Mechanism for Cooperative Adsorption in Metal-Organic Frameworks. *Nature* **2017**, *550*, 96–100. https://doi.org/10.1038/nature23674.

(179) Lu, Z.; Godfrey, H. G. W.; Da Silva, I.; Cheng, Y.; Savage, M.; Tuna, F.; McInnes, E. J. L.; Teat, S. J.; Gagnon, K. J.; Frogley, M. D.; Manuel, P.; Rudić, S.; Ramirez-Cuesta, A. J.; Easun, T. L.; Yang, S.; Schröder, M. Modulating Supramolecular Binding of Carbon Dioxide in a Redox-Active Porous Metal-Organic Framework. *Nat. Commun.* **2017**, *8*, 14212. https://doi.org/10.1038/ncomms14212.

(180) Wu, H.; Gong, Q.; Olson, D. H.; Li, J. Commensurate Adsorption of Hydrocarbons and Alcohols in Microporous Metal Organic Frameworks. *Chem. Rev*., **2012**, 112 (2), 836–868. https://doi.org/10.1021/cr200216x.

(181) Rodenas, T.; Luz, I.; Prieto, G.; Seoane, B.; Miro, H.; Corma, A.; Kapteijn, F.; Llabrés I Xamena, F. X.; Gascon, J. Metal-Organic Framework Nanosheets in Polymer Composite Materials for Gas Separation. *Nat. Mater.* **2015**, *14* (1), 48–55. https://doi.org/10.1038/nmat4113.

(182) Rodenas, T.; Van Dalen, M.; García-Pérez, E.; Serra-Crespo, P.; Zornoza, B.; Kapteijn, F.; Gascon, J. Visualizing MOF Mixed Matrix Membranes at the Nanoscale: Towards Structure-Performance Relationships in CO_2/CH_4 Separation over NH_2-MIL-53(Al)@PI. *Adv. Funct. Mater.* **2014**, *24* (2), 249–256. https://doi.org/10.1002/adfm.201203462.

(183) Dechnik, J.; Gascon, J.; Doonan, C. J.; Janiak, C.; Sumby, C. J. Mixed-Matrix-Membranen. *Angew. Chem. Int. Ed.* **2017**, *56* (32), 9292–9310. https://doi.org/10.1002/ange.201701109.

(184) Llewellyn, P. L.; Bourrelly, S.; Vagner, C.; Heymans, N.; Leclerc, H.; Ghoufi, A.; Bazin, P.; Vimont, A.; Daturi, M.; Devic, T.; Serre, C.; De Weireld, G.; Maurin, G. Evaluation of MIL-47(V) for CO_2-Related Applications. *J. Phys. Chem. C* **2013**, *117* (2), 962–970. https://doi.org/10.1021/jp308525k.

(185) Salles, F.; Jobic, H.; Devic, T.; Guillerm, V.; Serre, C.; Koza, M. M.; Ferey, G.; Maurin, G. Diffusion of Binary CO_2/CH_4 Mixtures in the MIL-47(V) and MIL-53(Cr) Metal-Organic Framework Type Solids: A Combination of Neutron Scattering Measurements and Molecular Dynamics Simulations. *J. Phys. Chem. C* **2013**, *117* (21), 11275–11284. https://doi.org/10.1021/jp403225t.

(186) Salles, F.; Jobic, H.; Devic, T.; Llewellyn, P. L.; Serre, C.; Férey, G.; Maurin, G. Self and Transport Diffusivity of CO_2 in the Metal-Organic Framework MIL-47(V) Explored by Quasi-Elastic Neutron Scattering Experiments and Molecular Dynamics Simulations. *ACS Nano* **2010**, *4* (1), 143–152. https://doi.org/10.1021/nn901132k.

(187) Salles, F.; Ghoufi, A.; Maurin, G.; Bell, R. G.; Mellot-Draznieks, C.; Férey, G. Molecular Dynamics Simulations of Breathing MOFs: Structural Transformations of MIL-53(Cr) upon Thermal Activation and CO_2 Adsorption. *Angew. Chem. Int. Ed.* **2008**, *47* (44), 8487–8491. https://doi.org/10.1002/anie.200803067.

(188) Salles, F.; Kolokolov, D. I.; Jobic, H.; Maurin, G.; Llewellyn, P. L.; Devic, T.; Serre, C.; Ferey, G. Adsorption and Diffusion of H_2 in the MOF Type Systems MIL-47(V) and Mil-53(Cr): A Combination of Microcalorimetry and Qens Experiments with Molecular Simulations. *J. Phys. Chem. C* **2009**, *113* (18), 7802–7812. https://doi.org/10.1021/jp811190g.

(189) Salles, F.; Jobic, H.; Maurin, G.; Koza, M. M.; Llewellyn, P. L.; Devic, T.; Serre, C.; Ferey, G. Experimental Evidence Supported by Simulations of a Very High H2 Diffusion in Metal Organic Framework Materials. *Phys. Rev. Lett.* **2008**, *100*, 245901. https://doi.org/10.1103/PhysRevLett.100.245901.

(190) Jobic, H.; Rosenbach, N.; Ghoufi, A.; Kolokolov, D. I.; Yot, P. G.; Devic, T.; Serre, C.; Férey, G.; Maurin, G. Unusual Chain-Length Dependence of the Diffusion of n-Alkanes in the Metal-Organic Framework MIL-47(V): The Blowgun Effect. *Chem. Eur. J.* **2010**, *16* (34), 10337–10341. https://doi.org/10.1002/chem.201001521.

(191) Rives, S.; Jobic, H.; Ragon, F.; Devic, T.; Serre, C.; Férey, G.; Ollivier, J.; Maurin, G. Diffusion of Long Chain N-Alkanes in the Metal-Organic Framework MIL-47(V): A Combination of Neutron Scattering Experiments and Molecular Dynamics Simulations. *Microporous Mesoporous Mater.* **2012**, *164*, 259–265. https://doi.org/10.1016/j.micromeso.2012.06.056.

(192) Déroche, I.; Rives, S.; Trung, T.; Yang, Q.; Ghoufi, A.; Ramsahye, N. A.; Trens, P.; Fajula, F.; Devic, T.; Serre, C.; Férey, G.; Jobic, H.; Maurin, G. Exploration of the Long-Chain N -Alkanes Adsorption and Diffusion in the MOF-Type MIL-47 (V) Material by Combining Experimental

and Molecular Simulation Tools. *J. Phys. Chem. C* **2011**, *115* (28), 13868–13876. https://doi.org/10.1021/jp2039527.

(193) Ghoufi, A.; Maurin, G. Single-File Diffusion of Neo-Pentane Confined in the MIL-47(V) Metal-Organic Framework. *J. Phys. Chem. C* **2019**, *123* (28), 17360–17367. https://doi.org/10.1021/acs.jpcc.9b04308.

(194) Kulkarni, A. R.; Sholl, D. S. DFT-Derived Force Fields for Modeling Hydrocarbon Adsorption in MIL-47(V). *Langmuir* **2015**, *31* (30), 8453–8468. https://doi.org/10.1021/acs.langmuir.5b01193.

(195) Rives, S.; Jobic, H.; Kolokolov, D. I.; Gabrienko, A. A.; Stepanov, A. G.; Ke, Y.; Frick, B.; Devic, T.; Férey, G.; Maurin, G. Diffusion of Xylene Isomers in the MIL-47(V) MOF Material: A Synergic Combination of Computational and Experimental Tools. *J. Phys. Chem. C* **2013**, *117* (12), 6293–6302. https://doi.org/10.1021/jp400507w.

(196) Kolokolov, D. I.; Jobic, H.; Stepanov, A. G.; Ollivier, J.; Rives, S.; Maurin, G.; Devic, T.; Serre, C.; Férey, G. Experimental and Simulation Evidence of a Corkscrew Motion for Benzene in the Metal-Organic Framework MIL-47. *J. Phys. Chem. C* **2012**, *116* (28), 15093–15098. https://doi.org/10.1021/jp302995b.

(197) Alaerts, L.; Maes, M.; Jacobs, P. A.; Denayer, J. F. M.; De Vos, D. E. Activation of the Metal-Organic Framework MIL-47 for Selective Adsorption of Xylenes and Other Difunctionalized Aromatics. *Phys. Chem. Chem. Phys.* **2008**, *10* (20), 2979–2985. https://doi.org/10.1039/b719513c.

(198) Finsy, V.; Verelst, H.; Alaerts, L.; De Vos, D.; Jacobs, P. A.; Baron, G. V.; Denayer, J. F. M. Pore-Filling-Dependent Selectivity Effects in the Vapor-Phase Separation of Xylene Isomers on the Metal-Organic Framework MIL-47. *J. Am. Chem. Soc.* **2008**, *130* (22), 7110–7118. https://doi.org/10.1021/ja800686c.

(199) Alaerts, L.; Kirschhock, C. E. A.; Maes, M.; Van Der Veen, M. A.; Finsy, V.; Depla, A.; Martens, J. A.; Baron, G. V.; Jacobs, P. A.; Denayer, J. F. M.; De Vos, D. E. Selective Adsorption and Separation of Xylene Isomers and Ethylbenzene with the Microporous Vanadium(IV) Terephthalate MIL-47. *Angew. Chem. Int. Ed.* **2007**, *46* (23), 4293–4297. https://doi.org/10.1002/anie.200700056.

(200) Ghysels, A.; Vandichel, M.; Verstraelen, T.; van der Veen, M. A.; De Vos, D. E.; Waroquier, M.; Van Speybroeck, V. Host–Guest and Guest–Guest Interactions between Xylene Isomers Confined in the MIL-47(V) Pore System, in *Theoretical Chemistry in Belgium*, Springer, Berlin, **2014**, pp. 35–47. https://doi.org/10.1007/978-3-642-41315-5_4.

(201) Furukawa, S.; Reboul, J.; Diring, S.; Sumida, K.; Kitagawa, S. Structuring of Metal-Organic Frameworks at the Mesoscopic/Macroscopic Scale. *Chem. Soc. Rev.* **2014**, *43* (16), 5700–5734. https://doi.org/10.1039/c4cs00106k.

(202) Zhang, D.; Zhu, Y.; Liu, L.; Ying, X.; Hsiung, C.-E.; Sougrat, R.; Li, K.; Han, Y. Atomic-Resolution Transmission Electron Microscopy of Electron Beam–Sensitive Crystalline Materials. *Science* **2018**, *359* (6376), 675–679. https://doi.org/10.1126/science.aao0865.

(203) Ferreira Sanchez, D.; Ihli, J.; Zhang, D.; Rohrbach, T.; Zimmermann, P.; Lee, J.; Borca, C. N.; Böhlen, N.; Grolimund, D.; van Bokhoven, J. A.; Ranocchiari, M. Spatio-Chemical Heterogeneity of Defect-Engineered Metal–Organic Framework Crystals Revealed by Full-Field Tomographic X-Ray Absorption Spectroscopy. *Angew. Chem. Int. Ed.* **2021**, *60* (18), 10032–10039. https://doi.org/10.1002/anie.202013422.

(204) Soparawalla, S.; Weckhuysen, B. M.; Liu, Y.; Kalirai, S.; Andrews, J. C.; Morris, D.; Mesu, G.; Meirer, F. Life and Death of a Single Catalytic Cracking Particle. *Sci. Adv.* **2015**, *1* (3), e1400199. https://doi.org/10.1126/sciadv.1400199.

(205) Ameloot, R.; Vermoortele, F.; Hofkens, J.; De Schryver, F. C.; De Vos, D. E.; Roeffaers, M. B. J. Three-Dimensional Visualization of Defects Formed during the Synthesis of Metal-Organic Frameworks: A Fluorescence Microscopy Study. *Angew. Chem. Int. Ed.* **2013**, *52* (1), 401–405. https://doi.org/10.1002/ange.201205627.

(206) Choi, K. M.; Jeon, H. J.; Kang, J. K.; Yaghi, O. M. Heterogeneity within Order in Crystals of a Porous Metal-Organic Framework. *J. Am. Chem. Soc.* **2011**, *133* (31), 11920–11923. https://doi.org/10.1021/ja204818q.

(207) Fang, Z.; Bueken, B.; De Vos, D. E.; Fischer, R. A. Defect-Engineered Metal-Organic Frameworks. *Angew. Chem. Int. Ed.* **2015**, *54* (25), 7234–7254. https://doi.org/10.1002/anie.201411540.

(208) Barthelet, K.; Marrot, J.; Riou, D.; Férey, G. A Breathing Hybrid Organic–Inorganic Solid with Very Large Pores and High Magnetic Characteristics. *Angew. Chem. Int. Ed.* **2002**, *41* (2), 281-284 . https://doi.org/10.1002/1521-3773(20020118)41:2<281::AID-ANIE281>3.0.CO;2-Y.

(209) Yot, P. G.; Ma, Q.; Haines, J.; Yang, Q.; Ghoufi, A.; Devic, T.; Serre, C.; Dmitriev, V.; Férey, G.; Zhong, C.; Maurin, G. Large Breathing of the MOF MIL-47(VIV) under Mechanical Pressure: A Joint Experimental-Modelling Exploration. *Chem. Sci.* **2012**, *3* (4), 1100–1104. https://doi.org/10.1039/c2sc00745b.

(210) Vanpoucke, D. E. P. Linker Functionalization in MIL-47(V)-R Metal-Organic Frameworks: Understanding the Electronic Structure. *J. Phys. Chem. C* **2017**, *121* (14), 8014–8022. https://doi.org/10.1021/acs.jpcc.7b01491.

(211) Andrews, J. C.; Weckhuysen, B. M. Hard X-Ray Spectroscopic Nano-Imaging of Hierarchical Functional Materials at Work. *ChemPhysChem* **2013**, *14* (16), 3655–3666. https://doi.org/10.1002/cphc.201300529.

(212) Liu, Y.; Meirer, F.; Williams, P. A.; Wang, J.; Andrews, J. C.; Pianetta, P. TXM-Wizard : A Program for Advanced Data Collection and Evaluation in Full-Field Transmission X-Ray Microscopy. *J. Synchrotron Radiat.* **2012**, *19* (2), 281–287. https://doi.org/10.1107/S0909049511049144.

(213) Qian, Q.; Ruiz-Martínez, J.; Mokhtar, M.; Asiri, A. M.; Al-Thabaiti, S. A.; Basahel, S. N.; Van Der Bij, H. E.; Kornatowski, J.; Weckhuysen, B. M. Single-Particle Spectroscopy on Large SAPO-34 Crystals at Work: Methanol-to-Olefin versus Ethanol-to-Olefin Processes. *Chem. Eur. J.* **2013**, *19* (34), 11204–11215. https://doi.org/10.1002/chem.201300540.

(214) Gallagher, S. H.; Schlauri, P.; Cesari, E.; Durrer, J.; Brühwiler, D. Silica Particles with Fluorescein-Labelled Cores for Evaluating Accessibility through Fluorescence Quenching by Copper. *Nanoscale Adv.* **2021**, *3* (22), 6459–6467. https://doi.org/10.1039/d1na00599e.

(215) Chmelik, C.; Gläser, R.; Haase, J.; Hwang, S.; Kärger, J. Application of Microimaging to Diffusion Studies in Nanoporous Materials. *Adsorption* **2021**, *27* (5), 819–840. https://doi.org/10.1007/s10450-020-00279-4.

(216) Kortunov, P.; Chmelik, C.; Kärger, J.; Rakoczy, R. A.; Ruthven, D. M.; Traa, Y.; Vasenkov, S.; Weitkamp, J. Sorption Kinetics and Intracrystalline Diffusion of Methanol in Ferrierite: An Example of Disguised Kinetics. *Adsorption* **2005**, *11* (3–4), 235–244. https://doi.org/10.1007/s10450-005-5396-7.

(217) Mitchell, S.; Michels, N. L.; Kunze, K.; Pérez-Ramírez, J. Visualization of Hierarchically Structured Zeolite Bodies from Macro to Nano Length Scales. *Nat. Chem.* **2012**, *4* (10), 825–831. https://doi.org/10.1038/nchem.1403.

(218) Zečević, J.; Gommes, C. J.; Friedrich, H.; Dejongh, P. E.; Dejong, K. P. Mesoporosity of ZeoliteY: Quantitative Three-Dimensional Study by Image Analysis of Electron Tomograms. *Angew. Chem. Int. Ed.* **2012**, *51* (17), 4213–4217. https://doi.org/10.1002/anie.201200317.

(219) Friedrich, H.; De Jongh, P. E.; Verkleij, A. J.; De Jong, K. P. Electron Tomography for Heterogeneous Catalysts and Related Nanostructured Materials. *Chem. Rev.* **2009**, *109* (5), 1613–1629. https://doi.org/10.1021/cr800434t.

(220) Díaz, I.; Alfredsson, V.; Sakamoto, Y. Transmission Electron Microscopy in Formation and Growth of Ordered Mesoporous Materials. *Curr. Opin. Colloid Interface Sci.* **2006**, *11* (5), 302–307. https://doi.org/10.1016/j.cocis.2006.09.007.

(221) Gommes, C. J.; Friedrich, H.; Wolters, M.; De Jongh, P. E.; De Jong, K. P. Quantitative Characterization of Pore Corrugation in Ordered Mesoporous Materials Using Image Analysis of Electron Tomograms. *Chem. Mater.* **2009**, *21* (7), 1311–1317. https://doi.org/10.1021/cm803092c.

(222) Winter, D. A. M. De; Meirer, F.; Weckhuysen, B. M. FIB-SEM Tomography Probes the Mesoscale Pore Space of an Individual Catalytic Cracking Particle. *ACS Catal.* **2016**, 6 (5), 3158–3167. https://doi.org/10.1021/acscatal.6b00302.

(223) Liu, Y.; Meirer, F. ; Krest, C. M.; Webb, S.; Weckhuysen, B. M. Relating Structure and Composition with Accessibility of a Single Catalyst Particle Using Correlative 3-Dimensional Micro-Spectroscopy. *Nat. Commun.* **2016**, *7*, 12634. https://doi.org/10.1038/ncomms12634.

(224) Dasilva, J. C.; Mader, K.; Holler, M.; Haberthür, D.; Diaz, A.; Guizar-Sicairos, M.; Cheng, W. C.; Shu, Y.; Raabe, J.; Menzel, A.; Vanbokhoven, J. A. Assessment of the 3-D Pore Structure and Individual Components of Preshaped Catalyst Bodies by X-Ray Imaging. *ChemCatChem* **2015**, *7* (3), 413–416. https://doi.org/10.1002/cctc.201402925.

(225) Broccoli, A.; Vollertsen, A. R.; Roels, P.; Van Vugt, A.; van den Berg, A.; Odijk, M. Local Deposition of Nanoparticles on a Pdms Microfluidic Device. *MicroTAS 2021 - 25th Int. Conf. Miniaturized Syst. Chem. Life Sci.* **2021**, No. October, 1381–1382.

(226) Vollertsen, A. R.; de Boer, D.; Dekker, S.; Wesselink, B. A. M.; Haverkate, R.; Rho, H. S.; Boom, R. J.; Skolimowski, M.; Blom, M.; Passier, R.; van den Berg, A.; van der Meer, A. D.; Odijk, M. Modular Operation of Microfluidic Chips for Highly Parallelized Cell Culture and Liquid Dosing via a Fluidic Circuit Board. *Microsystems Nanoeng.* **2020**, *6* (1), 107. https://doi.org/10.1038/s41378-020-00216-z.

(227) Tas, N. R.; Elwenspoek, M.; Haneveld, J.; Brunets, N.; Jansen, H. V. Capillary Filling of Sub-10nm Nanochannels. *J. Appl. Phys.* **2008**, *104* (1), 014309. https://doi.org/10.1063/1.2952053.

(228) Tran, D.; Zhang, C.; Choi, K. Y. Effects of Silica Support Properties on the Performance of Immobilized Metallocene Catalysts for Ethylene Polymerization. *Macromol. React. Eng.* **2022**, *16* (6), 2200020. https://doi.org/10.1002/mren.202200020.

(229) Bolner, F. M.; Blazzio, Y. R.; Lara, B. R.; Machado, F.; McKenna, T. F. L. Impact of Silica Pore Structure on the Performance of Metallocene Catalysts in Ethylene Gas-phase Polymerization. *Can. J. Chem. Eng.* **2023**. https://doi.org/10.1002/cjce.24791.

(230) Weber, B. W. J. Proceedings of the American Society of Civil Engineers. **1963**, *89* (2), 31–59.

(231) Behrens, S. H.; Grier, D. G. The Charge of Glass and Silica Surfaces. *J. Chem. Phys.* **2001**, *115* (14), 6716–6721. https://doi.org/10.1063/1.1404988.

(232) Kosmulski, M. The PH Dependent Surface Charging and Points of Zero Charge. VIII. Update. *Adv. Colloid Interface Sci.* **2020**, *275*, 102064. https://doi.org/10.1016/j.cis.2019.102064.

(233) Bo, Z.; McCullough, L. R.; Dull, S.; Ardagh, M. A.; Wang, J.; Notestein, J. Strong Electrostatic Adsorption of Pt onto SiO2 Partially Overcoated Al_2O_3 - Towards Single Atom Catalysts. *J. Chem. Phys.* **2019**, *151* (21). https://doi.org/10.1063/1.5128934.

(234) Plecis, A.; Schoch, R. B.; Renaud, P. Ionic Transport Phenomena in Nanofluidics: Experimental and Theoretical Study of the Exclusion-Enrichment Effect on a Chip. *Nano Lett.* **2005**, *5* (6), 1147–1155. https://doi.org/10.1021/nl050265h.

(235) Alemdaroglu, F. E.; Wang, J.; Börsch, M.; Berger, R.; Herrmann, A. Enzymatic Control of the Size of DNA Block Copolymer Nanoparticles. *Angew. Chem. Int. Ed.* **2008**, *47* (5), 974–976. https://doi.org/10.1002/anie.200703466.

(236) Everett, D. H. Manual of Symbols and Terminology for Physicochemical Quantities and Units. *Pure Appl. Chem.* **1972**, *31* (4), 577–638. https://doi.org/10.1351/pac197231040577.

(237) Whiting, G. T.; Chung, S. H.; Stosic, D.; Chowdhury, A. D.; Van Der Wal, L. I.; Fu, D.; Zecevic, J.; Travert, A.; Houben, K.; Baldus, M.; Weckhuysen, B. M. Multiscale Mechanistic Insights of Shaped Catalyst Body Formulations and Their Impact on Catalytic Properties. *ACS Catal.* **2019**, *9* (6), 4792–4803. https://doi.org/10.1021/acscatal.9b00151.

(238) Meirer, F.; Weckhuysen, B. M. Spatial and Temporal Exploration of Heterogeneous Catalysts with Synchrotron Radiation. *Nat. Rev. Mater.* **2018**, *3* (9), 324–340. https://doi.org/10.1038/s41578-018-0044-5.

(239) Ristanović, Z.; Hofmann, J. P.; De Cremer, G.; Kubarev, A. V.; Rohnke, M.; Meirer, F.; Hofkens, J.; Roeffaers, M. B. J.; Weckhuysen, B. M. Quantitative 3D Fluorescence Imaging of Single Catalytic Turnovers Reveals Spatiotemporal Gradients in Reactivity of Zeolite H-ZSM-5 Crystals upon Steaming. *J. Am. Chem. Soc.* **2015**, *137* (20), 6559–6568. https://doi.org/10.1021/jacs.5b01698.

(240) Dong, B.; Pei, Y.; Zhao, F.; Goh, T. W.; Qi, Z.; Xiao, C.; Chen, K.; Huang, W.; Fang, N. In Situ Quantitative Single-Molecule Study of Dynamic Catalytic Processes in Nanoconfinement. *Nat. Catal.* **2018**, *1* (2), 135–140. https://doi.org/10.1038/s41929-017-0021-1.

(241) Chen, P.; Zhou, X.; Andoy, N. M.; Han, K. S.; Choudhary, E.; Zou, N.; Chen, G.; Shen, H. Spatiotemporal Catalytic Dynamics within Single Nanocatalysts Revealed by Single-Molecule Microscopy. *Chem. Soc. Rev.* **2014**, *43* (4), 1107–1117. https://doi.org/10.1039/c3cs60215j.

(242) Keh, H. J.; Chen, P. Y. Slow Motion of a Droplet between Two Parallel Plane Walls. *Chem. Eng. Sci.* **2001**, *56* (24), 6863–6871. https://doi.org/10.1016/S0009-2509(01)00323-2.

(243) Douglas, J. F.; Johnson, H. E.; Granick, S. A Simple Kinetic Model of Polymer Adsorption and Desorption. *Science* **1993**, *262* (5142), 2010–2012. https://doi.org/10.1126/science.262.5142.2010.

(244) Frantz, P.; Granick, S. Kinetics of Polymer Adsorption and Desorption. *Phys. Rev. Lett.* **1991**, *66* (7), 899–902. https://doi.org/10.1103/PhysRevLett.66.899.

(245) Michaelis, J.; Bräuchle, C. Reporters in the Nanoworld: Diffusion of Single Molecules in Mesoporous Materials. *Chem. Soc. Rev.* **2010**, *39* (12), 4731–4740. https://doi.org/10.1039/c0cs00107d.

(246) Lebold, T.; Michaelis, J.; Bräuchle, C. The Complexity of Mesoporous Silica Nanomaterials Unravelled by Single Molecule Microscopy. *Phys. Chem. Chem. Phys.* **2011**, *13* (11), 5017–5033. https://doi.org/10.1039/c0cp02210a.

(247) Volk, A.; Kähler, C. J. Density Model for Aqueous Glycerol Solutions. *Exp. Fluids* **2018**, *59* (5), 75. https://doi.org/10.1007/s00348-018-2527-y.

(248) Janzen, J.; Song, X.; Brooks, D. E. Interfacial Thickness of Liposomes Containing Poly(Ethylene Glycol)-Cholesterol from Electrophoresis. *Biophys. J.* **1996**, *70* (1), 313–320. https://doi.org/10.1016/S0006-3495(96)79572-3.

(249) Bergman, M. J.; Pedersen, J. S.; Schurtenberger, P.; Boon, N. Controlling the Morphology of Microgels by Ionic Stimuli. *Soft Matter* **2020**, *16* (11), 2786–2794. https://doi.org/10.1039/c9sm02170a.

(250) Sahai, N.; Sverjensky, D. A. Evaluation of Internally Consistent Parameters for the Triple-Layer Model by the Systematic Analysis of Oxide Surface Titration Data. *Geochim. Cosmochim. Acta* **1997**, *61* (14), 2801–2826. https://doi.org/10.1016/S0016-7037(97)00128-2.

(251) Krauskopf, K. B. Dissolution and Precipitation of Silica at Low Temperatures. *Geochim. Cosmochim. Acta* **1956**, *10* (1–2), 1–26. https://doi.org/10.1016/0016-7037(56)90009-6.

(252) Saxton, M. J. Lateral Diffusion in an Archipelago. Single-Particle Diffusion. *Biophys. J.* **1993**, *64* (6), 1766–1780. https://doi.org/10.1016/S0006-3495(93)81548-0.

(253) Simson, R.; Sheets, E. D.; Jacobson, K. Detection of Temporary Lateral Confinement of Membrane Proteins Using Single-Particle Tracking Analysis. *Biophys. J.* **1995**, *69* (3), 989–993. https://doi.org/10.1016/S0006-3495(95)79972-6.

(254) Vrljic, M.; Nishimura, S. Y.; Moerner, W. E. Single-Molecule Tracking, in *Lipid Rafts. Methods in Molecular Biology*, McIntosh, T. J., (Ed.), Humana Press, Springer, Berlin, **2007**, 398, pp. 193–219. https://doi.org/10.1007/978-1-59745-513-8_14.

(255) Saxton, M. J. Modeling 2D and 3D Diffusion, in *Methods in Membrane Lipids. Methods in Molecular Biology*, Dopico, A.M. (Ed.), Humana Press, Springer, Berlin, **2007**, 400, pp. 295–321. https://doi.org/10.1007/978-1-59745-519-0_20.

(256) Stokes, G. G. *On the Effect of the Internal Friction of Fluids on the Motion of Pendulums,* **1850**, *Transactions of the Cambridge Philosophical Society. Vol.* 9, p. [8]

(257) Katz, J. *Introductory Fluid Mechanics*; Cambridge University Press, Cambridge, **2010**. https://doi.org/10.1017/cbo9780511761348.

(258) Islam, M. R.; Hossain, M. E. State-of-the-Art of Drilling, in *Drilling Engineering*, Elsevier, Amsterdam, **2021**, pp. 17–178. https://doi.org/10.1016/B978-0-12-820193-0.00002-2.

(259) R. Byron Bird, Warren E. Stewart, E. N. L. *Transport Phenomena*; 2nd Ed., Wiley, Hoboken, 2007.

(260) De Graaf, J.; Peter, T.; Fischer, L. P.; Holm, C. The Raspberry Model for Hydrodynamic Interactions Revisited. II. the Effect of Confinement. *J. Chem. Phys.* **2015**, *143* (8), 084108. https://doi.org/10.1063/1.4928503.

(261) *Water/Glycerol viscosity and density calculator*. http://www.met.reading.ac.uk/~sws04cdw/viscosity_calc.html.

(262) Kohonen, M. M.; Karaman, M. E.; Pashley, R. M. Debye Length in Multivalent Electrolyte Solutions. *Langmuir* **2000**, *16* (13), 5749–5753. https://doi.org/10.1021/la991621c.

(263) Haustein, E.; Schwille, P. Fluorescence Correlation Spectroscopy: Novel Variations of an Established Technique. *Annu. Rev. Biophys. Biomol. Struct.* **2007**, *36* (1), 151–169. https://doi.org/10.1146/annurev.biophys.36.040306.132612.

(264) Tas, N. R.; Haneveld, J.; Jansen, H. V.; Elwenspoek, M.; Van Den Berg, A. Capillary Filling Speed of Water in Nanochannels. *Appl. Phys. Lett.* **2004**, *85* (15), 3274–3276. https://doi.org/10.1063/1.1804602.

(265) Essafri, I.; Morineau, D.; Ghoufi, A. Microphase Separation of a Miscible Binary Liquid Mixture under Confinement at the Nanoscale. *J. Comput. Mater.* **2019**, *5, 42*. https://doi.org/10.1038/s41524-019-0179-y.

(266) Xu, X.; Ray, R.; Gu, Y.; Ploehn, H. J.; Gearheart, L.; Raker, K.; Scrivens, W. A. Electrophoretic Analysis and Purification of Fluorescent Single-Walled Carbon Nanotube Fragments. *J. Am. Chem. Soc.* **2004**, *126* (40), 12736–12737. https://doi.org/10.1021/ja040082h.

(267) Sim, L. C.; Tai, J. Y.; Khor, J. M.; Wong, J. L.; Lee, J. Y.; Leong, K. H.; Saravanan, P.; Aziz, A. A. *Carbon Dots Synthesized from Green Precursors with an Amplified Photoluminescence: Synthesis, Characterization, and Its Application*, **2019**, Springer, Cham, pp. 1–33. https://doi.org/10.1007/978-3-030-16379-2_1.

(268) Xiong, Y.; Schneider, J.; Ushakova, E. V.; Rogach, A. L. Influence of Molecular Fluorophores on the Research Field of Chemically Synthesized Carbon Dots. *Nano Today* **2018**, *23*, 124–139. https://doi.org/10.1016/j.nantod.2018.10.010.

(269) Xia, C.; Zhu, S.; Feng, T.; Yang, M.; Yang, B. Evolution and Synthesis of Carbon Dots: From Carbon Dots to Carbonized Polymer Dots. *Adv. Sci.* **2019**, *6* (23), 1901316. https://doi.org/10.1002/advs.201901316.

(270) Dhenadhayalan, N.; Lin, K.-C.; Suresh, R.; Ramamurthy, P. Unravelling the Multiple Emissive States in Citric-Acid-Derived Carbon Dots. *J. Phys. Chem. C* **2016**, *120* (2), 1252–1261. https://doi.org/10.1021/acs.jpcc.5b08516.

(271) Zhu, S.; Zhao, X.; Song, Y.; Lu, S.; Yang, B. Beyond Bottom-up Carbon Nanodots: Citric-Acid Derived Organic Molecules. *Nano Today* **2016**, *11* (2), 128–132. https://doi.org/10.1016/j.nantod.2015.09.002.

(272) Kasprzyk, W.; Bednarz, S.; Żmudzki, P.; Galica, M.; Bogdał, D. Novel Efficient Fluorophores Synthesized from Citric Acid. *RSC Adv.* **2015**, *5* (44), 34795–34799. https://doi.org/10.1039/C5RA03226A.

(273) Yoo, D.; Park, Y.; Cheon, B.; Park, M.-H. Carbon Dots as an Effective Fluorescent Sensing Platform for Metal Ion Detection. *Nanoscale Res. Lett.* **2019**, *14*, 272. https://doi.org/10.1186/s11671-019-3088-6.

(274) Yarur, F.; Macairan, J.-R.; Naccache, R. Ratiometric Detection of Heavy Metal Ions Using Fluorescent Carbon Dots. *Environ. Sci. Nano* **2019**, *6* (4), 1121–1130. https://doi.org/10.1039/C8EN01418C.

(275) Gao, X.; Du, C.; Zhuang, Z.; Chen, W. Carbon Quantum Dot-Based Nanoprobes for Metal Ion Detection. *J. Mater. Chem. C* **2016**, *4* (29), 6927–6945. https://doi.org/10.1039/C6TC02055K.

(276) He, H.; Liu, X.; Li, S.; Wang, X.; Wang, Q.; Li, J.; Wang, J.; Ren, H.; Ge, B.; Wang, S.; Zhang, X.; Huang, F. High-Density Super-Resolution Localization Imaging with Blinking Carbon Dots. *Anal. Chem.* **2017**, *89* (21), 11831–11838. https://doi.org/10.1021/acs.analchem.7b03567.

(277) Wang, Q.; Feng, Z.; He, H.; Hu, X.; Mao, J.; Chen, X.; Liu, L.; Wei, X.; Liu, D.; Bi, S.; Wang, X.; Ge,

B.; Yu, D.; Huang, F. Nonblinking Carbon Dots for Imaging and Tracking Receptors on a Live Cell Membrane. *Chem. Commun.* **2021**, *57* (45), 5554–5557. https://doi.org/10.1039/D1CC01120K.

(278) Khan, S.; Verma, N. C.; Chethana; Nandi, C. K. Carbon Dots for Single-Molecule Imaging of the Nucleolus. *ACS Appl. Nano Mater.* **2018**, *1* (2), 483–487. https://doi.org/10.1021/acsanm.7b00175.

(279) Leménager, G.; De Luca, E.; Sun, Y.-P.; Pompa, P. P. Super-Resolution Fluorescence Imaging of Biocompatible Carbon Dots. *Nanoscale* **2014**, *6* (15), 8617-8623 . https://doi.org/10.1039/C4NR01970A.

(280) Bueno, C.; Villegas, M. L.; Bertolotti, S. G.; Previtali, C. M.; Neumann, M. G.; Encinas, M. V. The Excited-State Interaction of Resazurin and Resorufin with Aminesin Aqueous Solutions. Photophysics and Photochemical Reaction. *Photochem. Photobiol.* **2002**, *76* (4), 385–390. https://doi.org/10.1562/0031-8655(2002)0760385TESIOR2.0.CO2.

(281) Brühwiler, D.; Gfeller, N.; Calzaferri, G. Resorufin in the Channels of Zeolite L. *J. Phys. Chem. B* **1998**, *102* (16), 2923–2929. https://doi.org/10.1021/jp980019c.

(282) Sharma, A.; Gadly, T.; Gupta, A.; Ballal, A.; Ghosh, S. K.; Kumbhakar, M. Origin of Excitation Dependent Fluorescence in Carbon Nanodots. *J. Phys. Chem. Lett.* **2016**, *7* (18), 3695–3702. https://doi.org/10.1021/acs.jpclett.6b01791.

(283) Kasprzyk, W.; Świergosz, T.; Bednarz, S.; Walas, K.; Bashmakova, N. V.; Bogdał, D. Luminescence Phenomena of Carbon Dots Derived from Citric Acid and Urea – a Molecular Insight. *Nanoscale* **2018**, *10* (29), 13889–13894. https://doi.org/10.1039/C8NR03602K.

(284) Fu, M.; Ehrat, F.; Wang, Y.; Milowska, K. Z.; Reckmeier, C.; Rogach, A. L.; Stolarczyk, J. K.; Urban, A. S.; Feldmann, J. Carbon Dots: A Unique Fluorescent Cocktail of Polycyclic Aromatic Hydrocarbons. *Nano Lett.* **2015**, *15* (9), 6030–6035. https://doi.org/10.1021/acs.nanolett.5b02215.

(285) Khlebtsov, B. N.; Khlebtsov, N. G. On the Measurement of Gold Nanoparticle Sizes by the Dynamic Light Scattering Method. *Colloid J.* **2011**, *73* (1), 118–127. https://doi.org/10.1134/S1061933X11010078.

(286) Ryder, A. G., Power, S., Glynn, T. J. Fluorescence-Lifetime-Based PH Sensing Using Resorufin, Glynn, T. J., Ed.**,** *Opto-Ireland 2002: Optics and Photonics Technologies and Applications*. **2003,** Proc. SPIE 4876, https://doi.org/10.1117/12.463983.

(287) Strauss, V.; Wang, H.; Delacroix, S.; Ledendecker, M.; Wessig, P. Carbon Nanodots Revised: The Thermal Citric Acid/Urea Reaction. *Chem. Sci.* **2020**, *11* (31), 8256–8266. https://doi.org/10.1039/D0SC01605E.

(288) Williams, A. T. R.; Winfield, S. A.; Miller, J. N. Relative Fluorescence Quantum Yields Using a Computer-Controlled Luminescence Spectrometer. *Analyst* **1983**, *108* (1290), 1067. https://doi.org/10.1039/an9830801067.

(289) Zu, F.; Yan, F.; Bai, Z.; Xu, J.; Wang, Y.; Huang, Y.; Zhou, X. The Quenching of the Fluorescence of Carbon Dots: A Review on Mechanisms and Applications. *Microchim. Acta* **2017**, *184* (7), 1899–1914. https://doi.org/10.1007/s00604-017-2318-9.

(290) Liu, N.; Liu, J.; Kong, W.; Li, H.; Huang, H.; Liu, Y.; Kang, Z. One-Step Catalase Controllable Degradation of C_3N_4 for N-Doped Carbon Dot Green Fabrication and Their Bioimaging Applications. *J. Mater. Chem. B* **2014**, *2* (35), 5768. https://doi.org/10.1039/C4TB00772G.

(291) Hayes, W. I.; Joseph, P.; Mughal, M. Z.; Papakonstantinou, P. Production of Reduced Graphene Oxide via Hydrothermal Reduction in an Aqueous Sulphuric Acid Suspension and Its Electrochemical Behaviour. *J. Solid State Electrochem.* **2015**, *19* (2), 361–380. https://doi.org/10.1007/s10008-014-2560-6.

(292) Carnevale, L. *Microreactors for in Situ Single Catalyst Particle Characterization Using Advanced Imaging Techniques*, University of Twente, Enschede, The Netherlands, **2023**. https://doi.org/10.3990/1.9789036557566.

List of abbreviations

AAI:	Akzo Nobel Accessibility Index
AFM:	Atomic Force Microscopy
BC:	Boundary Condition
BET:	Brunauer, Emmet and Teller
BSE:	Backscatter Electron
CA:	Carboxylic Acid
CD:	Carbon Dot
CLSM:	Confocal Laser Scanning Fluorescence Microscopy
DESY:	Deutsches Elektronen-Synchrotron
DLS:	Dynamic Light Scattering
DMF:	Dimethylformamide
EDL:	Electric Double Layer
EM:	Electron Microscopy
EMCCD:	Electron-Multiplying Charge-Coupled Device Detector
E-MSD:	Ensemble Averaged Mean Squared Displacement
EV:	Eigen Vector
FCC:	Fluid Catalytic Cracking
FIB-SEM:	Focused Ion Beam Scanning Electron Microscopy
FRAP:	Fluorescence Recovery After Photobleaching
FRC:	Fourier Shell Correlation
HAADF:	High-Angle Annular Dark-Field
HRTEM:	High-Resolution Transmission Electron Microscopy
iART:	Iterative Algebraic Reconstruction Technique

IFM:	Interference Microscopy
IR:	Infrared
IRM:	Infrared Microscopy
MOF:	Metal Organic Framework
MSD:	Mean Squared Displacement
NASCA:	Nanometer Accuracy by Stochastic Chemical Reactions
PDMS:	Polydimethylsiloxane
PEG:	Polyethylene Glycol
PFG NMR:	Pulsed-Field Gradient Nuclear Magnetic Resonance
PL:	Photoluminescence
PP:	Polypropylene
PSF:	Point Spread Function
PZC:	Point of Zero Charge
QD:	Quantum Dot
QENS:	Quasi-Elastic Neutron Scattering
RMS:	Room Mean Squared
SE:	Secondary Electron
SEM:	Scanning Electron Microscopy
SLAC:	Synchrotron Linear Acceleration Center
SMLM:	Single-Molecule Localization Microscopy
SPT:	Single-Particle Tracking
SSRL:	Stanford Synchrotron Radiation Lightsource
STEM:	Scanning Transmission Electron Microscopy
TEM:	Transmission Electron Microscopy
TE-MSD:	Time–Ensemble Averaged Mean Squared Displacement
TLD:	Through-The-Lens Detector
TXM:	Transmission X-ray Microscopy
XRD:	X-ray Diffraction
XRM:	X-ray Microscopy

List of publications

Rafael Mayorga González†, Miguel Rivera-Torrente†, Nikolaos Nikolopoulos, Koen W. Bossers, Roozbeh Valadian, Joaquín Yus, Beatriz Seoane, Bert M. Weckhuysen, Florian Meirer, Visualizing Defects and Pore Connectivity within Metal-Organic Frameworks by X-ray Transmission Tomography. Chem. Sci., 2021, 12, 8458-8467

Alessia Broccoli†, Luca Carnevale†, Rafael Mayorga González†, Joren Dorresteijn, Bert M. Weckhuysen, Wouter Olthuis, Mathieu Odijk, and Florian Meirer, Accessibility Study of Porous Materials at the Single-particle Level as Evaluated within a Microfluidic Chip with Fluorescence Microscopy, Chem Catal. 2023, 3, 100791.

Rafael Mayorga González†, J.J. Erik Maris†, Marita Wagner, Yadolah Ganjkhanlou, Johan G. Bomer, Maximilian J. Werny, Freddy T. Rabouw, Bert M. Weckhuysen, Mathieu Odijk, Florian Meirer, Fluorescent-Probe Characterization for Pore-Space Mapping with Single-Particle Tracking, Angew. Chem. Int. Ed. 2023, 62, e202314528

Ina Vollmer†, Michael J. F. Jenks†, Rafael Mayorga González, Dr. Florian Meirer, Prof. Dr. Bert M. Weckhuysen, Plastic Waste Conversion over a Refinery Waste Catalyst. Angew. Chem. Int. Ed. 2021, 60, 16101.

†These authors contributed equally to this work.

Samenvating

Massa transport is een cruciaal aspect in heterogene katalyse, omdat het de activiteit, selectiviteit en de totale levensduur van een katalysatormateriaal kan beïnvloeden. Daarom heeft het rationele geometrische ontwerp van de poriën een immens potentieel voor verdere verbetering van de katalytische prestaties in bestaande vaste katalysatoren en voor het maken van nieuwe poreuze katalysatormaterialen. Om te onderzoeken hoe de syntheseparameters de poreuze netwerken van de katalysatormaterialen beïnvloeden, zijn porositeits-karakterisatie-methoden met een hoge resolutie en een hoge doorvoercapaciteit vereist. De momenteel beschikbare karakterisatie-methoden hebben echter enkele uitdagingen. Enerzijds vertrouwen verschillende methoden op analytische bulkmetingen, waarbij de heterogeniteit binnen en tussen katalysatordeeltjes wordt genegeerd. Anderzijds zijn methoden met hoge resolutie extreem complex en duur, en kunnen ze maar een beperkt aantal deeltjes meten. In dit proefschrift worden nieuwe analytische methoden verkend om de poriënruimte van heterogene katalysatoren te bestuderen met behulp van fluorescente probes.

In **Hoofdstuk 2** hebben we Transmission X-ray Microscopy (TXM) gebruikt, een state-of-the-art hoge resolutie techniek, om voor het eerst de macroporositeit van een MIL-47(V) Metal Organic Framework (MOF) kristal te bestuderen. Macroporeuze defecten - tot op de micrometer schaal - waren aanwezig in het hele katalysatordeeltje, wat werd bevestigd door te snijden met een Focus Ion Beam (FIB) , en via Scanning Electron Microscopy (SEM). Het bleek echter dat de macroporeuze netwerken binnen MIL-47(V) zeer lokaal en slecht verbonden waren. Daarom hebben deze defecten waarschijnlijk slechts een beperkt effect op de massatransport binnen het MOF kristal. Interessant genoeg vertonen de macroporeuze netwerken een voorkeursoriëntatie die gerelateerd zou kunnen zijn aan de groei van het MOF kristal.

In **Hoofdstuk 3** wordt een goedkope en eenvoudige analysemethode gepresenteerd om de toegankelijkheid van individuele poreuze deeltjes te karakteriseren. Hiervoor wordt de temporele opname van een fluorofoor in de vaste katalysatordeeltjes gebruikt. De apparatuur die nodig is om deze experimenten uit te voeren, bestaat uit een conventionele fluorescentie microscopie opstelling en een PDMS-gemaakt microfluïdisch apparaat en kan tientallen vaste katalysatordeeltjes tegelijkertijd bestuderen. Om de methode te demonstreren, hebben we poreuze silica modeldeeltjes gebruikt met uniforme verdelingen van poriegrootte en vergelijkbare porositeiten. Interessant genoeg werden er aanzienlijke opname heterogeniteiten tussen deze deeltjes waargenomen, ondanks dat de deeltjes binnen een monster relatief homogeen zijn, wat het belang van het bestuderen van materialen op het niveau van individuele deeltjes benadrukt. Bovendien correleerde de toegankelijkheid van de deeltjes positief met de poriegrootte. Ook is van belang dat het variëren van de probe-host elektrostatische interacties via de pH-waarde en de ionsterkte van het systeem resulteerde in significante verschillen in massatransport. Als deze elektrostatische interacties worden onderdrukt (bijv. via pH-omstandigheden), wordt de poriestructuur dominant voor het opnameproces, wat resulteert in een hogere gevoeligheid voor de kenmerken van het porienetwerk.

Hoofdstukken 4, 5 en 6 verkennen de mogelijkheid om single molecule(particle) localization microscopy (SMLM) en single particle tracking (SPT) te gebruiken om poreuze katalysatormaterialen te verkennen en in kaart te brengen met een subdiffractie-limietresolutie.

Vanwege de probe-host interacties is het bewegingsgedrag dat wordt waargenomen in SPT-experimenten in poriën extreem complex en heterogeen. Om eigenschappen van de poriënruimte te achterhalen, is het daarom noodzakelijk om eerst het bewegingsgedrag van de probe in goed

gedefinieerde poriën met bekende afmetingen en samenstelling te begrijpen. Om dit probleem aan te pakken, introduceren we in **Hoofdstuk 4** een tweedimensionaal (2D) silica model poriën systeem gemaakt met lithografie en chemisch etsen. Hier onderzochten we hoe het diffusie- en adsorptiegedrag van quantum-dots (QDs) wordt beïnvloed door de pH-waarde binnen 2D poriensystemen. In onze experimenten kan adsorptie niet worden onderscheiden van probe immobilisatie vanwege een significante toename van hydrodynamische weerstand dicht bij de poriewanden. We verwijzen daarom naar beide fenomenen als trapping. De duur en frequentie van trapping gebeurtenissen konden worden aangepast via de pH-waarde. Onder basische omstandigheden kon trapping bijna volledig worden onderdrukt, mogelijk vanwege een verhoogde probe-host elektrostatische afstoting. Verder demonstreerden we met succes het gebruik van QDs onder bijna niet-trapping omstandigheden voor het in kaart brengen van de poriënruimt van eendimensionale silica poriën en van een reëel polymerisatie katalysator ondersteunend deeltje, in resoluties in de orde van tientallen nanometers. Ten slotte stellen we een protocol voor om een volledige porositeitsverkenning in toekomstige SPT-mapping experimenten te waarborgen.

Eerder is aangetoond dat de hydrodynamische weerstand die door colloïden wordt ervaren, significant toeneemt in opsluiting, wat leidt tot een vermindering van de diffusiecoëfficiënt. In **Hoofdstuk 5** onderzoeken we of we dit kunnen benutten om poriegroottes in drie dimensies te onderzoeken, op basis van lokale diffusiecoëfficiënten gemeten met SPT. Daarom hebben we de model-porie gepresenteerd in **Hoofdstuk 4**, aangepast om verschillende poriedieptes te creëeren en bestudeerden we het bewegingsgedrag van individuele QDs onder niet-trapping omstandigheden. De concentratie van probes binnen de 2D poriën correleerde positief met poriediepte, wat bevestigde dat de poriën inderdaad verschillende afmetingen hadden. Bovendien ontdekten we de aanwezigheid van clusters binnen de grotere poriën en slaagden we erin deze uit de analyse te verwijderen. Verrassend genoeg vertoonden de clustervrije trajecten vrijwel dezelfde diffusiecoëfficiënten en was de duur van de tijdelijke trapping gebeurtenissen vrijwel gelijk voor alle bestudeerde poriedieptes. Dit stond in contrast met de hydrodynamische weerstand simulaties die we uitvoerden, waarbij werd voorspeld dat de diffusiecoëfficiënt aanzienlijk zou variëren met de 2D poriediepte. Hoewel meer werk nodig is om deze zeer intrigerende resultaten te begrijpen, kunnen we op dit moment concluderen dat dit probe-host-oplosmiddel systeem, op basis van de gemeten diffusiecoëfficiënt, niet geschikt is voor het onderzoeken van poriegroottes tussen 50 nm en 150 nm.

De quantum-dot probes die in **Hoofdstukken 4 en 5** werden gebruikt, zijn groter (diameter: ~14 nm) dan een significant deel van de poriën die typisch aanwezig zijn in hiërarchisch complexe poreuze katalysatoren. Daarom onderzochten we het gebruik van kleinere carbon-dot probes voor de verkenning van poriënruimte in **Hoofdstuk 6**. We slaagden erin de carbon-dot probes in te bedden met resorufin, waardoor hun fluorescerende eigenschappen en traceerbaarheid verbeterden. Dit stelde ons in staat om de carbon-dot vrije diffusie in een vloeistof met hoge viscositeit voor het eerst te volgen en hun grootteverdeling te bepalen. Hun kleine omvang (modus diameter: 2 nm) maakte het voor ons echter onmogelijk om ze binnen onze 2D model-porie te volgen. Echter, tijdelijke trapping gebeurtenissen konden worden waargenomen en gekwantificeerd, wat aantoont dat hun duur niet afhankelijk is van de poriegrootte. Bovendien konden we carbondots volgen binnen mesoporeuze silica deeltjes die ontoegankelijk waren voor de probes die in **Hoofdstukken 4 en 5** werden gebruikt, wat hun potentieel aantoont om materialen met kleinere poriën te verkennen. Verder werden tijdelijke trapping gebeurtenissen van verschillende duur waargenomen op niet-beperkte oppervlakken met verschillende samenstellingen. Mogelijk kan deze parameter worden gebruikt om materialen met verschillende samenstellingen in kaart te brengen. Ten slotte suggereerde de confocale laser scanning microscopie beelden van met -carbon-dots geladen mesoporeuze silica deeltjes, dat het trapping gedrag ook kan worden aangepast via de pH-waarde van het systeem.

Acknowledgements

This work would not have been possible without the following people:

Florian, there are no words to express how grateful I am to have had you as a daily supervisor. Not only are you one of the smartest people I know, you are also an incredibly kind and positive person. It didn't matter how stressed or worried I was about my research; every time I had a meeting with you, I came out of your office with a smile and the certainty that things were going to work out in the end. You cannot imagine how important that was for me. I hope we will stay in touch in the future. I wish you all the best, and I know that you will continue pursuing the truth and not 'shiny' papers.

Bert and **Mathieu**, I am extremely thankful for the framework that you created for my PhD within the MCEC consortium. The opportunities you provided were truly unparalleled. Not only did I have access to state-of-the-art equipment at two leading universities, which significantly enhanced the quality and scope of my research, but I also had the privilege of engaging in scientific discussions with two world-class experts in the fields of catalysis and nanofabrication. I am immensely grateful for your support and mentorship. None of this would have happened if it weren't for you, and I am deeply appreciative of all the opportunities and knowledge you have imparted to me. Thank you for everything!

Erik and **Yadi,** I think I owe at least four chapters of the thesis to you. **Yadi**, you added a magical drop of base to a sample, and that completely changed the course of my PhD—a true lab magician. **Erik**, on the other hand, taught me about object-oriented programming, optics, Illustrator, scientific writing… The list is long. I was super lucky to have collaborated with such ridiculously smart people, but more importantly, I really enjoyed spending time with you outside of the lab!

Miguel, apenas comencé el doctorado nos tomamos un café y me dijiste que tenias unos datos por ahí que nadie sabia como analizar. Al poco tiempo estábamos escribiendo un paper juntos sobre eso. Si no hubiera sido por ti, me hubiera pasado el primer año del doctorado perdido sin un objetivo fijo. No te imaginas lo importante que fue eso además de mil consejos que me diste. Gracias también por tantas frases célebres ("reimburse, reimburse, reimburse") y momentos mágicos en back and fourth.

The PhD was nice and everything, but the really important thing is the friends that one makes along the way. It didn't matter if we were on an inflatable boat on the canals of Utrecht, hiking in the middle of nowhere in "Perah", or running away from giants in Limburg, the **nautical people** made this period unforgettable. **Jenksy**, watching your transformation from a mayonnaise-loving pirate to an enlightened human has been amazing and inspiring, thank you so much for that. **Ash**, thank you for bringing joy into the group, always singing and dancing around. **Maddy**, thank you for making the "guy broth" possible in Oranjezon and for being the most flexible person I know. **Iris**, thanks for being the motor of our inflatable boat. **Møx**, thank you for all the nice afternoons playing spike ball at the park, reminding me that I have to go to the gym. **Koekie**, thank you for all the cynicism at work events and conferences; you made me feel at home. **Emma**, thanks for all the conversations about life at Francesco's balcony long into the night. Thank you, **nautical people**, I love you guys!

Sopravvivere a una pandemia non è facile per nessuno, ma io ho avuto la fortuna di trovare una nuova famiglia mentre facevo la quarantena. **Francesco**, grazie per aver creato questa situazione, ancora non ci credo che siamo andati a vivere lì tutti insieme, ma è stato uno dei periodi più belli della mia vita. Anche se te ne sei andato, continui a essere il dio di Kanaleneiland. Grazie pure per esserci stato sempre per brindare il giorno prima delle feste e dei viaggi perché eravamo troppo gassati. **Laurita**, grazie per averti presa cura di noi, sono certo che io e lo zio saremmo morti senza di te. Grazie per

tutte le birre in balcone, tutte le cose buonissime che hai cucinato sempre e per riempirci di ispirazione con il tuo sito Wikipedia! **Ciccio**, grazie per essere stato presente ogni sera sul telefono della zia e per tutte le jam session, non vedo l'ora che ti trasferisca più vicino. Vorrei ringraziare la multidottoressa Fornero per i bei momenti suonando "La canzone del sole" con la chitarra, per gli allenamenti in calisthenics e per apprezzare i miei piatti pieni di cumino. Lukas, danke, dass du immer mitgemacht hast, als ich versucht habe, auf Portugiesisch zu sprechen, saudade! Vi voglio un sacco di bene, ragazzi!

Maron sant..... Non posso continuare senza ringraziare **Luca** e **Alessia**. Veramente non penso di aver potuto fare questo dottorato se non fosse per voi! Mi sono goduto ogni after meeting dopo aver parlato con il mago, tutti i beamtrip lavorando tutta la notte mangiando pistacchi e imparando napiletan. Ma ancora più belli dei beamtrip sono stati i viaggi dopo! Anche se abbiamo capito di non avere neanche un po' di flow, è stato "bbbbbbbbbellissimo ragazzi!". Luca, grazie per aver intrappolato tante particelle, se non fosse per te non ci avrebbero mandati in tutti questi posti, e Alessia, grazie per aver sempre managerato la situazione, senza di te Luca e io non saremmo riusciti a prendere un solo aereo! Vi voglio tanto bene!

Vorrei anche ringraziare a **Guliver**, il planetary speaker, donna **Ilaria**, **Giorgio** e **Aida**. Mi diverto sempre un casino quando vi vedo. Non domentichero mai quell pranzo di natale al panuozzo dove ci siamo bevuti tutto il limoncello del locale!

The final stages of writing this little booklet were very stressful and emotionally challenging. **Sarah**, you have been incredibly supportive and kind to me in a very difficult moment and I will never forget that. Thank you so much, I love you!

Al final del día hay un pequeño grupo de personas que hicieron que este librito y toda mi trayectoria de vida sean posibles. Me gustaría dedicarle unas palabras a la mejor familia del mundo. **Mamá**, gracias por el cariño infinito que nos has dado todos estos años, gracias por haber pasado varias horas a la semana hablando por teléfono, escuchando mis problemas y alegrías. Gracias por haber rezado por mi hasta que a la virgen le dió un burnout. **Jime**, gracias por haber sido como mi segunda mamá durante mi adolescencia y por seguir siendo un punto de soporte y estabilidad esencial para todos. **Kiko**, gracias por haber siempre cuestionado todo, por hacer que quiera tener un trabajo con sentido y por haberme hecho descubrir la música. **Daniel**, si no fuera por ti no se me hubiera pasado por la cabeza hacer mil cosas: ir a estudiar a Alemania, el intercambio en Londres, aprender a programar, el doctorado,... No tienes idea de lo importante que ha sido para mí tener a un hermano que cada vez ponga la valla más alta. Aparte de todo lo que nos divertimos cuando nos vemos, tus consejos siempre han sido importantísimos para mí. Es lo máximo tener un hermano con una experiencia de vida tan parecida a la mía y que entienda lo que implica escribir este librito. **Papá** tienes una habilidad para mantenerte optimista aunque el mundo se esté cayendo a pedazos, eso vale oro. Gracias por enseñarnos desde muy chiquitos a atrevernos, a confiar en que si le ponemos ganas a las cosas, todo va a salir bien. Gracias por fomentar la curiosidad y el interés por temas técnicos. Gracias por trabajar como un loco y al mismo tiempo ser un papá increíble el fin de semana. Todo lo que he logrado en mi vida se los debo a ustedes, los quiero muchísimo!

About the author

Rafael Mayorga González was born on September 10, 1992, in Lima, Peru. After completing his secondary education at the Alexander von Humboldt High School in 2010, he pursued a bachelor's degree in process engineering at the Karlsruhe Institute of Technology (KIT). During his undergraduate studies, Rafael spent a year at University College London and completed his bachelor's thesis on the rheology of capillary suspensions under the supervision of Professor Norbert Willenbacher.

He continued his education at KIT, specializing in thermal and environmental process engineering for his master's degree. His master's thesis, focused on converting CO_2 to methanol, was a collaborative effort between the Fraunhofer Institute for Solar Energy Systems (ISE) and the Engler-Bunte Institute, supervised by Professor Thomas Kolb.

Post-graduation, Rafael joined the Fraunhofer Institute for Solar Energy Systems as a researcher, where he worked on projects related to E-fuels. In 2019, he relocated to Utrecht, Netherlands, to start a joint doctorate program involving the Inorganic Chemistry and Catalysis group at Utrecht University and the Bios Lab-on-a-chip group at the University of Twente. Supervised by Professor Bert Weckhuysen, Dr. Florian Meirer, and Professor Mathieu Odijk, his research was funded by the Gravitation Program Netherlands Center for Multiscale Catalytic Energy Conversion (MCEC). His PhD thesis includes significant findings from this research, some of which have been published in peer-reviewed scientific journals and presented at international conferences. As part of his project, Rafael supervised several MSc students as well as theoretical courses.